Planar Hall Sensor for Influenza Immunoassay

Ejsing, Louise Wellendorph; Hansen, Mikkel Fougt

Publication date:
2006

Document Version
Publisher's PDF, also known as Version of record

Citation (APA):
Ejsing, L. W., & Hansen, M. F. (2006). Planar Hall Sensor for Influenza Immunoassay.

Ph.D. Thesis, s021568

Planar Hall sensor for influenza immunoassay

Louise Wellendorph Ejsing

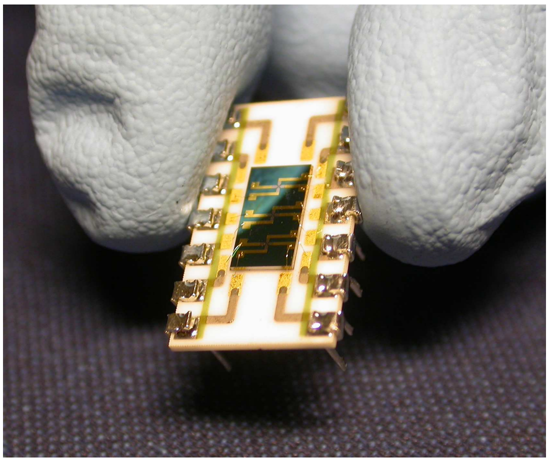

Supervisors: Aric K. Menon and Mikkel F. Hansen

MIC – Department of Micro and Nanotechnology
Technical University of Denmark

May 5, 2006

Abstract

The title of this thesis is *Planar Hall sensor for influenza immunoassay.* The thesis considers fabrication, characterization and demonstration of planar Hall sensors for influenza immunoassay detection.

The goal of this research project is, first of all, to design a magnetic sensor capable of detecting magnetic beads. These beads are polystyrene spheres with sizes ranging between a few hundred nanometers to a few micrometers, and can be magnetized in an applied field. In order to integrate this sensor into a device for clinical tests the sensing principle has to be sensitive as well as reliable. A signal-to-noise study for various sensor types, GMR, spin-valve, and planar Hall sensors, points towards the planar Hall effect as a promising sensing principle for DC detection. DC detection will probably be easier to handle on a chip than AC detection.

A second goal is to demonstrate a relevant application, where conventional techniques have failed. *Statens Serum Institut* has provided antibodies and antigens for the demonstration of influenza detection.

The theoretical analysis of single bead signal shows that the planar Hall sensor has potential for single bead detection. The active area of the sensor has to be designed to match the specific bead, and using areas below $1\mu\text{m}\times1\mu\text{m}$ offers the possibility of detecting a single 50 nm bead. The theoretical detection limit as a function of sensor size presents great possibilities for the planar Hall sensor, the main reason being its low noise level.

Following the single bead study, theoretical investigation of the specific sensor and bead combination used in the experimental part of this thesis is presented. The fabricated sensors $20\mu\text{m}\times20\mu\text{m}$ are used with 250 nm Nanomag-D beads. These sensors and beads are used for the influenza experiments. The approximate theoretical signal from a monolayer of beads is $\beta \approx 0.024(\xi_{\text{outside}}-\xi_{\text{sensor}})$, where ξ is the layer coverage. β is the field produced by the beads normalized to the applied field and can be compared to the experimental data.

Furthermore, the effect of screening the positive contribution from the total signal by placing a simple barrier adjacent to the sensor cross is evaluated. The barrier can be constructed in SU-8, which is used for attachment of biochemical species. Theoretically, the signal from a monolayer of magnetic beads can be enhanced by this procedure. Additionally, the capture of beads by fringing fields produced at the voltage leads can be reduced. The fringing fields capture beads at areas insignificant to the measurements but biologically active material would be lost at these capture sites.

Next, design, fabrication and characterization of planar Hall sensors for the influenza immunoassay is presented. The chip design match the prospect of detecting just a few 250 nm beads, and is prepared for use in biological experiments.

First the fabrication and results with nickel sensors are presented. Based on these results, the work with exchange bias for constructing an easy direction instead of an easy axis in permalloy planar Hall sensors continues. The nickel sensors are fabricated in MIC's clean room and constitute a compromise with respect to magnetic material, since only nickel is available in the clean room. However, the nickel sensors prove the concept of magnetic bead detection with planar Hall sensors.

The permalloy sensors are optimized with respect to the magnetic material and design of an easy direction. In an easy axis two equivalent magnetic states are present, which give identical electric signals with opposite signs. Exchange coupling of the easy axis to an antiferromagnet yields an easy direction. Thus the magnetization has always the same starting point in the absence of an applied field. This principle is utilized in the optimized sensors. Using DC sensor currents, these sensors can measure magnetic beads without a field applied. The magnetic field generated by the current is sufficient to magnetize the beads, which will be an advantage when designing a point-of-care chip.

Using lock-in technique, *i.e.* AC sensor currents, on average the field produced by the current vanishes. Hence, the bead field measured by the sensor is solely produced by the applied field. The planar Hall sensors' electronic noise is determined in a setup where external noise is reduced. Exactly the low noise level contributes to the high sensor sensitivity. However, the setup can be improved in several ways. A preamplifier for the lock-in amplifier together with increasing the applied field and the sensor current, would yield a factor 50-100 on the bead signal-to-noise. This is sufficient to offer single 250 nm bead detection with the studied sensors.

Hereafter, measurements of sensor signal versus antibody concentration are presented. Biotinylated influenza antibodies are immobilized on the surface of a planar Hall sensor. Afterwards magnetic beads with streptavidin surface coating bind to the biotin on the antibodies. The signal is increasing for increasing antibody concentration. Maximum value is $\beta = 0.011$ (normalized to the applied field), *i.e.* of the same order of magnitude as the theoretical estimate.

Finally, the actual influenza immunoassay detection is presented. First fluorescence detection with directly labelled detector antibodies. Second magnetic detection, where the total sandwich assay is performed on top of the planar Hall sensors. The detection principle is thus magnetic beads with influenza antibodies on the surface. S/NC is obtained as the signal from the sample (S) divided by the signal from the negative control (NC). $S/NC = 2$ is found for the magnetic immunoassay, and $S/NC = 5$ for the fluorescence immunoassay. The fluorescence assay is optimized, the magnetic is not.

The results obtained with the planar Hall sensors are promising for point-of-care diagnostics. However, the SU-8 design can be developed further.

Resumé

Denne Ph.D. afhandlings titel er *Planar Hall sensor anvendt på influenza immunkemisk detektion*. Afhandlingen omhandler fremstilling, karakteristik og demonstration af planare Hall sensorer til anvendelse indenfor influenza immunkemisk detektion.

Målet med dette forskningsprojekt er først og fremmest at designe en magnetisk sensor, som er i stand til at måle tilstedeværelsen af små magnetiske polystyren kugler. Disse kugler varierer i størrelsesorden fra hundrede nanometer til et par mikrometer i diameter og er magnetisérbare i et påtrykt magnetfelt. For at kunne integrere denne sensor i en klinisk test, skal sensorprincippet være følsomt og samtidig pålideligt. Studier af signal-støj forhold for flere sensortyper, GMR sensorer, spin-ventiler og planare Hall sensorer, peger på den planare Hall sensor som bedste valg mht. DC signal-støj forhold. DC målinger vil formentlig være lettere at håndtere på chip-niveau end AC målinger.

Et andet mål med Ph.D. studiet er at demonstrere de planare Hall sensorer i en relevant anvendelse, hvor konventionelle metoder har været utilstrækkelige. Statens Serum Institut har leveret antistoffer og antigener til demonstrationen af influenza detektion.

En omfattende teoretisk analyse af sensorer og små magnetiske kugler foretages for at belyse sensorernes anvendelsesmuligheder. Den teoretiske analyse af signalet fra en enkelt 250 nanometer magnetisérbar kugle viser, at de studerede planare Hall sensorer har potentiale for at måle tilstedeværelsen af blot en enkelt kugle. Dette gælder for de under Ph.D. studiet fremstillede sensorer. For at måle tilstedeværelsen af endnu mindre kugler, kan sensorerne designes til at matche anvendelsen. F.eks. kan 50 nanometer kugler måles, hvis det aktive areal er mindre end $1\mu\mathrm{m} \times 1\mu\mathrm{m}$. Den teoretiske grænse for detektion af magnetiske kugler som funktion af sensorstørrelse præsenterer gode muligheder for de planare Hall sensorer. En af grundene er disse sensorers lave interne støjniveau.

Efter studierne med kun en enkelt magnetisk kugle kommer en grundig teoretisk analyse af de renrumsfremstillede sensorer ($20\mu\mathrm{m} \times 20\mu\mathrm{m}$ sensorareal) i kombination med 250 nanometer store Nanomag-D magnetiske kugler. Netop sensorer og kugler af disse dimensioner benyttes til de efterfølgende eksperimentelle influenza målinger. Et teoretisk overslag på signalet fra et monolag af disse kugler er $\beta \approx 0.024(\xi_{\mathrm{outside}} - \xi_{\mathrm{sensor}})$, hvor ξ er dækningsgraden i forhold til et tætpakket monolag. β er normaliseret til det påtrykte felt og kan således sammenlignes med måleresultaterne.

Til sidst i det teoretiske afsnit kigges der på effekten af at skærme kuglernes positive bidrag med en barriere. Den omtalte barriere kan nemt fremstilles af SU-8, som også benyttes til biokemisk binding af biologisk aktivt materiale. De positive bidrag kan mere eller mindre fjernes ved at placere en sådan barriere ved siden af sensoren. Tilmed kan indfangning af magnetiske kugler pga. randfelter ved spændingslederne mindskes med denne barriere. Randfelterne indfanger magnetiske kugler på områder, der er af ringe betydning i forhold til målingerne, men biologisk materiale går tabt ved indfangningen.

Efter de teoretiske analyser følger beskrivelsen af det eksperimentelle arbejde. Her præsenteres design, fremstilling og karakteristik af planare Hall sensorer. Chip-designet matcher muligheden for at måle tilstedeværelsen af ganske få 250 nm magnetiske kugler. Chippen er skabt med henblik på brug i biologiske ekperimenter.

Først præsenteres fremstillingen og resultaterne med nikkelsensorer. De opnåede resultater danner grundlag for det videre arbejde med anvendelse af *exchange bias* til at lave en nem retning i stedet for en nem akse i permalloy baserede planare Hall sensorer. Nikkel sensorerne er fremstillet i MIC's renrum og udgør et kompromis i forhold til det magnetiske materiale, da det kun er nikkel, der anvendes i renrummet. Trods deres inoptimale egenskaber beviser nikkelsensorerne imidlertid, at den planare Hall effekt kan benyttes til at måle tilstedeværelsen af magnetiske kugler.

Permalloy sensorerne er optimerede mht. magnetisk materiale og design af en nem retning. Har man en nem akse, vil der være to ækvivalente magnetiske tilstande, som giver samme signalstyrke med modsat fortegn. Ved at *exchange*-koble den nemme akse til en antiferromagnet opnås en nem retning. Således har man altid samme udgangspunkt for magnetiseringen i fraværet af et ydre felt. Dette princip anvendes i de optimerede sensorer. Disse sensorer kan måle tilstedeværelsen af magnetiske kugler i fraværet af et påtrykt felt, når der anvendes DC strøm gennem sensoren. Magnetfeltet genereret fra strømmen er nok til at magnetisere kuglerne, hvilket vil være en fordel i en færdig chip.

Ved brug af *lock-in* teknik, dvs. AC strøm, magnetiseres kuglerne ikke af strømmen. Derfor magnetiseres kuglerne udelukkende af det påtrykte felt. Den elektriske støj i de planare Hall sensorer bestemmes eksperimentelt i en opstilling, hvor udefrakommende støj er minimeret. Netop det lave støjniveau er med til at give sensorerne deres høje følsomhed. Opstillingen kan imidlertid forbedres. Hvis en forforstærker til *lock-in* forstærkeren benyttes, og feltet og sensorstrømmen øges til det maksimale, kan signal-støj forholdet fra en magnetisk kugle forbedres 50-100 gange. Det ville betyde, at en enkelt 250 nanometer kugle kunne måles med de fremstillede sensorer.

Efterfølgende præsenteres målinger af sensorsignal som funktion af antistofkoncentration på overfladen. Der benyttes biotinyleret influenzaantistof, som fastgøres ovenpå en planar Hall sensor. Dernæst bindes magnetiske kugler med streptavidin på overfladen til biotinen på antistofferne. Signalet er voksende som funktion af antistofkoncentration. Den maksimalt opnåede værdi er $\beta = 0.011$ (normaliseret til det påtrykte felt). Denne værdi ligger indenfor størrelsesordenen af det teoretiske estimat for et monolag.

Afslutningsvis præsenterer afhandlingen egentlig immunkemisk detektion af influenza. Først fluorescensdetektion med direkte mærkede detektorantistoffer. Dernæst magnetisk detektion, hvor hele sandwichen er lavet ovenpå de planare Hall sensorer. Som detektionsprincip er således anvendt magnetiske kugler med influenzaantistoffer på overfladen. Resultatet af disse eksperimenter er $S/NC = 2$ for magnetisk detektion, hvor S/NC er signalet fra prøven divideret med signalet fra den negative kontrol. For fluorescens målingernes opnås $S/NC = 5$, men den immunkemiske sandwich er optimeret for fluorescens, og ikke for magnetisk detektion.

Resultaterne for de planare Hall sensorer ser lovende ud for diagnosticeringschips. Desuden kan SU-8 designet udvikles yderligere med forbedring af detektionsprincippet som resultat.

Preface

The work presented in this thesis is part of the road towards a magnetic approach in bioassaying. At least for the writer it has been a journey with many challenges, in biological as well as physical sciences. The work is not meant as a complete prototype of an influenza chip, only to demonstrate the planar Hall sensor's capability as sensing principle. Some improvements will be suggested though they are not experimentally validated due to time limitations of the project.

This thesis has been written as part of the requirements for obtaining the Ph.D. degree at the Technical University of Denmark (DTU). The Ph.D. project has been carried out at the Department of Micro and Nanotechnology (MIC) at DTU in the time period July 1st 2002 to May 5th 2006.

This Ph.D. project has been a part of the Magnetic Systems research group, Micro Electro Mechanical Systems (MEMS) section, at MIC, and it has been financed by a DTU Ph.D. grant. This project has been supervised by Professor Aric K. Menon and Associate Professor Mikkel F. Hansen, both employed at MIC.

Part of the work was carried out in the group of Prof. Freitas at Institute of Engineering of Systems and Computers - Microsystems and Nanotechnology (INESC-MN), Portugal, from September 1st 2003 to December 1st 2003.

Louise Wellendorph Ejsing
MIC – Department of Micro and Nanotechnology
Technical University of Denmark
5 May 2006

Acknowledgement

The author would like to thank the supervisors of the project for stimulating discussions and guidance towards the ultimate goal.
Professor Aric K. Menon, main supervisor during the main part of the project, who sadly passed away before the completion of the project.
Associate Professor Mikkel F. Hansen, co-supervisor and main supervisor during the last five months of the project.

The author acknowledges the contribution during the external stay in the group of Prof. Freitas at Institute of Engineering of Systems and Computers - Microsystems and Nanotechnology (INESC-MN), Rua Alves Redol 9, Lisbon 1000-029, Portugal (www.inesc-mn.pt), especially from Hugo Ferreira and Daniel L. Graham.

Other participation in processing comes from Prof. Hans-Heinrich Gatzen and Dipl.-Ing. Marc Wurz, Universitaet Hannover Institut für Mikrotechnologie, Schoenebecker Allee 2, 30823 Garbsen, Germany (www.imt.uni-hannover.de). Additionally by Laboratory Technician Inger Ninna Hansen, DELTA, Venlighedsvej 4, 2970 Hørsholm, Denmark (www.delta.dk). Electronic Engineer Jan Vasland Eriksen from Danchip is acknowledged for constructing the switch box.

For their great help and contribution with the influenza assay, Keld Andresen and Lars Peter Nielsen, Statens Serum Institut, Artillerivej 5, 2300 København S, Denmark (www.ssi.dk) are acknowledged together with Sandra Abel Nielsen, Aarhus University, who has assisted in the preface of the assay development. Statens Serum Institut has provided the antibodies for the influenza and reference assays.

Additional thanks goes to Associate Professor Martin Dufva for sharing his expertise in bioassays and Associate Professor Ole Hansen for his help with noise investigations, the other members of the group, Kristian Smistrup, Torsten Lund-Olesen, and Christian Danvad Damsgaard, and the rest of the employees at MIC and Danchip.

Finally, warm thanks to my family and friends, especially my husband Jacob for his enthusiastic interest in biological science, which has been a great help in understanding of this ”other” world.

Contents

List of Figures

List of Tables

List of symbols

Symbol	Description	Unit
A	Area	m^2
AMR	Anisotropic magnetoresistance effect	%
aw	Atomic weight	$\mathrm{g\ mol^{-1}}$
B	Magnetic flux density (magnitude)	T
$\mathbf{B}$	Magnetic flux density (vector)	T
c	Concentration	$\mathrm{g\ l^{-1}}$
d	Orbital	
e	Elementary charge	C
E	Electric field (magnitude)	$\mathrm{V\ m^{-1}}$
$\mathbf{E}$	Electric field (vector)	$\mathrm{V\ m^{-1}}$
$E(\phi)$	Magnetic energy density	$\mathrm{J\ m^{-3}}$
f	Frequency	Hz
$\mathbf{F}$	Force vector	N
H	Magnetic field strength (magnitude)	$\mathrm{A\ m^{-1}}$
$\mathbf{H}$	Magnetic field strength (vector)	$\mathrm{A\ m^{-1}}$
H_a	Effective anisotropy field	$\mathrm{A\ m^{-1}}$
H_E	Exchange coupling field	$\mathrm{A\ m^{-1}}$
H_K	Anisotropy field	$\mathrm{A\ m^{-1}}$
I	Current	A
Int	Normalized integral	
J	Current density (magnitude)	$\mathrm{A\ m^{-2}}$
$\mathbf{J}$	Current density (vector)	$\mathrm{A\ m^{-2}}$
$\mathrm{k_B}$	Boltzmann's constant	$\mathrm{J\ K^{-1}}$
K_u	Uniaxial anisotropy constant	$\mathrm{J\ m^{-3}}$
M	Magnetization (magnitude)	$\mathrm{A\ m^{-1}}$
$\mathbf{M}$	Magnetization (vector)	$\mathrm{A\ m^{-1}}$
$\hat{\mathbf{M}}$	Unit magnetization vector	1
M_S	Saturation magnetization	$\mathrm{A\ m^{-1}}$
n	Number of electrons, number of integrals	
$\hat{\boldsymbol{n}}$	Surface outward normal vector	1
N	Noise	$\mathrm{V\ Hz^{-1/2}}$
N_c	Number of charge carriers	

P_l	Legendre polynomials	
Q	Charge	C
$\boldsymbol{r}, \boldsymbol{\theta}, \boldsymbol{\phi}$	Spherical position vectors	m, rad, rad
$\hat{\boldsymbol{r}}, \hat{\boldsymbol{\theta}}, \hat{\boldsymbol{\phi}}$	Spherical unit vectors	1
R	Bead radius	m
R_e	Electrical resistance	Ω
$R(r)$	Radial scalar potential	T m
s	Orbital	
S_0	Sensitivity	V T^{-1} A^{-1}
S/N	Signal-to-noise ratio	
S_υ	Spectral noise density	V^2 Hz^{-1}
t	Sensor thickness	m
T	Temperature	K, °C
Trp	Trapezoidal sum	
U	Magnetic scalar potential	T m
$\mathbf{v}$	Velocity vector	m s^{-1}
V	Voltage	V
vol	Volume	m^3
w	Sensor width	m
$\boldsymbol{x}, \boldsymbol{y}, \boldsymbol{z}$	Cartesian position vectors	m
$\hat{\boldsymbol{x}}, \hat{\boldsymbol{y}}, \hat{\boldsymbol{z}}$	Cartesian unit vectors	1
α	*s-d* transition probability	
β	Normalized bead field (measured)	
γ_{H}	Hooge's constant	
Δf	Bandwidth	Hz
ΔV	Noise	V
$\Delta V/\sqrt{\Delta f}$	Noise	V $\mathrm{Hz}^{-1/2}$
η	Actual/saturation magnetization	
Θ	Debye temperature	K
$\Theta(\theta)$	Polar scalar potential	
μ_0	Magnetic permeability of free space	N A^{-2}
ξ	Coverage	
$\boldsymbol{\rho}, \boldsymbol{\phi}$	Polar position vectors	m, rad
$\hat{\boldsymbol{\rho}}, \hat{\boldsymbol{\phi}}$	Polar unit vectors	1
$\overline{\overline{\rho}}$	Resistivity tensor	Ω m
ρ_{av}	Average resistivity	Ω m
ρ_{H}	Hall resistivity	Ω m
$\rho_{\parallel}$	Parallel resistivity	Ω m
$\rho_{\perp}$	Perpendicular resistivity	Ω m
ϱ	Density	kg m^{-3}
τ	Lock-in time constant	s
χ_g	Magnetic mass susceptibility (intrinsic)	m^3 kg^{-1}
χ_i	Intrinsic magnetic susceptibility	
χ_m	Measured magnetic susceptibility	

ψ	Angle between magnetization vectors	rad

Chapter 1

Introduction

Making things smaller has advantages. As an example is the lab-on-a-chip concept, where all steps in analyzing a chemical/biological sample are integrated onto a single plastic or silicon chip. The advantages are numerous. There is need for less reagent, which can be expensive or hazardous to handle, and need for less sample, which can be difficult to obtain or only exists in small amounts. Moreover, the methodology gives quick results with an easy to use dispensable analysis chip.

Using magnetism in lab-on-a-chip systems induces additional benefits. First of all, magnetic actuation and sensing techniques are very well developed since they are used as the storage/reading basis of computer hard drives - another area of applied physics where miniaturization has led to astounding advances. Furthermore, existing knowledge on material properties is extensive and fabrication techniques are highly developed. In the past years magnetic sensing has been applied to bioassaying, with possible favorable outcome compared to existing techniques. The biomolecule is labelled with a magnetic bead and its presence detected via the label. This way of detecting a biomolecule is one of the only existing methods which are sensitive enough to detect a single molecule.

The most promising results of magnetic sensing in bioassaying has been obtained using sensors based on the giant magnetoresistive (GMR) effect of multilayered structures. This thesis demonstrates that sensors based on the planar Hall effect give comparable results with a sufficiently favorable signal-to-noise (S/N) ratio to detect a single magnetic label. The planar Hall sensors are easily fabricated and can be integrated with fluidics to account for the sensing part of a lab-on-a-chip for bioassaying.

1.1 What is a magnetic immunoassay?

An immunoassay imitates a higher organism's reaction towards an infection by a foreign microorganism, which expresses antigens. The antigens are recognized as foreign by the host's immune system. The immune system responds to the presence of antigens by producing specific antibodies against a selection of antigens expressed by the foreign microorganism. It is this specific reaction of antibodies with their corresponding antigen, like a key in a lock, which is used in immunoassays. In a sandwich immunoassay (Fig. 1.1)

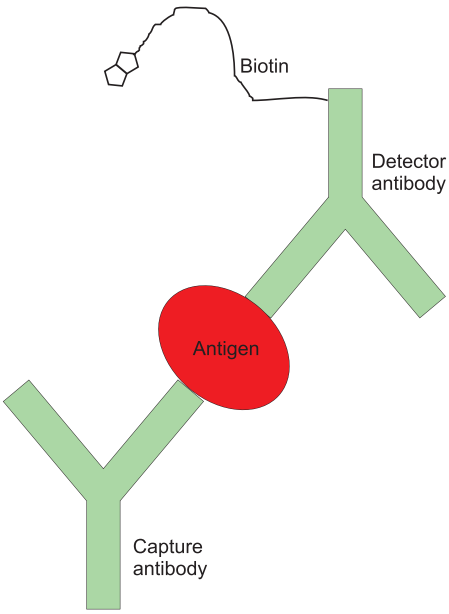

Figure 1.1: Sandwich immunoassay. The capture antibody is immobilized on the surface. Then the antigen is attached to the immobilized antibody and reaction with the detector antibody can take place. In this assay sketch the detector antibody is labelled with biotin.

the researcher is looking for certain antigens, e.g. A and B. An antibody against A is immobilized on a solid substrate (spot A) and an antibody against B at a different position (spot B). These are called capture antibodies. Then the sample is added to the substrate. If the sample contains antigen A, it will bind to the antibody of spot A, and if the sample contains antigen B, it will bind to the antibody of spot B. Then a mixture of antibodies against antigen A and B are added to the substrate. These antibodies are called detector antibodies and they can be marked prior to the experiment; in the figure they are marked with biotin. Biotin binds specifically to streptavidin. Streptavidin is a protein, which can carry a color dye or a fluorescein molecule. Then from the position of colored spots or fluorescent spots, the researcher is able to determine what antigen, A or B, was originally in the sample.

If streptavidin-coated magnetic beads are used instead of the labelled streptavidin, with color or fluorescent dye, the assay will be marked magnetically. This is the principle of a magnetic immunoassay.

1.2 How does a magnetic immunoassay work?

Recapitulate the sandwich immunoassay: capture antibodies are immobilized on a solid substrate, antigen reacts with the capture antibodies, and biotin labelled detector antibodies bind to the captured antigen. In a magnetic immunoassay the capture antibodies are immobilized on top of a magnetic sensor. Following antigen addition, biotin labelled

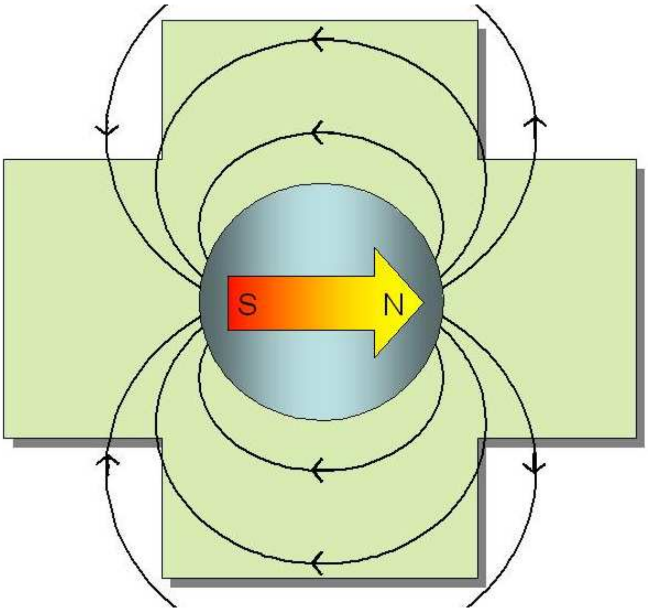

Figure 1.2: Schematic illustration of a magnetized bead on top of a planar Hall sensor, top view. The sensor is green and the magnetized bead is shaded grey - its magnetization illustrated as an arrow. The field lines just below the bead are opposite to the applied field.

detector antibodies are introduced, and streptavidin coated magnetic beads bind to the biotin. Finally the system is flushed to remove unbound beads. The outcome is a magnetic bead attached on top of a magnetic sensor, if and only if the antigen is contained in the sample. The positive situation is sketched in Fig. 1.2, where a magnetic bead is shown on top of a magnetic sensor. The presence of the bead alters the field registered by the sensor in comparison to the absence of the bead, see sketched field lines.

1.3 Why use a magnetic immunoassay?

Ordinary influenza, the viral disease that returns approximately every year, results in increased death rates. However, a pandemic, such as the 1918 Spanish Flu, will be lethal to a considerable part of the World's population. Antiviral drugs have been developed against influenza, and an early treatment decreases the duration of illness and alleviates the symptoms. These antiviral drugs are designed to help the body's own immune system fighting the infection, and although it is not necessarily fully effective, it might help individuals survive. In order to have an effect, however, it is essential that the drug is taken as soon as possible after the infection, compulsorily within 48 hours. Therefore, a quick and reliable diagnostic test is needed.

Today, reliable testing is done with polymerase chain reaction (PCR). PCR requires special equipment and skilled personnel, hence using the technique is expensive and time consuming in the sense that samples taken at the doctor's must be transported to special places and the test results must be communicated back to the consulting room. A variety of fast tests exist, based on immunochemistry, but they are not reliable. The reason for the failure of these immunochemistry based tests is partly a very low concentration of viral protein, the antigens, and partly because the samples contain enzymes that break down the antibodies the test is based on. The last issue is often solved by diluting the sample, but unfortunately this aggravates the first problem.

Using magnetic beads, we have the option of capturing the sample antigen by antibodies attached to the magnetic beads. On the surface of the beads the antibodies are immobilized in advance to the capturing event. These beads are suspended in the sample and antibodies attached to the beads are allowed to react with the antigens on the surface of the sample molecules. Afterwards, the antigens are held back with magnetic forces while the remaining contents are washed away. This solves both issues in one step. The antigen is held back, when diluting the enzymes from the sample.

Next step is to detect the magnetic bead in a magnetic immunoassay, which only binds to the capture antibodies on top of the sensor if an antigen is attached to the bead. By detecting the carrier, one avoids elution of the antigen into new buffer, which would decrease the antigen concentration and thus also the sensitivity of the assay. Unspecifically bound beads can be removed from the sensitive region of the sensor with magnetic forces. This would eliminate the need to wash the probe, which can be tedious especially for point-of-care diagnostic tests. The readout from the sensor is electronic, which means that control systems and calibration can be integrated on the chip, and neither laser scanner nor PCR equipment is needed. Magnetic sensors such as the planar Hall sensor are very sensitive and can potentially detect a single bead and thus potentially the presence of a single antigen.

1.4 How is this thesis related to magnetic immunoassays?

In the following chapters, the application of the planar Hall sensor to magnetic immunoassays will be addressed. The planar Hall sensor is an attractive choice for the sensing part of the significant challenge that a magnetic immunoassay presents. It turns out that in a comparison of competing technologies' signal magnitudes and noise levels for DC detection, the planar Hall sensor outperforms its competitors. The investigation is addressed in terms of the single bead signal-to-noise level.

During the research leading to this thesis, planar Hall sensors of various design and behavior have been fabricated and characterized. A large effort has been invested in design considerations and optimization, and these issues are addressed in different chapters, which follow the chronological development of the sensor design and performance. First, the nickel planar Hall sensors are presented. Though not optimal with respect to design and material, they represent an important first step in optimizing these aspects in the improved version of exchange biased permalloy sensors. During this period essential parts of the electrical characterization setup are constructed and put together and the extended efforts in noise suppression initialized. The nickel sensors demonstrate the use of the planar Hall effect as a magnetic sensing principle, and bead detection is demonstrated.

The results obtained with the nickel sensors guide the design and fabrication of the permalloy sensors. The new sensors are exchange-coupled to an antiferromagnetic material in order to induce a magnetic easy direction instead of only an easy axis, as is the case of nickel sensors. The exchange biased permalloy sensors are fabricated in collaboration with INESC-MN in Portugal and two batches are produced. Batch 1 is a bottom-pinned stack and Batch 2 is a top-pinned stack. Batch 1 is used to demonstrate bead detection in collaboration with INESC-MN, and Batch 2 is used for the influenza immunoassay experiments.

Resuming the efforts in noise suppression has lead to approximately 100 times less noise than connected to the experiments performed at INESC-MN. The planar Hall sensors of Batch 2 are then characterized magnetically, electrically, and the noise is determined along with the temperature dependence of the signal. Batch 2 sensors are applied to the influenza immunoassay. First detection of monoclonal antibodies is demonstrated, where the signal as a function of concentration is determined. Second successful detection of an influenza sandwich immunoassay is carried out with the planar Hall sensors.

On the biochemistry side of the thesis, a new immobilization method is developed in collaboration between people at MIC. DNA and antibodies are found to attach readily to the surface of SU-8, a photosensitive polymer widely used in MEMS fabrication. A protocol for the influenza sandwich assay on SU-8 is developed and test results with fluorescently labelled detector antibodies are presented.

1.5 Historical account of the Ph.D. study

1. During a literature survey for very sensitive magnetic sensors, an article by Montaigne *et al.* [1] was encountered. This article describes a magnetic field sensor with nanotesla resolution based on the planar Hall effect of permalloy. The interest for this planar Hall sensor had been rather low. Such sensors had not been considered for read heads in computer hard drives, where GMR sensors are preferred. Moreover, they had not been considered for bead detection either. The suggestion by Montaigne *et al.* is to use the planar Hall sensor as a micro-compass. A theoretical evaluation of the sensing principle (presented in Chapter 3) has lead to the understanding that this type of sensor is applicable to magnetic bead detection.

2. After theoretical validation of the sensing principle, an experimental validation was needed. The fabrication of nickel planar Hall sensors was carried out in MIC's clean room, and since the only ferromagnetic material available was nickel, nickel was used as active sensing material. The results from this investigation proved that the planar Hall sensing principle was sufficient to detect 2.8 μm Dynabeads, resulting in a conference proceeding [2]. During the work with nickel sensors, students at MIC built a set of Helmholtz coils [3], which were calibrated during this project. The calibration is 2.8 % too low compared with the recent, and more reliable, calibration. Hence, the results with the nickel sensors refer to a slightly different coil calibration than more recent results. For the electrical measurements and current control, a

lock-in amplifier was available but no high precision current source for sensors or coils (the electrical setup of Fig. 5.5 was used). Insights essential for the design of exchange biased permalloy sensors was obtained from the nickel sensor results. 1: Need for an easy *direction* instead of an easy axis. 2: Need for an exchange field to enhance the effective film anisotropy of permalloy as well as to create the easy direction.

3. Since it is not possible to deposit the preferred materials in MIC's clean room, the studied exchange biased permalloy sensors have been fabricated in collaboration with INESC-MN, Portugal. First Batch 1, the bottom-pinned stack, was fabricated completely in the laboratories in Portugal, and all characterization was made using their facilities. In collaboration detection of 2 μm Micromer-M beads and 250 nm Nanomag-D beads was demonstrated [4, 5]. The magnetic characterizations performed on MIC's VSM revealed an "extra" loop in the M vs. H measurements due to a magnetic seed layer for MnIr growth. This is undesirable and was subsequently eliminated using a top-pinned stack for Batch 2. The bead detection experiments with Batch 1 suffered from a considerable amount of electronic noise. The setup was without electrical screening and with ordinary unshielded wires. Encouraged by the potential for noise reduction, a substantial effort has been put into avoiding electronic noise in the author's own setup.

4. The fabrication of sensor Batch 2 has been carried out at four different places. The magnetic films were deposited at INESC-MN, the photolithography was made at MIC, and etching of the sensor structures at Universität Hannover. The subsequent processing was done at MIC apart from wire bonding, which was done at DELTA. Due to time constraints no further sensor batches were made, though possible improvements were discovered after finishing processing. The best example of a design parameter that could have been improved, is the SU-8 layer for immobilizing biomolecules. In the processed design, only the sensitive area of the sensor is covered with an SU-8 pad. The reason behind this choice is that biomolecules are supposed to attach only on top of the sensor. This would avoid wasting sample molecules at spaces, which cannot be sensed by the sensor. Unfortunately the molecules bind as easily to the residual monolayer adjacent to the SU-8 pad as to the pad itself. In this design, competitive positive and negative signals result in reduced average signals. This was not known at the time of processing, and the choice was at that time justified.

5. The setup for electrical characterization was built after completing the fabrication. At first the old setup used for the nickel sensor (Fig. 5.5) was available. A Keithley Model 6221 current source was borrowed for the Helmholtz coils, and the sensor current was controlled by the lock-in amplifier. A 5 kΩ low-noise resistor was connected in series with the sensor circuit to implement a better sensor current control. In this setup, the noise characterization of Batch 2 was made. Noise reduction was obtained by shielded coax cables and a shielded sensor box. The measured electronic noise is approximately 100 times less than that measured at INESC-MN.

6. The experimental setup was gradually rebuilt (resulting in the setup of Chapter 6, Fig. 6.5 and Fig. 6.6). One significant improvement is the introduction of two new Keithley Model 6221 high precision current sources for current control of the Helmholtz coils and the sensor current. Since the planar Hall sensor is temperature sensitive, the sensor box has been rebuilt with thermal insulation and temperature control. Additionally, a switch box was constructed to facilitate measuring all three sensors on a chip. The possibility of subtracting the reference sensor signal from the signal from the sensor measuring biological activity is thus introduced. Incorporated on the chip is sensor A for the sample, sensor B for the electrical reference, and sensor C for the negative control. As the three sensors are serially connected, they experience the same applied current.

7. In the final setup, the characterization of the planar Hall sensors of Batch 2 has been performed. Finally, theory and experiment compare reasonably. The temperature dependence of the sensors was measured and found reasonably linear. Then the procedure for measuring antibodies immobilized on top of a sensor was developed (the resulting procedure is presented in Appendix B).

8. The presented reference system is biotinylated monoclonal antibodies bound to streptavidin coated magnetic beads. The bead signal as a function of antibody concentration is determined. A general trend of increasing signal with increasing antibody concentration is obtained. However, the signal from the bead layer is positive instead of negative as expected from the theoretical estimates performed earlier. First physical alteration of the sensors during chemical processing was assumed, but the signal remained positive. Ultimately, when calculating the signal from a monolayer of beads with the chip's actual SU-8 configuration, it was discovered that the signal could indeed be positive (Chapter 4). The reason is a tradeoff between positive and negative field contributions. The field from beads adjacent to the sensor gives a positive contribution, and beads placed directly above the sensor's sensitive area give a negative contribution. The relative bead coverage determines whether the outcome is a positive or negative signal.

9. During the investigation of the positive sign from the monolayer of magnetic beads, it was found that another design of the SU-8 layer would be preferable. Namely a negative image of what was actually fabricated. If the positive contribution from beads placed outside the sensitive area of the sensor were shielded by a thicker SU-8 layer, the signal would not only become negative as it should, but bead capture at fringing fields from the voltage leads could also be reduced. Unfortunately, this was only found after the puzzle about the "wrong" sign was solved, which occurred at a very late stage of the Ph.D. study, so time did not permit to test it experimentally.

10. Finally, a successful influenza immunoassay on the planar Hall sensor chip was performed (Chapter 8). Taking the design and other issues into account, the results are promising for the planar Hall sensors.

1.6 Outline of thesis

The aim of this work is to fabricate magnetic sensors and demonstrate their feasibility as biosensors in point-of-care diagnostics of influenza infection.

Outline of chapters

1. Chapter 1 introduces the magnetic immunoassay.
2. Following a description of the physical sensing principle for various magnetic sensors in Chapter 2 comes a short review of completed experiments towards magnetic bioassaying in other research groups. Chapter 2 concludes the choice of the planar Hall sensor based on the signal-to-noise level compared to existing sensor types.
3. Theoretical background of the planar Hall sensor is the content of Chapter 3.
4. More theory underlying the study of single bead signal as well as the monolayer signal is presented in Chapter 4. Additionally, various SU-8 designs are considered with respect to the theoretically expected monolayer signal.
5. Chapter 5 deals with the clean room fabrication of nickel planar Hall sensors along with the characterization and bead detection results using this sensor batch.
6. Chapter 6 presents the permalloy sensor fabrication and characterization of Batch 1 and 2. Following a description of the experimental setup used for characterization are first the magnetic then the electric characterizations including sensitivity, noise, and temperature investigations.
7. The signal produced by magnetic beads attached to different surface concentrations of biotinylated monoclonal antibodies represents the baseline for detection experiments with immunoassays. Chapter 7 presents the procedure of immobilizing antibodies on SU-8 placed on top of the sensor, then follows the baseline studies with planar Hall sensors.
8. Chapter 8 deals with the actual influenza immunoassay realized using the planar Hall sensors. Three sensors are used, where one is a reference used to stabilize the signal from the other two, the second is used for the negative control, the third is reserved for the sample.
9. Chapter 9 concludes the thesis.

Chapter 2

Magnetic sensors

When deciding on a sensor for a magnetic immunoassay, the sensing principle and the signal that this principle produces is important. However, the detection limit of the sensor also depends on the noise generated during measurements. This chapter describes the various sensor principles along with a discussion of electronic noise. The planar Hall sensor offers the best DC signal-to-noise, S/N, from a single magnetic bead compared to the other types of sensors.

The chapter includes the requirements for magnetic sensors in magnetic bioassaying, a description of the physical sensing principles considered, and a review of results obtained prior to this thesis. Additionally the electronic noise in magnetic sensors is evaluated leading to the choice of the planar Hall sensor for magnetic bioassaying.

2.0.1 Requirements

Some requirements for a magnetic bead sensor are the geometry of the sensing principle, the range of fields the sensor is sensitive to, and the linearity of the sensor. If the sensor gives a linear response to the applied field, the sensor measures an average of the bead field over the entire sensing area.

First the sensing geometry of a magnetic field sensor placed in the xy-plane of a cartesian coordinate system is considered. If the sensing principle is based on the Lorentz force, the bead must be magnetized perpendicularly to the sensing plane, *i.e.* along z. If the sensing principle is based on magnetoresistance, the bead can be magnetized parallel to the sensing plane, *i.e.* along x.

A magnetic dipole moment oriented along z produces field lines that will enter and leave the sensor surface in equal amounts. This is due to flux closure. Thus the z-component of the bead field averages to zero when the area is large compared to the bead size. A sensor area has to be small compared to the bead for this average to approach a value for detection. For nanobeads, strong constraints on the fabrication procedure must be expected.

When the bead is magnetized along x, a rather large negative field component just below the bead dominates the dipole field. This component does not average to zero when the sensor area is large compared to the bead size, hence larger sensor areas can be used.

However, the single bead signal scales inversely with sensor size cubed (see Chapter 4), and for single bead detection an area, which is small compared to the bead, would be ideal. In biological sensors, we cannot rely on a single molecule to place itself just on top of a very tiny sensor, and in this context single bead detection is meaningless. Here we prefer an area that probes an average of the sample, and it must be large compared to the bead. For biological experiments a statistical bead count is important, thus only the sensing geometry along x can be used. If room for at least one thousand beads is needed, the sensor area becomes 1000× the bead size. Going to larger sensor areas clarifies the constraint of the sensing geometry, only the in-plane magnetization of beads can be used, not the out-of-plane magnetization which would mainly measure beads situated at the edges of the sensor.

Superparamagnetic beads are designed to avoid remanent magnetization and hence they must be magnetized by an external field. Therefore the sensor must be able to distinguish a very small field component compared to the background magnetic field. Chapter 4 explains that this component is approximately 1 % of the applied field. Hence the sensor should have a signal-to-noise ratio that enables detection of $\Delta B = 10$ nT in a flux density of $B = 1$ mT (a typical value for MR based sensors). It should also have a well-defined field response up to the applied $B = 1$ mT, or more generally up to 100 times the detection limit ΔB.

2.1 Sensor principles

This section describes the competing sensor technologies for magnetic bioassaying. These include GMR sensors, spin-valve sensors, and the planar Hall sensors, which have all been considered as possible sensing principles. The signal produced by the sensor in an applied field is presented.

2.1.1 Anisotropic magnetoresistance

Magnetoresistance (MR) is present in a ferromagnetic conductor [6]. MR stems from the spin-orbit coupling between electrons and magnetic moments of the lattice atoms and is thus quantum mechanical in origin as opposed to ordinary galvanomagnetic effects that have a classical origin in the Lorentz force. Extraordinary effects are created by the microscopic part of the flux density ($\mu_0 M$) whereas the ordinary effects are created by the macroscopic part ($\mu_0 H$). The GMR effect, the spin-valve sensor, and the anisotropic magnetoresistance (AMR) effect arise from the MR effect. The Hall effect arises from the ordinary galvanometric effect.

Anisotropic magnetoresistance (AMR) also stems from the spin-orbit coupling, but it is anisotropic. AMR depends on the crystal structure of the material and the spin of the atoms situated in the crystal. It depends on the domain structure of the ferromagnet. In general the resistivity is larger if the current is applied parallel to the magnetization than if the current were applied perpendicularly to the magnetization ($\rho_{\|} > \rho_{\perp}$). This difference between the two states of magnetization is measured as the AMR effect, $AMR =$

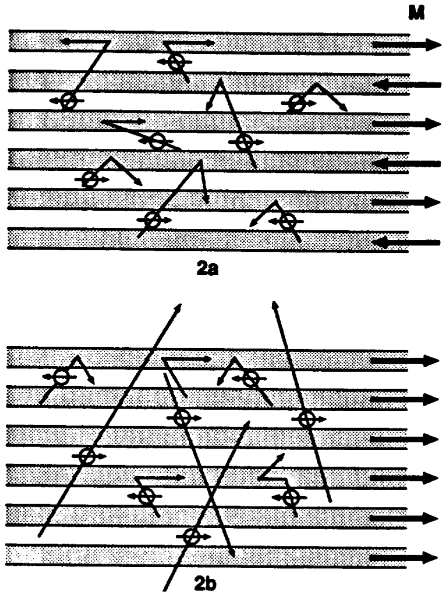

Figure 2.1: GMR stack (Fig. 3 in White, 1994). Schematic drawing of the conduction in a multilayered GMR film. Different scattering produces different resistances in the antiparallel (2a) and parallel (2b) cases of magnetization alignment, here shown through the mean free path, which is larger in the parallel case.

$(\rho_{\|} - \rho_{\perp})/\rho_{\mathrm{av}}$, where ρ_{av} is the average resistivity of the ferromagnetic material. It is the anisotropic magnetoresistance effect that is responsible for the planar Hall effect.

2.1.2 GMR sensor

The GMR effect reported by Baibich *et al.* [7] is based on antiferromagnetic coupling of Fe layers through thin Cr separation layers, called spacers. Electrons travelling through a magnetic layer in a GMR stack, as the one shown in Fig. 2.1 (Fig. 3 in Ref. [8]), have spins aligned according to the magnetization of the ferromagnetic layer. In the band structure of some ferromagnetic materials, the Fermi surface intersects the band of one spin component and not the other, hence only electrons of this spin are available to carry current. The result is a spin polarized current, which can only be accepted into bands of identical spin in adjacent layers. The resistance then strongly depends on the relative orientation of magnetization in the closely spaced ferromagnetic layers. Various spacing layers show different results. At specific Cr layer thicknesses the coupling is antiferromagnetic (Fig. 2.1, 2a), at other layer thicknesses the coupling is ferromagnetic (Fig. 2.1, 2b). The magnetoresistive effect observed for the antiferromagnetic coupling between layers reported by Baibich is up to 50 %, an order of magnitude higher than previous experiments with magnetoresistive materials.

The GMR effect is described by the change in resistivity, $\Delta\rho(\psi)$, normalized to the

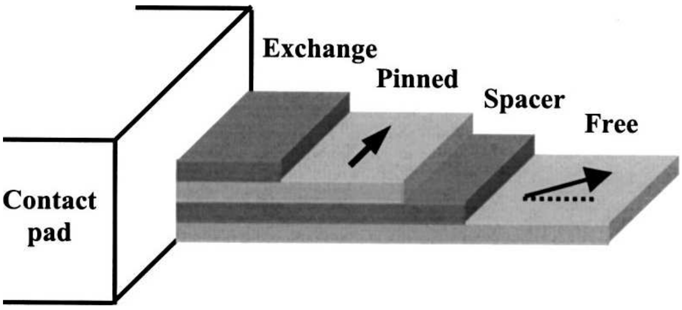

Figure 2.2: Spin valve sensor reported by Ferreira *et al*, 2003. Schematic drawing showing the configuration of magnetic moments in the sensing layer (free layer) and the pinned layer. The easy axis is indicated with a dotted line, and the external field is applied perpendicularly to this.

average resistivity, ρ, [6]

$$\frac{\Delta\rho(\psi)}{\rho} = \left(\frac{\Delta\rho}{\rho}\right)_{\text{(GMR)}} \frac{1-\cos\psi}{2} \tag{2.1}$$

where ψ is the angle between the magnetization in the two sets of layers, and the $(\frac{\Delta\rho}{\rho})_{\text{(GMR)}}$ is the maximum attained value, the GMR coefficient. For antiferromagnetically coupled layers (corresponding to Fig. 2.1, 2a) the stack can be used as a magnetic field sensor. The field, H, is applied along the hard axis of magnetization, which corresponds to H applied across the layers in the figure. The field dependence of Eq. (2.1) is to a first approximation [6]

$$\left(\frac{\Delta R_e(H)}{R_e}\right)_{\text{GMR}} = \left(\frac{\Delta\rho}{\rho}\right)_{\text{(GMR)}} \left[1-\left(\frac{H}{H_a}\right)^2\right] \tag{2.2}$$

where $\Delta R_e(H)/R_e$ is the normalized resistance change, and H_a is the effective anisotropy field.

2.1.3 Spin-valve sensor

The working principle of the spin valve sensor is sketched in Fig. 2.2 (Fig. 1 in Ref. [9]). When placed in an external magnetic field the magnetization of the free layer is rotated away from the easy axis (dotted line in the figure) and gives rise to a change in resistance through the sensor, ΔR_e, between the two contact pads. The resistance depends, as in the case of GMR sensors, on the relative orientation of the magnetization between the pinned and the free layer.

With the easy axis of the sensing layer perpendicular to the reference layer, *i.e.* the pinned layer, as shown in Fig. 2.2, the field dependence of the sensor is [6]

$$\left(\frac{\Delta R_e(H)}{R_e}\right)_{\text{SV}} = \frac{\Delta\rho}{\rho}\frac{(1-H/H_a)}{2} \tag{2.3}$$

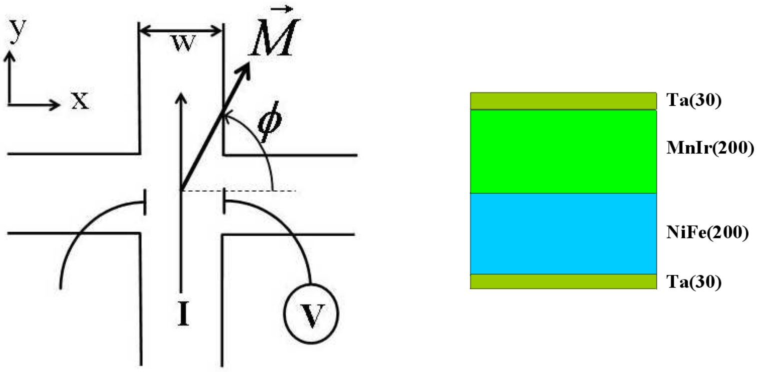

Figure 2.3: Left: Geometry of the planar Hall sensor. The magnetization vector, $\mathbf{M}$, has an angle ϕ with respect to the x-axis. $\mathbf{M}$ lies in the xy-plane, the current, I, is along y, and the voltage, V, is measured along x. The sensor cross has the width w and thickness t. Right: Cross sectional view of the sensor stack. Layer thicknesses are in Å. The sensing is governed by the NiFe layer, which is pinned by the MnIr layer.

where H is applied perpendicularly to the easy axis, and H_a is the anisotropy field of the free layer. The remaining parameters have been introduced for the GMR sensor. The voltage drop, V, in an applied field becomes

$$V_{\mathrm{SV}} = -\frac{1}{2} I \, R_e \frac{\Delta\rho}{\rho} \frac{H}{H_a} \tag{2.4}$$

where I is the current through the sensor. The spin-valve sensor is linear for applied fields up to H_a.

2.1.4 Planar Hall sensor

The planar Hall effect, Fig. 2.3, is generated when the magnetization, $\mathbf{M}$, is rotated with respect to the current, $\mathbf{I}$. The origin of the planar Hall effect is the anisotropic magnetoresistance effect, which is different from the origin of the Hall effect. Naming this effect *planar Hall* is bound to cause misunderstanding, but nevertheless, the term is well known and abundant in the literature. The connection between the Hall effect and the planar Hall effect is solely geometrical. The Hall effect is sensitive to magnetic fields applied perpendicularly to the sensor plane, and the planar Hall effect is sensitive to fields applied parallel to the sensing plane, hence the name *planar*.

The mathematical expression of the planar Hall sensor signal produced by an applied field is

$$V_{\mathrm{PH}} = I \frac{\Delta\rho}{\rho} \frac{\rho_{\mathrm{av}}}{t} \frac{H}{H_a} \tag{2.5}$$

in which H_a is the effective anisotropy field. The planar Hall sensor is linear within 2 % for $H < 0.23 H_a$.

Details of the working principle behind the planar Hall effect is given in Chapter 3, where Eq. (2.5) is derived.

2.1.5 Classical sensing principles, the Hall sensor

The Hall effect arises from the Lorenz force deflection of charge carriers, with charge Q and velocity $\mathbf{v}$, through a medium. The force, $\mathbf{F}$, is directly proportional to the cross product between the carrier velocity, $\mathbf{v}$, and the magnetic flux density, $\mathbf{B}$.

$$\mathbf{F} = Q(\mathbf{v} \times \mathbf{B})$$

This gives rise to a Hall resistivity, ρ_{H}, [6]

$$\rho_{\mathrm{H}} = \frac{B}{n\mathrm{e}}$$

where n is the density of free charge carriers of elementary charge e.

The Hall sensor's sensing geometry is suboptimal for magnetic bioassaying as discussed in the requirements subsection. Only in the case where the sensor size approaches the bead diameter, the flux through the sensor differs and a Hall signal can be obtained. Another way to break the symmetry is to apply a time-varying magnetic field, see Besse *et al.* [10].

2.2 Review of magnetic biosensors

Having described the physical detection principles, this section reviews the detection experiments performed using the magnetic sensors. Only experiments relevant to magnetic bioassaying or to this thesis are included.

Existing magnetic field sensors used for biomaterial detection by magnetic labelling are GMR sensors, spin-valve sensors, and Hall sensors. Planar Hall sensor have not previously been used as biosensors or to detect magnetic beads. Below is presented a review of biomolecular detection experiments performed using various sensor types.

2.2.1 GMR sensors

Giant magnetoresistance (GMR) was discovered in 1988 by Baibich *et al.* [7], who published MR ratios (the change in resistivity due to an applied field) an order of magnitude larger than seen before. The GMR effect was hereafter rapidly exploited first as a magnetic field sensor in 1994 [11] second by the recording industry to enhance the sensitivity of hard disk drives (IBM 1997). In 2000 Edelstein *et al.* published the detection of biological warfare agents using a bead array counter (BARC) biosensor, which was essentially an array of GMR sensors [12]. Later the same group demonstrated detection of DNA hybridization using similar BARC chips [13].

Recently, nanometer sized GMR sensors were fabricated and characterized [14]. The hereby obtained signal-to-noise level of the sensors was promising with respect to single 100 nm bead detection but no actual detection experiments were performed.

2.2.2 Spin-valve sensors

Spin valve sensors have been demonstrated as biosensors by Prof. Freitas' group (INESC-MN, Portugal, www.inesc-mn.pt) [9, 15, 16, 17, 18]. In Ref. [15] detection and manipulation of single 2 μm magnetic labels, Micromer-M, were demonstrated using on-chip current lines. In Refs. [9] and [16] streptavidin coated beads were bound to a biotinylated sensor surface and detected with the spin valve sensor. Recently, Graham *et al.* demonstrated detection of DNA hybridization events using their spin-valve chips [18]. Additionally, single bead detection of 2.8 μm labels, Dynabeads M-280, with spin-valve sensors has been performed by Li *et al.* [19].

2.2.3 Planar Hall sensors

In 2000, when publishing their work on sensors based on the planar Hall effect of permalloy, Montaigne *et al.* [1] suggested the possibility of using this type of sensor as a micro-compass. Their permalloy sensors were saturated in the Earth's magnetic field, *i.e.*, not feasible as bead detectors since saturation of the sensor would occur prior to magnetization of the beads.

Neither bead detection nor magnetic bioassaying has been demonstrated with planar Hall sensors prior to this thesis.

2.2.4 Hall sensors

In 2002 Besse *et al.* [10] published a miniaturized silicon Hall sensor capable of detecting a single microbead of diameter 2.8 μm (Dynabeads M-280). In order to do so they magnetized the bead with a constant external field and added an AC field either parallel to the constant field or perpendicular to the constant field. Detection of the bead via the apparent susceptibility (H_{AC} parallel to the applied field) or the second-harmonic (H_{AC} perpendicular to the applied field) was successful in both cases.

An InAs quantum-well Hall sensor was also proven capable of detecting a single bead [20], this time 1.2 μm in diameter.

2.3 Electronic noise in magnetic sensors

This section deals with electronic noise. After a description of three sources of intrinsic noise, the noise in planar Hall sensors and spin-valve sensors is compared.

Electronic noise in sensors arises from various sources. A very well-known source of noise is the Johnson noise, studied by Johnson in 1927 [21, 22], which has its origin in thermal agitation of the charge carriers in a resistor. Another type of noise, shot noise, is related to the current passing an energy barrier. The shot noise arises from the quantum nature of charge carriers, and is only expressed when the current fluctuates. Another sort of noise is the $1/f$ noise, which is of unknown origin but depends strongly on frequency. Hence the name $1/f$. Noise, $\Delta V/\sqrt{\Delta f}$, is measured in units of volt per square root of Hertz (V Hz$^{-1/2}$). Alternatively, the experimental noise, ΔV (standard deviation on the voltage), is measured in units of volt for a specific bandwidth, Δf.

2.3.1 Johnson noise

Any electronic device, that is sensor, amplifier, serial resistor, etc. exhibits Johnson noise. A resistor has thermal noise according to Eq. (2.6).

$$\Delta V_{\mathrm{J}}/\sqrt{\Delta f} = \sqrt{4\mathrm{k_B} T R_e} \tag{2.6}$$

where $\mathrm{k_B}$ is Boltzmann's constant, T the temperature, R_e the electric resistance, and Δf the measurement bandwidth.

2.3.2 Shot noise

When an alternating current (I_{AC}) is used, the current varies with time and is thus subject to the quantum mechanical distribution of the charge carriers that governs shot noise. The mathematical expression of shot noise is [23]

$$\begin{aligned} \Delta I_{\mathrm{sh}} &= \sqrt{2\mathrm{e} I \Delta f} \qquad (2.7)\\ \Delta V_{\mathrm{sh}}/\sqrt{\Delta f} &= R_e \cdot \Delta I_{\mathrm{sh}}/\sqrt{\Delta f} \\ \Delta V_{\mathrm{sh}}/\sqrt{\Delta f} &= R_e \sqrt{2\mathrm{e} I} \end{aligned}$$

where e is the elementary charge, and the rest of the parameters are presented previously.

2.3.3 1/*f* noise

A tricky sort of noise is the $1/f$ noise, named so due to its spectral dependence. At present, the origin of the $1/f$ noise is unknown, perhaps due to its ubiquitous nature. The mathematical expression of the spectral noise density, $S_v(f)$, is [24]

$$\begin{aligned} S_v(f) &= \gamma_{\mathrm{H}} V^2 (N_c f)^{-1} \qquad (2.8)\\ \Delta V_f/\sqrt{\Delta f} &= \sqrt{S_v(f)} = V\sqrt{\gamma_{\mathrm{H}} (N_c f)^{-1}} \end{aligned}$$

where f is the frequency, γ_{H} is Hooge's constant (dimensionless), V the voltage drop, and N_c is the number of charge carriers in the resistor.

Hooge's constant has been found to be $\gamma_{\mathrm{H}} = 10^{-3}$-$10^{-1}$ for permalloy in varying magnetic fields, where the magnitude depends on the internal domain structure [25]. For applied fields corresponding to $B = 0.5$ mT, Hooge's constant is $\gamma_{\mathrm{H}} \approx 10^{-2}$ [25]. The number of charge carriers can be estimated from the volume, density, and the atomic weight of the sensor material. In the following analysis, one carrier per atom is assumed.

2.3.4 Noise in planar Hall sensors and spin-valve sensors

An estimate of the electronic noise in a typical planar Hall sensor and spin-valve sensor of identical geometry yields the values presented in Table 2.1. The 2μm × 2μm active sensing area is chosen for detection of a single magnetic bead with a diameter of 2 μm. The parameters for the spin-valve sensor, including γ_{H}, are from Ref. [26]. γ_{H} for the planar Hall sensor is from [25], the remaining parameters will be given in Chapter 6.

	t (nm)	R_e (Ω)	I (mA)	γ_{H}	N_c	N_{J} ($\frac{\mathrm{nV}}{\sqrt{\mathrm{Hz}}}$)	N_{sh} ($\frac{\mathrm{nV}}{\sqrt{\mathrm{Hz}}}$)
PH	20	10.85	1	0.01	$7 \cdot 10^9$	0.4	0.2
SV	10	21.70	1	0.10	$3.5 \cdot 10^9$	0.6	0.4

Table 2.1: Electronic noise, N, in planar Hall sensors (PH) and spin-valve sensors (SV). Both sensors have 2μm × 2μm active sensing area. $R_e = \rho_{\mathrm{av}}/t$ is the resistance of the sensor material with thickness t. I is the sensor current, γ_{H} Hooge's constant, N_c the number of charge carriers. N_{J}: Johnson noise, N_{sh}: shot noise.

Fig. 2.4 shows the sensor noise as a function of frequency for both sensors. The white noise is the sum of Johnson noise and shot noise. For the planar Hall sensor the white noise is approximately half of that for the spin-valve sensors. However, the $1/f$ noise dominates the low frequency part of the spectrum, and the planar Hall sensor exhibits 10 times less $1/f$ noise than the spin-valve sensor. The figure indicates a lower noise level of the planar Hall sensor than of the spin-valve sensor, which is especially pronounced for low frequencies, *i.e.* in DC measurements.

2.3.5 Single bead S/N for planar Hall sensors and spin-valve sensors

To make a signal-to-noise estimate of the planar Hall sensor and the spin-valve sensor, the signal produced by a single 2 μm bead is studied. The signal produced by a bead centered directly on the surface of a 2μm × 2μm active sensing area is

$$\langle H_{\mathrm{bead}} \rangle = -\frac{\chi_m H/3}{(1+\widetilde{w}^2)(1+2\widetilde{w}^2)^{1/2}} \tag{2.9}$$

Eq. (2.9) will be derived in Chapter 4, Eq. (4.21). H is the applied field, χ_m the measured susceptibility of the magnetic bead, and $\widetilde{w} = w/2z_0$ is the width of the sensor, w, normalized to the distance between sensor and bead center, z_0. In this case, $\widetilde{w} = 1$, because $w = 2$ μm, and $z_0 = R = 1$ μm, where R is the radius of the bead.

The sensor signals are given by Eq. (2.5) (planar Hall sensor) and Eq. (2.4) (spin-valve sensor). Table 2.2 summarizes the sensor response to a magnetic bead in the two cases of sensors. The parameters for spin-valve sensors are from Ref. [26], parameters for planar Hall sensors will be given in Chapter 6.

The combination of signal (Table 2.2) and noise (Table 2.1 and Fig. 2.4) is summarized in Table 2.3 for selected frequencies. Clearly the planar Hall sensor outperforms the spin-valve sensor in the low frequency regime, where S/N is higher for the planar Hall sensor. However for large frequencies, when the spin-valve sensor is dominated by the white noise level, S/N is four times higher for the spin-valve sensor than for the planar Hall sensor. Their S/N match at $f \approx 1$ kHz.

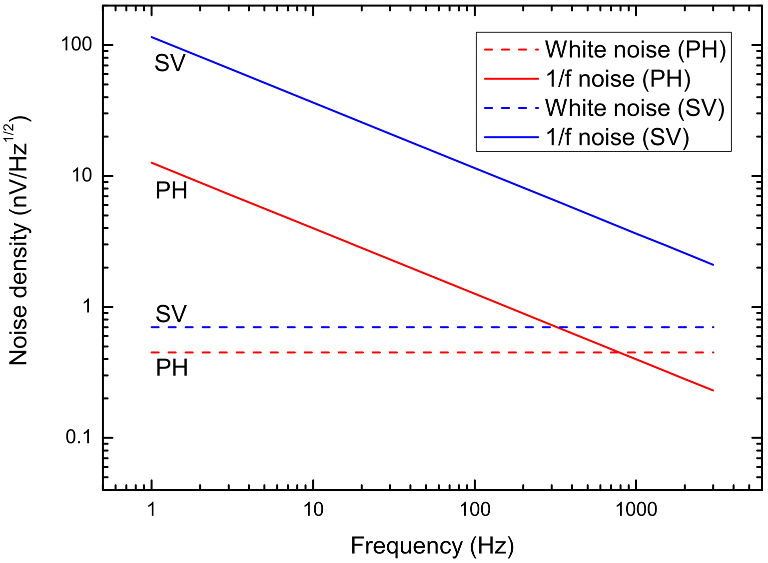

Figure 2.4: Spectral noise for planar Hall sensor (PH) and spin-valve sensor (SV) of comparable geometry and materials.

	AMR	H_a (A m^{-1})	H (A m^{-1})	H_{bead} (A m^{-1})	ΔV_{bead} (μV)
PH	0.02	4000	1200	-34.64	-1.9
SV	0.08	2400	1200	-34.64	12.5

Table 2.2: Signal from a single 2 μm magnetic bead at a planar Hall sensor (PH) and a spin-valve sensor (SV), both having 2μm × 2μm active sensing area, along with the parameters entering the calculations.

	N_{30} $(\frac{\text{nV}}{\sqrt{\text{Hz}}})$	S/N_{30}	N_{1000} $(\frac{\text{nV}}{\sqrt{\text{Hz}}})$	S/N_{1000}	N_{white} $(\frac{\text{nV}}{\sqrt{\text{Hz}}})$	S/N_{white}
PH	2.3	817	0.4	3161	0.45	4200
SV	21.0	595	3.6	3376	0.7	18000

Table 2.3: Single bead signal-to-noise relations for planar Hall sensors compared to spin-valve sensors. N is the expected noise level. Selected frequencies are very low: $f = 30$ Hz, intermediate: $f = 1$ kHz, and very high: white noise dominated.

2.4 Choice of sensor principle

In 2004, an investigation of the signal-to-noise for various magnetic biosensors was performed in the context of single bead detection by Freitas *et al.* [26]. The studied sensors were designed for detection of a single 2 μm bead and had comparable active sensing areas. Planar Hall sensors with active sensing areas of $2.5\mu\text{m} \times 2.5\mu\text{m}$ and spin-valve sensors, $2\mu\text{m} \times 3\mu\text{m}$, were evaluated along with other magnetic field sensors, including GMR and Hall sensors. The calculations were performed for the low frequency regime, $f = 30$ Hz, *i.e.* for spin-valve sensors dominated by the $1/f$ noise.

The results are listed in Table 2.4. The higher planar Hall S/N compared to my own estimate is mainly due a lower effective anisotropy field, $H_a = 2400$ A m^{-1}. The lower S/N for spin-valve sensors comes from the 2 μm^2 larger sensor area.

Sensor type	GMR	spin-valve	Hall	planar Hall
$\boldsymbol{S/N}$	382	442	367	1453

Table 2.4: Signal-to-noise for competitive sensor technologies in magnetic biosensing, from Freitas, 2004.

The most promising sensor in terms of bead detection limit is, according to this investigation, the planar Hall sensor. However, going to high frequencies ($f > 1$ kHz, see Fig. 2.4) would reduce the $1/f$ noise of spin-valve sensors considerably, their S/N in the white noise regime would be approximately four times better than that of planar Hall sensors, see Table 2.3. Then again, when considering the design for a prototype device to be used in the doctor's office, DC detection would probably be easier to handle on the chip than high frequency lock-in detection. The planar Hall sensor offers the highest signal-to-noise level with respect to DC bead detection.

Chapter 3

Theory of planar Hall sensors

This chapter describes the theory behind the planar Hall effect. The aim is to verify that the planar Hall sensor produces a linear signal as response to an applied magnetic field within a certain field range. Moreover, the hysteresis curves from an anisotropic material are presented and related to the sensor signal. Finally, possible sources to thermal effects are addressed.

The planar Hall effect stems from the anisotropic magnetoresistance effect of a magnetized ferromagnetic material. Electrons travelling along or perpendicular to the magnetization experience different resistances. This gives rise to an anisotropic response. In order to have a well defined starting point of the magnetization, an easy axis of magnetization is introduced during metal deposition. The easy axis can be pinned by an antiferromagnetic material in order to obtain an easy direction of magnetization. The nickel sensors constituting our initial work on planar Hall sensors [2] experience uniaxial anisotropy, and the improved exchange biased permalloy sensors [4, 5] experience both uniaxial and unidirectional anisotropy.

3.1 The planar Hall effect

The planar Hall sensor is based on the planar Hall effect of ferromagnetic materials. The resemblance to the ordinary Hall effect comes from the measuring geometry so the name is somewhat misleading. The origin of the planar Hall effect is from anisotropic scattering of electrons carrying current due to the magnetic moment of the lattice atoms. On the other hand, the ordinary Hall effect is caused by the Lorentz force interaction between charged particles moving in a magnetic field. The planar Hall effect gives rise to an induced electric field in the plane of the sensor when the anisotropic material is magnetized in the same plane. Hence the name *planar* as opposed to the perpendicularly induced electric field across a normal Hall element.

A drawing of the planar Hall sensor geometry is presented in Fig. 3.1. **H** is primarily along x. To begin with the magnetization vector lies in an arbitrary direction depending on all coordinates (x, y, z).

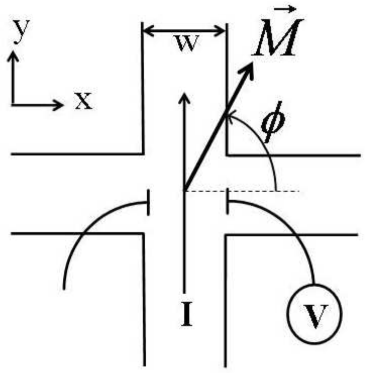

Figure 3.1: Geometry of the planar Hall sensor. The magnetization vector, **M**, has an angle ϕ with respect to the x-axis. **M** lies in the xy-plane, the current, I, is along y, and the voltage, V, is measured along x. The sensor cross has the width w and thickness t.

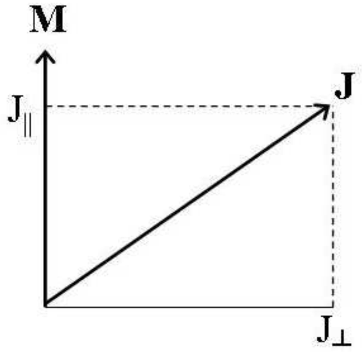

Figure 3.2: Decomposition of **J** into parallel and perpendicular components with respect to **M**. The angle between **J** and $\mathbf{J}_{\perp}$ is ϕ.

The relevant physical relation is Ohm's law,

$$\mathbf{E} = \overline{\overline{\rho}}\mathbf{J} \tag{3.1}$$

Generally, the resistivity $\overline{\overline{\rho}}$ is a tensor. In an anisotropic magnetoresistive (AMR) material, the following resistivities are encountered: ρ_{H} is the Hall resistivity, and $\rho_{\perp}$ and $\rho_{||}$ are the resistivities when the magnetization vector is perpendicular and parallel to the current density, respectively. For isotropic materials $\rho_{\perp}$ and $\rho_{||}$ are equal but for ferromagnetic materials, *e.g.* Ni, Fe, and Co, $\rho_{||} > \rho_{\perp}$ due to the AMR effect [6]. A unit vector is defined in the magnetization direction $\hat{\mathbf{M}}$, see Fig. 3.2, and the current density can be written in terms of its parallel and perpendicular components,

$$\mathbf{J} = J_{||}\hat{\mathbf{M}} + J_{\perp}\hat{\mathbf{M}}_{\perp} \tag{3.2}$$

$$\mathbf{J} = J_{||}\hat{\mathbf{M}} + \mathbf{J} - J_{||}\hat{\mathbf{M}} \tag{3.3}$$

E is found from Eq. (3.1)

$$\mathbf{E} = \rho_{||}J_{||}\hat{\mathbf{M}} + \rho_{\perp}(\mathbf{J} - J_{||}\hat{\mathbf{M}}) + \rho_{\mathrm{H}}\mathbf{M} \times \mathbf{J} \tag{3.4}$$

By definition (Fig. 3.2), $J_{||} = \mathbf{J} \cdot \hat{\mathbf{M}}$, and Eq. (3.4) can be written as [6]

$$\mathbf{E} = \hat{\mathbf{M}}(\mathbf{J} \cdot \hat{\mathbf{M}})[\rho_{||} - \rho_{\perp}] + \rho_{\perp}\mathbf{J} + \rho_{\mathrm{H}}\mathbf{M} \times \mathbf{J} \tag{3.5}$$

The current density is chosen along the positive y-direction (see Fig. 3.1) such that $\mathbf{J} = J_y\hat{\boldsymbol{y}}$. $J_y = I/wt$. I is the total current through the sensor, and w is the width and t the thickness of the sensor. Particularly interesting to the sensor problem is E_x which generates the voltage output of the sensor. In spherical coordinates (ϕ is defined in Fig. 3.1, and θ is the polar angle measured from the z-axis) the magnetization unit vector is

$$\hat{\mathbf{M}} = \begin{pmatrix} \sin\theta\cos\phi \\ \sin\theta\sin\phi \\ \cos\theta \end{pmatrix}$$

E_x can then be extracted from Eq. (3.5)

$$E_x = \sin^2\theta(\rho_\parallel - \rho_\perp)J_y \sin\phi\cos\phi - \rho_\mathrm{H}\cos\theta M J_y \tag{3.6}$$

In the planar Hall sensor (Fig. 3.1) $\mathbf{M}$ is restricted to the xy-plane, and Eq. (3.6) reduces to

$$E_x = (\rho_\parallel - \rho_\perp)J_y \sin\phi\cos\phi \tag{3.7}$$

In terms of planar Hall voltage $V = E_x \cdot w$ and total current, $I = J_y \cdot wt$, Eq. (3.7) becomes

$$V = \frac{I(\rho_\parallel - \rho_\perp)\sin\phi\cos\phi}{t} = \frac{I(\rho_\parallel - \rho_\perp)\sin 2\phi}{2t} \tag{3.8}$$

Now Eq. (3.8) can be rewritten in terms of the applied field and the anisotropic magnetoresistance coefficient ($AMR \equiv \frac{\rho_\parallel - \rho_\perp}{\rho_\mathrm{av}}$), where ρ_av is the average resistivity of the film. Defining $x = \cos\phi$, gives the following expression for the voltage drop across the width of the sensor

$$V = I\frac{AMR \cdot \rho_\mathrm{av}}{t}x\sqrt{1-x^2}. \tag{3.9}$$

3.1.1 Magnetic energy and expected field response

Uniaxial anisotropy

It is assumed that $\mathbf{H}$ is essentially in the x-direction of Fig. 3.1 because the applied external field is along x. The easy axis is along the y-direction, and the magnetization lies in the xy-plane at an angle ϕ with respect to the x-axis. For a ferromagnetic layer with uniaxial symmetry, using the first order approximation to the magnetic anisotropy gives the following energy density of the film

$$E(\phi) \approx -\mu_0\mathbf{M}\cdot\mathbf{H} + \frac{\mu_0}{2}MH_K\cos^2\phi \tag{3.10}$$

In which the the anisotropy field is defined

$$H_K \equiv \frac{2K_u}{\mu_0 M} \tag{3.11}$$

The total magnetic field intensity ($\mathbf{H}$) contains contributions from the applied field, the current through the sensor, the field from beads, and possibly the fringing field from the sensor itself. K_u is the uniaxial anisotropy constant of the layer.

The z-component of the film's magnetization is limited due to demagnetization effects. Furthermore, if the y-component of the magnetic field is small compared to the uniaxial anisotropy field, $H_y \ll H_K$, only the x-component, H_x, needs to be considered and Eq. (3.10) reduces to

$$E(\phi) = -\mu_0 M H_x \cos\phi + \frac{\mu_0}{2} M H_K \cos^2\phi \tag{3.12}$$

In thermodynamical equilibrium, the energy of the film attains its minimum value, and $\cos\phi$ can be found by minimizing the energy for $|H_x| \leq H_K$.

$$\cos\phi = \frac{H_x}{H_K} \tag{3.13}$$

For small applied fields, $\cos\phi \ll 1$, the first order approximation of Eq. (3.9) becomes

$$V = I\frac{AMR \cdot \rho_{\text{av}}}{t} x\sqrt{1-x^2} \approx I\frac{AMR \cdot \rho_{\text{av}}}{t}\frac{H_x}{H_K} \tag{3.14}$$

An expression for the sensitivity, S_0 which is independent of applied parameters, of the sensor can be found

$$S_0 \equiv \frac{V_x}{H_x I} = \frac{AMR \cdot \rho_{\text{av}}}{t \cdot H_K} \tag{3.15}$$

Fig. 3.3 shows the magnetic field dependence of the sensor with uniaxial anisotropy. The dotted line has the slope given in Eq. (3.15), which is accurate to within 2 % in the interval $-0.20 < H_x/H_K < 0.20$.

Uniaxial and unidirectional anisotropy

The ferromagnetic layer can be pinned with an adjacent antiferromagnetic layer [27]. The contribution to the magnetic energy density can be regarded as an additional energy with unidirectional properties, *i.e.* the exchange energy. If an exchange field, H_E, is added to Eq. (3.12), the first order magnetic energy density of the film is

$$E(\phi) \approx -\mu_0 M H_x \cos\phi + 1/2\mu_0 M H_K \cos^2\phi - \mu_0 M H_E \sin\phi \tag{3.16}$$

Minimization of Eq. (3.16) for small applied fields, *i.e.* angles close to $\phi = 90\ ^{\text{o}}$ and $\sin\phi \approx 1$, gives the $\cos\phi$ expression

$$\cos\phi \approx \frac{H_x}{H_K + H_E} \tag{3.17}$$

H_K is the anisotropy field, and H_E is the exchange coupling field.

For small applied fields the first order approximation of Eq. (3.9) becomes

$$V = I\frac{AMR \cdot \rho_{\text{av}}}{t} x\sqrt{1-x^2} \approx I\frac{AMR \cdot \rho_{\text{av}}}{t}\frac{H_x}{H_K + H_E} \tag{3.18}$$

And the sensitivity of the sensor becomes

$$S_0 \equiv \frac{V_x}{H_x I} = \frac{AMR \cdot \rho_{\text{av}}}{t(H_K + H_E)} \tag{3.19}$$

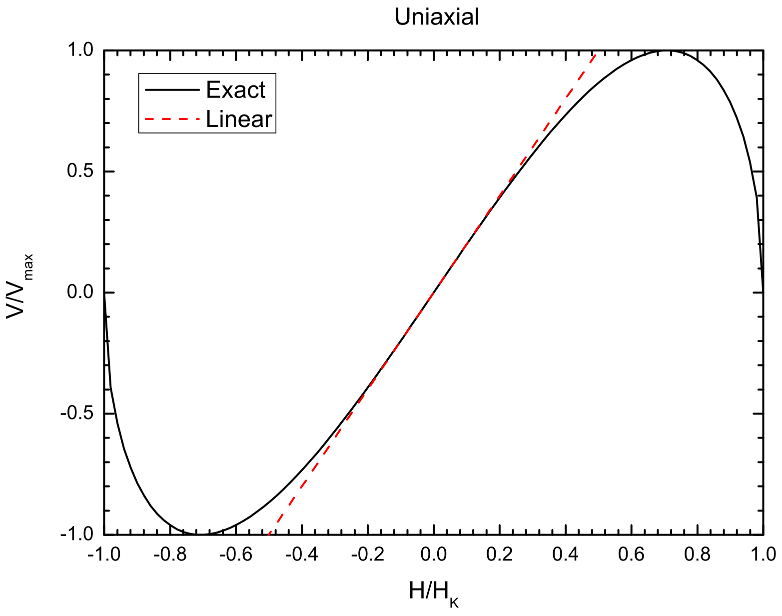

Figure 3.3: Expected sensor response as a function of applied magnetic field, H/H_K. The dotted line shows the linear approximation to Eq. (3.9).

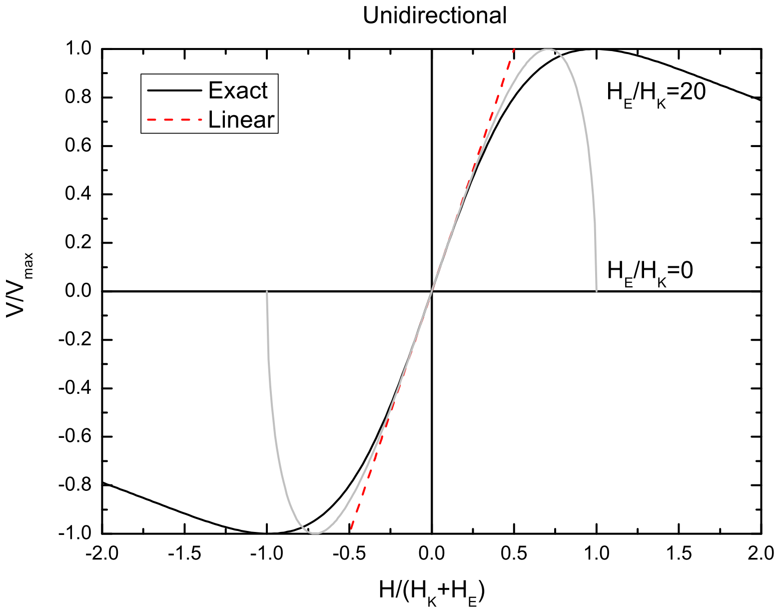

Figure 3.4: Expected sensor response as a function of applied magnetic field, $H/(H_K+H_E)$. The dotted line shows the linear approximation to Eq. (3.9). Also shown in the graph is the $H_E = 0$ special case of uniaxial anisotropy (grey line).

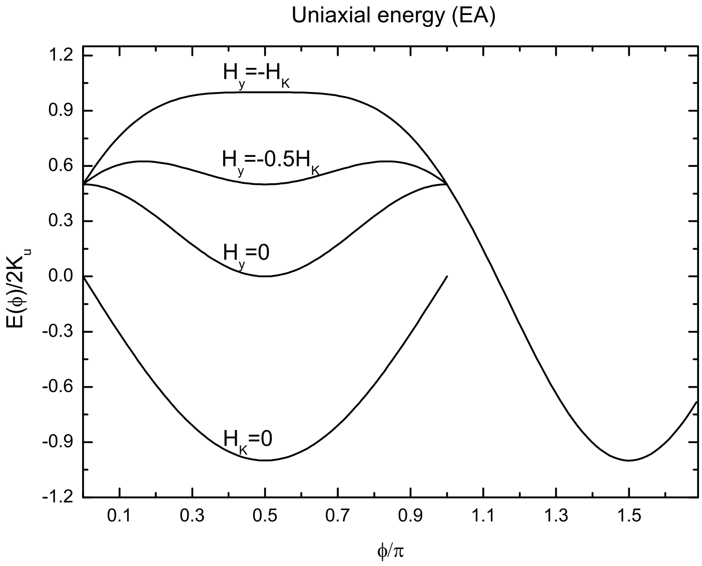

Figure 3.5: Normalized film energy, $E(\phi)/2K_u$, as a function of ϕ for different values of H_y/H_K.

Eq. (3.9) is plotted in Fig. 3.4 with x defined in Eq. (3.16) for exchange biased film anisotropy. The dotted line has the slope given in Eq. (3.19), which is accurate within 2 % in the interval $-0.23 < H_x/(H_K + H_E) < 0.23$.

3.2 Hysteresis curves

The energy expression of Eq. (3.10) can be used to find the behavior of the film's magnetization in an applied magnetic field along the x-direction (hard axis) and the y-direction (easy axis). The magnetization vector depicted in Fig. 3.1 is

$$\mathbf{M} = M_S \begin{pmatrix} \cos\phi \\ \sin\phi \end{pmatrix} \tag{3.20}$$

where M_S is the saturation magnetization of the film. For fields applied along the hard axis of magnetization, this means that the x-component of the magnetization is

$$M_x = M_S \begin{cases} \frac{H_x}{H_K} & \text{uniaxial } |H_x| \leq H_K, \\ \frac{H_x}{H_K+H_E} & \text{unidirectional, small } \phi,\ |H_x| \lesssim 0.2(H_K + H_E). \end{cases} \tag{3.21}$$

Easy axis hysteresis, uniaxial anisotropy

Considering fields applied along the easy axis of magnetization, the energy in uniaxial anisotropy is

$$E(\phi) = \mu_0 M(-H_y \sin\phi + 1/2 H_K \cos^2\phi) \tag{3.22}$$

Eq. (3.22) is shown in Fig. 3.5 for different values of H_y/H_K.

For large positive fields, $H_y \gg H_K$, the energy minimum is at $\sin\phi = 1 \Rightarrow \phi = \pi/2$ (Fig. 3.5, $H_K = 0$). Decreasing H_y destabilizes the minimum, and switching occurs where the second derivative disappears at $H_y = -H_K$,

$$\begin{aligned} &\frac{d^2E(\phi)}{d\phi^2}|_{\phi=\pi/2} = 0 \Rightarrow \\ &\frac{H_y}{H_K} = \frac{\cos 2\phi}{\sin\phi}|_{\phi=\pi/2} \end{aligned} \tag{3.23}$$

Moving backwards, switching occurs at $H_y = +H_K$,

$$\frac{H_y}{H_K} = \frac{\cos 2\phi}{\sin\phi}|_{\phi=-\pi/2} \tag{3.24}$$

The resulting magnetization versus applied field curves are shown in Fig. 3.6 for applied field along the hard axis (HA) or along the easy axis (EA).

Easy axis hysteresis, exchange biased anisotropy

For the exchange biased film, with the field applied along the easy axis, the energy is

$$E(\phi) = \mu_0 M(-(H_y + H_E)\sin\phi + \frac{1}{2} H_K \cos^2\phi) \tag{3.25}$$

which is identical to Eq. (3.22) exchanging H_y with $H_y + H_E$.

Switching of magnetization alignment from along $+y$ to along $-y$ occurs at

$$-(H_y + H_E)/H_K = 1 \Rightarrow H_y = -H_K - H_E$$

and switching from along $-y$ to along $+y$ occurs at

$$-(H_y + H_E)/H_K = -1 \Rightarrow H_y = H_K - H_E$$

The resulting magnetization versus applied field curves are shown in Fig. 3.7 both for the applied field along the hard axis (HA) and along the easy axis (EA). The exchange field is visualized as a shift towards negative field values in the EA hysteresis loop.

Measurements of the hysteresis loops can be performed using, *e.g.*, a vibrating sample magnetometer (VSM). The hysteresis loop with the field applied along the easy axis of magnetization can thus be used to determine H_K and H_E, which can be used to predict the sensor sensitivity using Eq. (3.19).

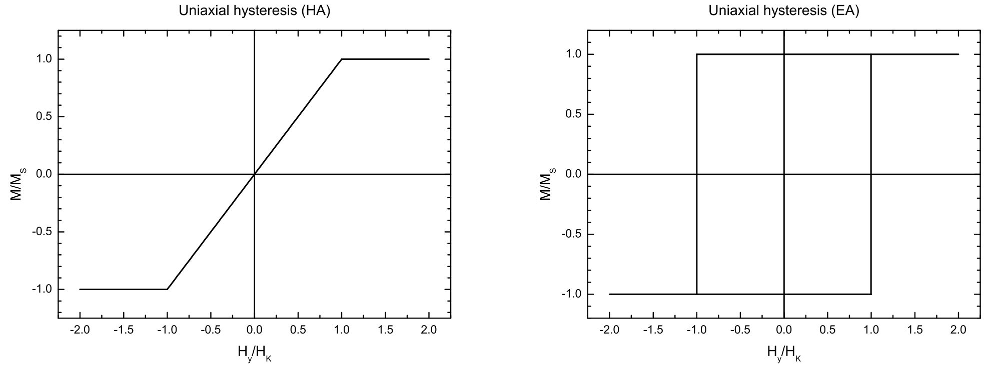

Figure 3.6: Hysteresis loops for uniaxial anisotropy. Left: applied field along the hard axis. Right: applied field along the easy axis.

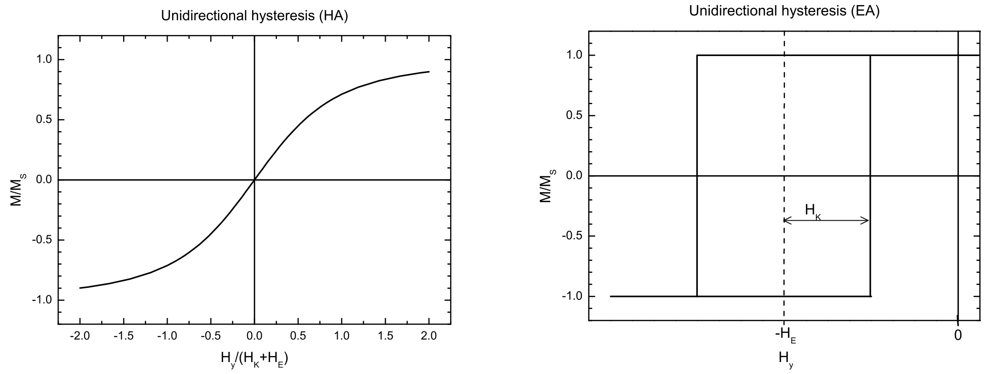

Figure 3.7: Hysteresis loops for unidirectional anisotropy of an exchange biased film. Left: applied field along the hard axis. Right: applied field along the easy axis.

3.3 Effects of temperature

Investigation shows that the planar Hall sensor is temperature dependent. The temperature dependence is approximately linear in the temperature range of interest, and subtracting the temperature drift from the signal should be fairly straight forward.

From Eq. (3.9) you will remember that five parameters enter the expression for the planar Hall voltage: I, t, $\sin\phi$, AMR, ρ_{av}. A high precision current source is used to control the current, and a thermal effect from the current can thus be ruled out. The thickness of the ferromagnetic material will also remain constant, and $\sin\phi$, which is determined by the external field, will fluctuate very little at the temperatures of interest, *i.e.* those close to room temperature. This leaves us with the AMR ratio and the average resistivity as possible contributors to a temperature dependence.

AMR varies approximately 0.1 % °C^{-1} according to the authors of Ref. [9, 16]. This was confirmed by personal communication with the late Prof. A. K. Menon. This variation is not enough to explain the temperature variation observed in the planar Hall sensors.

According to Bozorth [28] the resistivity of pure nickel changes considerably with temperature. In Figure 16-24 he quotes data reported by Mott [29] where the resistivity (normalized to the value at the Curie point) changes approximately from 0.21 to 0.38 when the temperature changes from 0 °C to 100 °C. The curve is concave, not linear, but in a small temperature window as the one the planar Hall sensor will experience, linearity is a very close approximation. A conversion of this sensitivity into a percentage value yields 0.57 % °C^{-1}.

The paper referred to, Ref. [29], proposes a model, where the resistivity is directly proportional to temperature times a correction term, which depends on η, the ratio of actual magnetization to saturation magnetization at $T = 0$ K

$$\rho = \text{const.}\frac{T}{M\Theta^2}\left(\frac{1}{(1-\eta)^{1/3}+\alpha}+\frac{1}{(1+\eta)^{1/3}+\alpha}\right)^{-1}$$

Θ is the Debye temperature, and α is a measure of transition probability between electronic orbitals s and d, at room temperature $\alpha \approx 0.25$. This correction term, in parentheses, is present but slowly varying at the temperature range of interest for the planar Hall sensor. Hence the contribution can be regarded as linear in planar Hall sensor applications. It should be noted that Mott obtains very close agreement with experiments when using this model.

The temperature dependence of the planar Hall effect in thin films was studied by Ky in 1968 [30]. Ky finds that the planar Hall effect increases with increasing temperature. A temperature drift of approximately 0.2-0.25 % °C^{-1} is reported for 22 nm thick Ni films in the temperature range 200 K to 300 K.

An earlier experimental study by Shirakawa [31] finds that ΔR_e drops approximately 0.22 % °C^{-1} for the permalloy composition of bulk nickel-iron alloys. However, the findings of Ky [30] for bulk nickel also show a decrease in the planar Hall effect with increasing temperature, whereas the tendency is increasing for thin films. The parameters of thin films clearly differ from their bulk values.

For thin permalloy films, Montaigne *et al.* finds a temperature dependence in the order of 0.3 % °C^{-1} for the isotropic part of the resistance, R_e, [1].

Chapter 4

Theoretical sensor signal from magnetic beads

This chapter presents a study of the single bead field with respect to sensor size and bead position both laterally and vertically above the sensor surface. This is followed by a summary of the theoretical detection limits based on the experimentally verified noise level. The aim is to verify the sensor's capability of detecting just a single bead based on the theoretical *S/N*. Hereafter, a study of a monolayer of non-interacting beads is presented for the sensors used for influenza immunoassay detection. An estimate of the signal magnitude produced by a monolayer of beads is obtained. Then a discussion of designing the SU-8 layer optimally for bead detection experiments follows. What design is the best for bead detection experiments? Given the choice of SU-8 design, what signal can be expected from a monolayer of beads?

For the medical diagnostic chips, the aim is simply a binary answer to the question whether beads are present or not. For the ensuing applications such as tracking cells, the aim is a truly quantitative measure of the number of beads in the sample. This chapter analyzes the signal produced by a single magnetic bead placed above a general magnetic sensor. In order to facilitate the computation and the interpretation of the results a quadratic sensor area is considered. It can readily be generalized to other geometries of active sensing area.

The position of the bead with respect to the sensor edges heavily influences the signal produced. Centered above the sensor, the signal is negative, just before the sensor edge the negative signal is enhanced, and passing the edge the bead gives a positive signal. This finding proposes a chip design that takes into account this change in signal when crossing the edge. The signal from a monolayer of beads can be enhanced considerably by removing the positively contributing beads.

4.1 Magnetic beads

This section describes the types of magnetic beads used for bead detection experiments. Their physical properties are described with the magnetic properties in focus. Included is an estimate of when the assumption of non-interacting beads holds for the studied bead products.

Magnetic beads come in a large number of varieties and qualities. Those chosen for this project are commercially available beads that exhibit nearly uniform properties: Dynabeads M-280 (www.dynal.no), Micromer-M and Nanomag-D (www.micromod.de) are close to spherical and have nearly uniform magnetic properties. They are polystyrene spheres with nanoparticles of iron oxide embedded in the matrix. The surface of the beads can be functionalized with various biochemical species, nucleic acids (DNA and RNA), proteins (specific antibodies), or even cells, which are all attached to the surface of the magnetic bead. Another option is to put magnetic beads inside cells by endocytosis. When the acquired species are related to the presence of the bead, attached to the surface of the bead, or filled up with beads, the presence and the whereabouts of the species can be revealed by tracking the bead.

4.1.1 Magnetic characterization of beads

Magnetic characterization of the beads is performed using a Lakeshore Model 7407 vibrating sample magnetometer (VSM). Fig. 4.1 shows the curve obtained for 18.95 mg of 250 nm beads, Nanomag-D. The size refers to the average diameter of the beads. Analysis of the low field slope with compensation for the diamagnetic contribution by the container yields the measured magnetic susceptibility, $\chi_m = 3.2 \pm 0.1$ (SI). The uncertainty on χ_m is estimated from the slope and assumes zero uncertainty on the bead density. Due to demagnetization effects, $\chi_m > 3$ is not possible if the beads are completely spherical.

The magnetic properties of various commercially available beads investigated with the VSM, and the physical properties provided by the supplier, are summarized in Table 4.1.

4.1.2 Bead-bead interaction

The assumption that the beads are not interacting is used throughout the study of the signal produced by a monolayer of beads. This assumption is valid, when the field produced by a bead is small compared to the external field, *i.e.* $H \gg H_{\text{bead}}$, which for a dipole field means [32]

$$H \gg \frac{MR^3}{3r^3} = \frac{\chi_m H R^3}{3r^3}$$

r is the distance from one bead center to the next, R the bead radius, and M is the magnetization. For a linear magnetic material $M = \chi_m H$, where χ_m is the measured susceptibility. Rearranging, we get

$$\left(\frac{r}{R}\right)^3 \gg \frac{\chi_m}{3} \tag{4.1}$$

For Nanomag-D beads, $\chi_m \approx 3$, we get that the assumption of non-interacting beads holds when

$$r \gtrsim R$$

The validity of the non-interacting beads approximation is summarized in Table 4.1 for the studied beads.

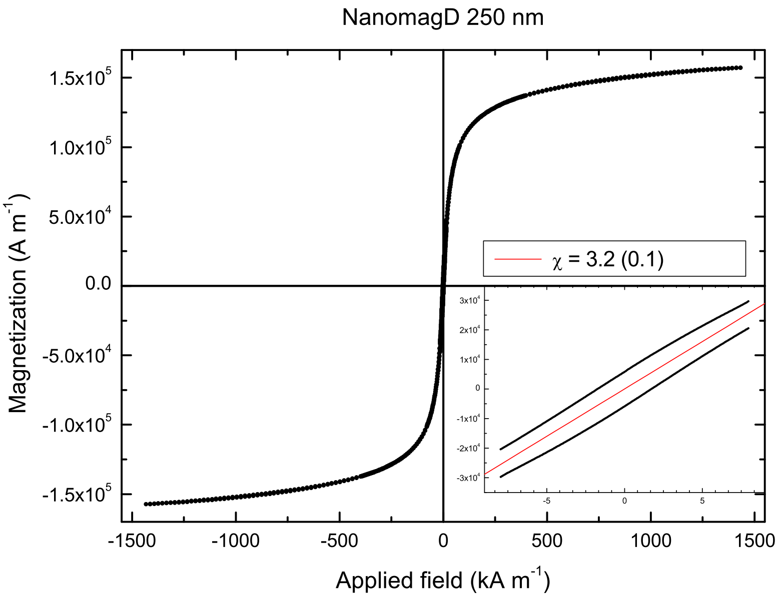

Figure 4.1: Vibrating sample magnetometry (VSM) measurements of 18.95 mg Nanomag-D beads, average diameter 250 nm. The insert shows the low-field response of the magnetic beads, where the slope is an estimate of the susceptibility of the beads. A remanent magnetization is present in the sample.

Bead	Diameter	Concentration	Density	χ_m	$\frac{r}{R} \gtrsim$
Dynabeads M-280	2.8 μm	10 mg ml^{-1}	1.3 g cm^{-3}	0.13 (SI)*	0.35
Micromer-M	2 μm	25 mg ml^{-1}	1.4 g cm^{-3}	0.3(0.1) (SI)	0.46
Nanomag-D	250 nm	10 mg ml^{-1}	2.5 g cm^{-3}	3.2(0.1) (SI)	1.02
Nanomag-D-spio	50 nm	10 mg ml^{-1}	1.4 g cm^{-3}	1.4(0.1) (SI)	0.78

Table 4.1: Physical properties of magnetic beads given by the supplier or measured on a VSM. The errors are determined from the slope assuming no error on the density. χ_m is the measured magnetic susceptibility. (*) χ_m of the Dynabeads is estimated from the information given by the supplier (www.invitrogen.com). $\frac{r}{R}$ is the bead-bead distance divided by the radius, tabulated are the values to which extent the non-interacting bead approach holds, Eq. (4.1).

4.2 Sensor and bead

After looking at their physical properties, the beads are considered with respect to a magnetic sensor. The planar Hall sensor, spin-valve sensor, and GMR sensor are magnetic field sensors sensitive to fields in the plane of the sensor. A linear magnetic field sensor is sensitive to the average field above the active sensing area. Therefore the mean value of the magnetic field produced by the bead is calculated for certain sensor geometries.

An applied external field magnetizes the bead. The field strength from the bead just below the bead opposes the external field. The field just below the bead represents a maximum value that can be detected by the sensor if it were possible to construct an infinitely small sensor. The planar Hall sensor uses all its active area for detection, which means that the field felt by the sensor is an average of the field strength at all locations of the sensitive area. This average is calculated by a weighted integral.

4.3 Analytical study of single bead signal

In this section the average bead field, $\langle H_x \rangle$, is calculated. Assuming uniform magnetic properties and spherical geometry, the field produced by a magnetic bead is the dipole field. The linear sensor measures the x-component of the field averaged over the sensor area. Therefore the measured field is estimated as the average of H_x, where the average is produced over the sensor area. Two sensor geometries, circular and quadratic, are evaluated.

The magnetic field strength produced by a single bead (assuming it is spherical and can be regarded as uniformly magnetized) magnetized by an external field, $H_0\hat{\boldsymbol{x}}$, is the well-known dipole field derived in Appendix A.

$$\mathbf{H} = \frac{M}{3}\frac{R^3}{r^3}(3(\hat{\mathbf{M}} \cdot \hat{\boldsymbol{r}})\hat{\boldsymbol{r}} - \hat{\mathbf{M}}) \tag{4.2}$$

M is the magnetization, and $\hat{\mathbf{M}}$ a unit vector in the direction of magnetization, i.e. along $\hat{\boldsymbol{x}}$. R is the bead radius, and r the distance from the center of the bead to the observation point. The geometry is sketched in Fig. 4.2, omitting $\mathbf{M}$ for clarity. In the following, $\hat{\boldsymbol{x}}$ and $\hat{\boldsymbol{r}}$ are unit vectors in the cartesian and spherical coordinate systems, respectively. $\hat{\boldsymbol{\rho}}$ and $\hat{\boldsymbol{\phi}}$ are unit vectors in an in-plane polar coordinate system, with ϕ defined with respect to the x-axis. The spherical coordinate system consists of $\hat{\boldsymbol{r}}$, $\hat{\boldsymbol{\theta}}$, and $\hat{\boldsymbol{\phi}}$, where the azimuthal angle ϕ is identical to ϕ in the polar coordinate system, and θ is the polar angle defined with respect to the z-axis.

Due to demagnetization effects, which are opposing magnetization components perpendicular to the sensor plane, only in-plane field components are important. The y-component of the field produced by the bead is small compared to the effective anisotropy of the film, and thus only the x-component needs to be considered. The x-component of the field produced by the bead is sensed by the planar Hall sensor. Remembering $\hat{\boldsymbol{x}} \cdot \hat{\boldsymbol{r}} = \sin\theta\cos\phi$, and $\hat{\boldsymbol{x}} \cdot \hat{\mathbf{M}} = 1$, the x-component of the field can be extracted from

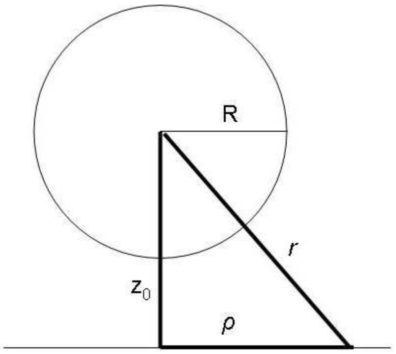

Figure 4.2: Schematic drawing of a bead of radius R placed above a magnetic sensor. r is the distance from the center of the bead to the observation point, z_0 is the vertical distance from the center of the bead to the sensor, and ρ is the distance in the sensor plane from the center of the bead to the observation point.

Eq. (4.2).

$$H_x = \mathbf{H} \cdot \hat{\boldsymbol{x}} = \frac{M}{3}\frac{R^3}{r^3}(3\sin^2\theta\cos^2\phi - 1) \tag{4.3}$$

In the case of maximum produced field at a right angle to the bead magnetization $r = z_0$, where z_0 is the normal distance along z, see Fig. 4.2. The maximum value found from Eq. (4.3) is

$$H_{\max} = -\frac{M}{3}\frac{R^3}{z_0^3} \tag{4.4}$$

If, additionally, the field is measured just below the bead, at $z_0 = R$, $H_{\max}$ reduces to $-M/3$.

The trigonometric sine function in Eq. (4.3) can be rewritten in terms of the distances involved as $\sin\theta = \frac{\rho}{r}$, where ρ is the distance in the xy-plane identical to the radius in the polar coordinate system. With these definitions Eq. (4.3) becomes

$$H_x = \frac{MR^3}{3}\frac{(3\rho^2\cos^2\phi - r^2)}{r^5} \tag{4.5}$$

Using Pythagoras' relation eliminates the last mixed variable: $r = \sqrt{\rho^2 + z_0^2}$

$$H_x = \frac{MR^3}{3}\frac{3\rho^2\cos^2\phi - (\rho^2 + z_0^2)}{(\rho^2 + z_0^2)^{5/2}} \tag{4.6}$$

To obtain an estimate of the field strength influencing the sensor, H_x is integrated over a general sensor area, A, below the bead, the integral is evaluated at a distance $z_0 \geq R$.

$$\langle H_x \rangle = \frac{1}{A}\int H_x dA \tag{4.7}$$

where A is the sensor area and dA the differential area element.

4.3.1 Circular sensor geometry

For a circular sensor cross section of radius ρ_0 with the bead placed above the center, the integral turns out to be fairly straightforward. In polar coordinates $dA = \rho d\rho d\phi$, and $A = \pi\rho_0^2$.

$$\langle H_x \rangle = \frac{1}{\pi\rho_0^2} \int_0^{2\pi} \int_0^{\rho_0} H_x \rho d\rho d\phi \tag{4.8}$$

$$\langle H_x \rangle = \frac{1}{\pi\rho_0^2} \int_0^{2\pi} d\phi \int_0^{\rho_0} \rho d\rho \frac{MR^3}{3} \frac{3\rho^2 \cos^2\phi - (\rho^2 + z_0^2)}{(\rho^2 + z_0^2)^{5/2}} \tag{4.9}$$

First the ϕ-integral is evaluated, in which the integral of $\cos^2\phi$ is π, and the integral of 1 is 2π. Eq. (4.9) thus reduces to

$$\langle H_x \rangle = \frac{MR^3}{3\rho_0^2} \int_0^{\rho_0} \rho d\rho \frac{(3\rho^2 - 2(\rho^2 + z_0^2))}{(\rho^2 + z_0^2)^{5/2}} \tag{4.10}$$

$$\langle H_x \rangle = \frac{MR^3}{3\rho_0^2} \int_0^{\rho_0} d\rho \frac{(\rho^3 - 2\rho z_0^2)}{(\rho^2 + z_0^2)^{5/2}} \tag{4.11}$$

Introduction of the dimensionless variables $\widetilde{\rho} = \rho/z_0$ and $\widetilde{R} = R/z_0$ yields the dimensionless integral

$$\langle H_x \rangle = \frac{M}{3} \frac{\widetilde{R}^3}{\widetilde{\rho_0}^2} \int_0^{\widetilde{\rho_0}} d\widetilde{\rho} \frac{(\widetilde{\rho}^3 - 2\widetilde{\rho})}{(\widetilde{\rho}^2 + 1)^{5/2}} \tag{4.12}$$

This, normalized to $|H_{\max}| = \widetilde{R}^3 M/3$, gives

$$\langle \widetilde{H}_x \rangle = \frac{1}{\widetilde{\rho_0}^2} \int_0^{\widetilde{\rho_0}} d\widetilde{\rho} \frac{(\widetilde{\rho}^3 - 2\widetilde{\rho})}{(\widetilde{\rho}^2 + 1)^{5/2}} \tag{4.13}$$

Eq. (4.13) can be solved analytically

$$\langle \widetilde{H}_x \rangle = -\frac{1}{(1 + \widetilde{\rho_0}^2)^{3/2}} \tag{4.14}$$

Eq. (4.14) shows that the average field produced by a magnetic bead is indeed negative. It also shows that for large sensor areas or very small bead diameters, where edge effects are unimportant, the signal from the bead scales inversely to sensor size cubed, $\langle H_x \rangle \propto \rho_0^{-3}$. When considering the z_0 dependence, the normalization of R should be kept in mind, and we get a scaling which is inversely proportional to separation distance cubed, $\langle H_x \rangle \propto z_0^{-3}$, for large separations compared to the sensor size.

The result of Eq. (4.14) is plotted in Fig. 4.3 as a function of sensor size, ρ_0.

4.3.2 Quadratic sensor geometry

The bead is placed in the center of the sensor at $(x, y) = (0, 0)$. The sensor has the area $A = w^2$. In cartesian coordinates Eq. (4.6) becomes

$$H_x = \frac{MR^3}{3} \frac{2x^2 - y^2 - z_0^2}{(x^2 + y^2 + z_0^2)^{5/2}} \tag{4.15}$$

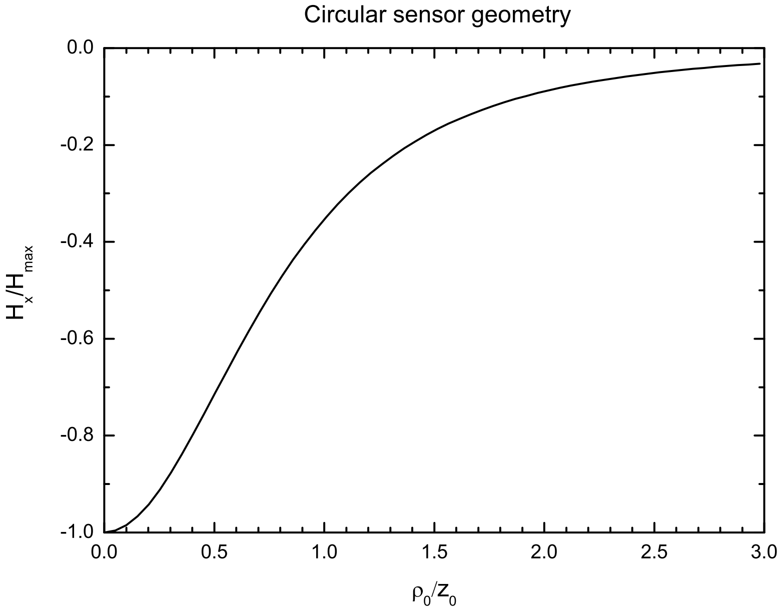

Figure 4.3: Scaling of $\langle\widetilde{H}_x\rangle$ for a single bead at the center of a circular sensor with sensor size $\widetilde{\rho}_0 = \rho_0/z_0$, Eq. (4.14).

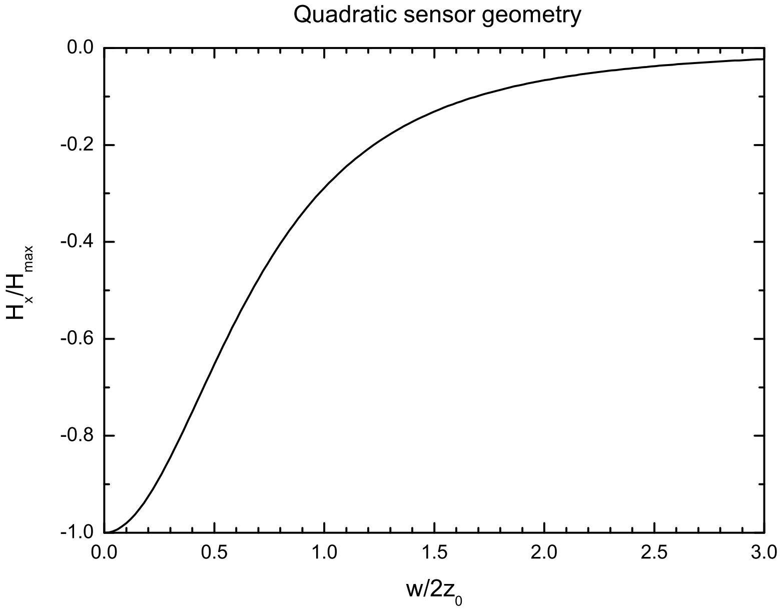

Figure 4.4: Scaling of $\langle\widetilde{H}_x\rangle$ for a single bead at the center of a quadratic sensor with sensor size $\widetilde{w} = w/2z_0$, Eq. (4.19).

And Eq. (4.7), the average of Eq. (4.15), is

$$\langle H_x(w, z_0)\rangle = \frac{MR^3}{3w^2}\int_{-w/2}^{w/2} dx \int_{-w/2}^{w/2} dy \frac{2x^2 - y^2 - z_0^2}{(x^2 + y^2 + z_0^2)^{5/2}} \tag{4.16}$$

Again the introduction of dimensionless variables ($\widetilde{x} = x/z_0$, $\widetilde{y} = y/z_0$, $\widetilde{w} = w/2z_0$, and $\langle\widetilde{H}_x\rangle = \langle H_x\rangle/H_{\max}$, where $H_{\max} = \widetilde{R}^3M/3$) simplifies the expression to

$$\langle\widetilde{H}_x(\widetilde{w})\rangle = \frac{1}{4\widetilde{w}^2}\int_{-\widetilde{w}}^{\widetilde{w}} d\widetilde{x} \int_{-\widetilde{w}}^{\widetilde{w}} d\widetilde{y} \frac{2\widetilde{x}^2 - \widetilde{y}^2 - 1}{(\widetilde{x}^2 + \widetilde{y}^2 + 1)^{5/2}} \tag{4.17}$$

$$= \frac{1}{\widetilde{w}^2}\int_{0}^{\widetilde{w}} d\widetilde{x} \int_{0}^{\widetilde{w}} d\widetilde{y} \frac{2\widetilde{x}^2 - \widetilde{y}^2 - 1}{(\widetilde{x}^2 + \widetilde{y}^2 + 1)^{5/2}} \tag{4.18}$$

The result of the integration is

$$\langle\widetilde{H}_x(\widetilde{w})\rangle = -\frac{1}{(1 + \widetilde{w}^2)(1 + 2\widetilde{w}^2)^{1/2}} \tag{4.19}$$

$\langle\widetilde{H}_x\rangle$ as a function of $\widetilde{w}$ is plotted in Fig. 4.4. For large values of $\widetilde{w}$, $\langle\widetilde{H}_x\rangle$ approaches zero.

Eq. (4.19) proves the initial intuition that the signal from a magnetic bead centered above a magnetic sensor is negative. According to this equation the average field from the bead scales as the inverse cube of the sensor size, $\langle H_x\rangle \propto w^{-3}$, for large sensor sizes compared to the diameter of the bead. Fig. 4.4 shows that the signal from the bead decreases rapidly as a function of sensor size. The ideal geometry of the sensor for single bead detection would thus be infinitely small, or small compared to the bead diameter.

4.3.3 Scaling with sensor size

Comparing Fig. 4.3 and Fig. 4.4 one can observe that the two sensor geometries behave similarly. It is only for sensor sizes near z_0 the two figures differ. For large values, Table 4.2 summarizes the scaling of ρ_0, w, and z_0.

Parameter	Scaling
ρ_0	$\langle H_x\rangle \propto \rho_0^{-3}$
w	$\langle H_x\rangle \propto w^{-3}$
z_0	$\langle H_x\rangle \propto z_0^{-3}$

Table 4.2: Scaling of the average bead field, $\langle H_x\rangle$, with sensor size ρ_0 (circular sensor) and w (quadratic sensor) and sensor-bead separation z_0 for a bead centered on the sensor.

4.4 Single bead detection limits for $20\mu\text{m} \times 20\mu\text{m}$ sensors

In this section an investigation of the signal-to-noise relation for various commercially available beads is performed. First the actual sensor properties are described. Then the

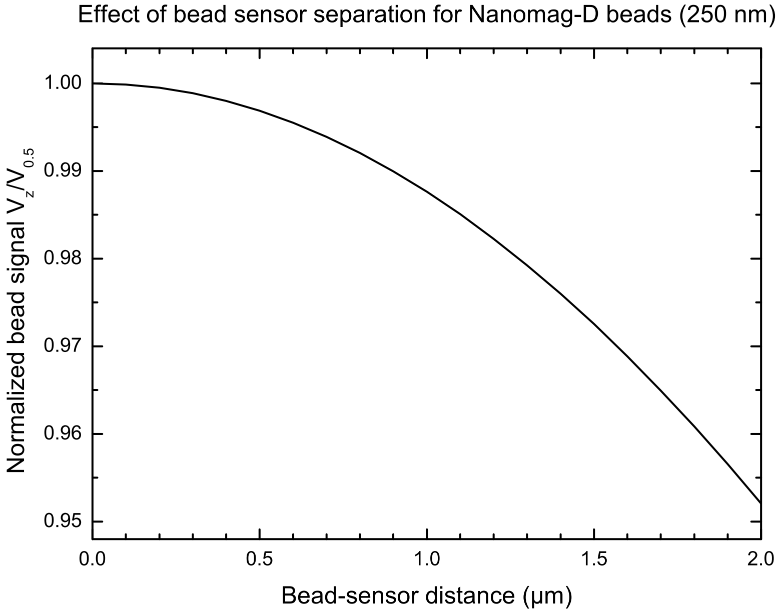

Figure 4.5: Effect of increasing the separation of the sensor and the bead. The bead is placed at the center of a quadratic sensor with $w = 20$ μm, and the average field is calculated from Eq. (4.19). The bead signal is normalized to the value at $z_0 = R$, where the bead is placed directly on top of the sensor.

single bead S/N is calculated for three commercial bead products. Finally, the sensor size is varied. The smaller the sensor, the higher the single bead S/N is found.

Eq. (4.19) gives the average field from a single bead of arbitrary size centered above a general magnetic sensor. Eq. (4.4) describes the properties of a specific bead, recalling that $M = \chi_m H$. The χ_m-values for the beads are in Table 4.1. If a specific sensor is considered, $\widetilde{w} = w/2z_0$ defines the geometry of the sensor with respect to the lateral bead position, and S_0 is the sensor sensitivity. As an example, the fabricated planar Hall sensors are 20μm × 20μm, *i.e.* $w = 20$ μm.

The signal produced by a bead, V_{bead}, is thus

$$V_{\text{bead}} = \langle H_x \rangle S_0 \tag{4.20}$$

$$V_{\text{bead}} = -\frac{S_0 \widetilde{R}^3 \chi_m H}{3(1+\widetilde{w}^2)(1+2\widetilde{w}^2)^{1/2}} \tag{4.21}$$

Fig. 4.5 visualizes the effect of increasing the separation of the sensor and a single Nanomag-D bead (250 nm in diameter). In this figure, the bead signal is normalized to its value at $z_0 = R$, and the bead-sensor distance is the increase in distance from $z_0 = R$. SU-8 is needed on the surface for binding chemistry, and a layer yielding $z_0 = 0.5\ \mu\text{m}$ is chosen as a reasonable tradeoff between single bead signal and the ability to do surface chemistry.

The experimental conditions are $B = 0.5$ mT and $I = 1$ mA giving $S_0 = 44\ \mu\text{V mT}^{-1}$ (Chapter 6). Under these conditions, a Nanomag-D bead placed at the sensor center and at $z_0 = 0.5\ \mu\text{m}$ will produce a signal of

$$B_{\text{bead}} = -7.3 \cdot 10^{-10}\ \text{T} = -0.73\ \text{nT}$$

$$H_{\text{bead}} = -5.8 \cdot 10^{-4}\ \text{A m}^{-1}$$

$$V_{\text{bead}} = -3.2 \cdot 10^{-11}\ \text{V} = -0.032\ \text{nV}$$

The experimental noise level for magnetic immunoassaying is $\Delta V \approx 1$ nV, which is the standard error on the average of 100 samples (Chapter 7). Physical and magnetic properties can be found in Table 4.1.

The single bead signal-to-noise relations and corresponding bead detection limits, realized as the number of beads needed to give $S/N = 2$, are presented in Table 4.3 and in Fig. 4.6. The single bead signal is given by Eq. (4.21). Table 4.3 describes what can be expected of the actual planar Hall sensors used in chapters 6, 7, and 8. The monolayer S/N assumes non-interacting beads and that $\langle H_x \rangle$ is invariant with position. The last assumption is inaccurate, but will be addressed in detail in later sections. Note that S/N produced by a monolayer of Nanomag-D beads exceeds that of Micromer-M in spite of their much lower single bead S/N.

Fig. 4.6 shows S/N and detection limits for the three commercial bead products as a function of sensor size. With areas smaller than 1 μm^2 it is theoretically possible to approach the detection of a single 50 nm magnetic label. Remarkably, this result is obtained optimizing only the sensor size, though the analysis assumes that a current of $I_{\text{AC}} = 1$ mA can be applied to all sensors including the smallest. $10\mu\text{m} \times 10\mu\text{m}$ sensors can sustain 10 mA DC [4], indicating that a $1\mu\text{m} \times 1\mu\text{m}$ sensor is likely to sustain 1 mA DC.

4.5 Quadratic sensor and any bead position

This section investigates how the bead's position influences the average field it produces. The bead is placed at (x', y'), different from the integration variables (x, y), and scanned across the sensor surface. First a small sensor is considered, then a $20\mu\text{m} \times 20\mu\text{m}$ sensor.

For a bead situated at an arbitrary position above the quadratic sensor, the integrals are solved numerically. Mathematica code is included in Appendix C.

Bead	Diameter	S/N	Detection limit	S/N per monolayer
Micromer-M	2 μm	1.55	1-2	155
Nanomag-D	250 nm	0.032	62	206
Nanomag-D-spio	50 nm	$1.1 \cdot 10^{-4}$	17700	18

Table 4.3: Single bead S/N and detection limits for a 20μm × 20μm planar Hall sensor. Experimental parameters for noise level of 1 nV, $B = 0.5$ mT, $I = 1$ mA, and χ_m in Table 4.1. The bead signal is obtained from Eq. (4.21). The detection limit is the number of beads needed to give $S/N = 2$. The monolayer S/N assumes non-interacting beads and that the average field does not change with bead position within the sensor area.

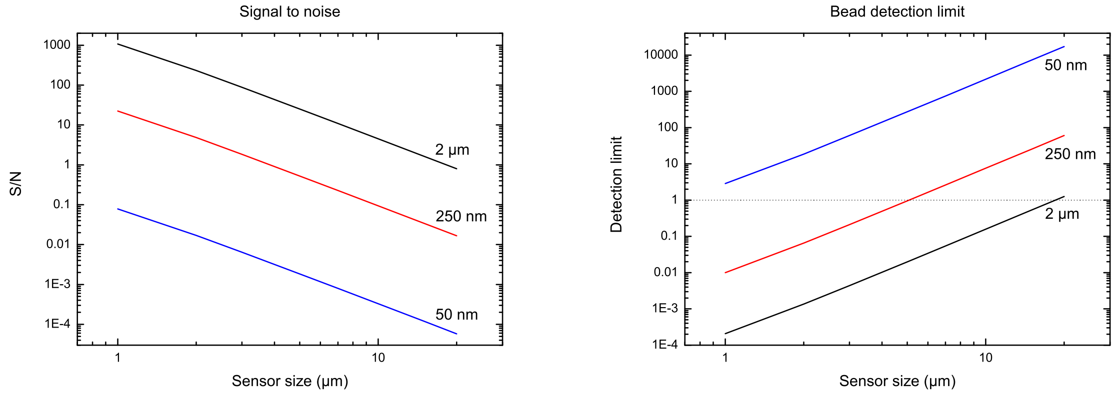

Figure 4.6: Single bead signal-to-noise relations and bead detection limit for increasing sensor sizes. The beads are placed at the center of a square sensor, and the sensor size refers to the edge length. The bead signal is obtained from Eq. (4.21). The bead detection limit is realized as the number of beads needed to give $S/N = 2$ for the specific experimental conditions described in the text. The bead types are: Micromer-M (2 μm), Nanomag-D (250 nm), Nanomag-D-spio (50 nm). (Properties in Table 4.1.)

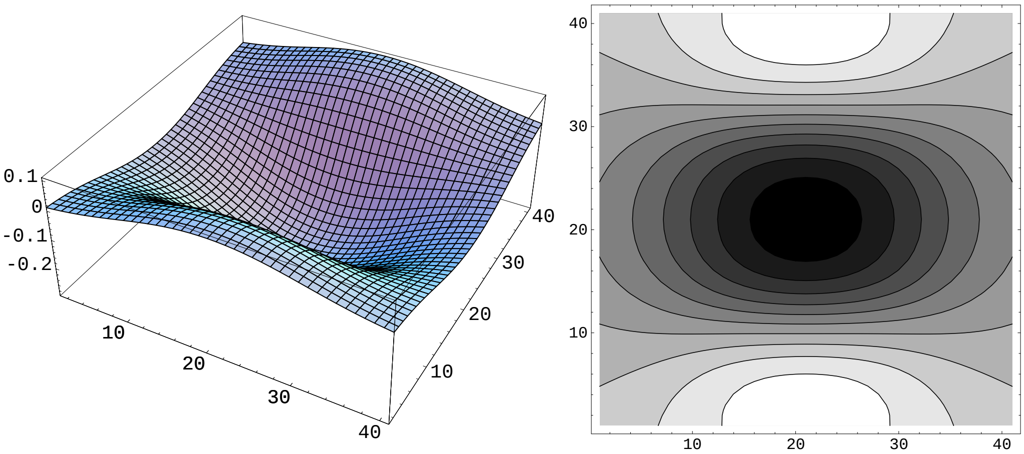

Figure 4.7: Visualization of the numerical values of $\langle \widetilde{H}_x(\widetilde{x}', \widetilde{y}') \rangle$ obtained from evaluation of Eq. (4.22). The x-y-axes show the matrix entry number. Left: Landscape plot for $-2 < \widetilde{x}', \widetilde{y}' < 2$. Right: Contour plot for $-2 < \widetilde{x}', \widetilde{y}' < 2$. White is the highest value attained, black is the lowest. The sensor edges are placed $\widetilde{x}' = \pm 1$ and $\widetilde{y}' = \pm 1$, which in the matrix corresponds to 10 and 30, respectively.

4.5.1 Small sensor compared to bead size

Choosing a sensor size of $\widetilde{w} = 1$ places the sensor edges at $(\widetilde{x}', \widetilde{y}') = \pm 1$. (Normalized coordinates: $\widetilde{x} = x/z_0$, $\widetilde{y} = y/z_0$, $\widetilde{w} = w/2z_0$, and $\langle \widetilde{H}_x \rangle = \langle H_x \rangle / H_{\max}$, where $H_{\max} = \widetilde{R}^3 M/3$.) The signal from the bead as a function of arbitrary bead position, $\widetilde{x}'$ and $\widetilde{y}'$, is, when rewriting Eq. (4.17),

$$\langle \widetilde{H}_x(\widetilde{x}', \widetilde{y}') \rangle = \frac{1}{4} \int_{-1}^{1} d\widetilde{x} \int_{-1}^{1} d\widetilde{y} \frac{2(\widetilde{x}' - \widetilde{x})^2 - (\widetilde{y}' - \widetilde{y})^2 - 1}{((\widetilde{x}' - \widetilde{x})^2 + (\widetilde{y}' - \widetilde{y})^2 + 1)^{5/2}} \tag{4.22}$$

The integral is evaluated for $\widetilde{x}' \in [-2; 2]$ and $\widetilde{y}' \in [-2; 2]$ in order to observe the effect of crossing the edges at $\widetilde{x}' = \pm 1$ and $\widetilde{y}' = \pm 1$. The numerical values are presented in Fig. 4.7.

From the figures it can be observed that a bead placed in the center of the sensor produces the maximum $|\langle H_x \rangle|$-value. From the list of integrals (data not shown), it can be seen that a bead placed at certain positions (at the edges, $\widetilde{x}' = \pm 1$) the contribution changes sign from negative to positive, and a bead placed here will thus decrease the total $|\langle H_x \rangle|$ from a layer of beads distributed evenly.

4.5.2 20μm × 20μm sensor

In order to analyze a specific sensor, the generalized form of Eq. (4.22) is considered

$$\langle \widetilde{H}_x(\widetilde{x}', \widetilde{y}') \rangle = \frac{1}{4\widetilde{w}^2} \int_{-\widetilde{w}}^{\widetilde{w}} d\widetilde{x} \int_{-\widetilde{w}}^{\widetilde{w}} d\widetilde{y} \frac{2(\widetilde{x}' - \widetilde{x})^2 - (\widetilde{y}' - \widetilde{y})^2 - 1}{((\widetilde{x}' - \widetilde{x})^2 + (\widetilde{y}' - \widetilde{y})^2 + 1)^{5/2}} \tag{4.23}$$

(Normalized coordinates: $\widetilde{x} = x/z_0$, $\widetilde{y} = y/z_0$, $\widetilde{w} = w/2z_0$, and $\langle \widetilde{H}_x \rangle = \langle H_x \rangle / H_{\max}$, where $H_{\max} = \widetilde{R}^3 M/3$.) *Int* will be defined as the integral

$$Int(\widetilde{x}', \widetilde{y}') = \int_{-\widetilde{w}}^{\widetilde{w}} d\widetilde{x} \int_{-\widetilde{w}}^{\widetilde{w}} d\widetilde{y} \frac{2(\widetilde{x}' - \widetilde{x})^2 - (\widetilde{y}' - \widetilde{y})^2 - 1}{((\widetilde{x}' - \widetilde{x})^2 + (\widetilde{y}' - \widetilde{y})^2 + 1)^{5/2}} \tag{4.24}$$

The normalized field from a single bead is thus defined as

$$\langle \widetilde{H}_x(\widetilde{x}', \widetilde{y}') \rangle = \frac{Int(\widetilde{x}', \widetilde{y}')}{4\widetilde{w}^2} \tag{4.25}$$

The sensors of chapters 6, 7, and 8 are studied. The dimension of the sensors is 20μm × 20μm and they are covered by a thin layer of SU-8, used for the binding chemistry. The SU-8 layer is constructed such that the bead's center is placed a distance $z_0 = 0.5$ μm above the sensor. The beads detected in chapters 7 and 8 are the Nanomag-D beads, of diameter 250 nm. Using these specific dimensions the dimensionless parameters are determined as: $\widetilde{w} = 20$ and $\widetilde{R} = 0.25$.

Using the specific values for the dimensionless parameters, the integral is

$$Int(\widetilde{x}', \widetilde{y}') = \int_{-20}^{20} d\widetilde{x} \int_{-20}^{20} d\widetilde{y} \frac{2(\widetilde{x}' - \widetilde{x})^2 - (\widetilde{y}' - \widetilde{y})^2 - 1}{((\widetilde{x}' - \widetilde{x})^2 + (\widetilde{y}' - \widetilde{y})^2 + 1)^{5/2}} \tag{4.26}$$

and the average field from a Nanomag-D bead situated at ($\widetilde{x}'$, $\widetilde{y}'$)

$$\langle H_x(\widetilde{x}', \widetilde{y}') \rangle = \frac{\widetilde{R}^3 M}{3} \cdot \langle \widetilde{H}_x(\widetilde{x}', \widetilde{y}') \rangle = \frac{\widetilde{R}^3 M}{3} \cdot \frac{Int(\widetilde{x}', \widetilde{y}')}{4\widetilde{w}^2} \tag{4.27}$$

The integral, *Int*, is symmetric with respect to $\widetilde{x}'$ and $\widetilde{y}'$, such that $Int(-\widetilde{x}') = Int(+\widetilde{x}')$ and $Int(-\widetilde{y}') = Int(+\widetilde{y}')$. Therefore only the expression in the positive quadrant is evaluated: $\widetilde{x}' \in \{0, 40\}$, and $\widetilde{y}' \in \{0, 40\}$. Expecting the $\widetilde{x}'$-value of the integral, *Int*, to give rise to the greatest variations, the integral along $\widetilde{x}'$ from the center of the sensor past the edge is considered. When the center of the bead reaches the edge of the sensor H_x goes from contributing negatively to the integral to contributing positively. This sign change is expected to have a great impact on the value of *Int*. Some positive contributions are removed from the integral, when the positive part of the bead field is placed outside the sensor.

Fig. 4.8 shows *Int* as a function of bead position starting from the center of the sensor, $(x', y') = (0, 0)$, and continuing across the edge with varying bead position along x (blue line). To underline that the change almost solely depends on the x position of the bead, *Int* along y is also included on the graph (red line). The edge, positioned at $x = 10$ μm (or $y = 10$ μm), is marked with a horizontal dotted line.

The first part of the path along x is relatively flat, then two parts with peaks in opposite directions follow, and in the end again a relatively flat path. It is clear from the behavior of *Int* along x that the absolute x-position of a bead with respect to the sensor has a strong influence on the field felt by the sensor. If beads are only situated inside the sensor's active area, their contribution to the applied field will be negative. If, however, beads have crossed the line and are positioned outside the sensor's active area, they will give a positive contribution to the field.

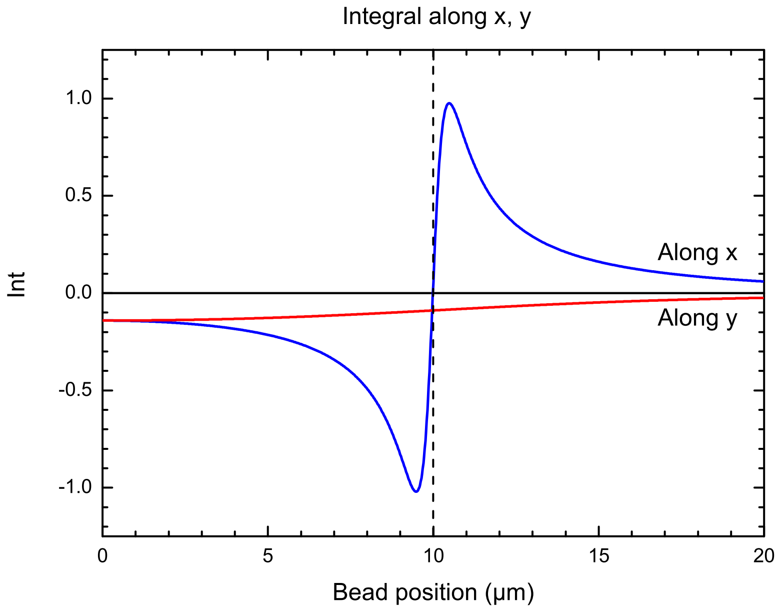

Figure 4.8: Normalized integral of magnetic field strength, *Int*, from a single bead with varying position with respect to the center of the sensor. Along x $(x', 0)$, and along y $(0, y')$. The edge of the sensor is marked with a dotted line at $x, y = 10$ μm.

4.5.3 Monolayer of Nanomag-D beads on 20μm $\times$ 20μm sensors

When the sensors are used for measuring the layer coverage resulting from bead detection experiments, it is important to know how a specific coverage of beads influences the sensor signal. The number of beads, which can be closely packed on a 20μm $\times$ 20μm sensor, is 7390. The sum of contributions from each individual bead in a monolayer of beads is estimated as the trapezoidal sum Trp of the integrals Int (Eq. (4.26)). The sum assumes non-interacting beads plus a statistical layer coverage, in which the beads are distributed evenly over the evaluated surface.

$$Trp = \sum_{i,j} 0.25(Int_{i,j} + Int_{i+1,j} + Int_{i,j+1} + Int_{i+1,j+1}) \tag{4.28}$$

Bead-bead interactions are disregarded in this evaluation. It should be noted that bead-bead interactions are expected to decrease the average field produced by a layer of beads in comparison to non-interacting beads. This is because the field produced by a single bead opposes the applied field, and hence lowers the field felt by its neighbor.

Since the variation of the bead signal is strongest near the sensor edges with respect to x, the sensor area is divided into two edge parts, $\mathrm{E_i}$ and $\mathrm{E_o}$ (inside and outside, respectively), and four parts, where the integral varies more slowly, C, $\mathrm{F_1}$, $\mathrm{F_2}$, $\mathrm{F_3}$ (central and flat 1, 2, 3, respectively).

Choosing the area to be evaluated equal to that spanned by x and y in Fig. 4.8, yields $x \in \{0\mu\text{m}, 20\mu\text{m}\}$ and $y \in \{0\mu\text{m}, 20\mu\text{m}\}$, which is identical to $\widetilde{x}' \in \{0, 40\}$, and $\widetilde{y}' \in \{0, 40\}$, as mentioned previously. This area is divided into six parts, listed in Table 4.4 and shown in Fig. 4.9. In terms of the x' value, the border between C and E$_\text{i}$ is set at $Int = -0.5$ in Fig. 4.8 and equivalently is the border between E$_\text{o}$ and F$_3$ at $Int = +0.5$ in Fig. 4.8. For the y' value, the border is chosen at 2 μm past the edge facilitating the evaluation of the integrals in F$_1$ and F$_2$.

The field from a monolayer of beads covering one of the areas is calculated using the following equation,

$$\langle H_x \rangle = 4 \cdot 7390 \frac{M\widetilde{R}^3}{3 \cdot 4\widetilde{w}^2} \frac{A}{A_\text{tot}} \frac{Trp}{n} \tag{4.29}$$

where M is the bead's magnetization, $\widetilde{R} = R/z_0$ the normalized bead radius, $\widetilde{w} = w/2z_0$ the normalized sensor width, A the area of the evaluated part, A_tot the total area of C+E$_\text{i}$+E$_\text{o}$+F (where F=F$_1$+F$_2$+F$_3$), Trp the trapezoidal sum, and n the number of integrals in the sum.

Normalized to the applied flux density (in mT), the normalized value β reflects the flux density produced by the beads in any applied field,

$$\beta \equiv \frac{\mu_0 \langle H_x \rangle}{B(\text{mT})} = 4 \cdot 7390 \frac{\chi_m \widetilde{R}^3}{3 \cdot 4\widetilde{w}^2} \frac{A}{A_\text{tot}} \frac{Trp}{n} \tag{4.30}$$

as long as the beads' susceptibility, χ_m, is linear with the applied field, *i.e.* for small applied fields.

The trapezoidal sum, Trp, of all Int's in an area like C is evaluated numerically and presented in Table 4.5. The intervals at which an integral is evaluated, $\Delta\widetilde{x}'$ and $\Delta\widetilde{y}'$, are listed along with the number of Int's in the sum, n. n can be related to the number of beads on the area by $n_\text{beads} = n \cdot 7390/4221$ for a monolayer of beads. β is calculated from Eq. (4.30) for a monolayer of beads covering the area in question. Included is the other three quadrants giving identical contributions to the evaluated one. Marked in bold are the expected values for a full coverage of beads at a distance of $z_0 = 0.5$ μm (Fig. 4.10-1). This is the sum of all contributions positive as well as negative.

The average field from a monolayer of beads is negative. This is expected since the negative contributions from the bead field should dominate the positive contributions.

The last two lines of Table 4.5 gives the signal from the beads, when only the sensor (C+E$_\text{i}$) or outside the sensor (E$_\text{o}$+F) is covered with beads. It is evident that not much misplacing of beads is required to flip the sign of the sum from negative to positive. The two contributions have almost the same magnitude though with opposite signs. If most of the beads from E$_\text{i}$ were instead placed in E$_\text{o}$, the sign of the field from the beads would change.

	Position	x'	y'	$\widetilde{x}'$	$\widetilde{y}'$
C	Central area	(0-8) μm	(0-12) μm	(0-16)	(0-24)
E_i	Edge, inside	(8-10) μm	(0-12) μm	(16-20)	(0-24)
E_o	Edge, outside	(10-11.7) μm	(0-12) μm	(20-23.4)	(0-24)
F_1	Flat 1	(0-11.7) μm	(12-20) μm	(0-23.4)	(24-40)
F_2	Flat 2	(11.7-20) μm	(12-20) μm	(23.4-40)	(24-40)
F_3	Flat 3	(11.7-20) μm	(0-12) μm	(23.4-40)	(0-24)

Table 4.4: Division of total area, A_{tot}, of the positive quadrant of the sensor plus the area in its immediate vicinity. A_{tot} is divided in terms of the magnitude and sign of the respective contributions to the total signal from a monolayer of beads.

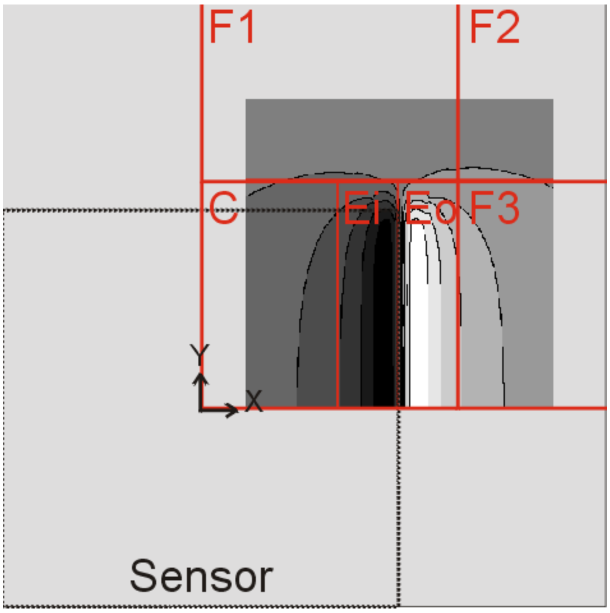

Figure 4.9: Area division of the evaluated trapezoidal sum. The red lines and characters show this division listed in Table 4.4. The coordinate system is placed at $(x, y) = (0, 0)$ in the center of the sensor (the sensor border is indicated with a dotted black line). The contour plot shows the integral, Int, as a function of position of the bead in the critical area where the integral peaks. It is included in order to illustrate the position of the boundaries between positive, negative, and ”flat” areas.

	$\Delta\widetilde{x}'$	$\Delta\widetilde{y}'$	$n = n_x \cdot n_y$	Trp	β monolayer
C	0.2	2	1053	-182.238	-0.0128
$\mathrm{E_i}$	0.2	2	273	-143.844	-0.0097
$\mathrm{E_o}$	0.2	2	234	+126.033	+0.0085
$\mathrm{F_1}$	0.2	2	1062	-32.9518	-0.0022
$\mathrm{F_2}$	0.2	2	756	+9.81117	+0.0007
$\mathrm{F_3}$	0.2	2	1092	+140.949	+0.0099
All	**0.2**	**2**	**4221**	**-82.2856**	**-0.0057**
$\mathrm{C+E_i}$	0.2	2	1313	-326.127	-0.0225
$\mathrm{E_o+F}$	0.2	2	2908	243.841	+0.0168

Table 4.5: Trapezoidal sums, Trp, of the integrals, Int, and the average magnetic field, $\beta = \mu_0\langle H_x\rangle/B$, Eq. (4.30), produced by a monolayer of beads covering the respective area. $\Delta\widetilde{x}'$ and $\Delta\widetilde{y}'$ are the interval lengths, and n is the number Int's contributing to the trapezoidal sum of integrals. n can be related to the number of beads on the area by $n_{\mathrm{beads}} = n \cdot 7390/4221$ (for a close packed monolayer - see text for details).

4.6 Design of SU-8 layer

This section discusses the design of the SU-8 layer used for binding chemistry. The constraint of the design is that $z_0 = 0.5$ μm on top of the sensor area. This distance is chosen as a reasonable compromise between single bead signal (Fig. 4.11) and the ability to do surface chemistry.

Fig. 4.10 shows various possible designs of the SU-8 layer, The design denoted (1), where $z_0 = 0.5$ μm throughout the entire chip, is used to obtain the results listed in Table 4.5. The figure also shows two alternative designs of the SU-8 layer (2) and (3). (2) corresponds to the design of the sensors used for immunoassay experiments, and (3) is the protective capping layer design, where the positive contributions from beads adjacent to the sensor have been diminished using an SU-8 capping layer.

In the following, the average field produced by a monolayer of beads covering design (2) and (3) will be analyzed. The parameter z_0 will be varied on the sensor area ($\mathrm{C+E_i}$) or outside the sensor area ($\mathrm{E_o+F}$). Hence, the integration will be performed in ordinary coordinates as opposed to normalized.

The signal from a monolayer of beads covering an area is calculated using the following equation.

$$\beta = \frac{\mu_0\langle H_x\rangle}{B(\mathrm{mT})} = 4 \cdot 7390\frac{\chi_m R^3}{3w^2}\frac{A}{A_{\mathrm{tot}}}\frac{Trp'}{n} \tag{4.31}$$

in which the trapezoidal sum, Trp', sums the non-normalized integrals, Int',

$$Int'(x', y') = \int_{-10}^{10} dx \int_{-10}^{10} dy \frac{2(x-x')^2 - (y-y')^2 - z_0^2}{((x-x')^2 + (y-y')^2 + z_0^2)^{5/2}} \tag{4.32}$$

and the rest of the parameters have been defined in connection with Eq. (4.29) and Eq. (4.30). Eq. (4.31) assumes non-interacting beads.

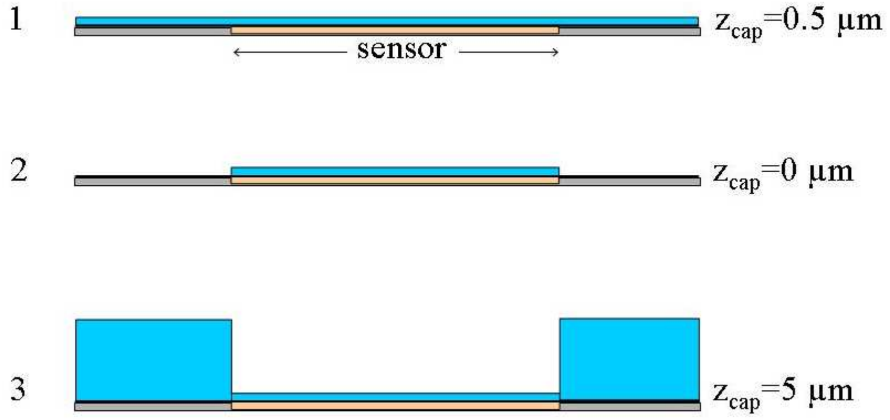

Figure 4.10: Design of the SU-8 capping layer. (1): 0.5 μm covering all. (2): 0.5 μm SU-8 only covering the sensor area. (3): protective capping layer of $z_{\mathrm{cap}} = 5$ μm adjacent to the sensor.

Design 1

Design 1 has been evaluated in Table 4.5. For a monolayer coverage $\beta = -0.006$ is obtained. Large negative values from the central area (C+E$_{\mathrm{i}}$, $\beta = -0.023$) dominates large positive values from outside the sensor (E$_{\mathrm{o}}$+F, $\beta = +0.017$). Therefore this design is sub-optimal in terms of bead detection.

Design 2

The best possible situation for bead detection would be only to cover the sensor area with beads. This way the positive contribution from E$_{\mathrm{o}}$+F would vanish.

The average field of such an arrangement of a monolayer of beads is calculated using Eq. (4.32) on area C and E$_{\mathrm{i}}$. A numerical evaluation of the integrals is conducted. The results are shown in Fig. 4.11 for increasing sensor-bead distance, z_0. The maximum obtained value for $z_0 = 0.125$ μm is $\beta = -0.030$. The field produced by a monolayer of beads at $z_0 = 0.5$ μm is $\beta = -0.023$.

The monolayer field resulting from the SU-8 design with $z_0 = 0.5$ μm is thus reduced 26 % with respect to the maximum obtainable value.

Design 3

Another approach could be to shield the positive contribution from beads outside the sensor area, *i.e.* lift area E$_{\mathrm{o}}$+F to a distance, where the positive contribution is diminished. Fig. 4.10 (3) shows the design of the SU-8 layer for this approach. z_{cap} is the capping layer covering E$_{\mathrm{o}}$+F. The relation to z_0 is $z_{\mathrm{cap}} = z_0 - R$, where R is the bead radius.

$z_{\mathrm{cap}} = 0$ μm coincides with design (2), but this time beads adjacent to the sensor are included. Eq. (4.32) is evaluated on area C and E$_{\mathrm{i}}$ for $z_0 = 0.5$ μm. On area E$_{\mathrm{o}}$ and F

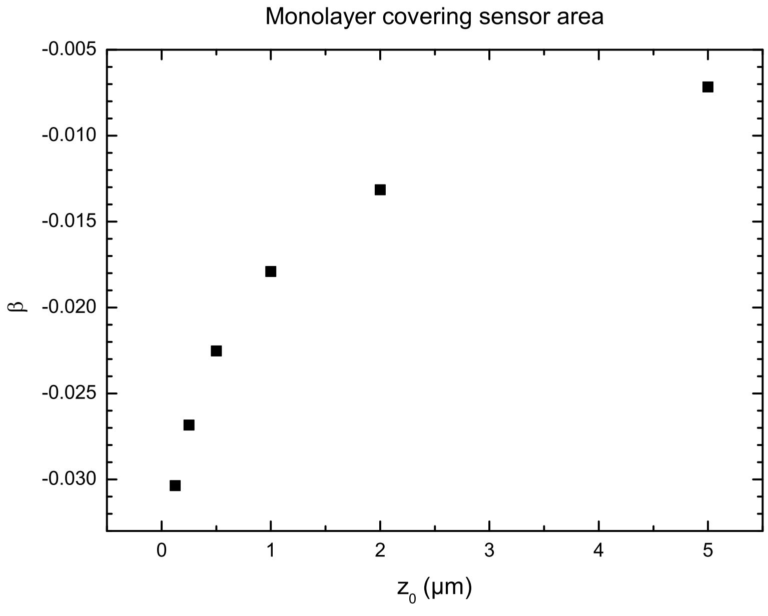

Figure 4.11: Theoretically expected signal, $\beta = \mu_0 \langle H_x \rangle / B$, Eq. (4.31), from a monolayer of Nanomag-D beads covering only the sensor area as a function of distance, z_0. The design is shown in Fig. 4.10 (2).

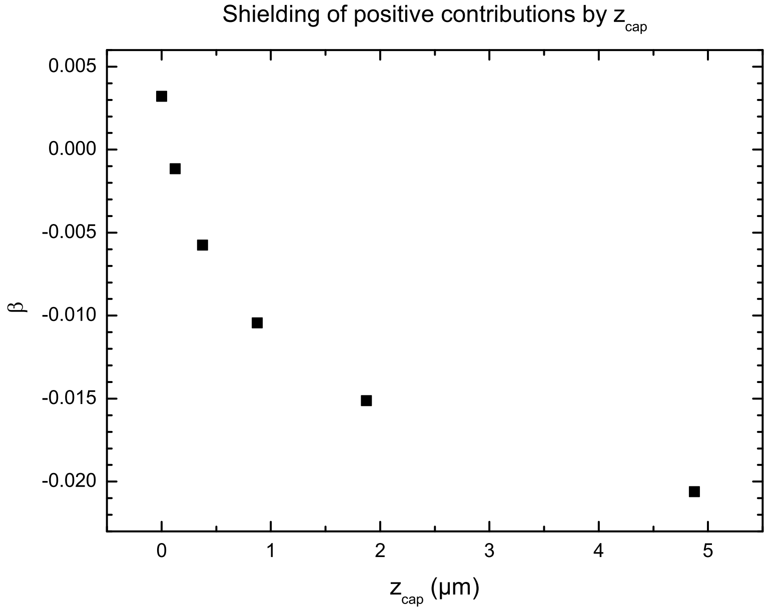

Figure 4.12: Theoretically expected signal, $\beta = \mu_0 \langle H_x \rangle / B$, Eq. (4.31), from a monolayer of Nanomag-D beads with SU-8 capping layer outside the sensor, z_{cap}. The design of z_{cap} is shown in Fig. 4.10 (3).

Eq. (4.32) is evaluated for z_0 defined by z_{cap}.

Fig. 4.12 shows the average field dependence as a function of increasing SU-8 capping layer. The average field at $z_{\mathrm{cap}} = 0$ μm is $\beta = +0.003$, and at $z_{\mathrm{cap}} = 5$ μm the average field is $\beta = -0.021$. Compared to $z_{\mathrm{cap}} = 0$ μm the magnitude of the average field from the beads is considerably increased by a 5 μm thick capping layer.

Concluding remarks concerning SU-8 design

A layer of SU-8 is needed for the binding chemistry, and an SU-8 layer yielding $z_0 = 0.5$ μm is chosen as the sensor coverage. Summarizing the average field produced by a monolayer of beads covering the SU-8 layer gives: $\beta_1 = -0.006$ (Design 1), $\beta_2 = -0.023$ (Design 2), and $\beta_3 = -0.021$ (Design 3). Based on the first two numbers, Design 2 of the SU-8 layer is chosen. Unfortunately, the idea of Design 3 has been introduced too late in the process to realize experimentally. The smaller β_3 than β_2 is fully compensated for by avoiding the risk of positive contributions.

4.6.1 Numerical values for Design 2

This subsection describes the SU-8 design chosen for bead detection experiments. The average field produced by beads in the different parts of the sensor is evaluated separately for each individual part. Contributions outside the sensor ($\mathrm{E_o}$+F) are now included. $z_0 = 0.5$ μm at the sensor (C+$\mathrm{E_i}$), and $z_0 = R$ outside ($\mathrm{E_o}$+F).

Table 4.6 reports the numerical values obtained for the SU-8 design chosen for assay experiments. The last two lines separates the contributions outside the sensor area ($\mathrm{E_o}$+F) from those inside the sensor area (C+$\mathrm{E_i}$). The magnitude of these two contributions are close to each other but the positive contribution from the sensor area dominates such that the total field becomes positive.

	$\Delta x'$	$\Delta y'$	A/A_{tot}	z_0 (μm)	Trp'	β monolayer
C	0.2	2	0.24	0.5	-364.566	-0.0128
$\mathrm{E_i}$	0.1	1	0.06	0.5	-287.689	-0.0097
$\mathrm{E_o}$	0.1	1	0.051	0.125	+511.380	+0.0172
$\mathrm{F_1}$	0.1	1	0.234	0.125	-66.085	-0.0022
$\mathrm{F_2}$	0.1	1	0.166	0.125	+19.770	+0.0007
$\mathrm{F_3}$	0.1	1	0.249	0.125	+289.328	+0.0102
C+$\mathrm{E_i}$	0.2	2	0.3	0.5	-	-0.0225
$\mathrm{E_o}$+F	0.2	2	0.7	0.125	-	+0.0257

Table 4.6: Trapezoidal sums, Trp', of the integrals, Int' (non-normalized), and the average magnetic field, $\beta = \mu_0\langle H_x\rangle/B$ Eq. (4.31), produced by a monolayer of beads covering the respective area. The design of the SU-8 layer is shown in Fig. 4.10 (2).

Both extremes, beads covering only the sensor area or beads covering only the area outside the sensor, leads to large average fields of $|\beta| \approx 0.02$. But a combination of the two would lead to a decrease in the average field. This average field will be approximately linear with the difference in coverage,

$$\beta = 0.0257 \cdot \xi_{\text{outside}} - 0.0225 \cdot \xi_{\text{sensor}} \Rightarrow \tag{4.33}$$

$$\beta \approx 0.024(\xi_{\text{outside}} - \xi_{\text{sensor}})$$

where ξ is the bead coverage with respect to a closely packed monolayer of beads. Eq. (4.33) assumes non-interacting beads.

4.7 Conclusion

In summary, this theoretical analysis has shown that the planar Hall sensor is capable of detecting a single bead. For specific commercial bead products the sensor can be designed for single bead detection based on the single bead S/N study presented.

The signal from a monolayer of closely packed beads is estimated for non-interacting beads. Given the constraint that $z_0 = 0.5$ μm at the sensor area, an SU-8 design, where only the sensor area is covered, should be optimal in terms of the average bead field, namely $\beta = -0.023$ (normalized to the applied field). If beads are spilled outside the sensor area, Eq. (4.33) approximates the normalized field average.

Chapter 5

Nickel planar Hall sensors

Having decided on the planar Hall sensor for magnetic detection in immunoassays, the first experimental test of the principle should be considered. In MIC's clean room, the only available anisotropic magnetoresistive material is nickel, and obviously our first attempt on constructing planar Hall sensors is with nickel as sensing material [2].

This chapter describes the fabrication and characterization of nickel planar Hall sensors. The aim is to verify that the sensing principle can be used for bead detection experiments.

5.1 Design

In this section the design of the nickel planar Hall sensor is described. The design includes the appearance of the sensor, viewed in a microscope, the sensing material, and a biologically active material for attachment of biomolecules.

The design of sensor appearance has changed considerably during the work with the nickel sensors as can be observed by comparison of Fig. 5.1 and Fig. 5.2. The magnetic stack for sensing is: Si-substrate/Ni(250Å)/Au(20Å), where the nickel layer is the active sensing material and the gold layer is a protective layer. Gold and SU-8 surfaces have been considered for attachment of biomolecules.

5.1.1 Sensor appearance

If a current runs through an AMR material, the planar Hall effect induces an electric field perpendicularly to the current, as calculated in Eq. (3.7). This sensing geometry suggests a cross geometry of the sensor design as illustrated in Fig. 5.1.

The planar Hall sensor uses all its active area for detection, hereby is understood that the sensor will measure an average of the field felt by the total area in between the four leads. This yields the possibility of tuning the design to match exactly the requirements of an application. The first demonstration is detection of superparamagnetic Dynabeads M-280 with a diameter of 2.8 μm. Choosing a sensitive area of $20\mu\text{m}\times20\mu\text{m}$ there will be room for approximately 50 beads on top of the sensor, which gives a statistical probability of getting beads on the sensor by random methods.

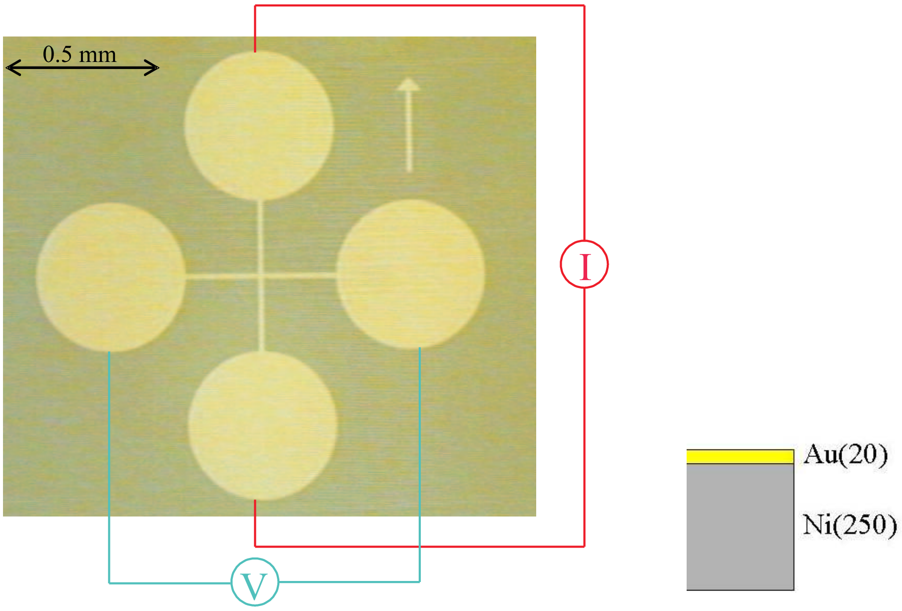

Figure 5.1: Left: Micrograph of the first nickel planar Hall sensor. Yellow is metal, green is the silicon wafer. The metal arrow shows the direction of the easy axis. The measuring geometry is indicated in the figure, I is the current, and V the voltage. Right: Cross sectional view of the layer stack: substrate/Ni(250Å)/Au(20Å). Layer thicknesses are in Å.

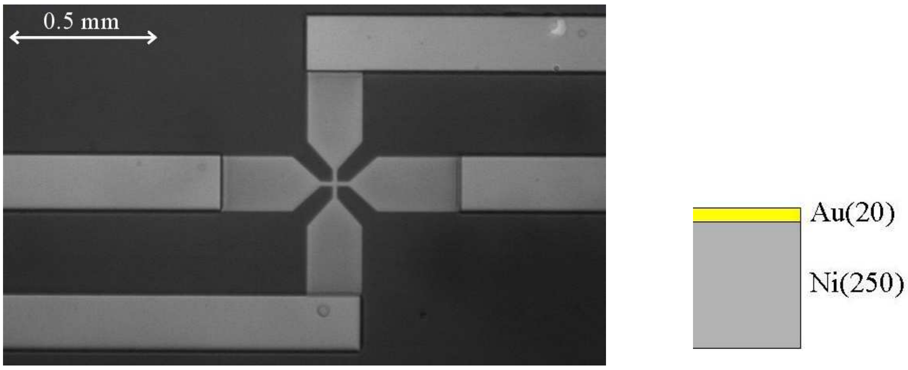

Figure 5.2: Left: Micrograph of a later design of the nickel planar Hall sensor. The gold leads are much closer to the sensor cross. Right: Cross sectional view of the magnetic stack: substrate/Ni(250Å)/Au(20Å). Layer thicknesses are in Å.

A picture of the first operational device is presented in Fig. 5.1. Only one sensor cross with four bonding pads, two for current and two for voltage, is contained on the chip. The sensitive area is $20\mu\text{m}\times 20\mu\text{m}$.

During the nickel sensor project this first appearance has evolved into the sensor design shown in Fig. 5.2. The chip now contains three sensors, A, B, and C, which can be used as references against each other. Furthermore, the electrical leads are moved closer to the sensor cross. This configuration ensures that the majority of the voltage drop lies across the sensor cross. The active sensing area of $20\mu\text{m}\times 20\mu\text{m}$ is maintained.

5.1.2 Sensor material

An AMR sensor involves the material property, sensor geometry, and a detectable field range. If the AMR effect is absent as in isotropic magnetoresistive materials it cannot be used as a magnetic field sensor in this context. Most materials are actually isotropic with respect to magnetoresistance, only ferromagnetic materials exhibit anisotropic magnetoresistive effects. Ferromagnetic materials are, *e.g.*, iron, nickel, and cobalt, or alloys involving these. Nickel has an AMR of approximately 2 % [6], which is deficient with respect to permalloy that has an AMR of 5 %. These are bulk values, for thin films less must be expected. For permalloy films with a thickness of 20 nm, an AMR of 2.2 % has been reported [33].

The sensitivity of the resulting sensor is theoretically inversely proportional to the thickness of the AMR layer, indicating that the thinnest layer possible should be chosen for the devices. It is, however, unfeasible to make the layer infinitely thin, because at some point the AMR effect disappears. An investigation of AMR as a function of permalloy thickness can be found in Ref. [33]. A relatively steep rise is reported for thicknesses up to 20 nm after which the curve flattens considerably. If nickel behaves similarly, thicknesses of 20-25 nm are optimal.

Nickel has a low electron affinity and corrodes easily. For protection against corrosion a 2 nm gold layer is deposited on top of the nickel layer as proposed in Ref. [1]. Additionally, since it is conducting, protection with gold ensures electrical contact to the bonding pads.

Montaigne *et al.* [1] constructed an easy axis of magnetization by step bunching a silicon wafer misoriented with respect to the [111] crystal direction. The reported magnetic moments of the film are thus oriented parallel or perpendicular to the steps depending on which material is deposited. In the case of permalloy, the easy axis is induced parallel to the steps [1].

In stead of step bunching we use an applied magnetic field during deposition. The magnetic field is produced by a magnetic frame, see drawing in Fig. 5.3. The frame is constructed of two bars of soft iron held together by permanent magnets. The magnetization of the two arrays of permanent magnets are aligned parallel resulting in two adjacent loops of magnetic flux as sketched in the figure. The sketch is oversimplified but gives an idea of how the principle of flux-closure creates a relatively homogeneous field in the gap of the magnetic frame. This configuration produces a magnetic flux density of $B = 8$ mT in the center of the frame. When experiencing a field during deposition, the minimum energy configuration of the ferromagnetic material depends on the field. The

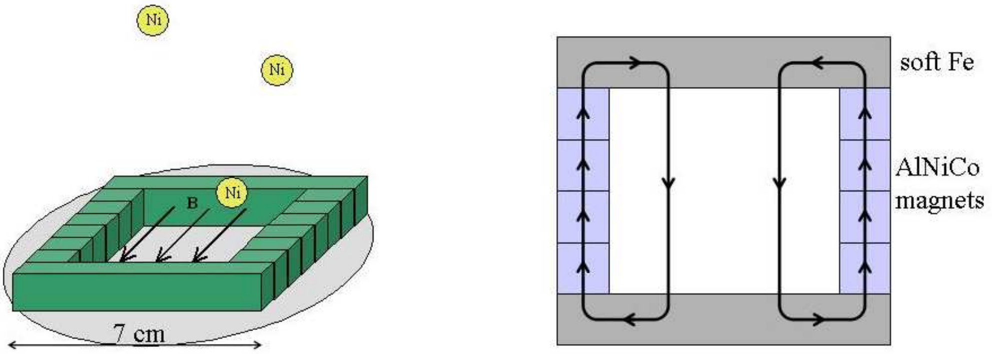

Figure 5.3: Schematic drawing of the magnetic frame used during Ni deposition. It produces a magnetic flux density of $B = 8$ mT in the center of the frame. The field lines are shown as arrows. Left: Frame on top of wafer. Right: Frame viewed from above.

crystal structure adapts in accordance with this energy minimization and thus experiences uniaxial anisotropy.

5.1.3 Biologically active material

For attachment of biomolecules, three approaches have been considered, though no actual bio-experiments have been performed with the Ni sensors.

1. Attachment to gold
2. Attachment to gold on SU-8
3. Attachment to SU-8

The first attempt of attaching thiolated DNA to the thin gold layer covering the sensor is unsuccessful because the gold layer is too thin to be properly activated. The second attempt is to separate the sensor and a much thicker gold layer by 0.5 μm SU-8. It is difficult to adhere the gold to the SU-8 surface. At this point, another approach is pursued, namely attaching DNA directly to SU-8, which in the successful case will facilitate not only the functionalization of planar Hall sensors but also other micro-fabricated sensors [34]. During this study, SU-8 reveals a great binding capacity towards both DNA and proteins. The details on attachment of biomolecules to the SU-8 surface will be given in Chapter 7.

5.2 Nickel sensor fabrication

This section describes the fabrication procedure for nickel planar Hall sensors. It is a description of the initial clean room work leading to a conference proceeding [2] and supporting the design and choices for the exchange biased sensors. The nickel planar Hall sensors are fabricated on standard silicon wafers without electrical insulation.

5.2.1 Deposition of magnetic Ni films

For deposition of nickel films an e-beam deposition system, Alcatel Model SCM600, is used. In the e-beam system, the metal is placed in a crucible and heated by an electron beam extracted from a tungsten filament. Due to the beam profile, heating can be controlled locally in the crucible and sublimation is achieved without melting all the metal. This reduces cross contamination from the crucible or other metals placed in different crucibles. Four different materials can be deposited without breaking the vacuum, hence we are able to deposit first the Ni sensing layer and then the Au protective layer.

The deposition is controlled by manually opening and closing a shutter between the metal crucible and the wafer. Since our metal layers are very thin compared to normal standards, we use lower deposition rates in order to facilitate the opening and closing of the shutter. The layer thickness of deposited material is measured during deposition by a quartz crystal that changes its resonance frequency proportionally to the mass deposited on top of it.

A consequence of the deposition method is a high probability of obtaining polycrystalline nickel films. Hence, the nickel films will exhibit magnetic domains. This is in contrast to epitaxial films, which are more likely to exhibit single domain behavior.

5.2.2 Photolithography

Sensors are built on top of a silicon wafer using conventional photolithography. The photoresist, which is a polymer that changes its chemical properties when exposed to ultraviolet light, is used to create microscopic structures of resist on top of the wafer. A positive resist becomes soluble in a solvent, called the developer, when exposed to UV light, and a negative resist becomes insoluble in the developer.

First the photoresist is spun on to the wafer, the spinning creates a uniform layer of the resist. Then the resist is exposed to UV light through a mask. The mask is a glass plate transparent to UV light with chromium deposited at predefined patterns in order to avoid resist exposure here. The patterns, *e.g.* corresponding to sensor crosses, are thus transferred to the photoresist. When the wafer is subsequently flushed with developer, the soluble part of the resist is dissolved in the liquid, and the transferred pattern remains.

This mould of photoresist can be used for general purposes. One can etch away material in the bottom of the grooves defined by the resist, or one can fill the grooves with material and build up structures. If we choose to deposit a layer of metal on top of all and dissolve the photoresist in acetone, this type of process is called a lift-off. The remaining pattern of metal will be identical to the original pattern of the mask.

5.2.3 Process steps

Patterning the nickel-gold film for sensors and the thicker gold film for leads is done by lift-off. The negative imaging exposure process is used to facilitate the lift-off. Following clean room processing, the devices are cut from the wafer with a dicing saw and wire bonded to a chip carrier constructed of an Al_2O_3 substrate and 14 CrAu bonding pads.

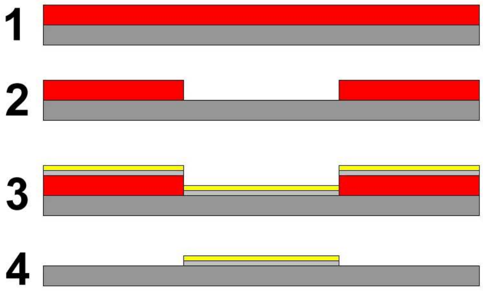

Figure 5.4: Lithography steps for nickel sensor. 1. The wafer is covered in photoresist. 2. Structured resist. 3. Deposition of Ni/Au film. 4. After lift-off the sensor pattern remains.

- A 4" silicon wafer is used as substrate. Typical resistivity $\sim 1 - 20\ \Omega$ cm. Surface oxide is removed in HF buffer for better adhesion of photoresist.
- 1.5 μm photoresist AZ5214e is spun onto the wafer. Use SSI System 150 Track 1. Conditions: program PR1-5.
- Sensor crosses and leads are defined in the photoresist by exposure through a mask. Use negative imaging procedure. Equipment: SUSS Mask Aligner MA6/BA6. Conditions: exposure dose 9 mW cm^{-2}. Negative procedure: 8 s exposure with mask, 2 min bake at 120 °C hotplate, 25 s flood exposure (without mask).
- Development in AZ531. Conditions: time: 55 s, stirring of solution.
- Nickel sensing layer and protective gold layer is deposited by e-beam evaporation in Alcatel Model SCM600. Stack: substrate/Ni(25nm)/Au(2nm). Conditions: background pressure: 10^{-6} mbar, processing pressure: $\approx 3 \cdot 10^{-6}$ mbar, RF voltage: 8 kV, deposition rates: 0.1 nm/s.
- Lift-off in acetone. Conditions: 30-60 s ultrasonic agitation.
- 1.5 μm photoresist is spun on, patterned into bonding pads by negative imaging process, and developed. Conditions as above.
- Deposition of 0.5 μm Au for current/voltage leads and bonding pads in Alcatel Model SCM600. Conditions: background pressure: 10^{-6} mbar, processing pressure: $\approx 5 \cdot 10^{-5}$ mbar, RF voltage: 8 kV, deposition rate: 1 nm/s.
- Lift-off in acetone. Conditions: ultrasonic agitation. Ultrasonic agitation can be assisted by heating the acetone bath prior to stripping of the resist.
- Dicing with a Tempress Dicing Saw, and wirebonding using an ultrasonic wirebonder.

The lithography steps for fabricating a nickel planar Hall sensor are shown in Fig. 5.4.

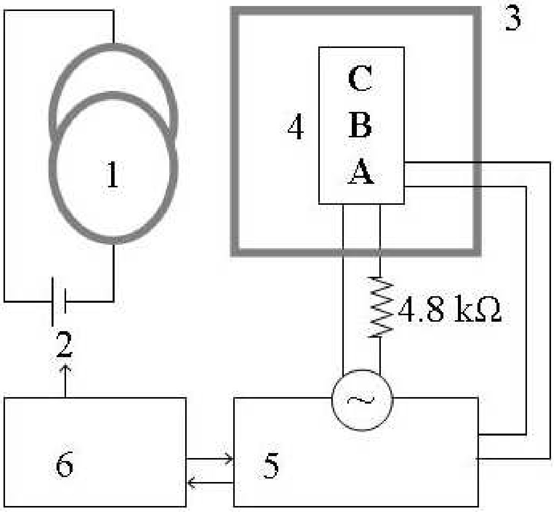

Figure 5.5: Schematical drawing of the electronic setup for Ni sensor characterization. 1: Helmholtz coils, 2: power supply, 3: sensor box, 4: chip with three sensors A, B, C, 5: lock-in amplifier, 6: computer.

5.3 Experimental

In this section the experimental setup constructed for Ni sensor characterization is described. It consists of magnetic field control, a sensor box, and sensor current control combined with voltage measurement.

5.3.1 Experimental setup and conditions

The experimental setup for nickel planar Hall sensors is presented in Fig. 5.5. Electrical connections are shown as solid lines, and data transfer is indicated with an arrow. Below is a description of the components shown in the drawing.

Magnetic field control

Two methods of producing magnetic fields have been conducted in the experiments with Ni sensors. One is a permanent magnetic frame much like the one used for nickel deposition (Fig. 5.3), only this frame is larger and produces a flux density of $B = 42$ mT. Using this frame, the sensor is always saturated along the direction of the external field.

The other method is to produce the field with a set of Helmholtz coils. The Helmholtz coils consist of two identical coils placed with their centers at a distance identical to the coil radius. This configuration ensures that the second derivative of the field vanishes in the point just between the two coils. Therefore a set of Helmholtz coils produces a very homogeneous field in the central volume between the two coils. A picture of the Helmholtz coils can be found in Fig. 6.6, number 1.

1. Helmholtz coils. The variable applied field is supplied by a set of homebuilt Helmholtz coils [3]. Due to heat generation the Helmholtz coils are suitable for use with currents of no more than $I_{\mathrm{DC}} = 2$ A and, when using this value, only for a few minutes. The calibration of the Helmholtz coils is 7.57 mT A^{-1} - $8.48{\cdot}10^{-3}$ mT [3]. This calibration, carried out in Ref. [3], is later found to be 2.8 % too low. Chapter 6 presents a more accurate calibration.

2. Midec Type SK 150-2 power supply. Supplies the current for the Helmholtz coils. The power supply is controlled via LabView [35].

Sensor box

3. Sensor box. The sensor box is mounted on a rotatable table with a protractor. This ensures that the angle between the applied field and the current can be controlled with ±0.5 ° resolution.

4. Chip with three sensors, A, B, and C. The user can switch between the three sensors manually by interchanging the cables.

Sensor current control and voltage measurement

5. Stanford Research Systems Model 830 lock-in amplifier [36]. The current through the sensor is controlled by the sine output from the lock-in amplifier. The modulation frequency is $f = 1.104$ kHz. A $V_{\mathrm{AC}} = 1.004$ V (maximum amplitude) sine function passed through a $R_e = 4.8$ kΩ shunt resistor in series with the sensor, $R_{\mathrm{sensor}} = 200$ Ω (measured with a multimeter), gives a current of $I_{\mathrm{AC}} \approx 200$ μA.

   The lock-in amplifier measures the voltage output from the sensor using the sine output as reference. Lock-in settings are given in Table 5.1.

Experiment control

6. Computer. The experiments are controlled via LabView [35].

V_{out} (V)	f (kHz)	Display	Sensitivity (μV)	Signal
1.004	1.104	X, Y	50	A-B
τ (s)	Filter slope (dB)	Reserve	Line filters	Sync filter
1	12	low noise	off	on

Table 5.1: Lock-in amplifier settings for Ni sensors. V_{out} is the output voltage from the lock-in amplifier (maximum amplitude) with frequency f. τ is the time constant.

5.4 Results and discussion

This section presents the results obtained for the nickel sensors. First the angular dependence of $V(\phi)$ in Eq. (3.8) is investigated. Then the sensor response versus applied field is presented and discussed. Finally bead detection experiments are quoted from the conference proceeding [2].

5.4.1 Sensor response vs. angle

In order to investigate the $\sin(2\phi)$ relation of Eq. (3.8) the sensor is saturated by the strong magnetic frame and the voltage drop is measured as a function of angle between the applied current and the saturation magnetization. No shunt resistor is included in the electrical circuit. Measurements of this dependence is shown in Fig. 5.6 for a sensor constructed of 25 nm thick nickel. A $\sin(2\phi)$ behavior is observed as theoretically predicted.

5.4.2 Sensor response vs. field

Procedure

Prior to each measurement, the magnetization of the sensor is saturated along the easy axis. For this procedure, the Helmholtz coils are used. The table is turned such that the field is aligned along the sensor's easy axis. Then the current through the coils is set at its maximum value and subsequently slowly reduced. This step ensures that the magnetization always has the same starting point. After resetting the magnetization along the easy axis, the table is turned 90 °. Now the applied field is aligned perpendicularly to the easy axis.

Results

Measurements of the sensor response as a function of applied field is presented in Fig. 5.7 for a nickel sensor of 20 nm thickness. This graph is typical for the nickel sensors. Observed is first a linear region as a function of increasing applied field, then a maximum is reached and afterwards a drop in signal in accordance with theory. When decreasing the field after reaching $B = 1.75$ mT, almost no signal response as a function of field is observed.

First the linear part of the curve is considered. From fabrication in the clean room, the magnetic moments of the nickel atoms are aligned in the direction of the applied field from the small magnetic frame. When an external field subsequently is applied perpendicularly to this direction, the moments rotate away from their original alignment and the sensor voltage changes in accordance with theory. When the moments are at 45 degrees to the current, the sensor signal attains its maximum value at $B = 1.3$ mT. For larger fields, and hence larger angles, the signal drops again.

At sensor saturation (not reached in Fig. 5.7), the magnetization will be fully aligned with the applied field, and when the applied field is subsequently reduced, the moments rotate back into the direction of the easy axis. However, at this point, no distinction between the two directions of the easy axis is possible. Due to this fact, the magnetic

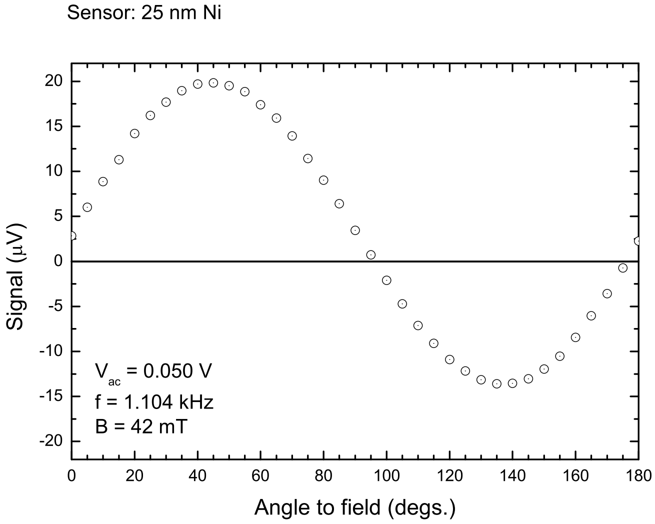

Figure 5.6: Angle dependence of the Ni planar Hall sensor. Experimental conditions are on the graph, no shunt resistor is in the electric circuit. The sensor is saturated ($B = 42$ mT) and the signal is measured as a function of angle between current and a saturating applied field.

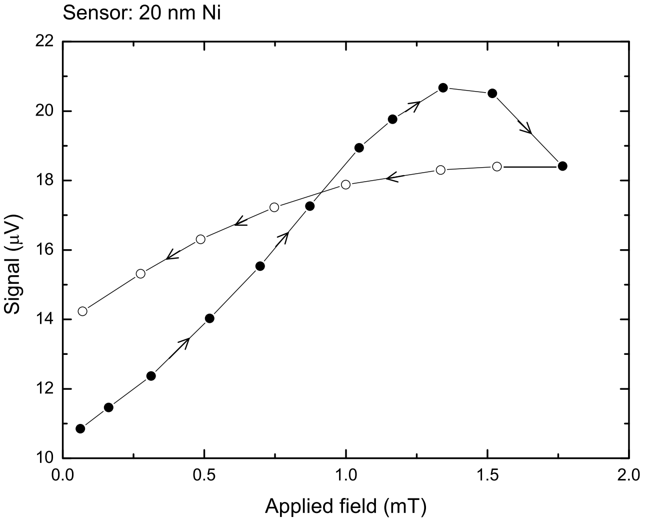

Figure 5.7: Signal vs. applied field for a nickel planar Hall sensor of 20 nm thickness. Experimental conditions are: a modulating frequency of $f = 1.104$ kHz, and a current of $I_{\mathrm{AC}} = 200\ \mu$A.

moments will distribute themselves randomly into the two antiparallel directions. These directions are magnetically equivalent, but the resulting electrical signals are of opposite signs. On average, the signal will be zero, or significantly reduced as observed in the graph. When sweeping the field forth and back between higher and higher values of magnetic fields, the effect of this redistribution of magnetic moments is enhanced as a function of max field.

What is also clear in Fig. 5.7 is that the zero applied field signal at the start of the measurement does not coincide with the signal at the end of the measurement. The reason for this observation is probably a temperature drift. A temperature drift towards a saturation value is observed in many measurements, and the sensors are usually left with applied current for an hour prior to the experiment in order to obtain an equilibrium before starting the measurements. Another explanation could be remanence in the magnetization state of the sensor.

Due to the magnetic equivalence of the two antiparallel states, the sensor has to be reset prior to each measurement. By reset, is meant, that all the magnetic moments are aligned along one direction by applying a magnetic field parallel to the easy axis as described above. When this is taken care of properly, the sensors show stable responses. For the planar Hall sensors of 20 nm thick nickel typical sensitivity values are $S_0 \approx 35$ μV mT^{-1} mA^{-1}, which are found as the slope of the signal versus applied magnetic field curve for small applied fields for repeated measurements of several sensors.

5.4.3 Bead detection experiments

Procedure

The magnetization is set along the easy axis as described in the procedure for sensor response vs. field.

Additionally, the sensors are left for minimum one hour with applied current prior to each measurement. The drift thus stabilizes at an equilibrium value, which can be subtracted from the measurements.

1. The slope of the sensor response as a function of applied magnetic flux density is measured under controlled experimental conditions. The current through the sensor is $I_{\mathrm{AC}} = 200$ μA, the modulation frequency is $f = 1.104$ kHz, the signal is measured using lock-in technique, and a large off-set is subtracted from the measurements.

2. A droplet containing beads is placed on top of the sensor using a syringe. The droplet is left to dry, and beads sediment on top of the sensor.

3. The slope is measured under the same experimental conditions as the first slope determination. Comparison of the two slopes give the signal from the beads.

Results

Fig. 5.8 shows bead detection measurements with the nickel planar Hall sensor presented at the Eurosensors 2003 conference [2]. Comparison of the two responses before and after

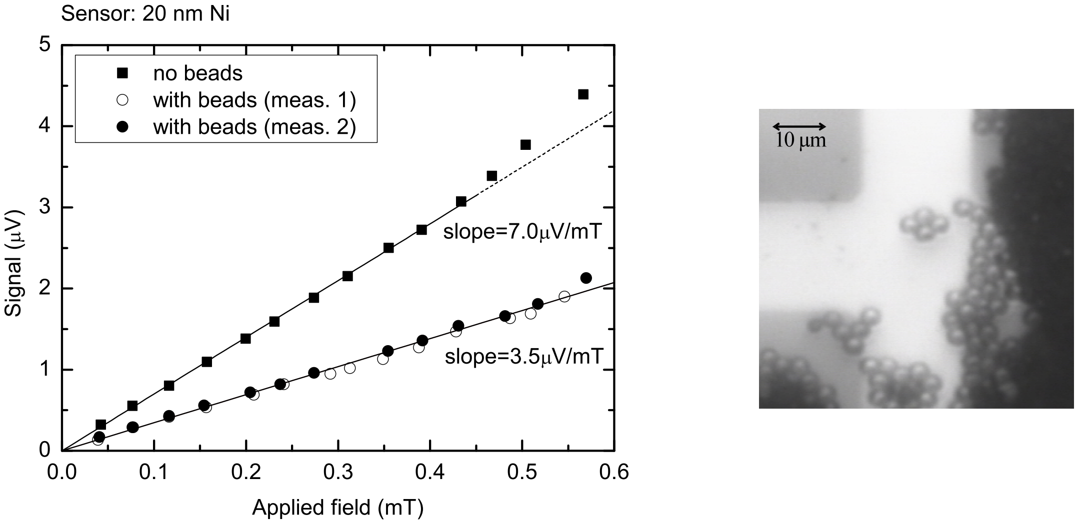

Figure 5.8: Bead detection with the nickel planar Hall sensor. Left: Electrical measurements of signal versus applied field. Experimental conditions are: a modulating frequency of $f = 1.104$ kHz, and a current of $I_{\mathrm{AC}} = 200\ \mu$A. The slope is reduced by the presence of beads. Right: Micrograph of the sensor with Dynabeads M-280.

beads have been placed on the sensor reveals the presence of the beads. The sensor signal versus applied field slope is reduced by the presence of beads. Visual inspection in the microscope shows adhesion of at least six Dynabeads M-280 within the sensitive area of the sensor, and more are present in close vicinity. After washing off the beads with water, the field response is restored to match the first experiment.

5.5 Conclusion

This chapter has shown that the planar Hall effect can function as detection principle for magnetic bead sensors. The angular dependence of a saturated sensor obeys the $\sin(2\phi)$ relation of Eq. (3.8). The sensitivity is $S_0 = 35\ \mu\mathrm{V\ mT^{-1}\ mA^{-1}}$, when the magnetization starting point of the sensors is specified prior to each measurement. Furthermore, detection of Dynabeads M-280 has been realized using the nickel planar Hall sensors.

An obvious deficient property of the nickel planar Hall sensor is the need for restoring the magnetization along one of the two antiparallel directions of the easy axis prior to each measurement. Another issue is the magnitude of anisotropic magnetoresistance, which is larger in permalloy. One of the characteristic properties of permalloy is, however, the very small anisotropy energy, which is the cause of the sensor saturation in the Earth's magnetic field experienced by Montaigne et. al. [1]. Nickel does not suffer from this deficiency.

One unsolved item is the temperature dependence of the sensor. When measuring the signal as a function of time, the signal is observed to drift from its initial value and approach an equilibrium value. This drift of the signal could be related to the actual temperature of the sensor during the measurements. When the sensor is heated above room temperature, the signal rises, and when the sensor subsequently is cooled below room temperature, the signal drops below the ”steady-state” value corresponding to room temperature. This observation will be addressed later along with the results of the permalloy sensors, which also exhibit temperature drift.

Finally, during the study of nickel planar Hall sensors, it has been found that SU-8 is an excellent material for attachment of biomolecules [34], see Chapter 7, where the results from this study are described.

Chapter 6

Exchange biased permalloy planar Hall sensors

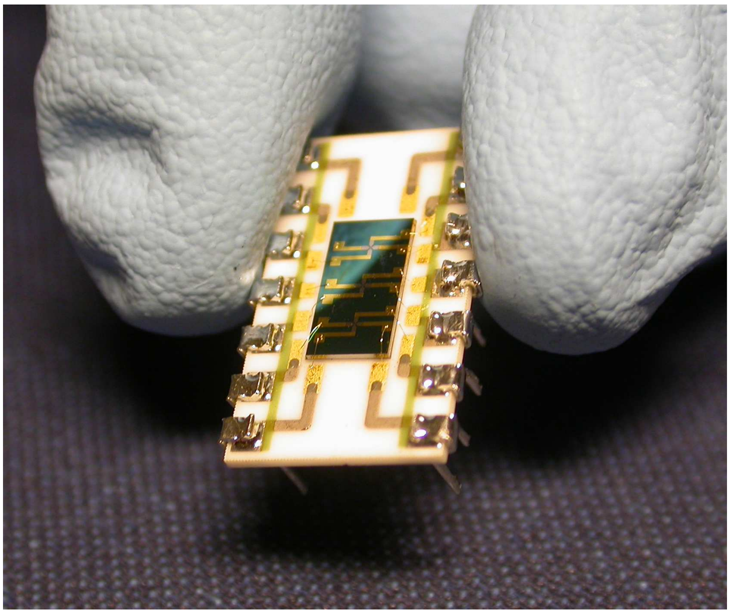

Figure 6.1: Final chip, Batch 2. The chip consists of three sensors, A, B, C, where B is the electrical reference, and A and C are used for bead detection experiments.

This chapter describes the fabrication and characterization of exchange biased permalloy planar Hall sensors. The reason for choosing permalloy as sensor material is the higher AMR compared to Ni [6]. Additionally, a well-defined starting point of the magnetization can be induced by exchange coupling the permalloy layer to an antiferromagnet [27].

The exchange coupling introduces a unidirectional anisotropy in addition to the uniaxial anisotropy of the easy axis. This means that the magnetization prefers one of the two directions along the easy axis instead of equal preference. Hence, the magnetization

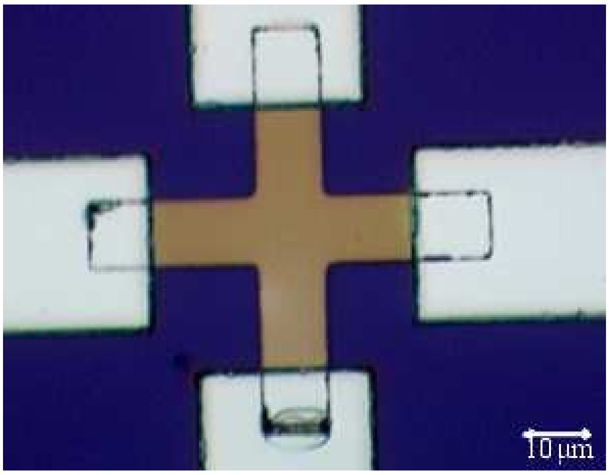

Figure 6.2: Sensor design, Batch 1. The central cross (brown), which is the active sensing area, is 10μm×10μm. The leads (white) are made of Al.

state is always well-defined in zero applied field, and there will be no need for magnetizing the sensor along the easy axis as is the case of nickel sensors.

Fig. 6.1 shows a picture of the final chip with three exchange biased permalloy planar Hall sensors used for immunoassay detection experiments. Planar Hall sensors have lower signal magnitude than existing magnetic field sensors [26], however the low noise level of the planar Hall sensor makes it theoretically superior to other types of AMR sensors in terms of the DC bead detection limit. Another beneficial characteristic of AMR sensors is the easy fabrication method, which enhances the speed of fabrication, limits the cost of a device, and promotes integration with micro-analysis biochips. The planar Hall sensor is no exception, though the exact thicknesses of the respective layers are less critical than for GMR and spin-valve sensors.

6.1 Design

This section presents the design of the exchange biased permalloy sensors. The design involves the sensor appearance and the sensor material as well as the design of the SU-8 layer used for binding chemistry, which has already been discussed in Chapter 4.

Two permalloy planar Hall sensor batches have been fabricated, Batch 1 and Batch 2.

6.1.1 Sensor appearance

Batch 1

In Fig. 6.2 the resulting appearance of a Batch 1 planar Hall sensor is shown. The total fabrication of Batch 1 took place at Institute of Engineering of Systems and Computers - Microsystems and Nanotechnology (INESC-MN), Portugal, and a chip design similar to their spin-valve chips [9, 16] was used. Sensor crosses of active area 5μm×5μm,

$10\mu\text{m}\times 10\mu\text{m}$, and $20\mu\text{m}\times 20\mu\text{m}$ were fabricated, in the figure one $10\mu\text{m}\times 10\mu\text{m}$ sensor is shown. Each final chip consists of 10 sensors, each with four electrical leads all gathered at a 1 cm^2 chip area.

Batch 2

Fig. 6.1 shows the final chip design of Batch 2 with three planar Hall sensors on each chip. Three sensors are needed for an immunoassay experiment, one for the electrical reference, one for the sample, and one for the negative control. The sensor design of Batch 2 is identical to that of the final design for Ni sensors (Fig. 5.2). The active sensing areas of the planar Hall sensors has been chosen to be $20\mu\text{m}\times 20\mu\text{m}$.

6.1.2 Sensor material

The aim is a permalloy sensor experiencing unidirectional anisotropy. The easy axis is constructed by applying a magnetic field during deposition. An easy *direction* is preferred instead of an easy axis. This is accomplished by exchange coupling the magnetic layer to an antiferromagnetic layer, see Eq. (3.16) and Ref. [27]. The exchange bias ensures a unique starting point for the magnetization in zero applied field. Permalloy has a higher AMR than nickel. However, one of the characteristic properties of permalloy is the very small anisotropy energy, which is the cause of the sensor saturation in the Earth's magnetic field experienced by Montaigne et. al. [1].

Fortunately, the two properties are coupled in a way that facilitates the modulation. In order to introduce a unique starting point for the magnetization, the ferromagnetic film of sensing material is coupled to an antiferromagnetic film by exchange coupling. The exchange energy is visualized by a shift of the easy axis loop to a lower field value in a magnetization versus applied field strength experiment. Since the energy of the permalloy film depends on both the anisotropy energy and the exchange energy, the rotation of magnetization away from the easy direction depends on these two contributions as calculated in Eq. (3.13) and Eq. (3.17).

Exchange coupling of the ferromagnetic film to an antiferromagnetic film thus improves the planar Hall sensor in three ways. First, the easy axis is substituted with an easy direction. Second, the exchange coupling introduces the possibility of using permalloy, which has superior magnetic properties compared to nickel. Third, the operation field range has been extended also due to the exchange energy.

In Ref. [33] an investigation of AMR as a function of permalloy thickness is performed. A relatively steep rise is found for thicknesses up to 20 nm after which the curve flattens considerably. This indicates that thicknesses of 20-25 nm are optimal with respect to AMR.

Batch 1

As sensing material a 20 nm thick layer of $\text{Ni}_{80}\text{Fe}_{20}$ (permalloy) is chosen. For the antiferromagnetic coupling a 20 nm thick $\text{Mn}_{74}\text{Ir}_{26}$ layer is used. There are several reasons for the choice of layer thicknesses. In the case of $\text{Ni}_{80}\text{Fe}_{20}$, Fig. 4 in Ref. [33] shows that the

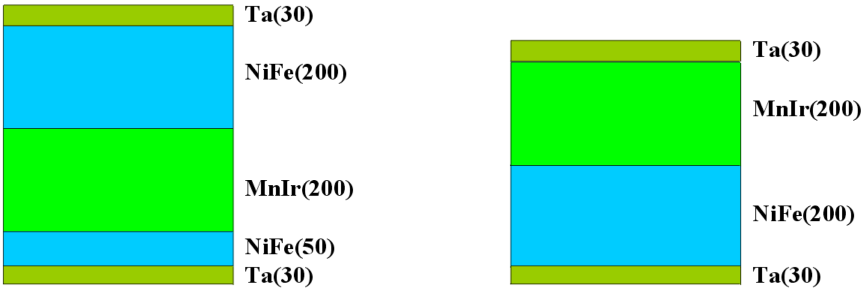

Figure 6.3: Cross sectional view of the IBD deposited stacks. Both deposited on an oxidized Si substrate. The sketch to the left shows the stack used for Batch 1 (bottom-pinned), and the sketch to the right is Batch 2 (top-pinned). Layer thicknesses are in Å.

maximum AMR is reached at 20 nm thickness. In the $Mn_{74}Ir_{26}$ case, an exchange field of $H_E = 30000$ A m^{-1} is obtained for MnIr thicknesses down to 6 nm, when the permalloy layers are 3 nm thick [33]. It is, however, not advisable to use very thin layers due to lack of thermal stability, and based on the results of Ref. [33] 20 nm MnIr is thought to be a good compromise between thermal stability and AMR.

The magnetic dipole field, which is expected from a magnetic bead, see Eq. (A.17), falls off rapidly with distance, theoretically as the inverse cube of the distance. Therefore a sensing layer as close to the bead as possible is desired. 20 nm is, of course, negligible in comparison with a 2 μm bead, but possible future applications involves measurements with 50 nm beads, and sooner or later the spacing of the antiferromagnetic layer will play a role. Keeping this in mind, the ideal layer configuration is with the pinning layer below the sensing layer.

As adhesion layer, and for protection against corrosion, 3 nm thick Tantalum is used. On top of Ta, permalloy grows epitaxially, but in order to obtain MnIr single crystal growth a seed layer of CrNiFe or permalloy is needed. During my stay at INESC-MN CrNiFe was unavailable, and 5 nm permalloy was used as seed layer for MnIr. This results in a second loop in the magnetization versus applied field experiments presented below, and complicates theoretical investigation of the sensor field response.

The layer configuration of Batch 1 is: oxidized Si substrate/Ta(30Å)/NiFe(50Å)/MnIr (200Å)/NiFe(200Å)/Ta(30Å).

Batch 2

Due to the problems of depositing a proper seed layer for MnIr, a top-pinned stack is chosen for the second sensor batch. Batch 2 is thus: oxidized Si substrate/Ta(30Å)/NiFe(200Å) /MnIr(200Å)/Ta(30Å).

The cross-sectional view of the two stacks of Batch 1 and Batch 2 are shown in Fig. 6.3.

6.1.3 Biologically active material

Batch 1

The total chip of Batch 1 is protected by a 0.2 μm silicon oxide layer. This is also used for immobilizing biological material on top of the sensors [9, 16, 18]. The drawback of silicon oxide as a surface for biomolecular attachment is that the activation of the surface involves toxic chemicals. For large scale production of chips, toxic chemicals should be avoided due to environmental problems. For research applications the complications are less severe, but careful handling is mandatory.

Batch 2

In Batch 2, SU-8 is used to bind antibodies on top of the sensor, see Chapter 7 for details on the immobilization procedure. The SU-8 can be made as thin as necessary, and a fortunate thing about SU-8 as immobilization surface is that all chemical attachment steps can be made using a PBS solution (phosphorous based saline), which is both cheap and non-toxic.

At the time of processing, it was not known that antibodies stick as well to the residual SU-8 layer left after development. Therefore, 0.5 μm SU-8 pads are made on top of the sensors as illustrated in Fig. 6.4. The SU-8 pads are introduced to immobilize antibodies only on top of the sensor. The aim is to avoid loss of antigen at non-active areas of the chip. However, this is an unfortunate design with respect to bead signal from a monolayer, where both the sensor and the area outside the sensor is covered with beads. As discussed in Chapter 4, the monolayer signal is proportional to the difference between the coverage of beads inside and outside the sensor, Eq. (4.33). If the coverage is approximately equal inside and outside the sensor area, the resulting signal will approach zero.

6.2 Clean room fabrication of exchange biased sensors

In this section the fabrication process of the exchange biased sensors is described from wafer to the final chip seen in Fig. 6.1. The photograph shows the Batch 2 chip mounted on a chip carrier.

The processing involves deposition of the magnetic films and subsequent structuring of the films into sensors. Then electrical leads are constructed, and the biologically active material is deposited. Packaging involves mounting the diced chip on a carrier and wire bonding.

6.2.1 Deposition of magnetic thin films

The magnetic films for planar Hall sensor fabrication are deposited in collaboration with INESC-MN. The equipment used for deposition is the Nordiko N3000 ion beam system described in Ref. [33]. In comparison with other thin film techniques, where sputtering is the closest competitor, the ion beam deposition (IBD) technique offers good control of deposition conditions, such as low deposition rates and low processing pressures. The base pressure in the IBD chamber is below $7 \cdot 10^{-6}$ Pa, and during operation the pressure rises to $5.5 \cdot 10^{-3}$ Pa.

In Ref. [33], a description of the system operation is provided along with an examination of the level of cross-contamination from other targets and the shield. Contamination of the deposited films is approximately 400 ppm of which metallic impurity is below 140 ppm. The operation conditions are optimized in terms of the beam profile, and the resulting uniformity of the film thickness is ±1 % across a four inch wafer. The substrate is water cooled during deposition, which is especially important for ion milling processing, where considerable excess heat is generated. A permanent magnetic frame provides 3200 A m^{-1} magnetic field strength during deposition. The easy axis can be aligned with ±2 ^{o} accuracy.

Deposition is achieved by bombarding ions into the target. Xenon ions are extracted from the deposition gun by an acceleration voltage of -300 V and hit the target with an energy of 1450 eV. Target material is sputtered off the target and thus deposited on the substrate wafer. The beam current is set by the RF power to 29 mA. The resulting deposition rates are Ta 0.20 Å s^{-1}, $Ni_{80}Fe_{20}$ 0.32 Å s^{-1}, and $Mn_{74}Ir_{26}$ 0.31 Å s^{-1}.

6.2.2 Process steps Batch 1

Fabricating the planar Hall sensors of Batch 1 [4, 5] is a process sequence with three mask steps, four deposition steps, two etch steps and a lift-off, plus the intermediate preparations.

- A 3" silicon wafer is insulated electrically by a sputtered 0.5 μm Al_2O_3 layer. On top 15 nm antireflecting $TiWN_2$ is sputtered.

- The sensor material is deposited using ion beam deposition (IBD) Nordiko 3000. The stack is: substrate/Ta(30Å)/NiFe(50Å)/MnIr(200Å)/NiFe(200Å)/Ta(30Å). Deposition conditions: Substrate rotation 50 %, substrate pan: 80 ^{o}, magnetic field during deposition: 40 Oe, beam current: 29 mA.

- 1 μm photoresist is spun on. Pre-treatment: Vapor prime (5'). Conditions: Speed 3500 rpm.

- Sensor crosses are patterned using direct laser writing. Conditions: exposure power: 82 mW.

- Mask development. Conditions: Developer 5/2.

- The excess of material is etched away by ion milling leaving sensor crosses. Etch in Nordiko 3000. Conditions: RF power: 64 W, RF cycle: +488.5V/-194V, +29.5mA/-1.6mA, stabilization plasma: 8 sccm Ar, substrate rotation: 40 %, substrate pan: 70 ^{o}, chamber pressure: $5.4 \cdot 10^{-7}$ Torr, total etch time: 600 s.

- Resist stripping in Microstrip 2001. Conditions: 80 °C, ultrasonic agitation.

- 1 μm photoresist is spun on. Pre-treatment: Vapor prime (5'). Conditions: Speed 3500 rpm.
- Electrical connections are patterned using direct laser writing. Conditions: exposure power: 82 mW.
- Mask development. Conditions: Developer 5/2.
- 0.3 μm Al for electrical leads and 15 nm $TiWN_2$ protective layer is deposited in Nordiko 7000 sputter system. Conditions: Clean machine before run. Surface etch conditions: sputter etch 1: 40 s, 70 W, sputter etch 2: 40 s 50 W, stabilizing plasma: 50 sccm Ar. Al deposition conditions: total time: 80 s, DC power: 2 kW, stabilizing plasma: 50 sccm Ar. Protection layer conditions: total time: 27 s, DC power: 0.5 kW, stabilizing plasma: 50 sccm Ar + 10 sccm N_2.
- Electrical connections are defined by lift-off of the photoresist and the metal adjacent to the leads. Conditions: Microstrip 2001, 80 °C, ultrasonic agitation.
- 0.2 μm silicon oxide is sputtered on top the wafer. The oxide is used for surface protection and for immobilizing biochemical substances.
- 1 μm photoresist is spun on. Pre-treatment: Vapor prime (5'). Conditions: Speed 3500 rpm.
- Mask patterning of holes for wire contacts using direct laser writing. Conditions: exposure power: 82 mW.
- Mask development. Conditions: Developer 5/2.
- Reactive ion etching through the oxide to open contacts for wire bonding.
- Dicing and wire bonding remains to give the final functional chips.

6.2.3 Process steps Batch 2

Fabricating the planar Hall sensors of Batch 2 is a simple process sequence with only two mask steps, three deposition steps, one etch and a lift-off step, plus the intermediate preparations. However an additional mask step is introduced in order to place SU-8 on top of the sensors. The SU-8 functions as adhesion layer for biochemical species.

- A 4" silicon wafer is insulated electrically by a thermally grown 0.5 μm SiO_2 layer.
- The sensor material is deposited using ion beam deposition (IBD) with deposition conditions as in Batch 1. The stack is: substrate/Ta(30Å)/NiFe(200Å)/MnIr(200Å) /Ta(30Å). Deposition conditions: Substrate rotation 50 %, substrate pan: 80 °, magnetic field during deposition: 40 Oe, beam current: 29 mA.
- 1.5 μm photoresist AZ5214e is spun onto the wafer. Equipment: SSI System 150 Track 1. Conditions: program PR1-5.

- The sensor crosses are defined in the photoresist by exposure through a mask. Equipment: SUSS Mask Aligner MA6/BA6. Conditions: time 10 s, exposure dose 9 mW cm^{-2}.
- Development in AZ531. Conditions: time 55 s, manual stirring of solution.
- The excess of material is etched away by ion milling leaving sensor crosses when the photoresist is removed. Machine: Commonwealth IBE system located at Universität Hanover, Institut für Mikrotechnolgie, Germany.
- 1.5 μm photoresist AZ5214e is spun on, and the resist is structured with grooves in the pattern of the electrical connections. Same spin, exposure dose, and development conditions as above. Exposure conditions: Negative imaging procedure: 8 s exposure with mask, 2 min bake at 120 °C hotplate, 25 s flood exposure (without mask).
- 0.3 μm Au is deposited by e-beam evaporation in Alcatel Model SCM600 e-beam system. Conditions: background pressure: 10^{-6} mbar, processing pressure: $\approx 5{\cdot}10^{-5}$ mbar, RF voltage: 8 kV, deposition rate: 1 nm/s.
- Lift-off in acetone. Conditions: ultrasonic agitation.

Immunoassay SU-8

- The sensors produced for immunoassays are subjected to another mask step. First the wafer is dehydrated. Equipment: HMDS oven, IMTEC star2000. Conditions: time 1 hour, temperature 100 °C, vacuum (no HMDS vapor).
- The wafer is covered with very thin SU-8 photoresist (0.5 μm). Equipment: Karl Suss RC8-THP spin coater. Conditions: 2000 rpm.
- Prebake. Equipment: Karl Suss RC8-THP spin coater. Conditions: hotplate set to 90 °C. Bake sequence: 30 s at 5 mm distance above the spinner hotplate, 30 s at 2 mm distance, 2 min directly on hotplate, 30 s at 2 mm distance, 30 s at 5 mm distance.
- Photolithography to structure the SU-8 into small squares covering only the sensing area of a sensor, that is the central $20\mu\text{m}\times 20\mu\text{m}$. Equipment: SUSS Mask Aligner MA6/BA6. Conditions: time 30 s, exposure dose 9 mW cm^{-2}.
- Postbake. Equipment: Karl Suss RC8-THP spin coater. Conditions: hotplate set to 90 °C. Bake sequence: as prebake.
- Development: 1 min in clean PGMEA (1-methoxy-2-propyl acetate). Rinse briefly in isopropanol. Dry with N_2 gas.
- Dicing and wire bonding remains to give the final functional chips.

A schematic drawing of the process sequence is given in Fig. 6.4 along with photos of the sensors at the various stages.

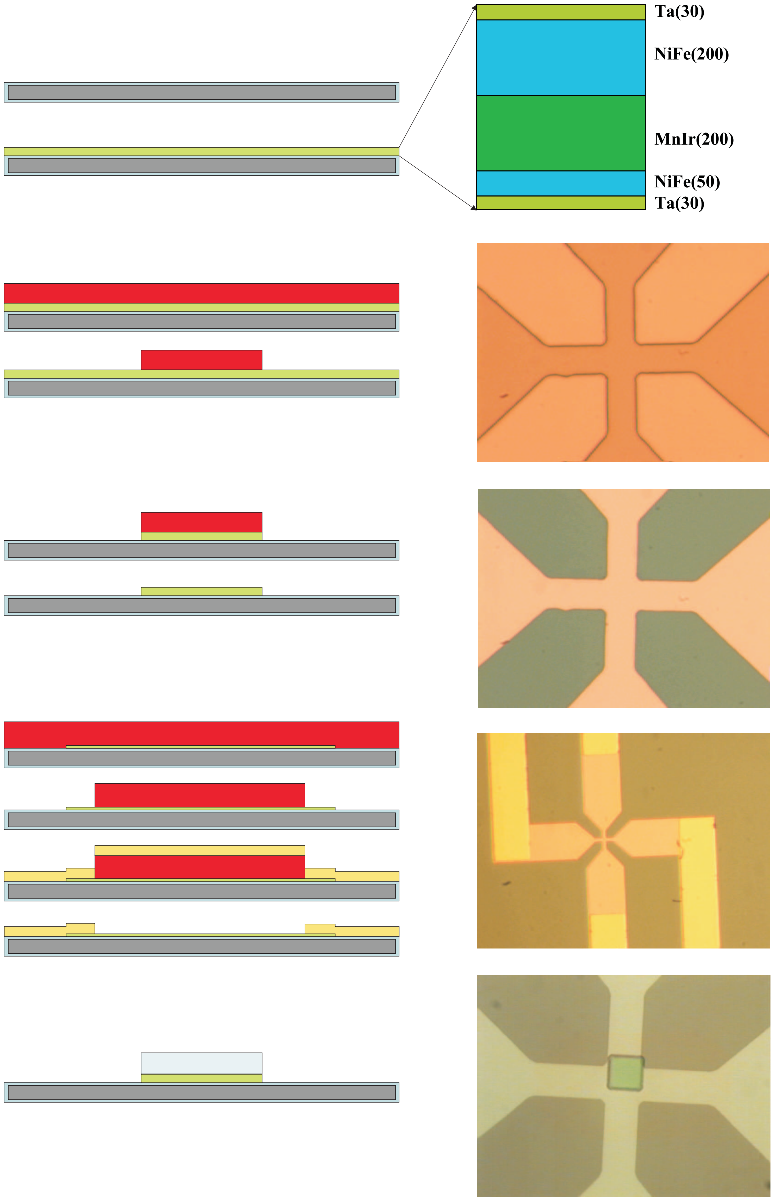

Figure 6.4: Lithography steps Batch 2. Left: schematic drawing of the lithography process, cross sectional view. Right: The top drawing is the cross section of the deposited material, the others are pictures of the wafer when processing moves along, the pictures are viewed from above. The picture sequence is: Structured photoresist, Dry-etch patterned sensors, Au leads, and SU-8 pads.

6.3 Experimental

In this section the experimental characterization equipment is described. First the VSM used for magnetic characterization of the films. Then the electrical setup used for electrical characterization of the Batch 2 sensors and bead detection measurements with Batch 2 sensors. The electrical setup consists of magnetic field control, temperature control, sensor control, and sensor output measurement.

Finally, the experimental conditions for Batch 2 sensors are described. The lock-in amplifier settings for noise characterization, sensor sensitivity, and biological detection conditions are summarized in Table 6.1.

6.3.1 Vibrating sample magnetometry

The magnetization curves of the IBD deposited films are investigated using a vibrating sample magnetometer (VSM), Lakeshore Model 7407. The sample is placed in the center of a detector coil assembly and two electromagnetic coils producing a variable magnetic field. The sample is set to vibrate at a specific frequency which induces an electromotive force in the detector coil assembly due to Faraday induction. The voltage is directly proportional to the magnetization of the sample. Hence the absolute magnetic moment can be obtained after calibration with a known sample. Sweeping the magnetic field and measuring the magnetization of the sample as a function of applied field reveals the magnetic properties of the sample.

6.3.2 Electrical characterization setup, Batch 2

Fig. 6.5 shows a schematic drawing of the experimental setup constructed for sensor characterization. Electrical connections are shown as solid lines, dashed when an optional path can be chosen, and data transfer is indicated with an arrow. Below is a description of the components shown in the drawing. Fig. 6.6 is a photograph of the experimental setup, and the picture shown in Fig. 6.7 (left) reveals the inside of the sensor box. Fig. 6.7 (right) is a schematic drawing of the setup controlling the temperature of the chip.

Magnetic field control

1. Helmholtz coils. The variable applied field is supplied by a set of homebuilt Helmholtz coils [3]. Due to heat generation the Helmholtz coils are suitable for no more than $I = 2$ A and, when using this value, only for short periods of time. The calibration of the Helmholtz coils is 7.7819(0.020) mT A^{-1} + 0.024(0.025) mT.

2. Keithley Model 6221. The current through the coils is controlled by a Keithley Model 6221 high precision AC/DC current source. The source can deliver only $I = 100$ mA DC, and hence the risk of over heating the coils is avoided when using the Keithley current source. The maximum obtainable magnetic flux density is $B = 0.78$ mT when using the Keithley current source; this value corresponds to approximately $H = 620$ A m^{-1} in terms of magnetic field strength. This is sufficient to determine

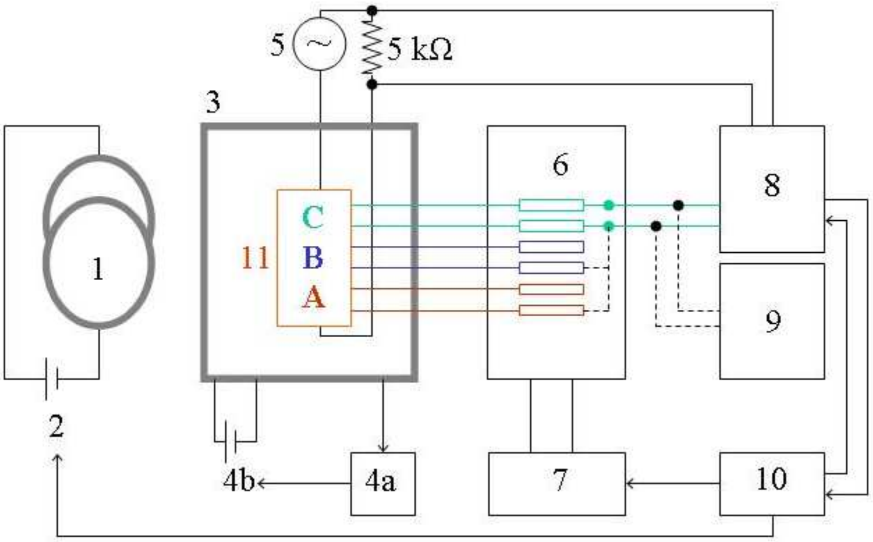

Figure 6.5: Schematic drawing of the electronic setup for permalloy sensor characterization. 1: Helmholtz coils, 2: K 6221 current source, 3: sensor box, 4: temperature control setup, 4a: temperature control, 4b: power supply, 5: K 6221 for sensor current, 6: switch box, 7: LabJack, 8: SR 830 lock-in amplifier, 9: K 2182A nanovoltmeter, 10: computer, 11: chip with three sensors A, B, C.

the slope of the sensor response in the low-field linear region but insufficient to determine the high field sensor response where saturation is reached. Alternatively, a Midec Type SK 150-2 is used for generating the high field values.

Temperature control

3. Sensor box. The box is made of aluminium in order to shield the experiments electrically. In Fig. 6.6 the thermal insulation is visible and not the metal box.

4. 4a: West Instruments Model 6100+ temperature control in combination with a 4b: Kepco Model BOP 50-8 bipolar operational power supply (not visible in Fig. 6.6) to provide the voltage for the Peltier elements. A schematic drawing of the temperature control of the sensor box is shown in Fig. 6.7, right.

   Two Peltier elements and a thermocouple K-type (PE-241-14-15 and 397-1236 from RS: www.rsonline.dk).

   Controlling the actual temperature of the planar Hall sensor is accomplished by controlling the temperature of the environment. The temperature of the box is controlled externally by Peltier elements in combination with copper heat reservoirs, see Fig. 6.7 (right). The excess heat produced by the Peltier elements is removed by heat sinks. The thermocouple is buried within a copper heat reservoir thus

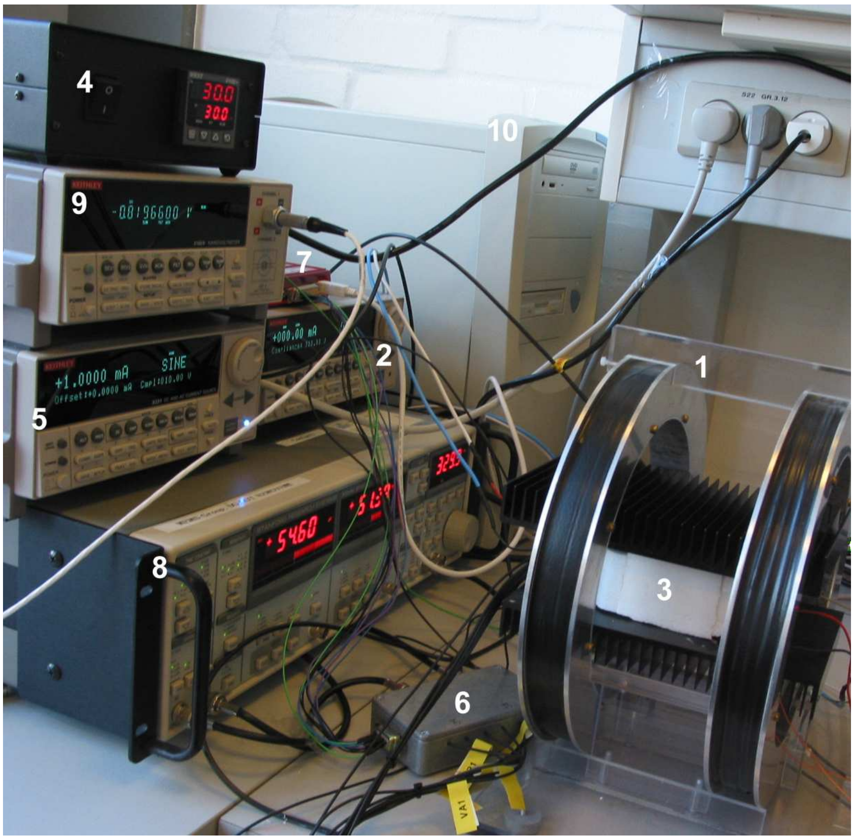

Figure 6.6: Experimental setup for sensor characterization. 1: Helmholtz coils, 2: K 6221 current source, 3: sensor box, 4: temperature control box, 5: K 6221 for sensor current, 6: switch box, 7: LabJack, 8: SR 830 lock-in amplifier, 9: K 2182A nanovoltmeter, 10: computer.

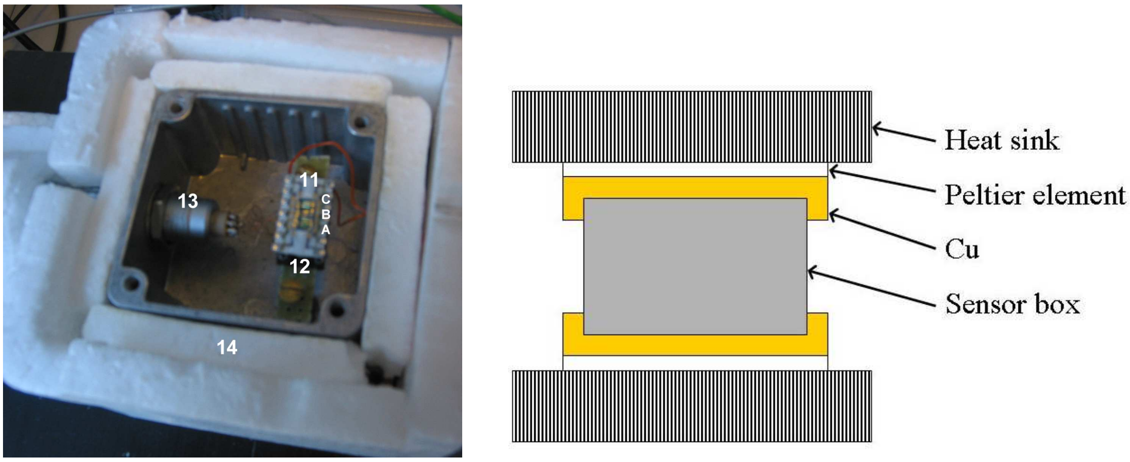

Figure 6.7: Left: Inside of sensor box (3 in Fig. 6.6). 11: chip with three sensors A, B, C, 12: socket, 13: LEMO connector, 14: thermal insulation. Right: Schematic drawing of the temperature control setup (connected to 4 in Fig. 6.6).

connecting the temperature control to the temperature of the copper heat reservoirs. The temperature of the copper plates is transferred to the internal of the sensor box and, though with a time delay, the outcome is a stable temperature after equilibrium has been reached.

Sensor current control

5. Keithley Model 6221. The sensor current is applied by a Keithley Model 6221 high precision current source. I_{AC} is reported as the maximum amplitude of the sine function generated by the current supply.

Sensor switch control

6. Switch box. In order to quickly measure the signal from all sensors, a switch box is introduced. The switch box consists of six Reed relays Model B05-1A72-BV619 (MEDER electronics AG, www.meder.com), one for each connection, that are turned on in pairs hereby closing the electrical path across the desired sensor and connecting the sensor to the proper input on the lock-in amplifier or the nanovoltmeter. The switch box introduces an additional source of noise to the setup of $\Delta V \approx 2$ nV but facilitates measurements considerably.

7. LabJack Model U12. Supplies the voltage for the Reed relays in the switch box (6).

Sensor output measurement

8. Stanford Research Systems Model 830 [36]. A Stanford Research Systems Model 830 lock-in amplifier is used for the noise characterization measurement and the bead detection measurements. The reference signal for the lock-in amplifier is produced by passing the current from (5) through a low noise serial resistor of $R_e = 5$ kΩ (RS92N/AN, www.vishay.com). The voltage drop across the resistor is sufficient for the lock-in reference in all experiments.

   The basic operation of the lock-in amplifier is governed by multiplying the detected signal with a reference signal and averaging over a predefined period of time, τ. The time constant defines the bandwidth as $\Delta f = 1/8\tau$ for 12 dB oct^{-1} [36]. The synchronous filter is on because of the low oscillation frequency. The lock-in settings in the various experiments are summarized in Table 6.1.

9. Keithley Model 2182A nanovoltmeter. The nanovoltmeter functions as an alternative to the lock-in amplifier (8), mostly for trouble-shooting.

Experiment control

10. A computer controls the experiments via LabView.

Display	Signal	Reserve	Filters	Filter slope
R, θ	A-B	low noise	sync	12 dB Oct^{-1}

Experiment	f (Hz)	τ	Sensitivity (μV)	
Noise	30	10 ms - 1 s	10	
Sensitivity	330	1 s	100	
Temperature	330	1 s	50	
Antibody	330	100 ms	100	
Influenza	330	100 ms	100	

Table 6.1: Lock-in amplifier settings for different experiments with permalloy sensors, Batch 2. f is the applied frequency and τ is the lock-in time constant.

Sensor box

11. Chip with three planar Hall sensors A, B, C.
12. Chip holder. The chip is placed in a dedicated socket to the right inside the box with sensor C above B and A, respectively. Mounted below the chip is a PT100 temperature sensor (www.rsonline.dk).
13. LEMO Connector Type 1B308 [37]. The electrical connections to the chip are passed through the box by a LEMO Connector, which has an eight connector multipole, two for current and six for the sensor output voltages. The six voltage connections all carry the output signal from the three sensors. Two connections per sensor to give the voltage drop across the sensor. These six outputs are connected to the switch box (6) used to switch between the sensors.
14. Thermal insulation.

6.3.3 Experimental conditions for permalloy sensors

This subsection describes the experimental conditions for the various experiments of Table 6.1. Only conditions differing from described above are included.

Noise characterization conditions

The noise characterization measurements are performed in the setup described in Chapter 5, Fig. 5.5. A $V_{\text{out}} = 1.004$ V amplitude sine output from the lock-in amplifier controls the current through the sensor. A low noise resistor of $R_e = 5$ kΩ (substituting the $R_e = 4.8$ kΩ ordinary resistor) is inserted in the series to stabilize the magnitude of current at $I_{\text{AC}} = 196$ μA. The settings for the lock-in amplifier are in Table 6.1.

Sensor signal versus field

For the experiments with permalloy planar Hall sensors at high field values, $B > 0.78$ mT, the current through the Helmholtz coils is controlled by the Midec Type SK 150-2 power supply. For the sensitivity measurements at low magnetic fields, the Keithley Model 6221 is used.

Antibody detection conditions

In the antibody detection experiments, the experimental conditions are identical to those described above for the experimental setup. The Keithley Model 6221 current source is used to control the B-field. The settings for the lock-in amplifier are in Table 6.1. Details on data acquisition and analysis are provided in Appendix B. The experimental results are presented in Chapter 7.

Immunoassay detection conditions

In the immunoassay detection experiments, the experimental conditions, data acquisition, and data analysis are identical to the antibody detection experiments described above. The experimental results are presented in Chapter 8.

6.4 Results

This and the following three sections present the experimental results obtained for the two batches of permalloy planar Hall sensors. First the VSM measurements of the thin films. Then the electrical characterization of the fabricated sensors. The biological results are reserved for the next two chapters.

6.4.1 Vibrating sample magnetometry of the magnetic films

Fig. 6.8 shows the magnetization versus applied field experiments for the bottom-pinned (Batch 1) and top-pinned (Batch 2) stacks presented in Fig. 6.3. The left stack (Fig. 6.3) corresponds to the left graph (Fig. 6.8), and vice versa. The VSM measurements are performed with the applied field along the easy direction. Both measurements show successful exchange-coupling, visualized as a shift of the hysteresis loop towards negative applied field strength. The left graph reveals two loops of magnetization versus field, where the larger loop is attributed to the 20 nm thick NiFe film, and the smaller one is attributed to the 5 nm thick NiFe seed layer.

The largest loop deviates from the square appearance expected for a single domain. This may be due to domain effects, which probably arise from deviation from single crystallinity. It seems, the MnIr film is not truly single crystalline as expected from epitaxial growth. It is also clear, that the seed layer, which is the smallest loop, has multiple domain behavior. The domain structure of the seed layer is probably causing the non-epitaxiality of the pinning layer, again causing the deviation from single domain behavior of the sensing layer. The majority of the sensing will be governed by the 20 nm NiFe layer.

In the top pinned stack, Fig. 6.8 right, similar domain behavior, again caused by deviation from perfect crystallinity, can be observed. In this magnetic layer configuration the anisotropy field is very low compared to the bottom pinned stack, but the larger

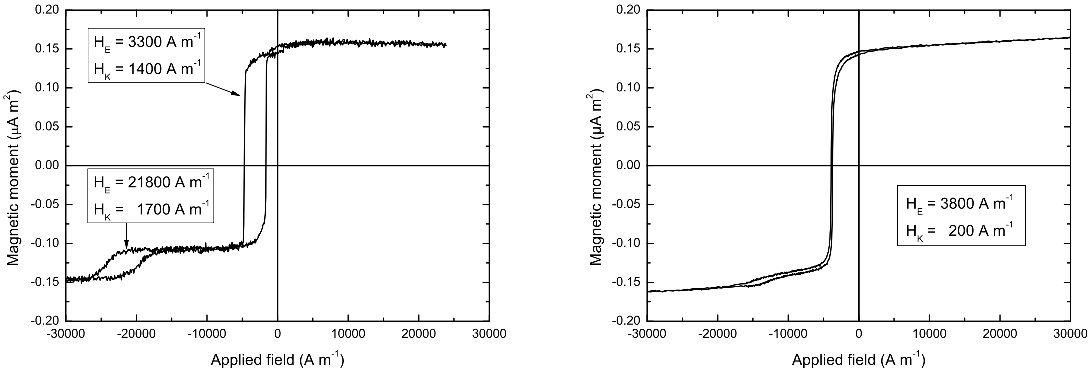

Figure 6.8: Vibrating sample magnetometer (VSM) measurements of magnetization versus applied field strength for the two planar Hall stacks shown in Fig. 6.3. Left: substrate/Ta(30Å)/NiFe(50Å)/MnIr(200Å)/NiFe(200Å)/Ta(30Å) (bottom-pinned, Batch 1). Right: substrate/Ta(30Å)/NiFe(200Å)/MnIr(200Å)/Ta(30Å) (top-pinned, Batch 2). The measurements are performed with the applied field along the easy axis of the film. The left graph reveals a second loop attributed to the 5 nm NiFe seed layer.

exchange coupling compensates for that in terms of sensor sensitivity. The slight opening of the loop at negative field values may be due to impurities from the deposition process.

From the data presentation it is clear that the magnetic properties behind sensing are governed almost singularly by the exchange coupling in the case of the top pinned stack. Whereas a considerable anisotropy contribution is present in the bottom pinned sensor. The sum of the two contributions are comparable in the two cases and therefore the sensitivities of the two versions of planar Hall sensors will be comparable too. However, the difference in arriving at the similar sensitivity might be important for design considerations at a later stage of sensor development and is therefore worth mentioning.

The sensitivity, S_0, depends inversely on the sum of H_K and H_E, and thus the sensitivity is lower for higher H_K and H_E. However, the linear region of the sensor is proportional to these parameters, linearity within 2 % is expected in the interval $-0.23 < H_x/(H_K + H_E) < 0.23$, see Chapter 3. With the measured H_K and H_E a good sensitivity is combined with an extended linear field region between $H = \pm 900$ A m^{-1}, in flux density units $B = \pm 1$ mT.

6.5 Electrical characterization of permalloy sensors

This and the following two sections present the electrical characterization of the fabricated exchange biased permalloy planar Hall sensors. Sensor Batch 1 was characterized at INESC-MN, and sensor Batch 2 has been characterized at MIC in the setup described above.

The presented characterization of Batch 1 includes sensor resistance, sensitivity, and experimental noise. Additionally bead detection experiments are shown. The characterization of Batch 2 includes sensor resistance, noise investigation, field response, statistical sensitivity, and temperature effects.

6.6 Batch 1

The electrical characterization measurements of Batch 1, summarized in Table 6.2, are from Refs. [4, 5]. The characterization was performed at INESC-MN. A Batch 1 chip was mounted on a protoboard and a horseshoe electromagnet provided the magnetic field. Batch 1 was characterized using only DC measurements in a setup, which was not shielded for electronic noise.

Property	**Unit**	**Theoretical**	**Experimental**	**Exp. std. var.**
R_{DC}*	Ω	25	51.9	0.5
AMR	%	1.9	1.3	0.02
V_0	μV	458	515	10
S_0	$\mu\mathrm{V}\ \mathrm{mA}^{-1}\ \mathrm{mT}^{-1}$	38.6	30.6	2
ΔV**	nV	11	250	-

Table 6.2: Theoretical values versus experimental values of the planar Hall sensors of Batch 1. Last column is the experimental standard variation. (*) The DC electrical resistance, R_{DC}, is calculated as a parallel connection of: two layers of 3 nm Ta ($\rho_{\mathrm{Ta}} = 154\ \mu\Omega$ cm), one layer of 20 nm MnIr ($\rho_{\mathrm{MnIr}} = 175\ \mu\Omega$ cm), and two layers of 5 nm + 20 nm NiFe ($\rho_{\mathrm{NiFe}} = 21.7\ \mu\Omega$ cm) (resistivities from Gehanno *et al.* 1999) for a sensor geometry of 10μm × 10μm. (**) The noise, ΔV, is measured during bead detection measurements in a setup without electrical shielding.

6.6.1 Bead detection, Batch 1

This subsection presents a summary of the bead detection experiments of Ref. [4]. The aim is to verify that the exchange biased permalloy planar Hall sensor is suitable for bead detection and only the concluding graph is presented.

First the procedure for measuring the number of beads and subsequently the signal they produce is stated. Then the results are shown in Fig. 6.9.

Procedure

During an experiment the signal from the sensor is measured as a function of time. Experimental conditions are a sensor current of $I_{\mathrm{DC}} = 10$ mA, and an applied field of $H = -1200$ A m^{-1}. First water is added to the chip and the signal is observed to stabilize. The signal stabilization might be due to stabilization of the temperature of the chip. Water acts as a heat reservoir.

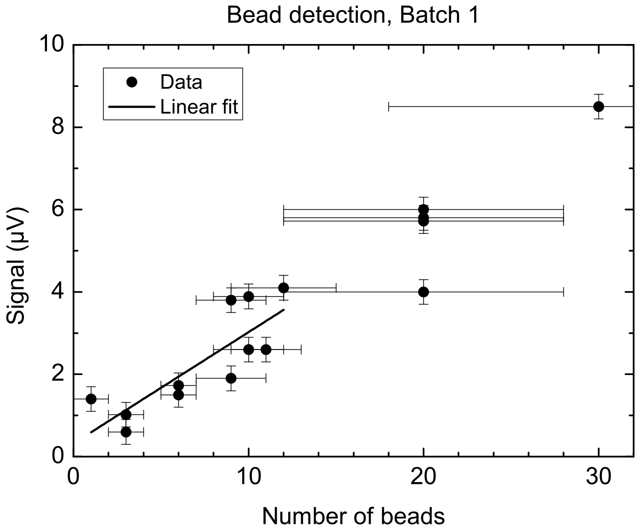

Figure 6.9: Bead detection experiments from Ejsing *et al.* 2004. Experimental conditions: $I_{\mathrm{DC}} = 10$ mA, $H = -1200$ A m^{-1}. The signal is the sensor signal for a variable number of beads. The number of beads is estimated by visual inspection during a bead detection experiment. For low bead numbers, the linear fit gives 0.27(0.06) μV bead^{-1}.

After the signal has stabilized, a solution of Micromer-M beads, diameter 2 μm, is added to the chip using a micro pipette. The beads are flushed with water and occasionally pass by the sensor. When a cluster of beads is observed to pass the sensor, the time is written down along with an estimate of the number of beads in the cluster. The estimate is done by visual inspection through the microscope. For large numbers of beads, it is difficult to judge the number due to the limited time available and due to the clustering of beads. Hence the large error bars on the large numbers of beads.

The signal from the sensor is recorded as a function of time. When clusters of beads are above the sensor, the signal peaks, and when the clusters leave the sensor, the signal drops to the baseline value. The signal changes are identified with the number of beads by matching the recorded time with the time of observing the bead clusters. Hence the signal produced by the cluster is $V_{\mathrm{cluster}} = V_{\mathrm{peak}} - V_{\mathrm{baseline}}$.

Results

The bead detection results are presented in Fig. 6.9. The signal as a function of the number of beads above the sensor is close to linear. A linear fit for the small amounts of beads yields an experimental single Micromer-M bead signal of

$$V_{\mathrm{bead}} \approx 0.27(0.06)\ \mu\mathrm{V}$$

The noise level is $\Delta V \approx 0.25\ \mu$V.

Discussion

Analysis of the single bead signal from a 2 μm Micromer-M bead has shown that the sensor current contributes to magnetizing the beads. Additionally, the detection of Micromer-M beads in zero applied field is published in Ref. [5]. In this study the beads are solely magnetized by the DC current through the sensor. This is potentially an advantage in a future chip design. As the external field can be excluded, there will be no need for coils, which will facilitate the fabrication and assist miniaturization.

6.7 Batch 2

Below is presented the electrical characterization measurements performed on Batch 2. Batch 2 is characterized using only AC measurements, and the setup is shielded for electronic noise. The electrical characterization setup has been described above. The contribution to magnetization of beads by the AC current averages to zero. Thus only applied fields should be considered, when detected by lock-in technique.

6.7.1 Investigation of noise, Batch 2

The mathematical expressions for electronic noise are given in Chapter 2. Table 6.3 summarizes the estimates of noise contributions to the planar Hall sensors characterized in this subsection.

The number of charge carriers of the $\mathrm{Ni_{80}Fe_{20}}$ film is estimated from the volume (vol), density (ϱ), and atomic weight (aw) of the active sensing layer. $vol = 20\mu\mathrm{m}\times 20\mu\mathrm{m}\times 20\mathrm{nm}$, $\varrho = 8.89$ g cm^{-3}, and $aw = 58.69$ g mol^{-1}. The number of charge carriers thus becomes $N_c = 7 \cdot 10^{11}$ assuming one carrier per atom.

Procedure

Experimental characterization of the noise level is done at a frequency of $f = 30$ Hz for bandwidths set by the lock-in time constant, $\tau = 10$ ms, $\tau = 30$ ms, $\tau = 100$ ms, and $\tau = 300$ ms. The experimental noise is measured in an applied field of $B = 0.5$ mT in the setup described above with a $20\mu\mathrm{m}\times 20\mu\mathrm{m}$ planar Hall sensor mounted. The current through the sensor is set by the lock-in amplitude of $V_{\mathrm{AC}} = 1.004$ V, giving $I_{\mathrm{AC}} = 0.196$ mA. The experimental noise level is estimated as the standard deviation of a series of measurements with constant experimental conditions.

Results

Fig. 6.10 shows the measured experimental noise (data points) and two theoretical estimates (lines). The theoretical noise level for the sensor alone (red dashed line) compared to the experimental noise is very low, including Johnson noise, shot noise, and $1/f$ noise. The noise from the sensor lies well below the noise from the setup (black solid line) and is thus not visible in the experimental measurements. The magnitude of experimental noise corresponds well to the noise from the lock-in amplifier.

w (μm)	t (nm)	R_e (Ω)	γ_{H}	N_c
20	20	127	0.01	$7 \cdot 10^{11}$
Johnson ($\frac{\mathrm{nV}}{\sqrt{\mathrm{Hz}}}$)	Shot ($\frac{\mathrm{nV}}{\sqrt{\mathrm{Hz}}}$)	$1/f$ (30 Hz) ($\frac{\mathrm{nV}}{\sqrt{\mathrm{Hz}}}$)	$1/f$ (330 Hz) ($\frac{\mathrm{nV}}{\sqrt{\mathrm{Hz}}}$)	
1.45	2.3	2.8	0.8	

Table 6.3: Electronic noise in planar Hall sensors, Batch 2. First row gives the value of the parameters for the actual sensor batch, second is the calculated noise estimates, Eq. (2.6), Eq. (2.7), and Eq. (2.8), respectively. Hooge's constant, γ_{H}, is from Briaire *et al.* 1997.

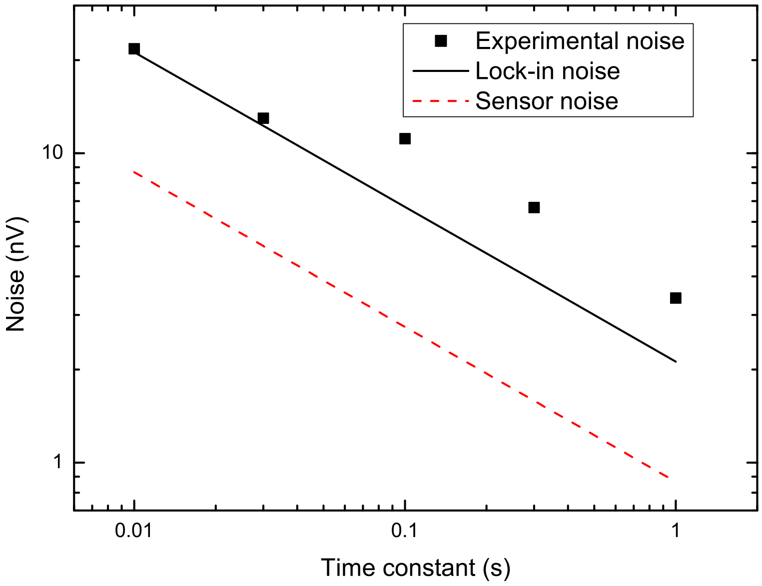

Figure 6.10: Experimental and theoretical noise of the sensor and setup, Batch 2. The data points are the measured noise of the setup and the solid lines are the theoretical noise of the sensor (dashed red) and the lock-in amplifier (solid black). Experimental conditions are $B = 0.5$ mT, $f = 30$ Hz, and $I_{\mathrm{AC}} = 0.196$ mA. The theoretical sensor noise is the sum of the Johnson, shot noise, and the $1/f$ noise for a $20\mu\mathrm{m}\times 20\mu\mathrm{m}$ planar Hall sensor. The graph is a log-log plot revealing the inverse square root dependence of the theoretical noise level.

The noise spectrum of the setup is inspected with a Spectrum Analyzer (Hewlett Packard Model 4396A, Network/Spectrum Analyzer). The outcome of that experiment proves that $f = 30$ Hz and $f = 330$ Hz are good choices of measurement frequencies as they are situated at relatively quiet positions in the noise spectrum.

Assay noise

Increasing the time constant on the lock-in amplifier decreases the expected noise, and increasing the frequency to $f = 330$ Hz decreases the $1/f$ noise level to $\Delta V/\sqrt{\Delta f} = 0.8$ nV/$\sqrt{\text{Hz}}$. For integration times of $\tau = 100$ ms ($\Delta f = 1.25$ Hz) and averaging over 100 data points the theoretical noise level of one experiment becomes: $N_{\text{tot}} \cdot \sqrt{\Delta f}/\sqrt{(\#\text{meas} - 1)} \approx$ 0.3 nV, where N_{tot} is the sum of Johnson noise, shot noise, and $1/f$ noise added using the law of error propagation. An experimental standard error of $\Delta V \approx 1$ nV is obtained, which is the background for the bead detection limit estimate in Chapter 4.

6.7.2 Sensor response vs. field, Batch 2

The characterization of the field response of permalloy planar Hall sensors are presented in Fig. 6.11, and Fig. 6.12. For ease of comparison to theoretical calculations, the value measured at 30 °C is chosen for all presented data though a temperature interval between 15 °C and 45 °C has been investigated.

The planar Hall signal's behavior up to high field values is shown in Fig. 6.11. The generated curve is Eq. (3.9) with $V_0 = I\,AMR\,\rho_{\text{av}} t^{-1} = 223.5$ μV and $H_E + H_K$ estimated from the hysteresis measurements, Fig. 6.8 (right). From the experimental data an off-set of $V = 3.45$ μV has been subtracted before comparing to the theoretical curve. Good agreement is observed at low applied fields up to approximately $B = 2$ mT, where the curves start deviating.

The insert of Fig. 6.11 presents a fit to the experimental data. The best fit yields parameters: $H_E = 3458$ A m^{-1}, $H_K = 1.86$ A m^{-1}, and $V_0 = 191.4$ μV. These are close to the expected values. Expected values: $H_E = 3800$ A m^{-1}, $H_K = 200$ A m^{-1} obtained from the VSM measurements (Fig. 6.8), and $V_0 = 223.5$ μV. However, the VSM measurements will most likely over-estimate the value of H_K, which is small compared to the experimental accuracy.

The sensor response as a function of applied magnetic field yields a straight line with the slope $S_0 = 44.8(0.2)$ μV mT^{-1} mA^{-1} at $T = 30$ °C. This value is the average value of the sensitivity of 31 sensors, presented in Fig. 6.12. Fig. 6.12 shows the sensitivity for different planar Hall sensors of equal design (20μm × 20μm sensitive areas). The larger error bars associated with the second half of the measurements are due to less data points used to determine the slope. The reason is to save time on the measurements. The deviation between the highest and the lowest sensitivity is approximately 10 %. The dotted line shows the theoretically expected value given by Eq. (3.19), which is $S_0 = 44.3$ μV mT^{-1} mA^{-1}.

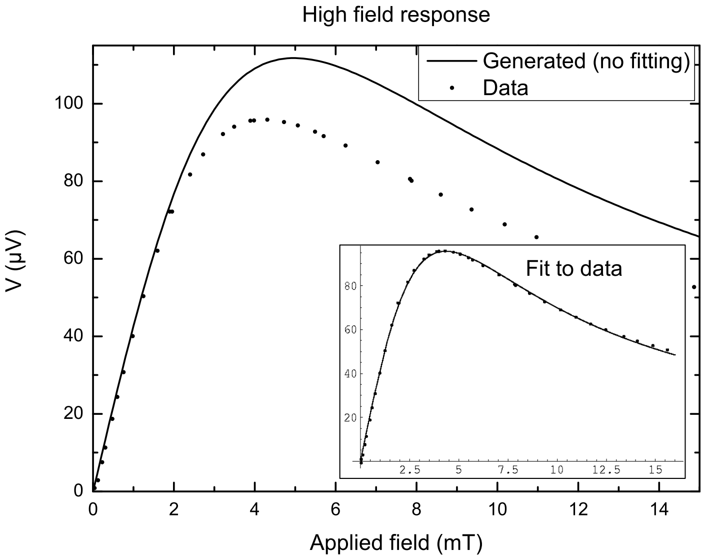

Figure 6.11: Experimental and theoretical (generated from VSM measurements of H_K and H_E) high field behavior of the permalloy planar Hall sensor. In the experimental data, an off-set of 3.45 μV has been subtracted. The insert shows a fit of the combined Eq. (3.9) and Eq. (3.16) to the experimental data. This yields $H_E = 3458$ A m^{-1}, $H_K = 1.86$ A m^{-1}, and $V_0 = 191.4$ μV.

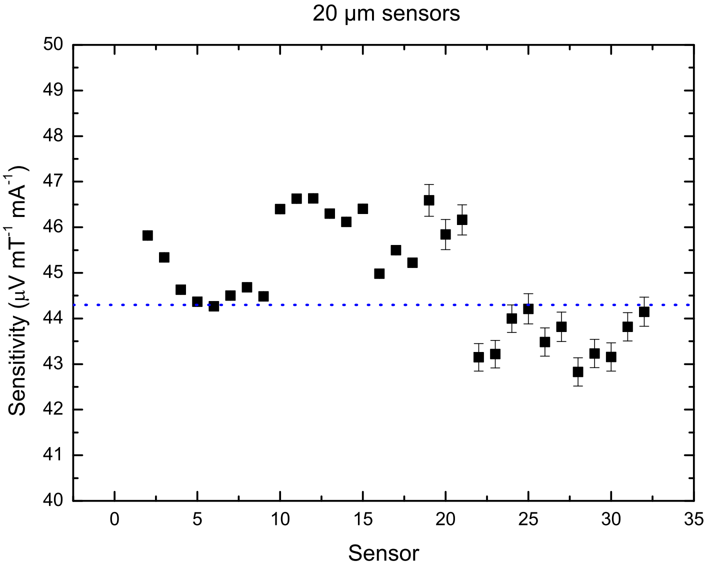

Figure 6.12: Experimental sensitivities for 31 planar Hall sensors of $20\mu\text{m}\times 20\mu\text{m}$ sensitive areas. The dotted line is the theoretical value.

6.7.3 Investigation of temperature dependence, Batch 2

Due to fluctuations in room temperature, the sensor signal is observed to vary with temperature. When the temperature rises, the signal rises, and when the temperature drops, the signal drops, see Fig. 6.13 and Fig. 6.14.

Procedure

A constant field of $B = 0.54$ mT is applied during the measurements. The temperature of the copper plates is set at $T = 20$ °C through $T = 40$ °C and back with step sizes of $\Delta T = 5$ °C. The actual temperature inside the box is measured with the Pt100 element and the values are reported on the graph, Fig. 6.13. Each value corresponds to the end time at each temperature interval, which is the most stable value and approaches an equilibrium value. Evidently the measured temperatures vary more than is attempted by setting the temperature of the copper plates.

Results

Fig. 6.13 shows a nine hour time trace of the sensor signal, in which the temperature is changed every hour. There is a clear stepwise dependence when altering the temperature. One can observe that the signal comes to rest when the temperature equilibrium is reached, the steps flatten, and the temperature of $T = 30.9$ °C, setpoint $T = 30$ °C, is the most stable operating temperature of the ones tested. At this setpoint, the power supply for the Peltier elements has less work load in maintaining a constant temperature due to the vicinity of room temperature.

The results are summarized in Fig. 6.14 (left), where the signal is plotted as a function of temperature. The path up differs slightly from the path down showing a tendency of hysteresis. However, it is difficult to determine the actual signal at the time where the temperature measurement is taken due to a much higher noise level than usual. This extra noise probably arises because of temperature fluctuations when adjusting the temperature. Rather large errors to the data points result. A linear curve is fitted to the data points to obtain an estimate of the magnitude of the signal temperature dependence. $\Delta V \approx 55$ nV $^{\circ}\mathrm{C}^{-1}$ corresponding to a change of approximately 0.2 % $^{\circ}\mathrm{C}^{-1}$.

Additionally, the sensitivity, S_0, and the electrical resistivity, R_e, are measured as a function of temperature. These are plotted in Fig. 6.14 (right) along with V. S_0 changes approximately 0.24 % $^{\circ}\mathrm{C}^{-1}$. The change in R_e as a function of temperature is sufficient to account for the changes in V and S_0 within experimental errors.

Discussion

These temperature variations are comparable to those of Ky's experimental data [30]. Ky gets a temperature variation of thin nickel films in the order of 0.2-0.25 % $^{\circ}\mathrm{C}^{-1}$, see Chapter 2. Since the permalloy films are composed of 80 % nickel, their behavior is likely to be similar. Montaigne *et. al.* reports approximately 0.3 % $^{\circ}\mathrm{C}^{-1}$ change in R_e for their permalloy films [1].

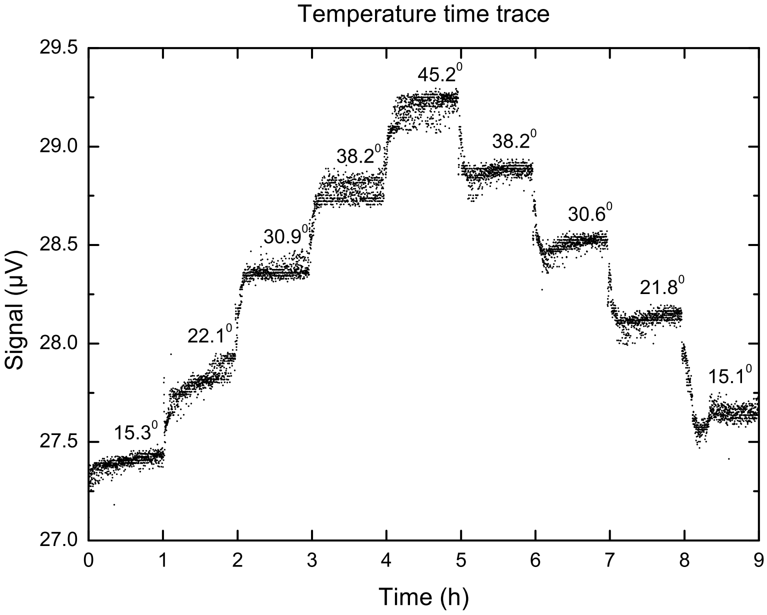

Figure 6.13: Temperature dependence of the sensor signal. The graph shows a nine hour time trace of the sensor signal, where the temperature has been changed every hour. The measured temperature values are included on the graph.

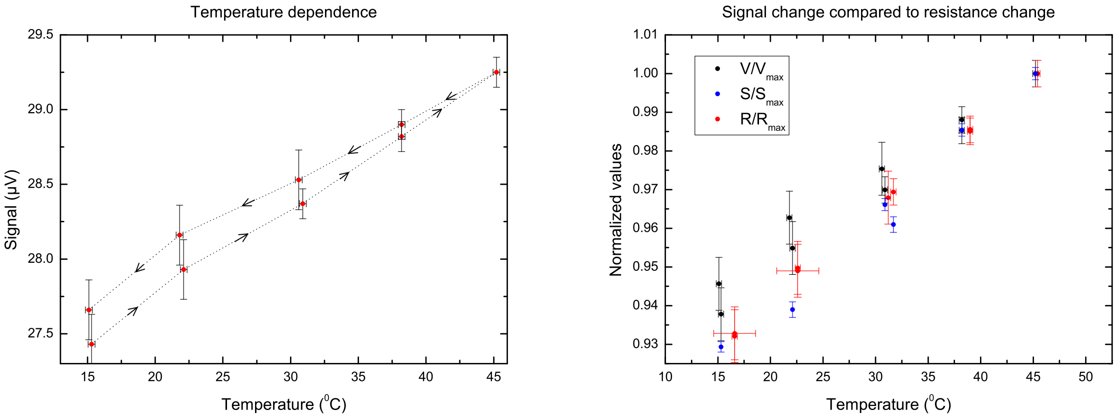

Figure 6.14: Temperature dependence of the sensor signal. Left: sensor signal as a function of temperature. A linear fit reveals the change as 55 nV °C^{-1} corresponding to 0.2 % °C^{-1} change in signal. Right: signal magnitude, V, and sensitivity, S_0, of the sensor is compared to the change in resistance, R_e. V, S, and R_e are normalized to their value at the highest temperature.

The experiment is repeated with no field applied in order to observe the off-set as a function of temperature. This results in the same temperature dependence. Hence the magnetic field dependent contributions, anything apart from the resistivity, can be ruled out as they depend on the magnetic state of the film.

A possible approach to controlling these effects would be to keep the voltage constant instead of the current. If only the electrical resistance changes, the sensor output voltage would be constant for a constant applied voltage.

6.7.4 Summary, Batch 2

All the above investigations of Batch 2 sensors are summarized in Table 6.4. Generally good agreement is observed between expected or calculated values and experimentally observed values. In the experimental value for S_0, the current is assumed to flow solely through the permalloy layer of the stack. Shunting of the current through the other layers of the stack can be simulated using the commercially available package FEMlab, this yields $V_0 = 211\ \mu$V and $S_0 = 49.3\ \mu$V mA^{-1} mT^{-1} for the experimental values.

Property	**Unit**	**Expected**	**Measured**	**Exp. std. var.**
ρ_{stack}*	$\mu\Omega$ cm	42.8	46.8	0.5
AMR	%	1.9	2.06	0.02
H_E**	A m^{-1}	3800 (VSM)	3500 (fit)	-
H_K**	A m^{-1}	200 (VSM)	2 (fit)	-
V_0	μV	223.5	190	10
S_0	μV mA^{-1} mT^{-1}	44.3	44.8	0.2
Noise***	nV	0.9	3.9	0.5
Assay noise	nV	0.3	1	-
Temperature drift	% °C^{-1}	0.2-0.25 (Ky) 0.3 (Montaigne)	0.2 (V) 0.24 (S_0)	0.01 (V) 0.02 (S_0)

Table 6.4: Calculated/expected values versus measured values of the planar Hall sensors of Batch 2. Last column is the experimental standard variation on the measured value. (*) ρ_{stack} is calculated as a parallel connection of two 3 nm thick Ta layers ($\rho_{\mathrm{Ta}} = 154\ \mu\Omega$ cm), 20 nm MnIr ($\rho_{\mathrm{MnIr}} = 175\ \mu\Omega$ cm), and 20 nm NiFe ($\rho_{\mathrm{NiFe}} = 21.7\ \mu\Omega$ cm) (resistivities from Gehanno *et al.* 1999) for a sensor geometry of 20μm $\times$ 20μm. (**) The values given as the "measured" H_K and H_E are obtained from the fitted curve to the experimental data, Fig. 6.11, whereas "expected" are from the VSM measurements, Fig. 6.8 (right). (***) The bandwidth is set by the time constant $\tau = 1$ s, and the temperature is $T = 30$ °C. The expected noise value is the sum of the Johnson noise, shot noise, and the $1/f$ noise for the sensor alone.

6.8 Discussion of S/N improvement

This section discusses briefly some possibilities of improving S/N in the electrical setup used for characterizing the Batch 2 sensors.

The noise level of the planar Hall sensors is independent of the applied magnetic flux density. In the sensor Batch 2, the sensor response starts deviating from linear with respect to the applied field at approximately $B = 1$ mT, which puts a natural limit to the field for magnetizing the beads. Furthermore, currents of up to $I = 10$ mA can be applied without destroying the sensor, and the tests are done with much less current than that. Due to practical circumstances only $I_{\mathrm{AC}} = 1$ mA (maximum amplitude) is used. Pushing the limit of field and current, a factor of 10-20 could be gained.

The noise from the planar Hall sensors is dominated by the noise from the lock-in amplifier, see Fig. 6.10. The introduction of a low-noise pre-amplifier between the sensor and the lock-in amplifier would help to utilize the full scale of the planar Hall sensor. An estimate of the signal-to-noise enhancement following this procedure is approximately 5. In total it should be possible to enhance S/N 50-100 times, which makes detection of single 250 nm beads within reach of the actual sensor batch. Table 4.3 predicts that 62 Nanomag-D beads on a sensor will yield $S/N = 2$.

6.9 Conclusion

This chapter has presented two approaches of exchange biasing permalloy planar Hall sensors. Batch 1 constitutes a bottom-pinned approach and Batch 2 a top-pinned. The fabrication procedure of the two sensor batches has been described in detail.

Batch 1 was fabricated and characterized completely during the author's stay at INESC-MN, Portugal. The characterization was only DC, and no electrical shielding of noise was conducted during the measurements. Batch 2 has been fabricated essentially at MIC, and efforts are put into electrical shielding and noise reduction in the experimental setup described in the text.

The VSM measurements show that a successful exchange coupling is induced in the thin magnetic films. Thus the zero field starting point of the film's magnetization is, and will be, well-defined.

For Batch 1, electrical characterization measurements have been presented and compared to theory. The comparison is reasonable except from R_{DC}. Additionally, bead detection experiments obtained in [4] are included. The single bead signal reported from a Micromer-M bead is 0.27 μV, though with a sensor noise level in the same order of magnitude [4]. Using DC sensor currents, Micromer-M beads can be detected in zero applied field [5], which will facilitate the electronics in an eventual point-of-care device. No biological experiments have been performed with Batch 1 sensors.

For Batch 2, sensor noise, sensor field response, and temperature dependence have been thoroughly investigated. The experimental values compare well with theory, see Table 6.4. Finally, it is estimated that S/N could be improved 50-100 times in the present setup by adjusting field, current, and introducing a pre-amplifier. Since the calculated detection limit is 62 Nanomag-D beads, single bead detection should be within reach for Batch 2 sensors.

Chapter 7

Antibody detection

In this chapter, detection of antibodies immobilized on top of the planar Hall sensors is realized. Batch 2 sensors are used. Biotinylated monoclonal antibodies in varying concentrations are immobilized on top of a sensor and streptavidin coated beads bind specifically to the biotin label. The presence of antibodies is detected by detecting the beads.

As the surface where proteins are immobilized, SU-8 photoresist is chosen. SU-8 is a negative tone photosensitive polymer, and can thus be patterned directly by lithography described previously. The polymer is non-conducting and shunting of the sensor current is avoided. Furthermore, SU-8 can be spun on the wafer in a very thin layer, 0.5 μm, which is an advantage since the sensitivity of the sensor towards the beads strongly depends on distance.

7.1 Immobilizing antibodies

In order to use the planar Hall sensor in an immunoassay, the appropriate antibodies must be immobilized on the surface. When discovering that the photosensitive polymer SU-8 has a high binding capacity for biomolecules, this property was immediately pursued for detection of DNA samples [34]. During this work, it was discovered that SU-8 has a high binding capacity not only to DNA fragments but also to proteins. This is the motivation for choosing SU-8 for attaching antibodies on top of the planar Hall sensors though the system is new and the binding mechanism so far not known.

This section presents the immobilization procedure. First coating and structuring of SU-8 is addressed, then the binding of antibodies to the SU-8 surface.

7.1.1 SU-8

The negative tone photosensitive polymer SU-8 can be purchased at MicroChem (www.micro-resist.de) and both the first SU-8 series and the SU-8 2000 series can be used to attach DNA and proteins. The only difference is the solvent on which the solution is based. For the coating of planar Hall sensors, diluted SU-8 2002 is used.

During experiments with DNA [34] a very high autofluorescence from SU-8 has been observed. This calls for using a very thin layer of SU-8 for the fluorescence detection. Additionally, the planar Hall sensors are sensitive to the sensor-bead separation, which also implies the need for thin SU-8 layers. When SU-8 2002 is mixed in a 1:1 weight relation with cyclopentanone, the solvent for the 2000 series, a thickness of approximately 0.5 μm is obtained at a spinning speed of 2000 rpm. This reduces the fluorescence background signal considerably, and the spacing between sensor and beads is theoretically tolerable, see Fig. 4.5. Today, this solid content is available directly as the product SU-8 2000.5.

Processing of the SU-8 is simply following the instructions given by the supplier, though with minor modifications. An important condition for SU-8 to stick tightly to the surface is a dry and clean surface. The recommended procedure to ensure this is to dehydrate the wafer before coating at T = 250 °C for at least four hours. Usually the wafer is left in the oven over night and ready for coating the following morning. This procedure is not compatible with magnetic sensor technology. The magnetic properties of the film are destroyed at temperatures above T = 100-150 °C. Instead of using the 250 °C oven for sensor Batch 2, the dehydration is done at T = 100 °C for one hour in a vacuum chamber.

The SU-8 2000.5 yields a layer thickness of approximately 0.5 μm at a spinning speed of 2000 rpm. After coating a prebake is performed directly on the spinner using the following procedure:

1. The wafer is placed at a 5 mm distance above the spinner hotplate, which is set at T = 90 °C. Here it bakes for 30 s.
2. Then the wafer is moved to 2 mm distance, where it bakes for 30 s.
3. Then it is placed directly at the hotplate for 2 min.
4. The two preliminary steps are repeated backwards (2 and 1), and the wafer is transferred out of the spinner hotplate.

The stepped sequence is recommended by the supplier in order to avoid rapid heating of the SU-8 when baking out the solvent. Too rapid heating or cooling can result in cracks in the SU-8 layer. After baking, the wafer is exposed through a mask at the desired locations for cross linking, see Fig. 6.4 fifth step. The light is UV and the power continuously 9 mW cm^{-2} (setting: Cl2 on the KS-aligner), the exposure lasts 30 s. Cross linking is hereafter completed in a postbake step, which is identical to the prebake sequence just described, and the wafer is developed for 1 min in 1-methoxy-2-propyl acetate (PGMEA) and rinsed in isopropanol (IPA). The procedure is summarized in Table 7.1.

Dehydration	Coating	Pre-bake	Exposure	Post-bake	Development
1 h, 100 °C (vac.)	2000 rpm	1-4	30 s (Cl2)	1-4	1 min (PGMEA)

Table 7.1: SU-8 process for 0.5 μm.

7.1.2 Antibody binding to SU-8

This subsection describes how antibodies are bound to the SU-8 surface. The antibodies are biotinylated monoclonal influenza antibodies [38] provided by *Statens Serum Institut* (www.ssi.dk). Two detection systems are used, fluorescent magnetic beads coated with streptavidin, and Cy-3 conjugated streptavidin. The fluorescent signal is obtained by scanning the microscope slide in an Applied Precision Model ArrayWorx laser scanning system.

First the properties of the fluorescent magnetic beads are described, then the immobilization procedure, the results, and the fluorescent reference system is presented.

Beads

For the biotin-streptavidin reference system, two commercial bead products are used. The Sphero^{TM} beads are fluorescent as well as magnetic, whereas the Nanomag-D beads are only magnetic. The properties of the beads are summarized in Table 7.2. χ_m of the Sphero^{TM} beads has not been measured on the VSM, but their χ_m is small compared to the Nanomag-D beads.

Bead	Diameter	Surface	Fluorescence	χ_m
Sphero^{TM} Nile Red	360 nm	Streptavidin	0.2-0.39 μm	small
Nanomag-D	250 nm	Streptavidin	none	3.2(0.1) (SI)*

Table 7.2: Physical properties of magnetic beads (suppliers: www.spherotech.com and www.micromod.de). (*) χ_m for the Nanomag-D beads is measured on the VSM, see Chapter 4.

Procedure

Monoclonal antibodies are dissolved in PBS (phosphorous buffered saline) in concentrations $c = 0.5$, 1.0, 5.0, 10, 50, 100, 500, and 5000 μg ml^{-1}. Hereafter 0.5 μl of the various antibody concentrations are placed on the SU-8 surface using a micro pipette. The sample is left at $T = 37$ °C for one hour in a humid atmosphere. During this time period the antibodies adsorb on the SU-8 surface, where they are immobilized.

Washing in PBS removes the unbound antibodies, and blocking the rest of the surface is done in a solution of $c = 5$ mg ml^{-1} BSA (bovine serum albumin) in PBS with addition of 5 % fat free milk. Other blocking systems, such as BSA, rabbit serum, and bovine serum have been tested, but the most promising results in terms of minimizing unspecific binding are found for the BSA + milk system. Then the slide is washed 5 minutes in PBS and rinsed briefly in DI water.

Streptavidin coated fluorescent beads, Sphero^{TM} beads, are placed on the microscope slide and left for half an hour at room temperature. The beads bind to the antibodies on the SU-8 surface via the biotin-streptavidin bond.

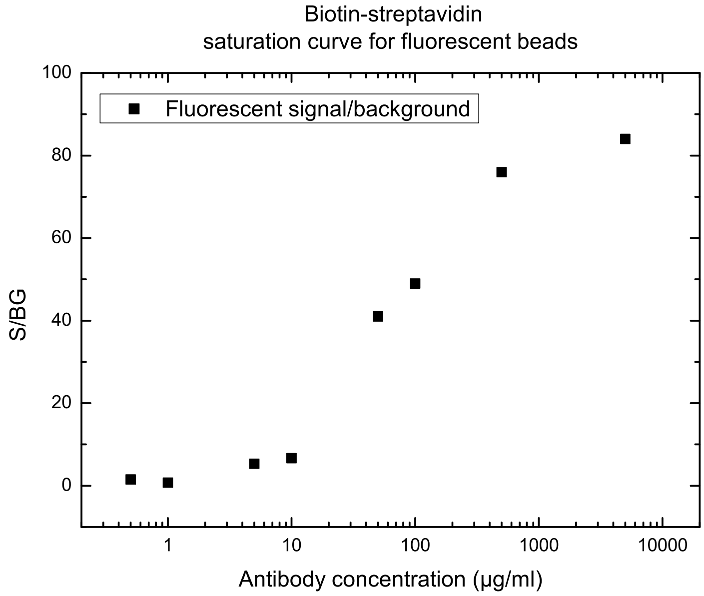

Figure 7.1: Saturation curve for the biotin-streptavidin system of Sphero$^{\mathrm{TM}}$ beads, fluorescent and magnetic. S: signal, BG: background. Approximate linearity of signal to concentration is found for protein concentrations between $c = 10$ μg ml^{-1} and $c = 1000$ μg ml^{-1}.

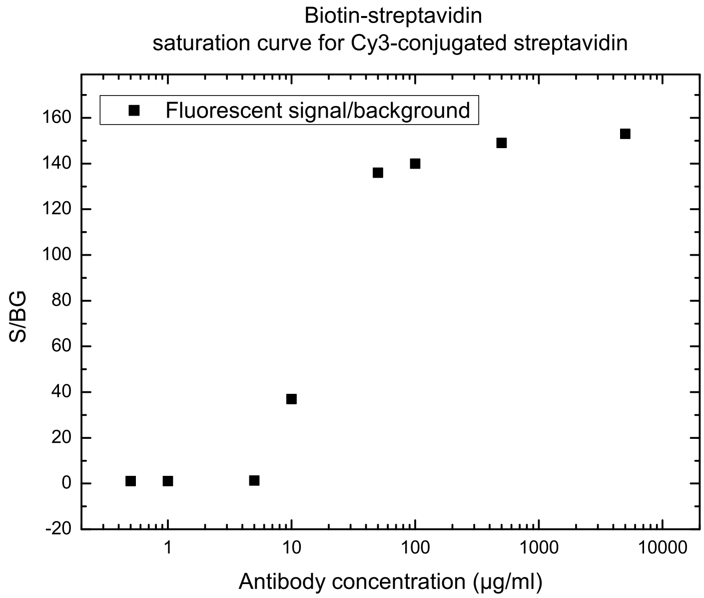

Figure 7.2: Saturation curve for the biotin-streptavidin system with Cy3-conjugated streptavidin. S: signal, BG: background.

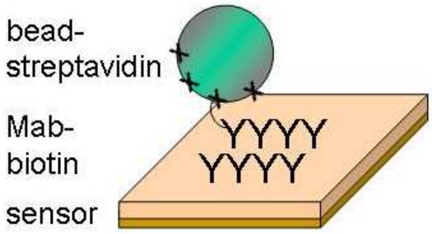

Figure 7.3: Procedure for measuring biotinylated monoclonal antibodies (Mab-biotin). The magnetic sensor measures the presence of the streptavidin coated magnetic bead, which is bound to the sensor by the biotinylated antibodies.

Results

The signal to background curve obtained by scanning the fluorescent signal from the beads is presented in Fig. 7.1. The signal, S, is measured as the average intensity of the fluorescent spots minus the background intensity, and BG is the average intensity of the background. It is clear that protein concentrations below $c = 10$ μg ml^{-1} are undetectable, and that for protein concentrations above $c = 1000$ μg ml^{-1} saturation is reached. Between these two antibody concentrations an approximately linear relation between signal and concentration is obtained.

Reference system

An identical experiment is performed using Cy3-conjugated streptavidin as detection system instead of streptavidin coated fluorescent beads (Fig. 7.2). For this system a protein concentration of $c = 5$ μg ml^{-1} is the lower detection limit, and saturation is reached at approximately $c = 100$ μg ml^{-1}. For most concentrations the signal-to-noise is approximately 50 % higher than that of the fluorescent bead detection system.

7.2 Antibody binding realized using the planar Hall sensor

This section describes the detection of monoclonal antibodies by the planar Hall sensor. First the chemical binding procedure is described, then how to obtain the resulting signal from the beads. Results are presented without and with subtraction of the reference.

7.2.1 Procedure

A drawing of the procedure for detection of monoclonal influenza antibodies using the planar Hall sensor is shown in Fig. 7.3. Below the procedure steps are described.

1. The signal from the sensor and a reference sensor is measured. A correlated drift is observed, which disappears when the reference signal is subtracted from the sensor signal. See Fig. 7.4 and Fig. 7.5.

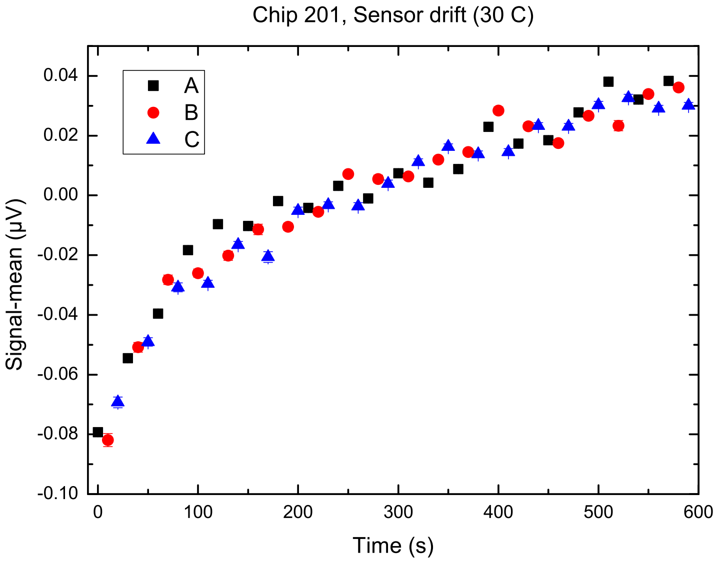

Figure 7.4: Initial signal from three sensors, V_{A}, V_{B}, V_{C}, as a function of time. Measured before processing and without beads. The mean value has been subtracted in order to visualize the drift, which on average is in the order of 0.2-0.5 % of the total signal. One measurement is the average of 100 points and lasts 10 s. Experimental conditions are $B = 0.5$ mT, $I_{\mathrm{AC}} = 1$ mA (K6221), $T = 30$ °C.

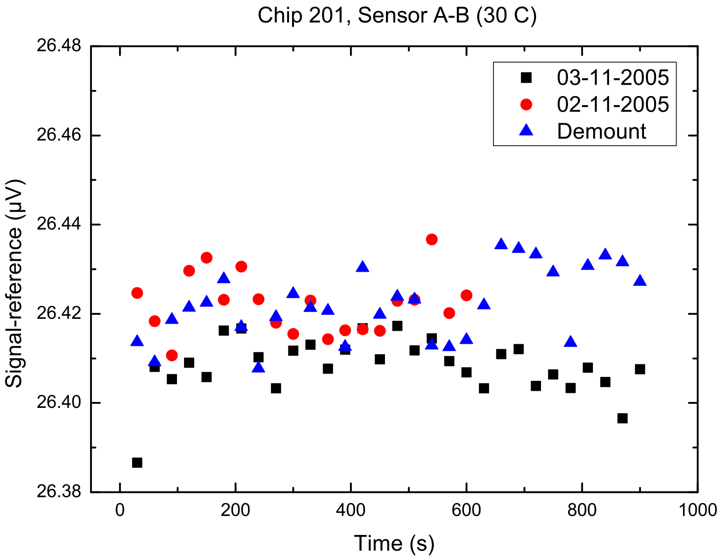

Figure 7.5: Signal from sensor A where the reference sensor B has been subtracted, $V_{\mathrm{A}} - V_{\mathrm{B}}$. Measured before processing and without beads. Time and demounting the sensor (take the chip out of the socket and put it back in) leave the response unchanged. Experimental conditions are $B = 0.5$ mT, $I_{\mathrm{AC}} = 1$ mA (K6221), $T = 30$ °C.

2. Monoclonal antibodies are immobilized on top of the sensors. The concentration is varied between $c = 0$ μg ml^{-1} and $c = 100$ μg ml^{-1} in PBS. The antibodies used are labelled with biotin. Procedure: 1 hour at $T = 37$ °C in a humid atmosphere.

3. The remaining SU-8 surface is blocked with BSA and milk. Blocking the surface with a protein solution ensures that the detector antibody cannot attach to the surface. It can only attach to the antigen, thus decreasing the background signal. Procedure: Half an hour at room temperature. Blocking solution: $c_{\mathrm{BSA}} = 5$ mg ml^{-1} in PBS + 5 % fat free milk.

4. Streptavidin coated magnetic beads are washed three times in PBS. A bead concentration of $c = 1$ mg ml^{-1} is used. The bead solution is placed on the chip for the streptavidin-biotin binding to take place. Half an hour at room temperature with "stirring" on a micro titer.

5. The unbound beads are washed off in PBS (5 min. + stirring), and the chip is left overnight to dry.

6. The signal from the sensor is measured, the reference signal is subtracted, and comparison with the previous signal gives the signal from the beads, $V_{\mathrm{beads}} = V_{\mathrm{after}} - V_{\mathrm{before}}$.

Procedure details

Before measuring care must be taken not to damage the chip during chemical processing. The wire bonds are very fragile and can be damaged by chemicals, rough or careless handling, air flow from the nitrogen valve, or by electrical pulses in the system. To provide protection against handling, the wire bonds are covered in silicon gel (Elastosil E 41, Wacker, Germany). This protects the chip against most physical and chemical handling. However, electrical pulses must be avoided in order not to blast the wire bonds or the leads on the chip.

Another issue is that no beads must come into contact with the reference sensor. Only a few beads can be detected by the sensor and in the case where the reference is contaminated a false baseline would be subtracted. Contamination is avoided using a fat barrier on top of the reference sensor that repels liquids and thus solutions with beads.

One measurement is the average of the sensor signal from 100 observations. The duration of 100 samples is approximately 10 s. Then the switch box switches to the next sensor and the measurement of another 100 samples is performed. The measurement sequence is sensor A, sensor B, sensor C, and then back to sensor A, and the sequence is run a prespecified number of times. The time delay between the actual biochemistry sensor and the reference sensor is thus 10 s plus the switching time, which is 100 ms. This means that subtracting the reference is not done simultaneously as in differential measurements.

This is the reason for controlling the temperature of the experiment. After stabilization, the temperature variations are small compared to the electrical noise, and the reference can be used to correct for an eventual change in off-set from demounting and remounting the sample. That the procedure is accurate can be seen from the investigations presented in Appendix B.

When the signal without beads has been measured, the biotinylated monoclonal antibodies are immobilized on top of sensor A. Sensor B has a fat barrier on top, and sensor C is left without antibodies to measure the background signal from unspecifically bound beads. The immobilization procedure is described above for the fluorescence detection measurements along with blocking of the residual SU-8 surface.

After immobilization of antibodies, the chip surface is carefully dried in a nitrogen flow. The surface should be more or less dry for the bead solution to stay where it is placed on top of the chip. 1-2 μl of streptavidin coated beads are placed on top of sensor A and sensor C, where they are left for half an hour to react with the biotin on the surface. Stirring of the chip during the reaction ensures that beads come into contact with the biotinylated antibodies and minimizes gravitational settlement at undesired places.

After the biotin-streptavidin bond is formed the chip is washed in order to remove unspecifically bound beads. It is however impossible to remove all beads. They have a tendency to get stuck everywhere on the chip. Despite all efforts of removing them with a magnet or putting soap in the buffer there still remain beads where they are not supposed to be. The signal from zero antibody concentration corresponds to the background signal from the unspecifically bound beads.

Water on the chip will have an effect on the temperature of the chip. Therefore it is essential that the chip is completely dry before measuring the signal from the beads. The chip is dried with a nitrogen flow and left overnight, which ensures a completely dry chip. After remounting in the socket the chip is left for an hour with applied current and temperature control before starting a measurement. This way the temperature of the chip as well as the electrical offset will be stable during the measurement.

With beads on top of the sensor, the signal stabilizes slowly after the applied field is switched from $B = +0.5$ mT to $B = -0.5$ mT, see Fig. 7.6. Hence after switching the field, the signal stabilizes for 10 s before performing the electrical measurement.

This observation is not due to the lock-in amplifier or the switch box. It only happens when the applied field is changed, not when the switch box changes back to the sensor. Additionally, everything is left for an hour to stabilize, which has also been verified experimentally to be sufficient for stabilization (data not shown). The only thing that is changed is the applied magnetic field, hence it must be a reaction to a changed magnetic field. The speculation is, that what is seen is due to domain effects in the permalloy film, but no proof for that has been found.

7.2.2 Results

The measured signals are normalized to the sensor sensitivity, applied current and the applied flux density, B (measured in mT), as shown in Eq. (7.1). This yields a number, β, which is independent on sensor specific parameters, and only depends on the field sensed

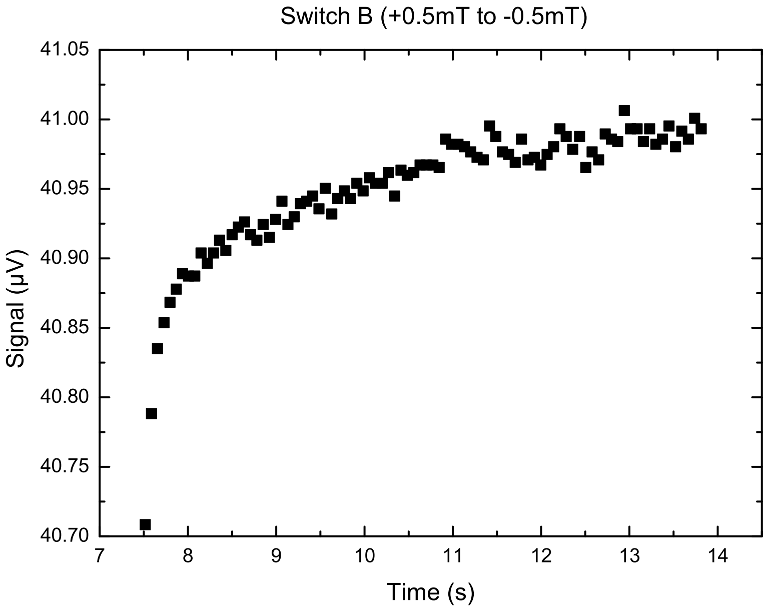

Figure 7.6: Stabilization time for a planar Hall sensor with beads. The applied field is switched from $B = +0.5$ mT to $B = -0.5$ mT at time = 7.0 s.

by the sensor.

$$\beta = \frac{\text{signal}}{\text{sensitivity} \cdot \text{sense current} \cdot B(\text{mT})} \tag{7.1}$$

Taking the mean of the values at $B = +0.5$ mT and $B = -0.5$ mT subtracts the offset.

$$\Delta\beta = \frac{1}{2}\beta(+0.5 \text{ mT}) + \frac{1}{2}\beta(-0.5 \text{ mT}) \tag{7.2}$$

The reference, sensor B, is then subtracted from the sample, *e.g.* sensor A.

$$\Delta\beta_{\text{A}} - \Delta\beta_{\text{B}} \tag{7.3}$$

The reference does not change when beads are added on top of sensor A, and thus Eq. (7.4) gives the signal from the beads normalized to $B = 1$ mT applied flux density.

$$\Delta\beta_{\text{beads}} = (\Delta\beta_{\text{A}} - \Delta\beta_{\text{B}})_{\text{after}} - (\Delta\beta_{\text{A}} - \Delta\beta_{\text{B}})_{\text{before}} = \Delta\beta_{\text{after}} - \Delta\beta_{\text{before}} \tag{7.4}$$

For a detailed description of data acquisition and analysis, see Appendix B. In the measurements, the normalization is to $B = \pm 0.5$ mT, but taking the mean value corresponds to a magnetic flux span of 1 mT. Hence, the normalization will be referred to as $B = 1$ mT.

Without reference

The first measurements of antibody detection are performed without subtracting the reference sensor, and the results are shown in Fig. 7.7. A single measurement point seems not to follow the trend of increasing signal for increasing antibody concentration. However, visual inspection of this sensor in the microscope shows that only a few beads are present on top of the sensor. Not enough beads have come into contact with the sample or the chemical reaction is not sufficient in this case.

Table 7.3 compares the data points of Fig. 7.7 to the fluorescent measurements of Fig. 7.1 and Fig. 7.2. The signal-to-noise, S/N, is calculated as the signal from the Nanomag-D beads divided by the error related to the measurement. Compared with fluorescent signal divided by background, S/BG, the magnetic signal is much lower for the highest antibody concentration. However, for low antibody concentrations the magnetic signal is more promising than the fluorescent signal.

With reference, experiment 1

Detection of monoclonal antibodies with a reference sensor subtracted is shown in Fig. 7.8.

The figure shows the signal from the beads as a function of antibody concentration. The value $\Delta\beta_{\text{beads}} = \Delta\beta_{\text{after}} - \Delta\beta_{\text{before}}$ reflects the magnetic flux produced by the beads at the sensor surface in an applied magnetic flux density of $B = 1$ mT, and the highest value is $\Delta\beta_{\text{beads}} = 0.011$.

Two observations are extracted from the figure. First, the signal rises with increasing antibody concentration. Second, a rather large signal arises from zero concentration. This is a problem because it reduces the sensitivity of the bead assay.

Fig. 7.9 shows pictures taken after the immobilization of streptavidin coated beads. Left: antibody concentration $c = 50$ μg ml^{-1}. Right: antibody concentration $c = 5$ μg ml^{-1}. The bead coverage is larger in Fig. 7.9 (left) than in (right) as expected since the antibody concentration in higher.

The pictures show that more beads are bound at sites outside the SU-8 pad covering the sensor than on the SU-8 pad itself. This is unfortunate since the aim is to have antibodies only on top of the sensor. There is a residual monolayer of SU-8 left after development, and it seems just as good as the thicker layer when it comes to binding antibodies.

With reference, experiment 2

Repeating the measurements yields the response shown in Fig. 7.10. Again an increasing signal as a function of increasing antibody concentration is obtained. The slope of the curve is similar to the slope in Fig. 7.8 but the signal obtained from the zero concentration point has decreased. This is fortunate because the sensitivity depends on the magnitude of unspecific binding.

Pictures of the sensors with different antibody concentrations are presented in Fig. 7.11. The respective antibody concentrations are: top left: $c = 100$ μg ml^{-1}, top right: $c = 50$ μg ml^{-1}, bottom left: $c = 10$ μg ml^{-1}, bottom right: $c = 0$ μg ml^{-1}. The bead coverage

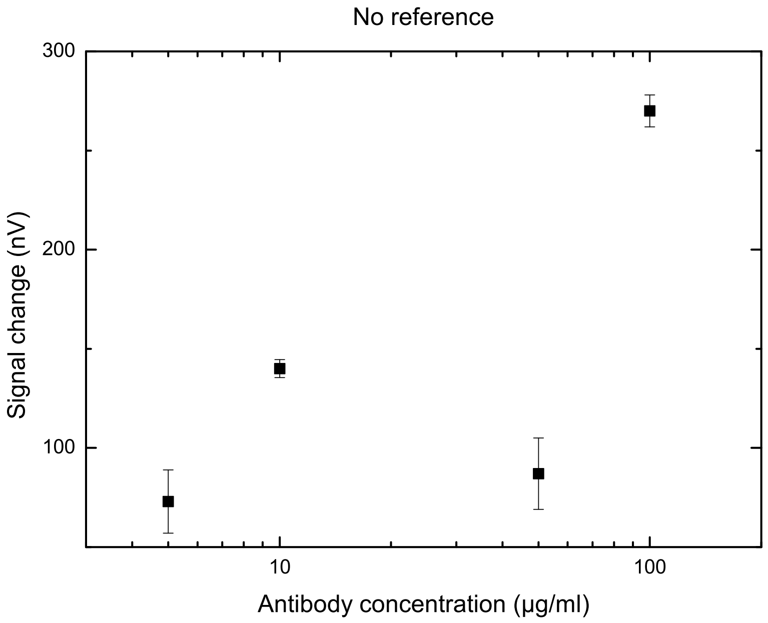

Figure 7.7: Detection of monoclonal antibodies using the planar Hall sensor. These measurements are performed without subtracting the reference sensor from the sensor with antibodies.

Antibody concentration	5 μg ml^{-1}	10 μg ml^{-1}	50 μg ml^{-1}	100 μg ml^{-1}
S/N Magnetic beads	4.5	31	5	34
S/BG Cy3-streptavidin	1.3	37	136	140
S/BG Fluorescent beads	5.3	6.7	41	49

Table 7.3: Comparison between magnetic and fluorescent detection systems. The magnetic beads are Nanomag-D beads, 250 nm in diameter. The signal is obtained without reference subtraction, data from Fig. 7.7. S/N is the signal from the beads divided by the statistical error, S/BG is the fluorescent signal intensity minus the background divided by the background intensity.

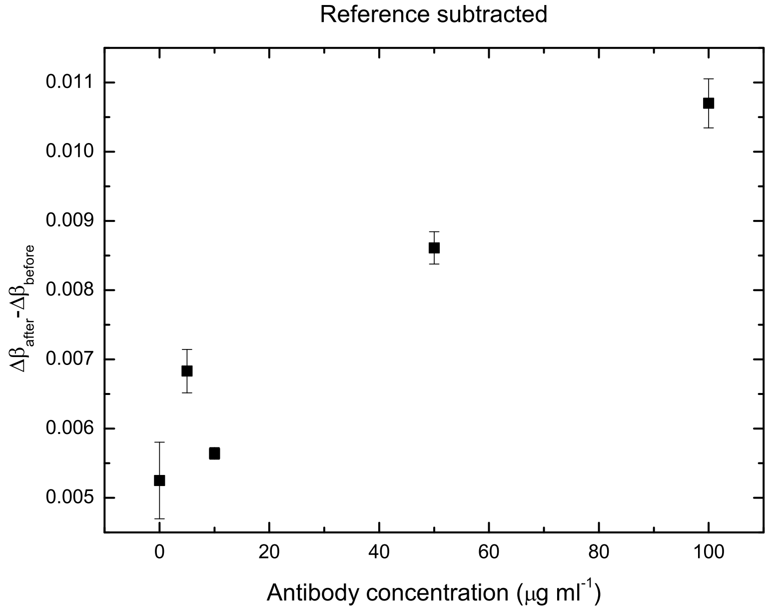

Figure 7.8: Detection of monoclonal antibodies realized using the planar Hall sensor. The signal from the beads, $\Delta\beta_{\mathrm{beads}} = \Delta\beta_{\mathrm{after}} - \Delta\beta_{\mathrm{before}}$, is normalized to the applied field. For details on data acquisition and analysis see Appendix B.

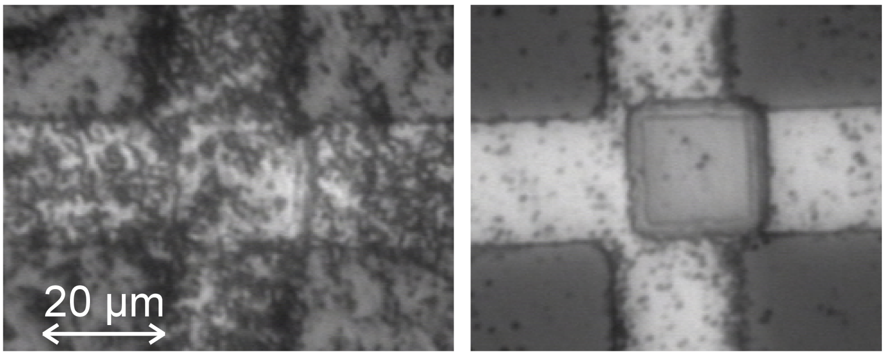

Figure 7.9: Pictures of the bead coverage for antibody concentrations of $c = 50$ μg ml^{-1}(left) and $c = 5$ μg ml^{-1}(right). These correspond to the respective electrical measurements of Fig. 7.8.

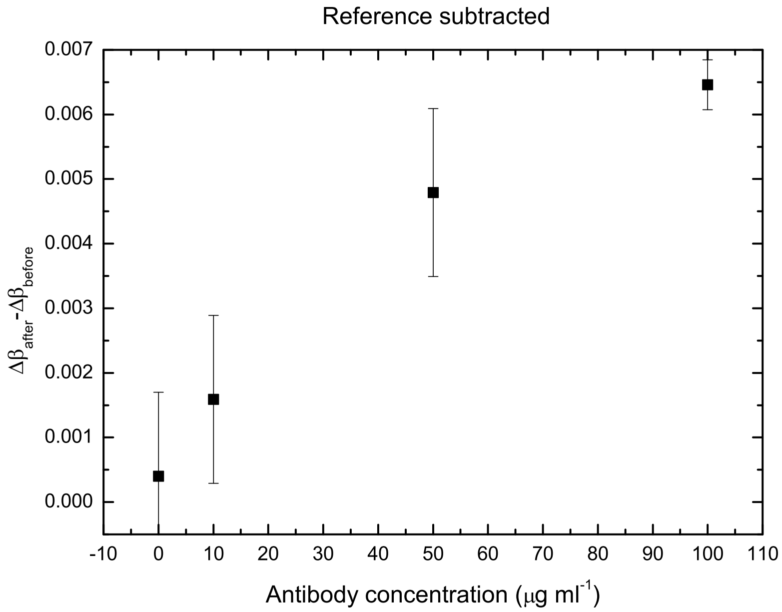

Figure 7.10: Detection of monoclonal antibodies realized using the planar Hall sensor. The signal from the beads, $\Delta\beta_{\text{beads}} = \Delta\beta_{\text{after}} - \Delta\beta_{\text{before}}$, is normalized to the applied field. For details on data acquisition and analysis see Appendix B.

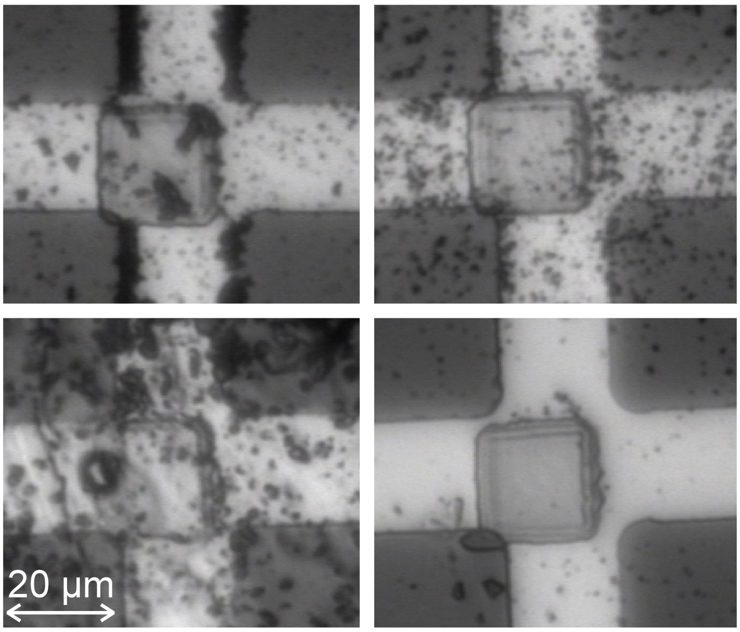

Figure 7.11: Pictures of the bead coverage corresponding to different antibody concentrations. Decreasing antibody concentration from left to right. Top left: $c = 100$ μg ml^{-1}, top right: $c = 50$ μg ml^{-1}, bottom left: $c = 10$ μg ml^{-1}, bottom right: $c = 0$ μg ml^{-1}.

Experiment 1	c_{mab} (μg ml^{-1})	ξ_{outside}	ξ_{sensor}	β_ξ	$\Delta\beta_{\text{beads}}$ (Fig. 7.8)
Fig. 7.9 (left)	50	0.75	0.50	0.008	0.0086
Fig. 7.9 (right)	5	0.25	0.10	0.004	0.0068

Table 7.4: Estimates of layer coverage, ξ, obtained from the pictures of the sensors with beads, Fig. 7.9. The corresponding estimates of the field produced, β_ξ (normalized to the applied field), are calculated using Eq. (4.33). The $\Delta\beta_{\text{beads}}$ values are obtained experimentally, Fig. 7.8.

decreases with decreasing antibody concentration. Though the picture in the bottom left corner at a first glimpse shows a higher bead concentration than its predecessor, dirt is obstructing the view of the beads, and the true coverage is probably less than observed in the picture.

7.3 Discussion

The positive signal in Fig. 7.8 and Fig. 7.10 has been addressed in Chapter 4, Eq. (4.33).

$$\beta = 0.0257 \cdot \xi_{\text{outside}} - 0.0225 \cdot \xi_{\text{sensor}}$$

where ξ is the bead coverage with respect to a closely packed monolayer. The equation assumes non-interacting beads. If rough estimates on the bead coverage are obtained by visual inspection of Fig. 7.9, the field produced by the respective layer coverage can be estimated using Eq. (4.33). The resulting estimates are presented in Table 7.4 along with the experimentally determined $\Delta\beta_{\text{beads}}$-values from Fig. 7.8. The estimates compare reasonably well with the data, at least the order of magnitude is in place.

The maximum value obtained in the experiments is $\beta = 0.011$. This corresponds roughly to an estimated difference in layer coverage of one half for the approximation to Eq. (4.33), $\beta \approx 0.024(\xi_{\text{outside}} - \xi_{\text{sensor}})$. It is fair to assume that the layer coverage is less than one. A closely packed coverage of beads cannot be expected due to steric hindrance when the streptavidin on the beads reacts with the biotin on the surface. It is also fair to assume that the layer coverage on top of the sensor is less than outside. The beads have to jump a step of 0.5 μm, twice their diameter, to bind to the biotin immobilized here.

The zero points in the figures reflect the unspecific binding in the system. The unspecific binding is considerably reduced in Fig. 7.10 compared to Fig. 7.8. The reason for the decrease in unspecific binding is probably a slight change in the washing procedure. The tweezers holding the chip in the PBS buffer are tapped gently on the rim of the glass. The mechanical kick might have loosened the unspecifically bound beads. Another explanation could be that the streptavidin is older and thus binds less tightly to biotin and perhaps other proteins. Reducing the unspecific binding will be an issue of great importance in future work with this assay.

A general observation extracted from Fig. 7.8 and Fig. 7.10 is that the signal increases for increasing antibody concentration. This is exactly the observation which is desired from this study. The more beads attached to the surface, the higher the signal from the beads. This finding indicates that a negative control in an immunoassay will produce lower signal than the sample assuming that the sample binds more beads than the negative control.

The images, Fig. 7.9 and Fig. 7.11, show where the beads are attached after incubation. There is a general tendency of catching some beads at the edges of the SU-8 pad. There is however a more striking tendency of bead capture at the edges of the voltage leads. These leads are made of the same material as the sensor, *i.e.* the pinned ferromagnetic stack shown in Fig. 6.3. The easy axis is horizontal with respect to the photos and thus the only place where the fringing field has a gradient is at the edges of the voltage leads, vertically in the photos. These arguments suggest, it is likely that the fringing field from the sensor captures the beads. A recent study by Ferreira *et al.* [39] shows that the magnetostatic fields created by the combined pinning and free layers in spin-valve sensors contribute significantly to the magnetization of beads. In zero applied field Ferreira gets field values comparable to the applied otherwise field ($H = 1200$ A m^{-1}). Therefore the magnetostatic fields from planar Hall sensors should also be sufficient to attract beads, since the pinning layer is the same and the sensing layer is twice as thick as the spin-valve sensor's free layer.

The fringing fields are not significant in magnetizing the beads detected by the planar Hall sensor. The beads feeling this fringing field are situated at places, F_1 and F_2, where they are not detected by the planar Hall sensor. Beads inside the areas F_1 and F_2 give small contributions to the over-all average field, see Chapter 4. The effect of capturing beads at the voltage leads should be avoided, nevertheless, due to loss of biologically active material. Maybe shielding by the SU-8 layer could be used for this purpose.

Finally, the field produced by the AC current through the sensor should be considered in the theoretical analysis. When calculating the magnitude of this contribution with respect to magnetizing the beads, one gets that it averages to zero. Thus only the applied field needs to be considered in the theoretical analysis, as is indeed the case of Eq. (4.33).

7.4 Conclusion

This chapter has provided a procedure for immobilizing antibodies on an SU-8 surface. The procedure is very simple and involves only PBS solutions, which are non-toxic and cheap.

Detection of monoclonal antibodies has been realized using the planar Hall sensors, Batch 2. Increasing antibody concentrations result in increasing sensor signals. The signal is positive because more beads are bound outside the sensor than on top of the sensor.

It can be concluded that the chosen SU-8 design is unfortunate since the signal depends on the difference in layer coverage between outside and on top of the sensor. However, the aim of the SU-8 design has been to avoid the positive signal from beads attached outside the sensor area, and the design is thus justified. That the antibodies bind equally well to the residual SU-8 layer left after development has been realized too late in the process to take into account in the SU-8 design.

Another SU-8 design, where the positive contributions from beads outside the sensor area are shielded by a thicker layer, would be optimal in this case. A closely packed monolayer of beads would thus give a normalized signal of $\beta \approx -0.021$, see Chapter 4. Another benefit would be the possibility of avoiding bead capture by the fringing fields from the voltage leads.

Chapter 8

Influenza

In Denmark an influenza epidemic strikes 5-7 times on 10 years, during which 10-30 % of the population is infected with the influenza virus and develops the disease. It is estimated by *Statens Serum Institut* (SSI, www.ssi.dk) that influenza causes approximately 1000 deaths per year. Especially elderly or weak people are subjected to increased death rates.

Influenza can be treated with antiviral drugs, but the treatment must be given to the patient within 48 hours after infection to have an effect. The earlier the treatment is given the better result of alleviating the symptoms and reducing the duration of the illness. For this reason quick diagnostics is important.

Influenza exists in a large genetic variety, and to complicate things further many other diseases resemble influenza in their symptoms. Hence a diagnostic test is necessary in order to prescribe adequate drugs. Besides enabling the prescription of the drug, a reliable diagnostic test will also enable clinical testing of the antiviral drug against influenza. *I.e.* whether the cure is effective or not, and how effective is it.

Furthermore, in case of a pandemic, a quick diagnostic test would be very helpful to map the spread of the disease and to isolate infected individuals. A similar test would also be a great help for diagnosing avian flu in deceased birds.

Existing diagnostic tests for influenza are PCR and a number of quick tests based on immunochemistry. In contrast to the immunochemistry based tests, the PCR technique is reliable, but the sample must be treated carefully to avoid contamination. A contaminated sample would give a false result. Furthermore, the PCR equipment is expensive and requires skilled personnel for operation. Hence the transport of a sample to, *e.g.*, SSI as well as the reporting back after processing is time consuming. There is clearly need for a quick and reliable diagnostic test.

The existing quick influenza tests, based on immunochemistry, are unreliable due to the following reasons:

1. Low concentration of vira in the sample.
2. Aggressive enzymes in the sample, which can break down the antibodies on the chip.

2 is often solved by diluting the sample, but this of course increases the problem of 1. Introduction of magnetic beads offers possible solutions to both problems.

Magnetic beads and magnetic immunoassay

In a future application, the antigen can be captured from the sample with magnetic beads and the rest of the components can subsequently be washed away. This approach will solve the problems of 1 and 2 in one step. Afterwards, the presence of the antigen is measured in a magnetic immunoassay, where instead of eluding the antigen into clean buffer, the carrier magnetic bead is detected.

The long-term aim of the magnetic immunoassay is to combine the advantages of immunochemistry with those of magnetic detection:

1. Magnetic capturing. This step increases the antigen or virus concentration and dilutes unwanted molecules in the sample simultaneously.
2. Magnetic detection. The carrier magnetic bead is detected directly after virus capture. The planar Hall sensors are very sensitive, it is theoretically possible to distinguish a single bead. Hence very low virus or antigen concentrations can potentially be detected.
3. Unspecifically bound beads can potentially be removed with magnetic forces. This eliminates washing after sample incubation.

Chapter outline

This chapter demonstrates the magnetic immunoassay performed with two Batch 2 chips, each consisting of three planar Hall sensors. Development of the influenza-chip introduces the medical treatment for influenza but the principle is general and can be expanded to include numerous diseases as well as genetics, mutations, genetical diseases, etc. Monoclonal antibodies [38] are supplied by SSI.

8.1 Immunochemistry

The basic principle of immunochemistry is an indirect detection of an antigen by reaction with a specific antibody. Specific antibody proteins, called capture antibodies, are immobilized on a predefined spot on the surface of a chip. The antigen and antibody fit like a key in a lock, and the sample molecules bind specifically to the capture antibodies. Afterwards, labelled detector antibodies, which in most existing immunoassays are labelled with enzymes or fluorescent molecules, bind specifically to the sample antigen. Optical detection of the fluorescence molecule reveals the presence of the detector antibody, and the specific location reveals the identity of the antigen in case of a sample of multiple investigated molecules.

Antibodies are generally known from the immune system, where they play an important role in fighting intruding diseases. The Human IgG molecule, Fig. 8.1, is an example of such an antibody. IgG's immobilized on the surface have similar appearance and are usually drawn like a Y, where the antigen is attached to one of the "arms".

Fig. 8.2 shows a typical sandwich assay experiments. The capture antibody is immobilized on a solid support, antigen is added and binds to one of the binding sites. Then the

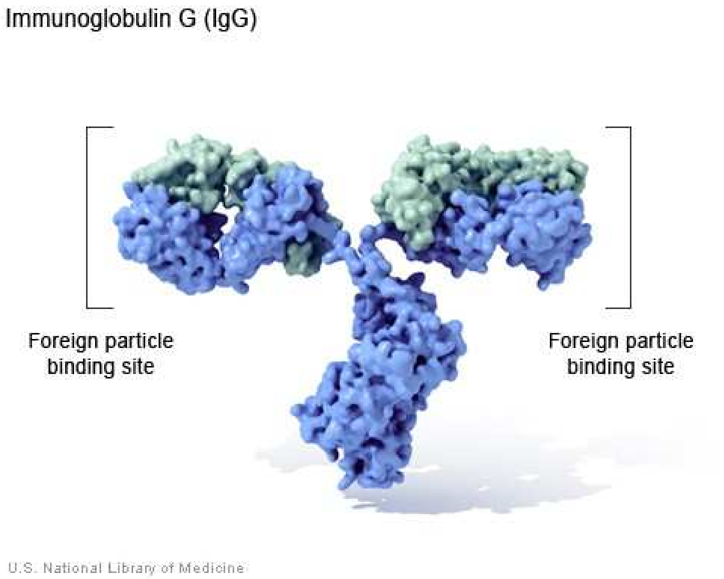

Figure 8.1: Human IgG molecule. This image shows the functional version of the antibody in human blood, where the binding sites capture foreign intruder molecules. The image is produced by the US National Library of Medicine (http://www.nlm.nih.gov).

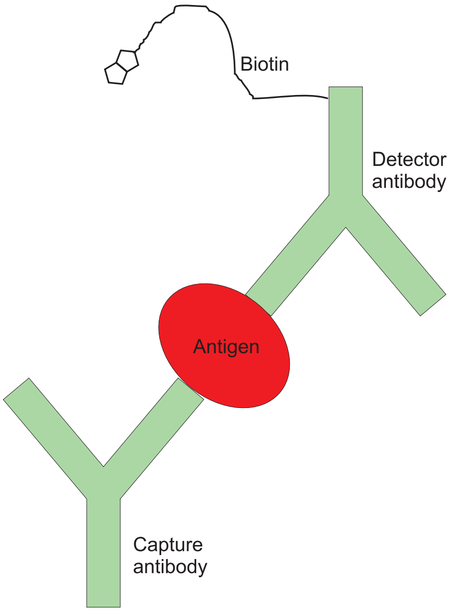

Figure 8.2: Immunochemistry. The capture antibody is immobilized on the surface. Then the antigen is attached to the immobilized antibody and reaction with the detector antibody can take place. In this assay sketch the detector antibody is labelled with biotin, which binds tightly and specifically to streptavidin. Detection is thus made with fluorescence labelled streptavidin or streptavidin coated magnetic beads.

detector antibody binds to the antigen. In this sketch the detector antibody is labelled with biotin, which can be visualized by fluorescent streptavidin.

In a magnetic immunoassay, the fluorescence label is exchanged with a magnetic bead, and the presence of the antigen detected via the presence of the bead. This gives the possibility of an electronic readout realized by the planar Hall sensor.

In the magnetic sandwich assay presented in this chapter, the detector antibodies are immobilized directly on the surface of the magnetic beads. This way the extra biotin-streptavidin binding step is bypassed.

8.2 Fluorescent influenza immunoassay

This section presents the procedure and the results obtained for the fluorescent influenza sandwich immunoassay. First the tests on various blocking systems are summarized, based on which BSA and milk is chosen. Then the assay procedure is described, and finally the results are presented.

Blockers

A blocker is a solution of proteins that attach readily to the surface. These proteins are adsorbed at spaces where no antibodies are attached and occupy the space such that the detector antibodies cannot attach to the surface. Thus the signal from the negative control is decreased, and preferably identical to the background.

The different blocking systems that have been tested are:

1. BSA, $c_{\mathrm{BSA}} = 5$ mg ml^{-1} in PBS.
2. BSA + milk, $c_{\mathrm{BSA}} = 5$ mg ml^{-1} in PBS + 5 % fat free milk.
3. Rabbit serum, diluted 10 times.
4. Bovine serum, diluted 10 times.

For the fluorescent biotinylated antibody-streptavidin system (Chapter 7), BSA (1) is insufficient to block the entire SU-8 surface. High background signals are observed. The addition of fat free milk powder (2) decreases the background. The lowest background is obtained with diluted rabbit serum (3). Thus rabbit serum has been used as blocking system for a while. Bovine serum (4) has not been tested for this system.

When introducing the influenza sample to the detection system, the signal obtained with the rabbit serum (3) as blocker vanishes. Therefore all blockers are tested with the influenza system. The concluding results are: Rabbit and bovine serum (3 and 4) erase all traces of influenza. BSA alone (1) is insufficient as blocking system, but BSA and milk (2) works well enough to get a significant signal from the influenza sample compared to the negative control.

Thus BSA and milk (2) is chosen as blocking system for both the biotin-streptavidin system and the influenza assay.

8.2.1 Procedure

Fig. 8.2 is a schematic drawing of the sandwich immunoassay. As detection system Cy5 labelled monoclonal antibodies are used. Biotinylated monoclonal antibodies are avoided since high unspecific binding is observed when using biotin-streptavidin as detection system. The influenza antibodies and antigens are provided by *Statens Serum Institut* (SSI).

1. Monoclonal antibodies are immobilized on the SU-8 surface. Concentrations used are $c_{\mathrm{mab}} = 0.1$ mg ml^{-1}, $c_{\mathrm{mab}} = 0.5$ mg ml^{-1}, and $c_{\mathrm{mab}} = 5$ mg ml^{-1} in PBS. The positive control is $c_{\mathrm{mab}*} = 0.1$ mg ml^{-1} Cy5 labelled monoclonal antibodies, and the negative control is $c_{\mathrm{mab}} = 5$ mg ml^{-1} unmarked antibodies. A fat barrier separates the controls from the samples. Procedure: 1 hour at $T = 37$ °C in a humid atmosphere.

2. The surface is blocked with BSA and milk. Blocking solution: $c_{\mathrm{BSA}} = 5$ mg ml^{-1} in PBS + 5 % fat free milk. Procedure: half an hour at room temperature.

3. Antigens are allowed to react with the antibodies overnight at $T = 4$ °C. Then additional antigens are placed on the sample spots and the slide is left 1 hour at $T = 37$ °C. The concentration is approximately $c = 10^6$ vira ml^{-1}. Procedure: >10 hours at $T = 4$ °C + 1 hour at $T = 37$ °C in a humid atmosphere.

4. The microscope slide is washed in BSA. $c_{\mathrm{BSA}} = 5$ mg ml^{-1} in PBS. Procedure: 1/2 hour at room temperature.

5. Cy5 labelled monoclonal antibodies with a concentration of $c_{\mathrm{mab}*} = 5$ mg ml^{-1} in PBS are added on the total slide area including both sample spots and control spots. Procedure: 1 hour at $T = 37$ °C in a humid atmosphere.

6. Finally the slide is washed in PBS (procedure: 5 minutes in a beaker with manual stirring) and rinsed with DI water (removes the salt). After drying in a nitrogen flow, it is ready for scanning.

8.2.2 Results

The scanning results are shown in Fig. 8.3. The positive controls are clearly visible due to the success of direct Cy5 labelling of antibodies. The negative controls are not visible, and the intensity of their fluorescence signal equals the background. This proves that antibody-antibody binding does not occur. The signal from the sample spots is approximately five times the signal from the negative control for the highest concentrations of capture antibodies.

Capture antibody concentration	0.1 mg ml^{-1}	0.5 mg ml^{-1}	5 mg ml^{-1}
Signal sample/negative control	1.6	4.8	5.3
Positive control/negative control	> 100	> 100	> 100
Negative control/background	≈ 1	≈ 1	≈ 1

Figure 8.3: Scanning results of the influenza immunoassay. The microscope slide is viewed from above, the slide is 2.5 cm wide (top to bottom in the image). The left column consists of four clearly visible positive controls. To their immediate right are the negative controls, which are not visible. A fat barrier separates the controls from the samples. The three columns of sample spots are barely visible. The concentrations of capture antibodies for the sample are from left to right: $c_{\text{mab}} = 5$ mg ml^{-1}, $c_{\text{mab}} = 0.5$ mg ml^{-1}, and $c_{\text{mab}} = 0.1$ mg ml^{-1} with the concentration from top to bottom unchanged.

8.2.3 Discussion

The signal compared with the negative control is on average 5 for the two highest capture antibody concentrations. This is a low signal. The virus concentration used is high ($c = 10^6$ vira ml^{-1}). Ideally speaking, detection of a concentration of $c = 10^3$ vira ml^{-1} would be desirable for clinical trials.

It will not be possible to detect $c = 10^3$ vira ml^{-1} using fluorescence scanning, since the 1000 times lower signal would not be seen in the scanning results. The system is optimized on SU-8, and signal enhancement is unlikely. Thus it can be concluded that the fluorescence detection system will probably fail in influenza diagnostic tests.

8.3 Magnetic influenza immunoassay

This section provides the procedure for the magnetic sandwich immunoassay including antibody adsorption onto beads and preparation of the planar Hall chip. Successful detection is presented in Table 8.1, Fig. 8.4, and Fig. 8.5.

8.3.1 Procedure: antibody adsorption to beads

Antibodies can be adsorbed onto polystyrene readily and permanently [40]. The following procedure has been developed for adsorption of proteins onto polystyrene beads by Bangs Laboratories, Inc. [40], and modified using the experiences from SSI.

1. Washing procedure. 50 μl of plain Nanomag-D beads (original concentration $c = 25$ mg ml^{-1}) are suspended in 500 μl of PBS. The beads are captured with a magnet

and re-suspended in 500 μl fresh PBS three times. The bead concentration is now: $c = 2.5$ mg ml^{-1}.

2. Mix monoclonal antibodies, $c_{\text{mab}} = 5$ mg ml^{-1}, and Nanomag-D beads $c_{\text{beads}} = 2.5$ mg ml^{-1}. Solution: 25 μl beads + 20 μl antibodies + 55 μl PBS.
3. Place the vial at $T = 37$ °C for 3 hours. Procedure: shake every 5 minutes during the first 20 minutes. Shake occasionally (every 20 or 30 minutes) for the remaining time.
4. Wash three times in 100 μl PBS.
5. Use the beads immediately after preparation. Long term storage in PBS should be avoided due to eventual degradation of the antibodies.

8.3.2 Procedure: planar Hall chip

1. The signals from the three sensors, A, B, C, are measured. The drift is subtracted from the sample sensor by use of a reference sensor as described in Chapter 7, see Appendix B for details on data acquisition and analysis.
2. Monoclonal antibodies are immobilized on the SU-8 on top of the planar Hall sensors for the sample and for the negative control. Sensor A is the sample, sensor B the reference, and sensor C is the negative control. The antibody concentration used is Assay 1: $c_{\text{mab}} = 5$ mg ml^{-1} in PBS, and Assay 2: $c_{\text{mab}} = 0.5$ mg ml^{-1} in PBS. A fat barrier is placed on top of sensor B to avoid contamination of the reference sensor. Procedure: 1 hour at $T = 37$ °C in a humid atmosphere.
3. The remaining surface is blocked with BSA and milk. Blocking solution: $c_{\text{BSA}} = 5$ mg ml^{-1} in PBS + 5 % fat free milk. Procedure: half an hour at room temperature.
4. Antigens are placed on sensor A and allowed to react with the surface antibodies. $c_{\text{virus}} \approx 10^6$ ml^{-1}. Procedure: 1 hour at $T = 37$ °C in a humid atmosphere.
5. The chip is washed in BSA. Blocking solution: $c_{\text{BSA}} = 5$ mg ml^{-1} in PBS. Procedure: half an hour at room temperature.
6. Magnetic beads with monoclonal antibodies are added to sensor A and sensor C. Procedure: 1 hour at $T = 37$ °C.
7. Finally the chip is washed 5 minutes in PBS and left overnight in order to be completely dry before proceeding with the electrical measurements.
8. The signals from the three sensors are measured, and the reference signal is subtracted from the sample and the negative control. Comparison with the previous signal gives the signal from the beads, $\Delta\beta_{\text{beads}} = \Delta\beta_{\text{after}} - \Delta\beta_{\text{before}}$.

Assay	c_{cab} (mg ml^{-1})	$\Delta\beta_{\text{sample}}$ ($\times 10^{-3}$)	$\Delta\beta_{\text{negative control}}$ ($\times 10^{-3}$)	S/NC
1	5	4.7(0.5)	3.0(0.4)	1.6
2	0.5	5.9(0.3)	2.4(0.9)	2.5

Table 8.1: Magnetic immunoassay results. c_{cab} is the concentration of capture antibodies, $\Delta\beta$ the measured signal from the beads (normalized to the applied field), and the numbers in parentheses are the experimental uncertainties. S/NC is calculated as the signal from the assay divided by the signal from the negative control.

8.3.3 Results

Two experiments are performed with the influenza assay, and the results are presented in Table 8.1. Assay 1 is constructed with a capture antibody concentration of $c_{\text{mab}} = 5$ mg ml^{-1}, and Assay 2 with a capture antibody concentration of $c_{\text{mab}} = 0.5$ mg ml^{-1}.

Fig. 8.4 and Fig. 8.5 compare the results from the influenza assay with those from the reference assay. The influenza assay is plotted on top of the reference assay (Fig. 7.10, Chapter 7) to obtain a rough estimate of the magnitude of unspecific binding. Additionally, to verify that the signal from the sample does not exceed the saturation value from the reference curve.

In both figures, the top graph shows the electrical results with the sample in red and the negative control in blue, the grey points are the reference measurements of signal as a function of antibody concentration, Fig. 7.10. The bottom row shows two pictures of the sensors taken just after the biochemical process has been completed, the left is the negative control sensor and the right is the sample sensor.

In both experiments the signal of the sample can be clearly distinguished from the signal of the negative control. In Assay 1 the difference between the sample and the negative control is visible in the pictures of the sensors with beads, whereas the pictures of Assay 2 show less clear differences.

The S/NC of the assay, measured as the signal from the sample divided by the signal from the negative control, is $S/NC = 1.6$ (Assay 1) and $S/NC = 2.5$ (Assay 2). This is on average $S/NC = 2$.

8.4 Discussion

The influenza magnetic sandwich immunoassay presented in Table 8.1, Fig. 8.4, and Fig. 8.5 captures the presence of the virus. In both cases, the electrical measurements are clearly able to distinguish between the sample and the negative control.

Looking at the pictures of the sensor just after the biochemistry has been performed it is not clear why the largest difference between sample and negative control is observed in Assay 2. The higher signal from Assay 2 can be attributed to a combination of more beads placed at positively contributing sites and less beads placed at negatively contributing sites. The analysis of bead signal in Chapter 4 supports this postulate. The analysis shows that a bead's position with respect to the sensor edge can have a strong influence

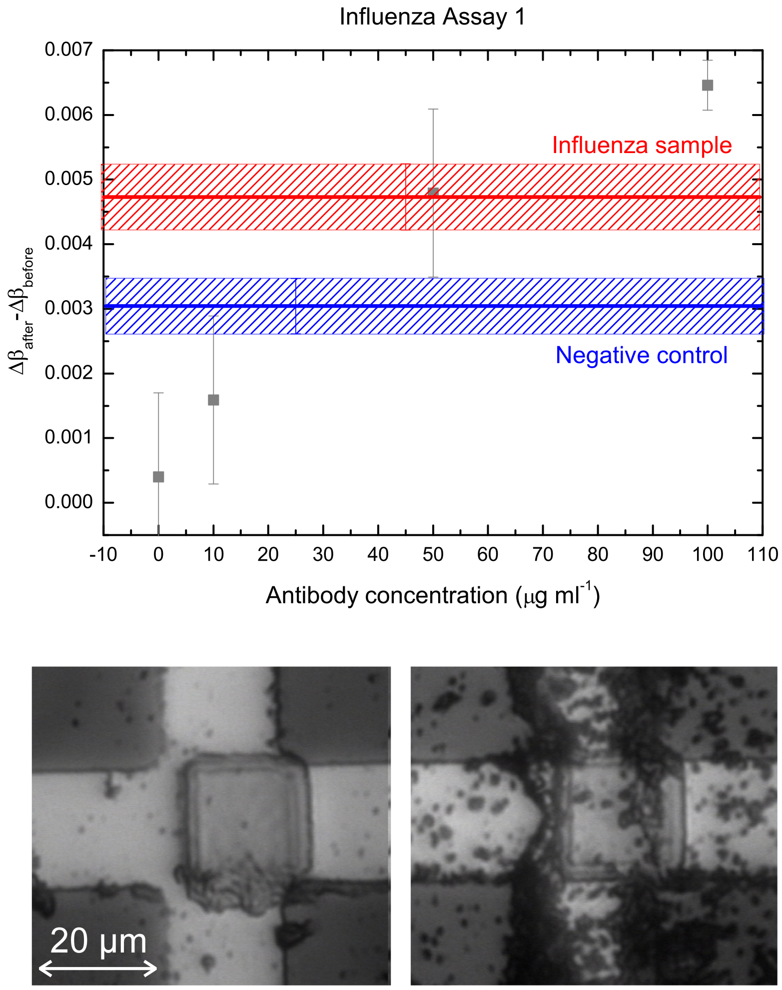

Figure 8.4: Results of influenza Assay 1 with $c_{\mathrm{mab}} = 5$ mg ml^{-1} capture antibody concentration. Top graph shows the electrical measurements with the sample (red) clearly distinguishable from the negative control (blue). The c-values can be estimated from the reference measurements of signal versus antibody concentration (grey) to verify that sample and negative control fall within the boundaries of the reference. The pictures of the sensor in the bottom row are taken just after the biochemical experiments. Left: the negative control. Right: the sample.

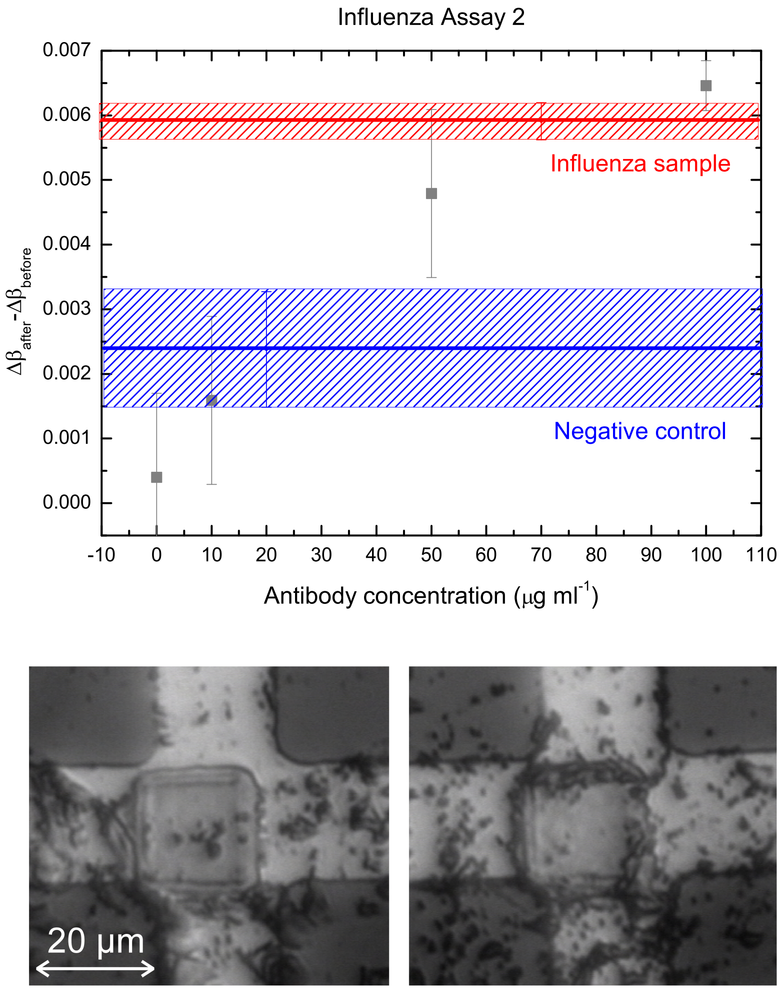

Figure 8.5: Results of influenza Assay 2 with $c_{\mathrm{mab}} = 0.5$ mg ml^{-1} capture antibody concentration. Top graph shows the electrical measurements with the negative control (blue) clearly below the sample (red). The c-values can be estimated from the reference measurements of signal versus antibody concentration (grey) to see that sample and negative control fall within the boundaries of the reference. The pictures of the sensor in the bottom row are taken just after the biochemical experiments. Left: the negative control. Right: the sample.

on the over-all signal. In this way Assay 2 contrasts Assay 1, where the picture clearly distinguishes between the sample and the negative control.

The signal to negative control of the two magnetic influenza assays are $S/NC = 1.6$ (Assay 1) and $S/NC = 2.5$ (Assay 2), on average $S/NC = 2$. This is of course not very impressive compared to approximately $S/NC = 5$ of the fluorescent sandwich assay (Fig. 8.3), but as a first result it is promising.

The signal from the negative control is $\Delta\beta = 0.002$-0.003 (normalized to the applied field), corresponding to an antibody concentration of $c_{\mathrm{mab}} = 20$-$30\ \mu\mathrm{g\ ml}^{-1}$. The fluorescent signal from $c_{\mathrm{mab}} = 30\ \mu\mathrm{g\ ml}^{-1}$ antibodies reaches approximately 75 % of the saturation signal obtained for biotinylated monoclonal antibodies in the Cy3-streptavidin detection system (Fig. 7.2). This is very high for a sandwich assay and relates to the problem of unspecific binding and/or bead adsorption to proteins or field gradients on the chip. Solving this particular issue of the magnetic immunoassay would improve the results considerably.

The possibility of an electrical signal-to-noise enhancement of 50-100 has been proposed in Chapter 6. The estimate is based on improving several features of the experimental setup. With these improvements the signal-to-noise from a single 250 nm Nanomag-D bead can amount to $S/N \approx 2$-3 (compared to Table 4.3) offering great sensitivities on immunoassays. However, the possibility of distinguishing the presence of a single bead can only be fully exploited when the unspecific binding from the negative control is solved.

8.5 Conclusion

This chapter has presented a detection procedure for influenza based on immunochemistry. The detection of proteins with antibodies immobilized on an SU-8 surface has not previously been explored to the author's present knowledge. The procedure of influenza detection has been optimized with respect to surface blocking system and the fluorescent detection system, using direct labelling of detector antibodies.

The results of the influenza assay have been obtained first with fluorescently labelled monoclonal antibodies, yielding $S/NC = 5$, then with the Batch 2 planar Hall sensors, $S/NC = 2$, where S/NC is the signal from the sample divided by the signal from the negative control.

The successful detection of influenza by the planar Hall sensors is promising. The high signal from the negative control gives a low assay sensitivity. Decreasing the unspecific binding will thus improve the assay result considerably. Also the capturing of beads at undesired places could possibly be avoided by SU-8 design considerations.

Chapter 9

Conclusion and outlook

9.1 Conclusion

Planar Hall sensors are promising candidates for a prototype diagnostic chip as they can be used for point-of-care diagnostics of influenza infection. Their inherent signal-to-noise characteristic outperforms competitive sensing principles, at least for DC detection measurements. Planar Hall sensors have proven capable of detecting relatively low antibody concentrations especially considering the SU-8 capping design, which result in competing positive and negative signals. Additionally, actual influenza sandwich immunoassays have been detected with the studied planar Hall sensors.

Design, fabrication and characterization of planar Hall sensors of different sensing materials have been investigated theoretically and experimentally. In the end, the optimal material for planar Hall sensors is chosen for the immunoassay experiments. This is the top pinned permalloy stack. However, the optimal design for the SU-8 capping layer is not put to the experimental test. This design has been realized too late in the process to implement in the fabrication.

For the electrical characterization of sensors, a setup has been built that eliminates much of the electrical noise observed in the first batch of sensors [4, 5]. The noise is reduced almost by a factor of 100 in the new setup. The experimental noise of the setup is dominated by the internal noise of the lock-in amplifier, and it would be troublesome to extract the experimental noise from the sensor itself. However, the introduction of a low-noise pre-amplifier between the sensor and the lock-in amplifier would help to utilize the full scale of the planar Hall sensor. An estimate of the signal-to-noise enhancement following this course is approximately 5. Combined with a factor of 10-20 from increasing the sensor current (requires rebuilding of the experimental setup), gaining a factor of 50-100 is possible. An S/N enhancement of 60 is sufficient for single 250 nm Nanomag-D beads to be easily distinguished with the actual sensor batch.

The theoretical prediction of the sensor resisitvity, AMR, sensitivity, and temperature drift accounts reasonably for the experimentally observed behavior (presented in Table 6.4). The same applies to the theoretical versus experimental signal from a monolayer of beads. The theoretical value for the studied sensors is $\beta \approx 0.024(\xi_{\text{outside}} - \xi_{\text{sensor}})$, where ξ

is the bead coverage, and the experimental maximum value is $\Delta\beta_{\mathrm{beads}} = 0.011$, implying the order of magnitude is correct.

The observed signals of magnetic immunoassays in Fig. 7.8, Fig. 7.10, and Table 8.1, range between $\Delta\beta_{\mathrm{beads}} = 0$ and $\Delta\beta_{\mathrm{beads}} = 0.011$. An increase in antibody concentration results in an increase in sensor signal. This is anticipated since more beads are expected to bind to the biotinylated antibodies, when their surface concentration is increased.

An experimental procedure for immobilizing antibodies on SU-8 has been established during this Ph.D. study. Various blockers has been investigated and the most promising results were obtained with the well-known combination of BSA and milk. Additionally, the full protocol of an influenza immunoassay has been produced and optimized with respect to time consumption. The author acknowledges that more efforts could have been put into this particular part of the study if time had allowed. Both procedures have been tested on the planar Hall sensors. The immobilization procedure of biotinylated monoclonal antibodies is studied with the planar Hall sensor as a function of antibody concentration (Fig. 7.8 and Fig. 7.10). Additionally, the influenza immunoassay is detected with the planar Hall sensors with an average $S/NC = 2$, measured as the signal from the sample divided by the signal from the negative control.

The obtained results are promising for implementing the planar Hall sensor in magnetic immunoassaying. Several improvements can be introduced, where particularly the SU-8 design should lead to improvements. Furthermore, when the large signal from the negative control is diminished, the resulting assay $S/NC = 2$ would be enhanced.

9.2 Outlook

This outlook provides the author's assessment of promising ways to pursue the work further. There is scope for further improvement in both sensor design and bead design, which is a prerequisite for the launch of a prototype device. The two main issues are described below.

9.2.1 Sensor technology

The size of the sensor can be tuned to match the application. For immunoassay detection, smaller sensors seem preferable to larger ones. In this case, sensitive areas of $20\mu\mathrm{m} \times 20\mu\mathrm{m}$ have larger signals from the respective antibody concentrations compared with areas of $1\mathrm{mm} \times 1\mathrm{mm}$ (data not shown). One should also investigate the theoretical signal from sensitive areas differing from square geometry. It might be possible to cut some positive contributions and optimize the sensor design with respect to the bead signal.

Another issue to look into is the design of the SU-8 layer covering the sensor. The design used in the work presented here represents a first step, which can be improved considerably. The focus of the current design was to ensure immobilization of antibodies only above the sensor area. However, the antibodies bind just as well to the SU-8 monolayer still present after development, and as a result the beads cover everything. Additionally, the beads get stuck at the edges of the SU-8 pad. They also have a tendency to stick to the edges of the permalloy layers at locations with high fringing fields.

Instead of only covering the sensitive parts of the sensor, a thick layer of SU-8 can be used to block the signal from the beads everywhere else than on top of the sensor. Leaving small grooves or wells on top of the sensor will allow easier placement of antibodies as well as shield the positive contributions from the beads. Another benefit will be to shield the largest part of the fringing field from the permalloy edges and thus limit the tendency of beads to stick in undesired locations.

9.2.2 Bead design

For immunoassays and DNA array detection it is essential to investigate further the above issues on sensor technology. However, a large number of researchers are involved in developing better and more sensitive systems for detection while an area, which is presently less in focus, is the design of beads for diagnostic purposes. The beads detected in this thesis are designed for separation, not for diagnostics, and some of the troubles encountered during this study could be directly related to this fact. Non-specific binding is one of the greatest issues. If quantitative measurements are desired, unspecific binding of the beads must be dealt with and preferably fully avoided.

One thing, which is feasible, is to go down in bead size. In this approach gravity will have less impact on the bead's settlement on the surface. This ought to be combined with higher magnetic moment, if bead sizes become very small. Alternatively, larger bead sizes could be chosen and in that way larger viscous forces are induced on the beads during washing.

It is also advisable to study the impact different buffers have on unspecific binding. For instance, adding a small amount of Triton X-100 to the bead solution might decrease unspecific binding. Also adjusting the pH of the buffer could have an effect if unspecific binding is related to electrostatic forces. Quantitative experiments have to be performed to fully understand the effects.

Another issue to address is how to avoid agglomeration when fishing antigens out of a solution. One virus with antigens on the surface can bind to more than one antibody covered bead and thus when concentrating the reagents by magnetic forces, long chains of bead-virus-bead-virus can easily form. This should be taken into account in the bead design or the preparation of the sample.

Appendix A

Analytical expressions

A.1 Analytical solution to the homogeneously magnetized sphere

Consider a sphere of linear permeability placed in an external field $H_0\hat{\mathbf{x}}$. The field variation in the xy-plane at a given distance, z, is of interest to the planar Hall sensor geometry. In the case of no free currents Maxwell's equations can be reduced to Laplace's equation for a magnetic potential, $U(r,\theta)$, defined as $\mathbf{B} = -\boldsymbol{\nabla} U(r,\theta)$.

$$\boldsymbol{\nabla}^2 U(r,\theta) = 0 \tag{A.1}$$

In spherical coordinates with no ϕ-dependence Eq. (A.1) becomes

$$\boldsymbol{\nabla}^2 U(r,\theta) = \frac{1}{r^2}\frac{\partial}{\partial r}\left(r^2 \frac{\partial U(r,\theta)}{\partial r}\right) + \frac{1}{r^2 \sin\theta}\frac{\partial}{\partial \theta}\left(\sin\theta \frac{\partial U(r,\theta)}{\partial \theta}\right) = 0 \tag{A.2}$$

The high symmetry of the solid sphere and the external field implies that the potential can be separated into a term depending only on r, $R(r)$, and a term depending only on θ, $\Theta(\theta)$. Inserting $U(r,\theta) = R(r)\Theta(\theta)$ into Eq. (A.2) and multiplying by r^2 yields

$$\boldsymbol{\nabla}^2 U(r,\theta) = \frac{\partial}{\partial r}\left(r^2 \frac{\partial R(r)}{\partial r}\right)\Theta(\theta) + \frac{1}{\sin\theta}\frac{\partial}{\partial \theta}\left(\sin\theta \frac{\partial \Theta(\theta)}{\partial \theta}\right)R(r) = 0 \tag{A.3}$$

Dividing by $U(r,\theta)$ and rearranging Eq. (A.3) one gets the following differential equation

$$\frac{1}{R(r)}\frac{\partial}{\partial r}\left(r^2 \frac{\partial R(r)}{\partial r}\right) = -\frac{1}{\Theta(\theta)\sin\theta}\frac{\partial}{\partial \theta}\left(\sin\theta \frac{\partial \Theta(\theta)}{\partial \theta}\right) \tag{A.4}$$

It is obvious from Eq. (A.4) that the LHS depends only on r and the RHS depends only on θ. This can only be fulfilled if both sides equals the same constant which without loss of generality can be called $l(l+1)$. First the LHS is solved, the differential equation is

$$\frac{d}{dr}\left(r^2 \frac{dR(r)}{dr}\right) = l(1+l)R(r) \tag{A.5}$$

Eq. (A.5) has the general solution

$$R(r) = Cr^l + \frac{D}{r^{l+1}} \tag{A.6}$$

which can be easily verified by insertion into the differential equation. Second, the RHS of Eq. (A.4) is considered

$$\frac{\partial}{\partial\theta}\left(\sin\theta\frac{\partial\Theta(\theta)}{\partial\theta}\right) = -l(l+1)\sin\theta\Theta(\theta) \tag{A.7}$$

The general solution to Eq. (A.7) is the Legendre polynomials

$$\Theta(\theta) = P_l(\cos\theta) \tag{A.8}$$

$$P_l(x) = \frac{1}{2^l l!}\left(\frac{d}{dx}\right)^l (x^2-1)^l$$

$$\frac{dP_l}{dx} = \frac{1}{2^l l!}\left(\frac{d}{dx}\right)^{l+1} (x^2-1)^l$$

The general solution to Eq. (A.4) is the product of Eq. (A.6) and Eq. (A.8)

$$U(r,\theta) = \sum_{l=0}^{\infty}\left(C_l r^l + \frac{D_l}{r^{l+1}}\right)P_l(\cos\theta) \tag{A.9}$$

Inside the sphere ($r \leq R$, where R is the radius of the sphere) the potential should be finite requiring $D_{(r\leq R)} = 0$, and outside the sphere ($r \geq R$) the potential should vanish at infinity requiring $C_{(r\geq R)} = 0$. Summarizing these requirements,

$$U(r,\theta) = \begin{cases} \sum_{l=0}^{\infty} C_l r^l P_l(\cos\theta) & r \leq R, \\ \sum_{l=0}^{\infty} \frac{D_l}{R^{l+1}} P_l(\cos\theta) & r \geq R. \end{cases} \tag{A.10}$$

The potential should be continuous at $r = R$

$$\sum_{l=0}^{\infty} C_l R^l P_l(\cos\theta) = \sum_{l=0}^{\infty} \frac{D_l}{R^{l+1}} P_l(\cos\theta) \tag{A.11}$$

for all l. This gives one constraint on C_l and D_l ($D_l = C_l R^{2l+1}$). The gradient, on the other hand, is discontinuous at the surface of the sphere, where the discontinuity is proportional to the normal part of the magnetization, $\mu_0\mathbf{M}$,

$$(\boldsymbol{\nabla}U_{\text{above}} - \boldsymbol{\nabla}U_{\text{below}})\cdot\hat{\boldsymbol{n}} = -\mu_0\mathbf{M}\cdot\hat{\boldsymbol{n}} \tag{A.12}$$

$$\frac{\partial U_{\text{above}}}{\partial r}|_{r=R} - \frac{\partial U_{\text{below}}}{\partial r}|_{r=R} = -\mu_0 M\cos\theta$$

$$\frac{\partial U}{\partial r} = \begin{cases} \sum_{l=0}^{\infty} C_l r^{l-1} P_l(\cos\theta) & r \leq R, \\ \sum_{l=0}^{\infty} -(l+1)\frac{C_l R^{2l+1}}{r^{l+2}} P_l(\cos\theta) & r \geq R. \end{cases}$$

$$\frac{\partial U_{\text{above}}}{\partial r}|_{r=R} - \frac{\partial U_{\text{below}}}{\partial r}|_{r=R} = \sum_{l=0}^{\infty} -C_l P_l(\cos\theta) R^{l-1}(2l+1)$$

$$\sum_{l=0}^{\infty} C_l P_l(\cos\theta) R^{l-1}(2l+1) = \mu_0 M \cos\theta \tag{A.13}$$

Because the Legendre polynomials are orthogonal, using Fourier's trick will simplify the problem considerably. The orthogonality relations of the Legendre polynomials are

$$\int_{-1}^{1} P_l(x) P_m(x) dx = \begin{cases} 0 & l \neq m, \\ \frac{2}{2l+1} & l = m. \end{cases}$$

Multiplication on both sides of Eq. (A.13) with $P_m(\cos\theta)$ and integration over all space spanned by the functions yields

$$\int_0^1 \sum_{l=0}^{\infty} C_l P_l(\cos\theta) R^{l-1}(2l+1) P_m(\cos\theta) d(\cos\theta) = \int_0^1 \mu_0 M \cos\theta P_m(\cos\theta) d(\cos\theta)$$

$$\begin{aligned} C_m &= \frac{1}{2} R^{1-m} \mu_0 M \int_{-1}^{1} \cos\theta P_m(\cos\theta) d(\cos\theta) \\ &= -\frac{1}{2} R^{1-m} \mu_0 M \int_0^{\pi} \cos\theta P_m(\cos\theta) \sin\theta d\theta \end{aligned}$$

Since $P_1 = \cos\theta$

$$C_m = \begin{cases} \frac{\mu_0 M}{3} & m = 1, \\ 0 & m \neq 1. \end{cases} \tag{A.14}$$

Finally, Eq. (A.14) can be inserted into the solution Eq. (A.10) to obtain the final solution

$$U(r,\theta) = \begin{cases} \frac{\mu_0 M}{3} r \cos\theta & r \leq R, \\ \frac{\mu_0 M}{3} \frac{R^3}{r^2} \cos\theta & r \geq R. \end{cases} \tag{A.15}$$

The magnetic flux density is obtained by taking the gradient of the potential Eq. (A.15).

$$\mathbf{B} = -\boldsymbol{\nabla} U$$

Outside the sphere the well known result of the magnetic dipole field [32] is obtained

$$\mathbf{B} = \frac{\mu_0 M}{3} \frac{R^3}{r^3} (2\cos\theta \hat{r} + \sin\theta \hat{\theta}) \tag{A.16}$$

And the magnetic field strength outside the sphere is

$$\mathbf{H} = \frac{M}{3} \frac{R^3}{r^3} (2\cos\theta \hat{r} + \sin\theta \hat{\theta}) \tag{A.17}$$

Appendix B

Data acquisition and analysis

B.1 Data acquisition

Temperature	I_{AC}	f	τ (lock-in)	Slope (lock-in)	Phase (lock-in)
30 °C	1 mA	330 Hz	100 ms	12 dB oct^{-1}	0 deg

Table B.1: Experimental settings of the lock-in amplifier during antibody detection experiments. I_{AC} is the current (maximum amplitude), f is the frequency, and τ is the time constant.

1. A chip with three sensors, A, B, and C, is placed in an electrically shielded box. The temperature of the whole box is controlled as described in Chapter 7 at a temperature of $T = 30$ °C. Thermal equilibrium of the box happens fast but the transfer of thermal equilibrium to the inside of the box must be assumed slower. Therefore the temperature of the box is always kept at $T = 30$ °C and the change of chips carried out as quickly as possible in order to minimize heat exchange with the surroundings. Immediately after mounting the chip in the box, the lid is closed and the current applied to all sensors in a series connection. The current is $I_{\mathrm{AC}} = 1$ mA (maximum amplitude) with a frequency of $f = 330$ Hz. The current is applied to all sensors in series and does not change throughout the entire measurement. With current applied, a waiting period of 1 hour is conducted for everything to stabilize. This includes equilibrium temperature and sensor offset.

2. The rest of an experiment is controlled via LabView.

3. First the external magnetic field is set to $B = +0.5$ mT. Then sensor A is chosen by the switch box and LabView waits 10 s before the experiment continues. The time constant is set to 100 ms, the slope is 12 dB oct^{-1}. The sensitivity of the lock-in matches this particular chip and sensor and is set prior to the measurement. Typical sensitivities are 50-100 μV.

4. The signal from sensor A is measured 100 times with the time constant 100 ms and the slope 12 dB oct^{-1}. Afterwards, the switch box switches to sensor B, and after a waiting time of 1 s the signal from sensor B is measured 100 times. Finally, the switch box switches to sensor C and after waiting 1 s the signal from sensor C is measured 100 times.

5. Then sensor A is switched back on and the sequence of 3 and 4 is repeated 50 times in total.

6. The magnetic field is changed from $B = +0.5$ mT to $B = -0.5$ mT. Sensor A is then chosen. Again LabView waits 10 s before proceeding. The measurements are repeated exactly as they were for the positive field, see 3-5.

The whole experiment takes 1 hour to complete, half an hour at each field value. After this half hour the signal is still stabilizing towards the specific field value. This approaching an equilibrium value is related to the change in magnetic field. Nothing else changes. Additionally, a difference between plus and minus the field value is observed which corresponds to the smaller and larger jumps in field. See Fig. B.1, left graph. When changing to $B = -0.5$ mT, the field is changed by a total amount of $\Delta B = 1$ mT (from $B = +0.5$ mT) whereas at $B = +0.5$ mT the change is only $\Delta B = 0.5$ mT (from $B = 0$ mT). Hence the difference between the first and last data points is larger when changing the field from $B = +0.5$ mT to $B = -0.5$ mT than it is when changing from $B = 0$ mT to $B = +0.5$ mT.

B.2 Data analysis

The signal from sensor A in $B = +0.5$ mT, $V_\mathrm{A}(+0.5\ \mathrm{mT})$, and the sensitivity, S_A, have arbitrary sign from chip to chip. All sensitivities on the same chip, S_A, S_B, S_C, have always the same sign but the offset might be large enough to change the sign of the actual signal in $B = +0.5$ mT internally on a chip. Since the phase can vary from one sensor to another, the signal reported is the R value (the norm of the vector). This value is always positive even when X changes sign. Therefore the sign of X is observed along with R. If two R values have corresponding X values with different signs, the sum is taken (R_1+R_2) when the difference is desired (X_1-X_2). Remember, that the behavior of X is of interest but R is used in order to avoid correcting for the phase.

1. The signal from one sensor is normalized to the sensitivity of that particular sensor and the current through the sensor. This yields a value related to the magnetic flux density felt by sensor A, B_A:

$$B_\mathrm{A} = \frac{V_\mathrm{A}}{S_\mathrm{A} \cdot I_\mathrm{AC}\ (\mathrm{mA})} \tag{B.1}$$

   with the unit of mT. In Eq. (B.1) V_A is the measured voltage of sensor A, S_A is the sensitivity of sensor A, and I_AC is the applied current (maximum amplitude). The scaled version of the data representation is shown in Fig. B.1, right graph.

2. When dividing by the applied flux density, B (measured in mT), a dimensionless number is obtained, β, which still reflects the magnetic field experienced by the sensor. Exactly the same arguments hold for the other sensors and we are left with three dimensionless values: β_A, β_B, and β_C.

$$\beta_\mathrm{A} = \frac{V_\mathrm{A}}{S_\mathrm{A} \cdot I_\mathrm{AC}\ (\mathrm{mA}) \cdot B\ (\mathrm{mT})} \tag{B.2}$$

3. The off-set $V_\mathrm{A}(0\ \mathrm{mT})$ stabilizes after approximately one hour with current applied to the sensor. Therefore a waiting time of one hour after mounting the sensor and applying the current is necessary to obtain correct results. The off-set can change considerably with demounting and remounting the sample. It also changes with temperature. Therefore the temperature is kept constant allowing for off-set correction by taking the mean value at negative and positive fields.

$$\Delta\beta_\mathrm{A} = \frac{1}{2}\beta_\mathrm{A}(+0.5\ \mathrm{mT}) + \frac{1}{2}\beta_\mathrm{A}(-0.5\ \mathrm{mT}) = \tag{B.3}$$

$$\frac{V_\mathrm{A}(+0.5\ \mathrm{mT})}{S_\mathrm{A} \cdot 1\ \mathrm{mA} \cdot 1\ \mathrm{mT}} + \frac{V_\mathrm{A}(-0.5\ \mathrm{mT})}{S_\mathrm{A} \cdot 1\ \mathrm{mA} \cdot (-1\ \mathrm{mT})} \approx 1$$

yielding a number close to one, see Fig. B.2, left graph.

4. Sensor B is always the reference. This sensor is never changed during the biochemical reactions and will thus always have a β-value close to one. Sensor A and sensor C measure the applied field plus the field from the beads on top of the respective sensor. Since the field from the beads is negative, their β-values are reduced due to the presence of beads.

5. Subtracting the reference yields

$$\Delta\beta_\mathrm{A,C} - \Delta\beta_\mathrm{B} \begin{cases} = 0 & \text{without beads,} \\ < 0 & \text{with beads.} \end{cases} \tag{B.4}$$

   In Eq. (B.4) "0" is to be understood as baseline since asymmetries can be connected with the normalizing procedure. The resulting data representation for sensor A without beads is shown in Fig. B.2, right graph.

6. With a very tiny amount of beads on top of sensor C, the $\Delta\beta$-value drops as expected, see Fig. B.3, left graph.

Investigation of reference stability

For a large number of measurements the reference sensor gives a stable output. During the measurements shown in Fig. B.3, right graph, the sensor socket has broken and is glued back to the box. This repair has no measurable effect on the reference $\Delta\beta$-value.

Also the introduction of beads to the chip does not alter the signal from the reference. Beads contaminating the reference has been a problem, but this is avoided simply by placing a fat barrier on top of the reference sensor. The fat barrier repels water and thus the bead containing solution does not come into contact with the reference.

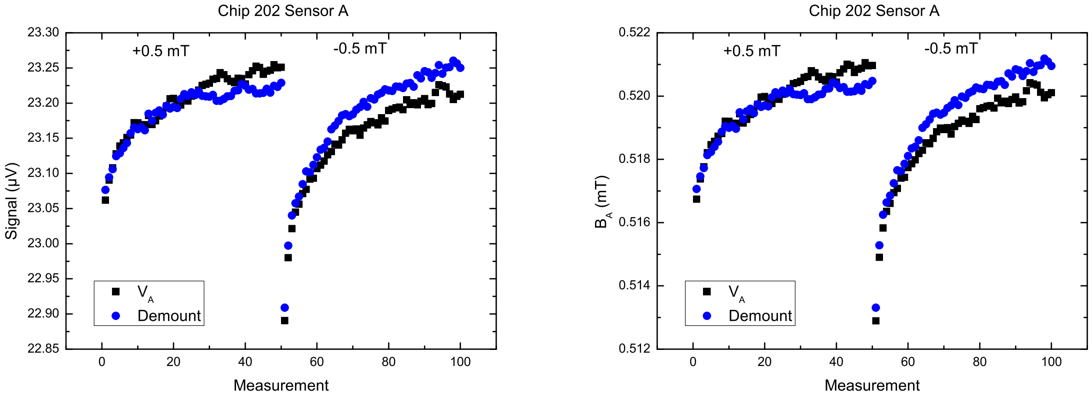

Figure B.1: Relaxation of the sensor signal in plus and minus applied field. Left: Measured data (μV). Right: Scaled with the sensitivity and current through the sensor (mT).

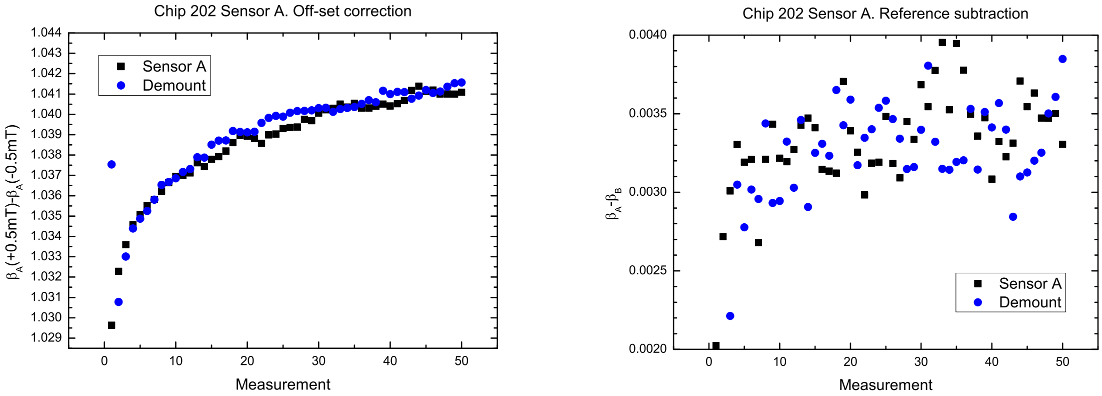

Figure B.2: Normalized off-set corrected sensor signal; the data representation is the dimensionless number β. Left: Off-set corrected values. Right: Off-set corrected and reference subtracted.

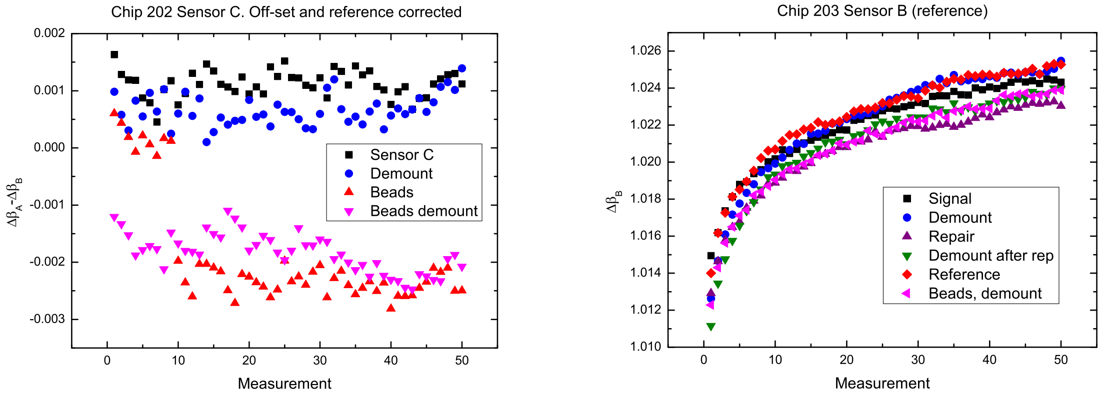

Figure B.3: Bead detection experiment. Left: The $\Delta\beta$-value drops as expected when beads are present on top of the sensor. Right: Reference stability. The $\Delta\beta$-value is unchanged in effect of demounting the sensor and repairing the socket.

Appendix C

Mathematica code

```
                               BEAD INTEGRALS.txt

CHAPTER 4
FIG 4.7
                                     Small sensor
X=-2+4*i/40
Y=-2+4*j/40
In[5]:=
F=(2*(x-X)^2-(y-Y)^2-1)/((x-X)^2+(y-Y)^2+1)^(5/2)/4
In[6]:=
For[i=1,i<41,i++,For[j=1,j<41,j++,m[i,j]=NIntegrate[F,{x,-1,1},{y,-1,1}]]]
In[7]:=
Q=Array[m,{40,40}]
In[8]:=
ListPlot3D[Q]
Export["C:\xy_plotax.eps",%]
In[9]:=
ListContourPlot[Q]
Export["C:\xy_contour.eps",%]


FIG 4.8
                                     Along x
X=40*i/1000
Y=0
F=(2*(x+X)^2-(y+Y)^2-1)/((x+X)^2+(y+Y)^2+1)^(5/2)
For[i=1,i<1000,i++,m[i]=NIntegrate[F,{x,-20,20},{y,-20,20}]]
Q=Array[m,{999}]
Export["C:\alongx_y1.dat",Q]
ListPlot[Q]
Export["C:\Data\Math\x_plot_alongx.eps",%]


                                     Along y
X=0
Y=40*i/1000
F=(2*(x+X)^2-(y+Y)^2-1)/((x+X)^2+(y+Y)^2+1)^(5/2)
For[i=1,i<1000,i++,m[i]=NIntegrate[F,{x,-20,20},{y,-20,20}]]
Q=Array[m,{999}]
Export["C:\alongx_y1.dat",Q]
ListPlot[Q]
Export["C:\Data\Math\x_plot_alongx.eps",%]


TABLE 4.5
                                     C
X=20*i/100-0.2
Y=20*j/10-2
L=0
F=(2*(x+X)^2-(y+Y)^2-1)/((x+X)^2+(y+Y)^2+1)^(5/2)
For[i=0,i<83,i++,For[j=0,j<15,j++,{K[0,j]=0,K[i,0]=0}]]
For[i=1,i<83,i++,
  For[j=1,j<15,j++,{m[i,j]=NIntegrate[F,{x,-20,20},{y,-20,20}]}]]
Q=Array[m,{81,13}]
For[i=1,i<82,i++,
  For[j=1,j<14,j++,K[i,j]=0.25*(m[i,j]+m[(i+1),j]+m[i,(j+1)]+m[(i+1),(j+1)])]]
For[i=1,i<82,i++,
  For[j=1,j<14,j++,L=L+K[i,j]]]
L
-182.283
ListPlot3D[Q]
Export["C:\Data\Math\xy_plot_C.eps",%]
ListContourPlot[Q]
Export["C:\Data\Math\xy_contour_C.eps",%]
ListDensityPlot[Q]
Export["C:\Data\Math\xy_density_C.eps",%]


                                     Ei
                                     Page 1
```

```
X=20*i/100+16-0.2
Y=20*j/10-2
L=0
F=(2*(x+X)^2-(y+Y)^2-1)/((x+X)^2+(y+Y)^2+1)^(5/2)
For[i=0,i<23,i++,For[j=0,j<15,j++,{K[0,j]=0,K[i,0]=0}]]
For[i=1,i<23,i++,
  For[j=1,j<15,j++,{m[i,j]=NIntegrate[F,{x,-20,20},{y,-20,20}]}]]
Q=Array[m,{21,13}]
For[i=1,i<22,i++,
  For[j=1,j<14,j++,K[i,j]=0.25*(m[i,j]+m[(i+1),j]+m[i,(j+1)]+m[(i+1),(j+1)])]]
For[i=1,i<22,i++,
  For[j=1,j<14,j++,L=L+K[i,j]]]
L
-143.844


                                      Eo
X=20*i/100+20-0.2
Y=20*j/10-2
L=0
F=(2*(x+X)^2-(y+Y)^2-1)/((x+X)^2+(y+Y)^2+1)^(5/2)
For[i=0,i<20,i++,For[j=0,j<15,j++,{K[0,j]=0,K[i,0]=0}]]
For[i=1,i<20,i++,
  For[j=1,j<15,j++,{m[i,j]=NIntegrate[F,{x,-20,20},{y,-20,20}]}]]
Q=Array[m,{18,13}]
For[i=1,i<19,i++,
  For[j=1,j<14,j++,K[i,j]=0.25*(m[i,j]+m[(i+1),j]+m[i,(j+1)]+m[(i+1),(j+1)])]]
For[i=1,i<19,i++,
  For[j=1,j<14,j++,L=L+K[i,j]]]
L
126.033


                                      F1

X=20*i/100-0.2
Y=20*j/10+22
L=0
F=(2*(x+X)^2-(y+Y)^2-1)/((x+X)^2+(y+Y)^2+1)^(5/2)
For[i=0,i<120,i++,For[j=0,j<11,j++,{K[0,j]=0,K[i,0]=0}]]
For[i=1,i<120,i++,
  For[j=1,j<11,j++,{m[i,j]=NIntegrate[F,{x,-20,20},{y,-20,20}]}]]
Q=Array[m,{118,9}]
For[i=1,i<119,i++,
  For[j=1,j<10,j++,K[i,j]=0.25*(m[i,j]+m[(i+1),j]+m[i,(j+1)]+m[(i+1),(j+1)])]]
For[i=1,i<119,i++,
  For[j=1,j<10,j++,L=L+K[i,j]]]
L
-32.9518


                                      F2
X=20*i/100+23.2
Y=20*j/10+22
L=0
F=(2*(x+X)^2-(y+Y)^2-1)/((x+X)^2+(y+Y)^2+1)^(5/2)
For[i=0,i<86,i++,For[j=0,j<11,j++,{K[0,j]=0,K[i,0]=0}]]
For[i=1,i<86,i++,
  For[j=1,j<11,j++,{m[i,j]=NIntegrate[F,{x,-20,20},{y,-20,20}]}]]
Q=Array[m,{84,9}]
For[i=1,i<85,i++,
  For[j=1,j<10,j++,K[i,j]=0.25*(m[i,j]+m[(i+1),j]+m[i,(j+1)]+m[(i+1),(j+1)])]]
For[i=1,i<85,i++,
  For[j=1,j<10,j++,L=L+K[i,j]]]
L
9.81117
```

```
                              F3
X=20*i/100+23.2
Y=20*j/10-2
L=0
F=(2*(x+X)^2-(y+Y)^2-1)/((x+X)^2+(y+Y)^2+1)^(5/2)
For[i=0,i<86,i++,For[j=0,j<15,j++,{K[0,j]=0,K[i,0]=0}]]
For[i=1,i<86,i++,
  For[j=1,j<15,j++,{m[i,j]=NIntegrate[F,{x,-20,20},{y,-20,20}]}]]
Q=Array[m,{84,13}]
For[i=1,i<85,i++,
  For[j=1,j<14,j++,K[i,j]=0.25*(m[i,j]+m[(i+1),j]+m[i,(j+1)]+m[(i+1),(j+1)])]]
For[i=1,i<85,i++,
  For[j=1,j<14,j++,L=L+K[i,j]]]
L
140.949


FIG 4.11+4.12
Z0=0.125
                              C
X=0.1*i-0.1
Y=j-1
Z=0.125
L=0
F=(2*(x-X)^2-(y-Y)^2-Z^2)/((x-X)^2+(y-Y)^2+Z^2)^(5/2)
For[i=0,i<83,i++,For[j=0,j<15,j++,{K[0,j]=0,K[i,0]=0}]]
For[i=1,i<83,i++,
  For[j=1,j<15,j++,{m[i,j]=NIntegrate[F,{x,-10,10},{y,-10,10}]}]]
Q=Array[m,{81,13}]
For[i=1,i<82,i++,
  For[j=1,j<14,j++,K[i,j]=0.25*(m[i,j]+m[(i+1),j]+m[i,(j+1)]+m[(i+1),(j+1)])]]
For[i=1,i<82,i++,
  For[j=1,j<14,j++,L=L+K[i,j]]]
L
-370.644


                              Ei
X=0.1*i-0.1+8
Y=j-1
Z=0.125
L=0
F=(2*(x-X)^2-(y-Y)^2-Z^2)/((x-X)^2+(y-Y)^2+Z^2)^(5/2)
For[i=0,i<23,i++,For[j=0,j<15,j++,{K[0,j]=0,K[i,0]=0}]]
For[i=1,i<23,i++,
  For[j=1,j<15,j++,{m[i,j]=NIntegrate[F,{x,-10,10},{y,-10,10}]}]]
Q=Array[m,{21,13}]
For[i=1,i<22,i++,
  For[j=1,j<14,j++,K[i,j]=0.25*(m[i,j]+m[(i+1),j]+m[i,(j+1)]+m[(i+1),(j+1)])]]
For[i=1,i<22,i++,
  For[j=1,j<14,j++,L=L+K[i,j]]]
L
-513.12


                              Eo
X=0.1*i+10-0.1
Y=j-1
Z=0.125
L=0
F=(2*(x-X)^2-(y-Y)^2-Z^2)/((x-X)^2+(y-Y)^2+Z^2)^(5/2)
For[i=0,i<20,i++,For[j=0,j<15,j++,{K[0,j]=0,K[i,0]=0}]]
For[i=1,i<20,i++,
  For[j=1,j<15,j++,{m[i,j]=NIntegrate[F,{x,-10,10},{y,-10,10}]}]]
Q=Array[m,{18,13}]
For[i=1,i<19,i++,
  For[j=1,j<14,j++,K[i,j]=0.25*(m[i,j]+m[(i+1),j]+m[i,(j+1)]+m[(i+1),(j+1)])]]
For[i=1,i<19,i++,
```

```
  For[j=1,j<14,j++,L=L+K[i,j]]]
L
511.38


                                    F1
X=0.1*i-0.1
Y=j+11
Z=0.125
L=0
F=(2*(x-X)^2-(y-Y)^2-Z^2)/((x-X)^2+(y-Y)^2+Z^2)^(5/2)
For[i=0,i<120,i++,For[j=0,j<11,j++,{K[0,j]=0,K[i,0]=0}]]
For[i=1,i<120,i++,
  For[j=1,j<11,j++,{m[i,j]=NIntegrate[F,{x,-10,10},{y,-10,10}]}]]
Q=Array[m,{118,9}]
For[i=1,i<119,i++,
  For[j=1,j<10,j++,K[i,j]=0.25*(m[i,j]+m[(i+1),j]+m[i,(j+1)]+m[(i+1),(j+1)])]]
For[i=1,i<119,i++,
  For[j=1,j<10,j++,L=L+K[i,j]]]
L
-66.0853


                                    F2
X=0.1*i+11.7-0.1
Y=j+11
Z=0.125
L=0
F=(2*(x-X)^2-(y-Y)^2-Z^2)/((x-X)^2+(y-Y)^2+Z^2)^(5/2)
For[i=0,i<86,i++,For[j=0,j<11,j++,{K[0,j]=0,K[i,0]=0}]]
For[i=1,i<86,i++,
  For[j=1,j<11,j++,{m[i,j]=NIntegrate[F,{x,-10,10},{y,-10,10}]}]]
Q=Array[m,{84,9}]
For[i=1,i<85,i++,
  For[j=1,j<10,j++,K[i,j]=0.25*(m[i,j]+m[(i+1),j]+m[i,(j+1)]+m[(i+1),(j+1)])]]
For[i=1,i<85,i++,
  For[j=1,j<10,j++,L=L+K[i,j]]]
L
19.7699


                                    F3
X=0.1*i+11.7-0.1
Y=j-1
Z=0.125
L=0
F=(2*(x-X)^2-(y-Y)^2-Z^2)/((x-X)^2+(y-Y)^2+Z^2)^(5/2)
For[i=0,i<86,i++,For[j=0,j<11,j++,{K[0,j]=0,K[i,0]=0}]]
For[i=1,i<86,i++,
  For[j=1,j<15,j++,{m[i,j]=NIntegrate[F,{x,-10,10},{y,-10,10}]}]]
Q=Array[m,{84,13}]
For[i=1,i<85,i++,
  For[j=1,j<14,j++,K[i,j]=0.25*(m[i,j]+m[(i+1),j]+m[i,(j+1)]+m[(i+1),(j+1)])]]
For[i=1,i<85,i++,
  For[j=1,j<14,j++,L=L+K[i,j]]]
L
289.328
```

FIT.txt

```
Chapter 6
FIG 6.11

expdata=Import["C:/Experimental2.dat"];
expdata=expdata[[Range[2,Length[expdata]]]]
pexp=ListPlot[expdata]
{{0.03982,-0.833},{0.12542,2.89},{0.22659,7.55},{0.30441,11.29},{0.47561,
    18.73},{0.60012,24.36},{0.75576,30.78},{0.98143,40.09},{1.24602,
    50.36},{1.5962,62.06},{1.95417,72.16},{2.39774,81.73},{2.72458,
    86.94},{3.21484,92.17},{3.48721,94.07},{3.97747,95.67},{4.31209,
    95.88},{4.72453,95.3},{5.06693,94.38},{5.48715,92.79},{6.242,
    89.21},{7.03575,84.91},{7.83729,80.58},{8.59991,76.54},{9.36254,
    72.71},{10.1796,68.88},{10.9656,65.55},{11.7205,62.55},{12.4753,
    59.88},{13.3858,56.91},{14.0784,54.84},{14.8643,52.69},{15.6192,
    50.76},{11.7205,62.45},{7.8762,80.09},{5.70505,91.64},{3.89186,
    95.59},{1.8997,72.18},{0.03982,0.85}}
g[Hc_,Hex_,H_]:=
    Evaluate[x/.Solve[{Hc*x*(1-x^2)^(1/2)-H*(1-x^2)^(1/2)+Hex*x\[Equal]0},
            x][[2]]];
V[V0_,Hc_,Hex_,H_]:=V0*g[Hc,Hex,H]*(1-g[Hc,Hex,H]^2)^(1/2)

fitfunc=Sum[Abs[((expdata[[ii,2]]-V[V0,Hc,Hex,expdata[[ii,1]]]))]^2
      ,{ii,Length[expdata]}];
FindMinimum[fitfunc,{V0,80.,90},{Hc,0.00001,0.5},{Hex,3.,6.},
  MaxIterations\[Rule]10000]
{48.1295,{V0\[Rule]191.372,Hc\[Rule]0.00142651,Hex\[Rule]4.34506}}

p1=Plot[V[191.37154365057953`,0.0014265135085513O5`,4.345056215392623`,H],{H,
        0,16},PlotRange\[Rule]All,DisplayFunction\[RuleDelayed]Identity];
Show[pexp,p1]
Export["C:/fit.eps",%]
```

Page 1

Appendix D

Publications

D.1 List of publications

Published journal papers and conference proceedings. The papers directly related to the subject of this thesis are included on the following pages.

Papers directly related to the subject of this thesis

- L. Ejsing, M. F. Hansen and A. K. Menon, "Planar Hall Effect magnetic Sensor for Micro-Bead Detection", *Conference proceedings: Eurosensors 2003*, September 2003.
- L. Ejsing, M. F. Hansen, A. K. Menon, H. A. Ferreira, D. L. Graham, P. P. Freitas, "Planar Hall effect sensor for magnetic micro- and nanobead detection", *Appl. Phys. Lett.*, **84**, p. 4729-4731, June 2004.
- L. Ejsing, M. F. Hansen, A. K. Menon, H. A. Ferreira, D. L. Graham, P. P. Freitas, "Magnetic microbead detection using the planar Hall effect", *J. Magn. Magn. Mater.*, **293**, p. 677-684, March 2005.
- R. Marie, S. Schmid, A. Johansson, L. Ejsing, M. Nordström, D. Häfliger, C. B. V. Christensen, A. Boisen and M. Dufva, "Immobilisation of DNA to polymerised SU-8 photoresist", *Biosensors and Bioelectronics*, **21**, p. 1327-1332, March 2005.

Papers not related to the subject of this thesis

- L. Ejsing, K. Smistrup, C. M. Pedersen, N. A. Mortensen and H. Bruus, "Frequency response in surface-potential driven electrohydrodynamics", *Phys. Rev. E*, **73**, p. 037302 1-4, March 2006.

Bibliography

[1] François Montaigne, Alain Schuhl, Frédéric Nguyen Van Dau, and Armando Encinas. Development of magnetoresistive sensors based on planar Hall effect for applications to microcompass. *Sensors and Actuators A*, 81(1-3):324–327, July 2000.

[2] Louise Ejsing, Mikkel F. Hansen, and Aric K. Menon. Planar Hall effect magnetic sensor for micro-bead detection. Conference proceedings, Eurosensors 2003, September 2003.

[3] Tobias Johansson, Peter Jensen, and Casper Krag. Helmholtz coils for characterization of magnetic sensors. Fagpakkeprojekt 10061, Mikroelektronik Centret (MIC), Technical University of Denmark (DTU), Ørstedsplads, 2800 Kongens Lyngby, April 2003.

[4] Louise Ejsing, Mikkel F. Hansen, Aric K. Menon, Hugo A. Ferreira, Daniel L. Graham, and Paulo P. Freitas. Planar Hall effect sensor for magnetic micro- and nanobead detection. *Applied Physics Letters*, 84(23):4729–4731, June 2004.

[5] Louise Ejsing, Mikkel F. Hansen, Aric K. Menon, Hugo A. Ferreira, Daniel L. Graham, and Paulo P. Freitas. Magnetic microbead detection using the planar Hall effect. *Journal of Magnetism and Magnetic Materials*, 293(1):677–684, May 2005.

[6] Robert C. O'Handley. *Modern Magnetic Materials.* John Wiley & Sons, Inc., New York, 2000.

[7] M. N. Baibich, J. M. Broto, A. Fert, F. Nguyen Van Dau, F. Petroff, P. Etienne, G. Creuzet, A. Friederich, and J. Chazelas. Giant magnetoresistance of (001)Fe/Cr magnetic superlattices. *Physical Review Letters*, 61(21):2472–2475, November 1988.

[8] Robert L. White. Giant magnetoresistance materials and their potential as read head sensors. *IEEE Transactions on Magnetics*, 30(2):346–352, March 1994.

[9] H. A. Ferreira, D. L. Graham, P. P. Freitas, and J. M. S. Cabral. Biodetection using magnetically labeled biomolecules and arrays of spin valve sensors (invited). *Journal of Applied Physics*, 93(10):7281–7286, May 2003.

[10] Pierre-A. Besse, Giovanni Boero, Michel Demierre, Vincent Pott, and Radivoje Popovic. Detection of a single magnetic microbead using a miniaturized silicon Hall sensor. *Applied Physics Letters*, 80(22):4199–4201, June 2002.

[11] M. A. Parker, T. L. Hylton, K. R. Coffey, and J. K. Howard. Microstructural origin of giant magnetoresistance in a new sensor structure based on NiFe/Ag discontinuous multilayer thin films. *Journal of Applied Physics*, 75(10):6382–6384, May 1994.

[12] R. L. Edelstein, C. R. Tamanaha, P. E. Sheehan, M. M. Miller, D. R. Baselt, L. J. Whitman, and R. J. Colton. The BARC biosensor applied to the detection of biological warfare agents. *Biosensors and Bioelectronics*, 14(10–11):805–813, January 2000.

[13] M. M. Miller, P. E. Sheehan, R. L. Edelstein, C. R. Tamanaha, L. Zhong, S. Bounnak, L. J. Whitman, and R. J. Colton. A DNA array sensor utilizing magnetic microbeads and magnetoelectronic detection. *Journal of Magnetism and Magnetic Materials*, 225(1–2):138–144, 2001.

[14] D. K. Wood, K. K. Ni, D. R. Schmidt, and A. N. Cleland. Submicron giant magnetoresistive sensors for biological applications. *Sensors and Actuators A*, 120(1):1–6, April 2005.

[15] D. L. Graham, H. Ferreira, J. Bernardo, P. P. Freitas, and J. M. S. Cabral. Single magnetic microsphere placement and detection on-chip using current line designs with integrated spin valve sensors: Biotechnological applications. *Journal of Applied Physics*, 91(10):7786–7788, May 2002.

[16] D. L. Graham, H. A. Ferreira, P. P. Freitas, and J. M. S. Cabral. High sensitivity detection of molecular recognition using magnetically labelled biomolecules and magnetoresistive sensors. *Biosensors and Bioelectronics*, 18(4):483–488, April 2003.

[17] D. L. Graham, H. A. Ferreira, and P. P. Freitas. Magnetoresistive-based biosensors and biochips. *Trends in Biotechnology*, 22(9):455–462, September 2004.

[18] D. L. Graham, H. A. Ferreira, N. Feliciano, P. P. Freitas, L. A. Clarke, and M. D. Amaral. Magnetic field-assisted DNA hybridisation and simultaneous detection using micron-sized spin-valve sensors and magnetic nanoparticles. *Sensors and Actuators B*, 107(2):936–944, June 2005.

[19] Guanxiong Li, Vikram Joshi, Robert L. White, Shan X. Wang, Jennifer T. Kemp, Chris Webb, Ronald W. Davis, and Shoueng Sun. Detection of single micron-sized magnetic bead and magnetic nanoparticles using spin valve sensors for biological applications. *Journal of Applied Physics*, 93(10):7557–7559, May 2003.

[20] G. Mihajlović, P. Xiong, S. von Molnár, K. Ohtani, H. Ohno, M. Field, and G. J. Sullivan. Detection of single magnetic bead for biological applications using an InAs quantum-well micro-Hall sensor. *Applied Physics Letters*, 87(11):112502–1–3, September 2005.

[21] J. B. Johnson. Thermal agitation of electricity. *Bell Laboratories Record*, 3(6):185–187, February 1927.

[22] J. B. Johnson. Thermal agitation of electricity in conductors. *Physical Review*, 32(1):97–109, July 1928.

[23] J. Wilson and J. Hawkes. *Optoelectronics an introduction.* Prentice Hall, Hertfordshire, third edition, 1998.

[24] B. Raquet. Electronic noise in magnetic materials and devices. Laboratoire de Physique de la Matière Condensée de Toulouse, LPMCT-LNCMP-INSA, France.

[25] J. Briaire, L. K. J. Vandamme, and M. A. M. Gijs. Resistance and 1/f noise dependence on magnetic field in single $\mathrm{Ni_{80}Fe_{20}}$ layers and $\mathrm{Ni_{80}Fe_{20}}$/Cu multilayers. Proceedings of the 14th International Conference on Noise in Physical Systems and 1/f Fluctuations, 1997.

[26] P. P. Freitas, H. A. Ferreira, D. L. Graham, L. A. Clarke, M. D. Amaral, V. Martins, L. Fonseca, and J. S. Cabral. *in M. Johnson (Ed.) Magnetoelectronics*, chapter 7: Magnetoresistive DNA chips, pages 331–373. Elsevier Academic Press, Oxford, first edition, December 2004.

[27] J. Nogués and I. K. Schuller. Exchange bias. *Journal of Magnetism and Magnetic Materials*, 192(2):203–232, February 1999.

[28] Richard M. Bozorth. *Ferromagnetism.* IEEE press, Wiley-Interscience, John Wiley & Sons, Inc., Hoboken, New Jersey, 2003.

[29] N. F. Mott. The resistance and thermoelectric properties of the transition metals. *Proceedings of the Royal Society of London. Series A, Mathematical and Physical Sciences*, 156(888):368–382, August 1936.

[30] V. D. Ky. Planar Hall Effect in Ferromagnetic Films. *Physica Status Solidi*, 26(2):565–569, 1968.

[31] Y. Shirakawa. On the Longitudinal Magneto-Resistance Effect at Various Temperatures in Iron-Nickel Alloys. *Tohoku Imperial University – Science Reports*, 27(4):485–531, January 1939.

[32] David J. Griffiths. *Introduction to electrodynamics.* Prentice-Hall, Inc., New Jersey, second edition, 1989.

[33] Véronique Gehanno, Paulo P. Freitas, Anabela Veloso, João Ferreira, Bernado Almeida, J. B. Sousa, A. Kling, J. C. Soares, and M. F. da Silva. Ion beam deposition of Mn-Ir spin valves. *IEEE Transactions on Magnetics*, 35(5):4361–4367, September 1999.

[34] Rodolphe Marie, Silvan Schmid, Alicia Johansson, Louise Ejsing, Maria Nordström, Daniel Häfliger, Claus BV Christensen, Anja Boisen, and Martin Dufva. Immobilisation of DNA to polymerised SU-8 photoresist. *Biosensors and Bioelectronics*, 21(7):1327–1332, March 2006.

[35] Dirch Hjorth Petersen and Peter Morten Moselund. Simulation and characterization of a Hall sensor with automated testing. Special course, Department of Micro and Nanotechnology (MIC), Technical University of Denmark (DTU), Ørstedsplads, 2800 Kongens Lyngby, July 2003.

[36] Stanford Research Systems. Model SR830 DSP Lock-in Amplifier. Manual, November 2002.

[37] Alexandre Pesci. LEMO Unipole & Multipole Connectors. Catalogue, April 2000.

[38] G. Glikmann, C. H. Mordhorst, and C. Koch. Monoclonal antibodies for the direct detection of influenza-A virus by ELISA in clinical specimens from patients with respiratory infections. *Clinical and Diagnostic Virology*, 3(4):361–369, 1995.

[39] H. A. Ferreira, N. Feliciano, D. L. Graham, and P. P. Freitas. Effect of spin-valve sensor magnetostatic fields on nanobead detection for biochip applications. *Journal of Applied Physics*, 97(10):10Q904,1–3, May 2005.

[40] Bangs Laboratories. Technote 201: Working with microspheres. Technical Report 201, Bangs Laboratories Incorporate, www.bangslabs.com, October 2002.

Planar Hall Effect Magnetic Sensor for Micro-Bead Detection

L. Ejsing, M. F. Hansen and A. K. Menon

Mikroelektronik Centret (MIC), Technical University of Denmark (DTU), Building 345 East,
2800 Kgs. Lyngby, Denmark
e-mail: loe@mic.dtu.dk http://www.mic.dtu.dk

Summary: *Magnetic sensors based on the planar Hall effect (PHE) of Ni have been fabricated and characterized. The response to an applied magnetic field has been measured without and with a coating of commercially available 2.8 mm magnetic beads for bioseparation (Dynabeads M-280, Dynal, Norway). It is demonstrated that the technique is capable of detecting just a few magnetic beads, i.e., that the technique is feasible for magnetic biosensors.*

Keywords: *Planar Hall effect, magnetic bead detection*
Category: *3 (Magnetic physical devices)*

1 Introduction

Planar Hall effect sensors have been used to detect nanotesla magnetic fields [1,2]. Also, the exchange anisotropy behavior can be characterized using thin films' planar Hall effect [3]. We demonstrate that a planar Hall effect sensor can be used to detect magnetic beads used for bioapplications.

The anisotropic magnetoresistance (AMR) effect is present in ferromagnetic materials. It results in a dependency of the resistivity on the orientation of the material's magnetization with respect to the current through the material. The electrical output signal in the planar Hall geometry (Fig. 1) is [4]

$$V_y = \frac{(r_{\parallel} - r_{\perp})I_x}{t}\sin(f)\cos(f)$$

where t is the thickness of the metal layer, I_x is the applied current, and f is the angle between the current and the in-plane magnetization vector. $r_{\parallel}$ and $r_{\perp}$ are the resistivities when the magnetization is parallel and perpendicular to the current, respectively. The difference between $r_{\parallel}$ and $r_{\perp}$ is responsible for the anisotropic magnetoresistance and the planar Hall effect. If they were equal, which is the common case, there would be no V_y response to a planar applied magnetic field, *i.e.*, a field applied in the y-direction. For Ni the resistivity variation is approximately 2%.

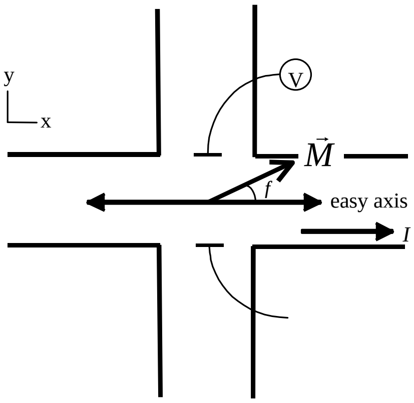

Fig. 1. Planar Hall sensor geometry: The magnetic field to be detected is in the detection plane, applied in the y-direction. In this plane, the current is applied in the x-direction and a voltage is measured in the y-direction.

A schematic drawing of the planar Hall sensor is presented in Fig. 1. Initially the magnetization vector lies along the easy axis and the current direction, in which I_x = 250 µA. A magnetic field applied in the y-direction induces a rotation of the magnetization by an angle f. This changes the electrical output signal by the amount V_y.

The planar Hall geometry is ideal for measuring magnetized beads because these have a significant in-plane field component when magnetized parallel to the sensor plane.

If the easy axis lies in the x-direction and an external field, B_y, is applied in the y-direction, a first approximation of the energy of a magnetisation vector at an angle f to the x-direction is

$$E = E_{an}\sin^2(f) - MVB_y\sin(f)$$

where E_{an} is the anisotropy energy, and V is the volume. At equilibrium

$$\sin(f) = \frac{B_y VM}{2E_{an}} \equiv \frac{B_y}{B_{an}}$$

where B_{an} is the anisotropy field. For small angles, sin(f)cos(f) reduces to sin(f), and the signal to

$$V_y = \frac{(r_{\parallel} - r_{\perp})I_x}{t}\frac{B_y}{B_{an}} \text{ for } B_y \le B_{an}$$

Therefore, in small applied fields with respect to the anisotropy field of the easy axis (typical values for our sensors are B_{an}= 2-3 mT) the response of the sensor is linear.

1.1 Dynabead signal

The low-field magnetic volume susceptibility of the M-280 Dynabeads is c = 0.13 [SI] [5]. From this the low-field magnetic moment of a Dynabead of 2.8 µm in diameter can be estimated as $m = cHV$, where H is the applied field intensity, and $V = \pi(2.8\mu\text{m})^3/6$ is the volume of the Dynabead.

The expression for a dipole's magnetic field in spherical coordinates is [6]

$$\vec{B}_{dip} = \frac{m_0 m}{4pr^3}\left(2\cos(q)\hat{r} + \sin(q)\hat{q}\right)$$

where r is the distance from the dipole to the observation point, q is the angle between the dipole moment and the observation point, and μ_0 is the vacuum permeability.

The bead is placed on top of the sensor with its magnetic moment aligned in the y-direction by the external field. Hence the dipole field from the bead will have the opposite direction just below the bead, *i.e.*, in the $-y$-direction. Because the magnetic field from the bead has the opposite direction of the applied external field, the presence of the beads will lead to a reduction of the magnetic field felt by the sensor. This change in sensitivity to an applied external magnetic field forms the basis of the bead sensing principle.

Assuming dipole behavior of the bead, and only taking the point directly under the dipole moment into account, the angle is q=90°, and the magnitude of the magnetic flux density from the bead at the sensor reduces to

$$B_{bead} \sim -\frac{m_0 H}{4p}\frac{cV}{r^3}$$

The distance from the magnetic moment to the observation point is, in this case, the distance from the center of the bead to the sensor surface. For a bead placed on the sensor surface $r \approx 1.4$ µm.

It should be noted that assuming dipole behaviour of a Dynabead is a very crude model. The bead consists of a large number (10^5-10^6) of superparamagnetic nanoparticles embedded in a polymer, and though these might behave as dipoles the sum is likely to be more complicated. Another problem is that the field produced by the bead is considered homogeneous at the sensor surface, which is only true for one dipole viewed from exactly q=90°. The purpose of this approach is to give an estimate of the order of magnitude, only.

2 Experiments and results

The sensors are fabricated using conventional lithography. Crosses are patterned on a resist coated silicon wafer, and 20 nm of Ni is deposited in an e-beam evaporation system. During deposition a uniform field of 8 mT is applied in order to ensure formation of an easy magnetic axis. A 2 nm thick gold cap is deposited on top in order to protect the nickel from corrosion. Finally, the resist is lifted off with the excess of metal to yield the PHE sensors. Bonding pads are made of gold using the same procedure.

Initially, the magnetization is set along one of the easy axes. When the magnetization is rotated away from the easy axis by a field applied in the y-direction, the change in magnetization produces an electrical output signal.

The output signal is measured as a function of applied field, $\mu_0 H_{ext}$, between 0 and 0.6 mT, first for the sensor without magnetic beads, then for the sensor with magnetic particles placed on top of the sensor (Fig. 2). The response change is due to the presence of beads.

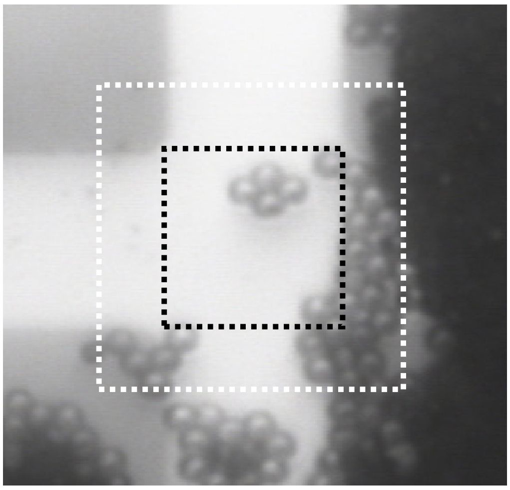

Fig. 2: Sensor area (20µm × 20µm) with 2.8 µm Dynabeads on top. To the right a large cluster of beads is positioned away from the sensing region. The black is sedimentary dirt from the Dynabeads' solution.

The sensor area with clusters of beads on top is shown in Fig. 2. The sample depicted was prepared in the following way. A droplet containing beads was placed on top of the sample with one sensor using a syringe. Then the sample was left to dry and the beads to settle on the surface. The black is sedimentary dirt from the Dynabeads' solution. The dirt covers a large cluster of beads positioned to the right of the sensing area.

In Fig. 2 the black dotted line shows the sensitive area of the sensor. Within this line, beads contribute to the signal with full magnitude. When counting, we get N=6 in this area. The white dotted lines show the detection limit for a single bead estimated from the uncertainty on the measurements. Outside this square the contribution from a single bead is less than the uncertainty on the slope. Between the black and the white line the signal from a particle decreases as $\sim 1/r^3$. Within the white square, N=31.

Calibration of the sensor in homogeneous applied fields up to 0.6 mT is conducted before placing beads on top of the sensor. The calibration yields a linear field response and the sensitivity S = 7.0 µV/mT. At 0.6 mT the dipole field at the sensor from one bead is $B_{bead} \sim 0.026$ mT and the expected signal change is V_{bead} ~ -0.18 µV. Thus to produce 1 µV change in the signal ~6 Dynabeads are needed.

The results of the output voltage as a function of applied magnetic field for the sensor with and without beads on top of the sensitive area are shown in Fig. 3. The distinction between the two types of response is clear, which indicates the potential for biosensor applications of this type of sensor.

When the beads are magnetized, the bead moments align with the applied field. Hence, the effective magnetic field at the sensor, H_{eff}, and the output signal will be reduced according to:

$$V_y = m_0 H_{eff} S \sim m_0 H_{ext} S\left(1 - \frac{NcV}{4pr^3}\right)$$

where N is the number of beads positioned on the sensor. An estimate of N from the slopes found in Fig. 3 according to this simple analysis leads to N ~ 12. It should be noted that the sensor is most sensitive to beads situated on the sensor, but also that clusters of beads in the vicinity of the sensor can contribute.

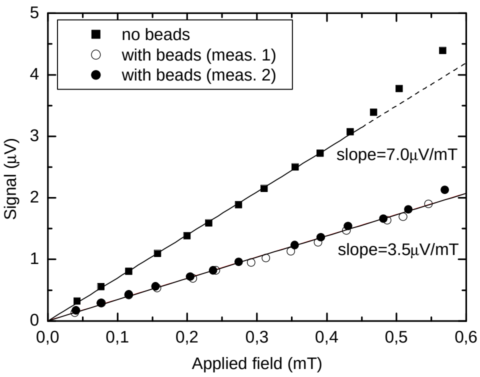

Fig. 3. Offset corrected sensor output signal as a function of applied magnetic field with and without beads. The measurements with beads are conducted twice to ensure repeatability.

After the first series of measurements, the beads were washed away with water and a droplet of diluted beads was placed on top of the sensor. The new sample is shown in Fig. 4. In this picture damages from the first experiments are visible along with the coating of just a few beads on top of the sensing area. Only two beads are situated within the sensitive area marked by black dotted lines. A third bead has the possibility of contributing to the signal; it is placed within the white dotted lines.

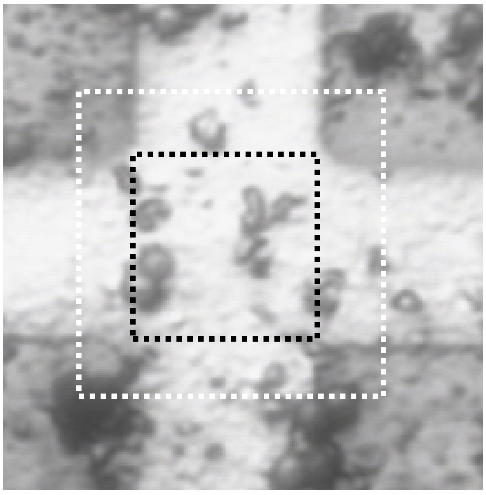

Fig. 4: Sensor area (20µm × 20µm) with a coating of less 2.8 µm Dynabeads on top compared to Fig. 2. Only two beads are situated at the sensing region.

Before placing the new coating of beads on top of the sensor, the sensor was calibrated again, and the sensitivity of S = 7.0 µV/mT was obtained once more.

The sensor output signal corresponding to this coating of beads is shown in Fig. 5. The black squares are measurements without any beads on top of the sensor, the open and filled circles are the measurements corresponding to the bead coverage shown in Fig. 2, and the open triangles are the measurements corresponding to the bead coverage shown in Fig. 4.

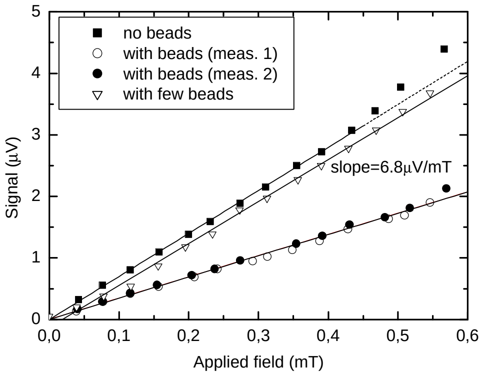

Fig. 5. Offset corrected sensor output signal as a function of applied magnetic field with and without beads. The open triangles (few beads) and the open+solid circles (more beads) correspond to the bead coverage shown in Fig. 4 and 2, respectively.

When estimating the number of beads contributing to the signal from the slopes in Fig. 5, we get N~2, which is also observed in the picture (Fig. 4). Remembering the very crude approximations made to give an order of magnitude estimate of the magnetic field from the bead, the simple estimate works surprisingly well.

Conclusion

It has been demonstrated that the planar Hall effect can be used for detecting commercial micrometer-sized magnetic beads used for bioapplications. The number of detected beads is in fine agreement with simple theoretical estimates. The PHE sensor is sensitive enough to detect just a few beads. Thus, the planar Hall effect has potential for use in magnetic biosensors, *e.g.*, for DNA detection. An advantage of the planar Hall effect sensor compared to giant magnetoresistive (GMR) sensors is the simple fabrication scheme, which reduces the fabrication cost.

Future work includes future theoretical work, sensor optimization and implementation with micro-fluidic systems. The sensor will furthermore be demonstrated as a biosensor where DNA fragments bind the beads to the surface.

References

[1] F. Montaigne, A. Schuhl, F. N. Van Dau, A. Encinas, *Sensors and Actuators* 81 (2000) 324-327.

[2] F. N. Van Dau, A. Schuhl, J. R. Childress, M. Sussiau, *Sensors and Actuators A* 53 (1996) 256-260.

[3] Z. Q. Lu, G. Pan, W. Y. Lai, *J. Appl. Phys.* 90 (2001) 1414-1418.

[4] R. C. O'Handley. Modern Magnetic Materials, *John Wiley & Sons, Inc.* (2000).

[5] http://www.dynal.no

[6] D. J. Griffiths. Introduction to electrodynamics, *Prentice-Hall, Inc.* (1989).

APPLIED PHYSICS LETTERS VOLUME 84, NUMBER 23 7 JUNE 2004

Planar Hall effect sensor for magnetic micro- and nanobead detection

L. Ejsing,[a] M. F. Hansen, and A. K. Menon
Department of Micro and Nanotechnology (MIC), Technical University of Denmark (DTU), Building 345 East, DK-2800 Kongens Lyngby, Denmark

H. A. Ferreira, D. L. Graham, and P. P. Freitas
Institute of Engineering of Systems and Computers—Microsystems and Nanotechnologies (INESC-MN), Rua Alves Redol 9, Lisbon 1000-029, Portugal

(Received 26 January 2004; accepted 8 April 2004; published online 20 May 2004)

Magnetic bead sensors based on the planar Hall effect in thin films of exchange-biased permalloy have been fabricated and characterized. Typical sensitivities are 3 μV/Oe mA. The sensor response to an applied magnetic field has been measured without and with coatings of commercially available 2 μm and 250 nm magnetic beads used for bioapplications (Micromer-M and Nanomag-D, Micromod, Germany). Detection of both types of beads and single bead detection of 2 μm beads is demonstrated, i.e., the technique is feasible for magnetic biosensors. Single 2 μm beads yield 300 nV signals at 10 mA and 15 Oe applied field.
[DOI: 10.1063/1.1759380]

Detection of magnetic beads for bioapplications has been carried out with giant magnetoresistance (GMR) sensors,[1–3] spin valve sensors,[4–7] and a silicon Hall sensor.[8] Planar Hall sensors have been used to detect nanotesla magnetic fields.[9,10] This letter demonstrates that an exchange-biased permalloy planar Hall sensor can be used to detect micro- and nanomagnetic beads used for bioapplications.

Formerly, a planar Hall sensor made of nickel was demonstrated capable of detecting superparamagnetic microbeads.[11] Here, we report on the use of permalloy as a sensing material since it has a higher anisotropic magnetoresistance (AMR) effect than nickel. To control the anisotropy and to achieve a well-defined single domain initial magnetization state, the permalloy layer is exchange coupled to a MnIr antiferromagnetic layer. The 200 Å thick exchange-coupled permalloy layer has an increased effective anisotropy field, $H_{\mathrm{an}} \approx 59$ Oe, defining the sensor saturation field.

The planar Hall effect is based on the AMR of ferromagnetic materials. The transverse voltage on a planar Hall cross depends on the orientation of the magnetization of the material with respect to the longitudinal current running through the material. The electrical output signal in the planar Hall geometry (inset of Fig. 1) is[12]

$$V_y = \frac{(\rho_\parallel - \rho_\perp) I_x}{t} \sin(\phi)\cos(\phi), \tag{1}$$

where t is the metal layer thickness, I_x is the applied current, and ϕ is the angle between the current and the in-plane magnetization vector, $\mathbf{M}$. $\rho_\parallel$ and $\rho_\perp$ are the resistivities when the magnetization is parallel and perpendicular to the current, respectively. $\Delta\rho = (\rho_\parallel - \rho_\perp)$ is responsible for AMR and the planar Hall effect. For a 200 Å thick permalloy film, the resistivity variation is approximately 2.2%.[13]

A schematic drawing of the planar Hall sensor is presented in the inset of Fig. 1. Initially, the magnetization lies along the easy axis, which is also the direction of the applied current, I_x. When a magnetic field, H_y, is applied in the y direction, the magnetization rotates by an angle ϕ in the sensor plane. This changes the electrical output signal by the amount V_y. For small angles, the signal can be expressed as

$$V_y = \frac{(\rho_\parallel - \rho_\perp) l_x}{t} \frac{H_y}{H_{\mathrm{an}}}. \tag{2}$$

Therefore, in small applied fields compared to the anisotropy field, the response of the sensor is linear. For bead detection, H_y in expression (2) represents the applied external field plus the sum of the y components of the field created by the homogeneously magnetized spherical beads weighed by the bead-to-sensor area fraction.

A micrograph of the cleanroom fabricated planar Hall sensor is shown in Fig. 1. The sensor layer structure Ta (30 Å)/NiFe (50 Å)/MnIr (200 Å)/NiFe (200 Å)/Ta (30 Å) (see

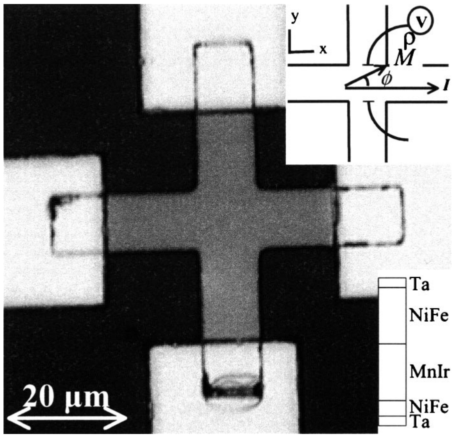

FIG. 1. Micrograph of the planar Hall sensor. The cross is made of exchange-biased permalloy, and the central area is the 10 μm×10 μm sensitive area of the sensor. Current leads are made of 0.3 μm thick Al. The top inset shows the planar Hall sensor geometry. The magnetic field to be detected is applied in the detection plane, along the y direction. In this plane, the current is applied in the x direction and the voltage, V_y, is measured in the y direction. The bottom inset illustrates the cross-sectional layer structure of the sensor.

---

[a] Electronic mail: loe@mic.dtu.dk

TABLE I. Physical properties of Micromod-M beads and Nanomag-D beads.[a]

	Diameter	Concentration	Density	χ^{b}
Micromer-M	2 μm	>25 mg/ml	1.4 g/cm^3	0.3±0.1 (SI)
Nanomag-D	250 nm	>10 mg/ml	4.0 g/cm^3	6±2 (SI)

[a] See Ref. 14.

[b] Measured at Institute of Engineering of Systems and Computers–Microsystems and Nanotechnologies (INESC–MN).

cross-sectional diagram in the inset of Fig. 1) was prepared by ion-beam deposition on a passivated 3 in. Si wafer, then covered by sputtered antireflecting TiWN (150 Å). Ion-beam deposition conditions are given in Gehanno *et al.*[13] Here, MnIr stands for $Mn_{76}Ir_{24}$ and NiFe stands for $Ni_{80}Fe_{20}$. During ion-beam metal deposition, a magnetic field of 40 Oe was applied in order to form an easy axis in the ferromagnetic NiFe layers. Sensors (crosses of 10 μm×10 μm) were patterned by direct write laser lithography and ion-beam milling. Al current leads (0.3 μm thick) were sputtered after a soft etch of the contact surface and defined by photolithography and lift off. The sensor structure was then passivated by a sputtered SiO_2 (2000 Å) layer and contact pads were opened by reactive ion etching.

The active sensing layer is the NiFe (200 Å) layer. For characterization of the planar Hall sensors, electromagnetic coils were used to provide a tuneable magnetic field and the sensor response signal was measured as a function of applied field strength. Direct currents of 1, 5, and 10 mA are applied and direct voltage drops are measured using a voltmeter; no electronic noise reduction is used. A typical sensitivity is $S = 3\ \mu\text{V/Oe mA}$ in the range of ±15 Oe, where the signal is linear within 2.8%. This sensitivity is reproducible for a specific sensor and for sensors on the same chip.

For demonstration of bead detection, a droplet containing superparamagnetic Micromod beads (2 μm or 250 nm diameter,[14] physical properties are summarized in Table I) was placed on top of the sensor while measuring the voltage drop. The beads were magnetized with a −15 Oe in-plane applied field generated by electromagnetic coils leading to estimated local dipole fields just below the beads of +1.5 Oe for 2 μm beads, and +30 Oe for 250 nm beads.

Figure 2 presents the bead detection results. Current through the sensor is 5 mA and the applied field is −15 Oe. At time $t = 100$ s, the 2 μm beads are added onto the chip and the signal rises as the beads settle on the sensor. Then, at time $t = 300$ s, the beads are washed away and the signal returns to the baseline. At times $t = 700$ s and $t = 1050$ s, respectively, the experiment is repeated yielding the same result. At time $t = 1400$ s, the 250 nm beads are added to the chip and at time $t = 1650$ s the beads are washed away. The experiment is repeated with the 250 nm beads at times $t = 2250$ s and $t = 2650$ s, respectively. The 250 nm beads give higher saturation signals than the 2 μm beads due to their higher susceptibility and higher number on top of the sensor area. Saturation of the signal occurs when the beads are piled up on top of the sensor and the addition of another bead is no longer sensed because it is too far away from the sensor to be detected.

Figure 3 shows sensor response to an increasing or decreasing number of beads over the sensing area (2 μm Micromod-M beads). Current through the sensor is 10 mA and applied field is −15 Oe. The estimate of how many beads are floating over the sensitive area at a given time is carried out by visual inspection through a microscope during the measurements. Specifically, the large numbers of beads

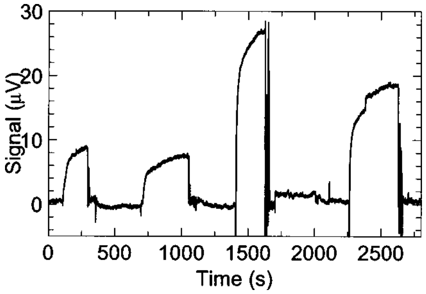

FIG. 2. Bead detection measurements. A constant voltage ($V_0 = -464\ \mu$V) is subtracted from the signal to give a baseline at 0 μV. At times $t = 100$ s and $t = 700$ s the 2 μm beads are added to the chip, and at times $t = 300$ s and $t = 1050$ s they are washed away. The same is done for 250 nm beads (added at $t = 1400$ s and $t = 2250$ s, removed at $t = 1650$ s and $t = 2650$ s). The signal rises when beads settle on top of the sensor and returns to the baseline when the beads are removed from the sensor.

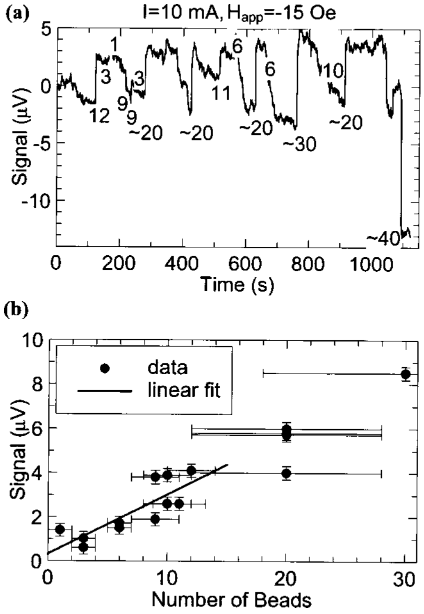

FIG. 3. Detection of clusters. The field applied with electromagnetic coils was $H_{app} = -15$ Oe. (a) The sensor signal measured while observing the sensor through an optical microscope keeping track of when beads were floating over the sensor. The numbers written on the chart are the numbers of beads entering or leaving the space over the sensitive area at the specified time. The estimate of bead number giving the voltage change at a specific time was made by visual inspection through the microscope. Specifically, the large numbers are connected with uncertainty due to the difficulty of counting beads in a limited amount of time. (b) Summary of the data from chart (a). The immediate change in signal for a given bead number entering or leaving the space over the sensor. For low bead numbers, the result is $V_{bead} \sim 0.3\ \mu$V.

are connected with uncertainty since it is difficult to judge the exact number of beads constituting a cluster. For low bead numbers, the resulting one-bead signal is $V_{\text{bead}} \sim 0.3\ \mu\text{V}$. The noise level for these dc measurements is 200–300 nV.

In conclusion, detection of commercially available 2 μm and 250 nm superparamagnetic beads (Micromer-M and Nanomag-D)[14] used for bioapplications was demonstrated using an exchange-biased permalloy planar Hall sensor. Hence, this planar Hall sensor has potential as a magnetic biosensor, e.g., for deoxyribonucleic acid detection. The technique is sufficiently sensitive to detect only a few magnetic beads and therefore also biomolecules even if only few are present in the sample. For small numbers of 2 μm beads, bead detection experiments showed a single-bead signal of $V_{\text{bead}} \sim 0.3\ \mu\text{V}$.

Due to the cross geometry, the planar Hall sensor uses all its active surface for bead/biomolecule detection, which is not the case for meandering-type GMR or spin valve sensors, where almost one-half of the target biomolecules will sit over a nonsensing area. A second advantage, not exploited here, concerns the theoretically higher signal-to-noise (S/N) ratio for planar Hall sensors when compared with GMR or spin valve sensors. For comparable sensing areas, although the spin valve sensor yields signals 5 to 10 times higher, the planar Hall sensor should have a noise level (in the $1/f$ dominated low-frequency regime) about 20 times lower offering the possibility of single bead detection for nanometer-sized beads.

Using a lock-in amplifier to obtain a bandwidth of 1 Hz will improve the S/N considerably. For the reported sensor size with an applied current of 15 mA and defining the minimum detectable signal as four times the noise level, the theoretical $1/f$ noise level is ≈ 0.6 nV and the sensor should be able to detect a single 250 nm bead. If the sensor size is reduced to $2.5\ \mu\text{m} \times 2.5\ \mu\text{m}$ and the current is reduced to 10 mA, it should be possible to detect a single 40 nm bead with $\chi = 6$ (SI).

Future work includes integration with microfluidic systems along with a demonstration of the planar Hall sensor as a biosensor and single micro- and nanobead detection.

[1] D. R. Baselt, G. U. Lee, M. Natesan, S. W. Metzger, P. E. Sheehan, and R. J. Colton, Biosens. Bioelectron. **13**, 731 (1998).

[2] R. L. Edelstein, C. R. Tamanaha, P. E. Sheehan, M. M. Miller, D. R. Baselt, L. J. Whitman, and R. J. Colton, Biosens. Bioelectron. **14**, 805 (2000).

[3] M. M. Miller, P. E. Sheehan, R. L. Edelstein, C. R. Tamanaha, L. Zhong, S. Bounnak, L. J. Whitman, and R. J. Colton, J. Magn. Magn. Mater. **225**, 138 (2001).

[4] D. L. Graham, H. Ferreira, J. Bernardo, P. P. Freitas, and J. M. S. Cabral, J. Appl. Phys. **91**, 7786 (2002).

[5] H. A. Ferreira, D. L. Graham, P. P. Freitas, and J. M. S. Cabral, J. Appl. Phys. **93**, 7281 (2003).

[6] D. L. Graham, H. A. Ferreira, P. P. Freitas, and J. M. S. Cabral, Biosens. Bioelectron. **18**, 483 (2003).

[7] G. Li, V. Joshi, R. L. White, S. X. Wang, J. T. Kemp, C. Webb, R. W. Davis, and S. Sun, J. Appl. Phys. **93**, 7557 (2003).

[8] P. A. Besse, G. Boero, M. Demierre, V. Pott, and R. Popovic, Appl. Phys. Lett. **80**, 4199 (2002).

[9] F. Montaigne, A. Schuhl, F. N. Van Dau, and A. Encinas, Sens. Actuators **81**, 324 (2000).

[10] F. N. Van Dau, A. Schuhl, R. J. Childress, and M. Sussiau, Sens. Actuators, A **53**, 256 (1996).

[11] L. Ejsing, M. F. Hansen, and A. K. Menon, *Proceedings of the 17th European Conference on Solid-State Transducers, Eurosensors 2003, 21–24 September 2003, Guimarães, Portugal* (University of Minho, Guimarães, Portugal, 2003), p. 1095.

[12] R. C. O'Handley, *Modern Magnetic Materials* (Wiley, New York, 2000).

[13] V. Gehanno, P. P. Freitas, A. Veloso, J. Ferreira, B. Almeida, J. B. Sousa, A. Kling, J. C. Soares, and M. F. Silva, IEEE Trans. Magn. **35**, 4361 (1999).

[14] http://www.micromod.de

Available online at www.sciencedirect.com

SCIENCE DIRECT®

Journal of Magnetism and Magnetic Materials 293 (2005) 677–684

Journal of magnetism and magnetic materials

www.elsevier.com/locate/jmmm

Magnetic microbead detection using the planar Hall effect

Louise Ejsing[a,*], Mikkel F. Hansen[a], Aric K. Menon[a], Hugo A. Ferreira[b], Daniel L. Graham[b], Paulo P. Freitas[b]

[a]*Department of Micro and Nanotechnology (MIC), Technical University of Denmark (DTU), Building 345 east, DK-2800 Kongens Lyngby, Denmark*

[b]*Institute of Engineering of Systems and Computers—Microsystems and Nanotechnologies (INESC-MN), Rua Alves Redol 9, Lisbon 1000-029, Portugal*

Abstract

Magnetic sensors based on the planar Hall effect of exchanged-biased permalloy have been fabricated and characterized. It is demonstrated that the sensors are feasible for detecting just a few commercial 2.0 μm magnetic beads commonly used for bioseparation (Micromer-M, Micromod, Germany) and that the sensor sense current is sufficient to generate a signal from the beads.

PACS: 75; 47; −m

Keywords: Hall effect (planar); Micromer-M; Magnetic sensor; Biosensor; Permalloy ($Ni_{80}Fe_{20}$); MnIr ($Mn_{76}Ir_{24}$); Detection of microspheres

1. Introduction

In the lab-on-a-chip concept all steps in analyzing a sample are assembled on a single chip. The idea is to use such a chip directly after taking, e.g., a blood sample to obtain an immediate answer as to the presence of a specific molecule. Our focus has been on the detection step, where we aim to use magnetic beads and integrate bead detection with microfluidic channels.

Detection of superparamagnetic beads for biosensor applications has been demonstrated using GMR sensors [1–3], spin valve sensors [4–7], and a silicon Hall sensor [8]. Planar Hall effect sensors have been shown to exhibit nano-Tesla sensitivity [9,10] and have recently been investigated for their use in magnetic biodetection [11]. We propose the use of microfabricated planar Hall effect (PHE) sensors and demonstrate bead detection in zero externally applied field using an exchange-biased permalloy sensor. This sensor is significantly

---

[*] Corresponding author. Tel.: +45 4525 6336; fax: +45 4588 7762.
E-mail address: loe@mic.dtu.dk (L. Ejsing).

0304-8853/$ - see front matter © 2005 Elsevier B.V. All rights reserved.
doi:10.1016/j.jmmm.2005.02.071

improved compared to the unbiased nickel PHE sensor previously demonstrated [11].

The purpose of exchange-biasing the sensor is to ensure a sufficient uniaxial anisotropy, a well-defined single domain state and to introduce a unidirectional anisotropy. The sign of the sensor output depends upon whether the film magnetization is initially parallel or antiparallel to the sensor current (Section 2) and thus it is important to have a well-defined initial orientation. For the previously demonstrated Ni sensor, which exhibited uniaxial anisotropy, this was achieved by saturating the sensor along one of the easy directions prior to each measurement. Due to the unidirectional anisotropy this step is now eliminated and, additionally, the higher anisotropic magnetoresistance of permalloy compared to Ni results in a larger signal.

2. Planar Hall effect sensor principle

The magnetic sensor is based on the anisotropic magnetoresistance of ferromagnetic materials. For such materials, Ohm's law can be written [12]

$$\vec{\mathbf{E}} = \hat{\mathbf{M}}(\mathbf{J}\cdot\hat{\mathbf{M}})[\rho_{||}-\rho_{\perp}] + \rho_{\perp}\mathbf{J} + \rho_{\mathrm{H}}\hat{\mathbf{M}}\times\mathbf{J}, \tag{1}$$

where $\hat{\mathbf{M}}$ denotes a unit vector along the magnetization direction and $\mathbf{J}$ is the current density. ρ_{H} is the ordinary Hall resistivity arising from the Lorentz force deflection of the charge carriers. $\rho_{||}$ and $\rho_{\perp}$ are the resistivities when the magnetization vector is parallel and perpendicular to the current density, respectively. Generally, $\rho_{||} > \rho_{\perp}$ and for Ni–Fe alloys $\Delta\rho\cdot\rho_{\mathrm{av}}^{-1} \equiv (\rho_{||}-\rho_{\perp})\cdot\rho_{\mathrm{av}}^{-1}$ attains values up to 3% at room temperature [13]. A sensor based on the planar Hall geometry illustrated in Fig. 1 can be used for detection of small magnetic fields [9–11,14]. The sensor consists of a thin ferromagnetic film through which a current I_x is applied in the x-direction and the voltage V_y is measured in the y-direction. The magnetization vector lies in the plane of the sensor at an angle ϕ to the current direction. For this geometry Eq. (1) reduces to

$$E_y = (\rho_{||}-\rho_{\perp})J_x \sin\phi\cos\phi \tag{2}$$

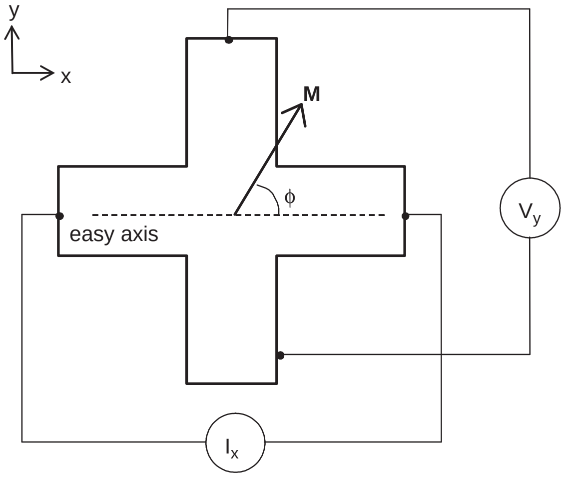

Fig. 1. Planar Hall geometry. A current is applied in the x-direction and a voltage is measured in the y-direction. The magnetization vector, $\mathbf{M}$, lies in the x–y-plane at an angle, ϕ, to the current direction. The easy axis is along the current direction.

and the measured voltage becomes

$$V_y = \tfrac{1}{2} I_x \Delta R \sin(2\phi), \tag{3}$$

where $\Delta R \equiv (\rho_{||}-\rho_{\perp})\cdot t_{\mathrm{film}}^{-1}$ and t_{film} is the film thickness. The basic principle of the sensor is the following. The easy axis and the easy direction of magnetization are defined in the film along the current direction by exchange-coupling to an antiferromagnetic material. If a magnetic field is subsequently applied perpendicular to the easy axis the magnetization vector rotates away from the easy direction, giving rise to an electrical response according to Eq. (3). To model the sensor response, we can to a first approximation write the magnetic energy density of the film as

$$U = K_{\mathrm{u}}\sin^2\phi - U_{\mathrm{E}}\cos\phi - \mu_0 M H_y \sin\phi, \tag{4}$$

where K_{u} is the uniaxial anisotropy constant, U_{E} is the exchange energy density, and H_y is the magnetic field affecting the sensor along the y-direction. For small angles, $\cos\phi \approx 1$, and minimization of the energy yields

$$\sin\phi \approx \frac{\mu_0 M H_y}{2K_{\mathrm{u}} + U_{\mathrm{E}}} \equiv \frac{H_y}{H_{\mathrm{C}} + H_{\mathrm{E}}}, \tag{5}$$

which is valid for $H_y \ll H_C + H_E$. H_C is the anisotropy field, and H_E is the exchange coupling field. Insertion in Eq. (3) yields the ideal sensor response

$$V_y \approx I_x \Delta R \frac{H_y}{H_C + H_E}. \tag{6}$$

The expected sensor response, plotted in Fig. 2, is linear to within 2% for $|H_y(H_C + H_E)^{-1}| < 0.2$ with the sensitivity

$$S_0 \equiv \frac{V_y}{H_y I_x} = \frac{\Delta R}{H_C + H_E}. \tag{7}$$

The PHE magnetic sensor is sensitive to magnetic fields in the sensor plane. This is utilized to detect the dipole field from magnetic beads as illustrated in Fig. 3. The applied magnetic field magnetizes the bead and creates a dipole field, which is antiparallel to the applied field in the sensor plane. Thus, the presence of magnetic beads gives rise to a reduction of the applied field, which can be detected.

The magnetic beads contain superparamagnetic nanoparticle inclusions and will show a linear response at low fields. Hence, the bead magnetization can be written $\mathbf{M} = \chi \mathbf{H}$, where χ is the bead susceptibility (including demagnetization effects) and $\mathbf{H}$ is the field intensity containing contributions from the applied field, the field generated by the current through the sensor, the field from other beads, and possibly the fringing field from the sensor itself. It will be assumed below that $\mathbf{H}$ is essentially in the y-direction. The magnetic field outside a homogeneously magnetized sphere is identical to the dipole field

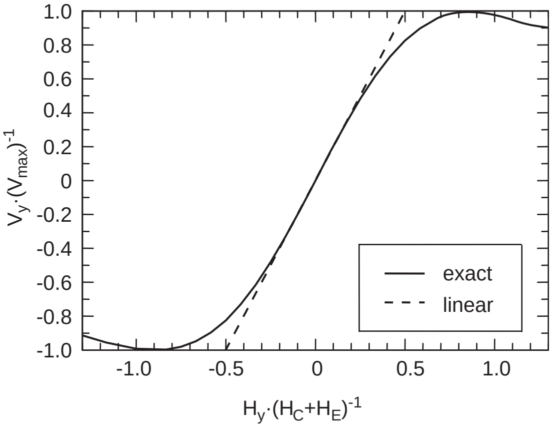

Fig. 2. Expected ideal sensor response as a function of applied magnetic field strength. The dotted line shows the approximation of Eq. (6) $V \propto H_y \cdot (H_C + H_E)^{-1}$.

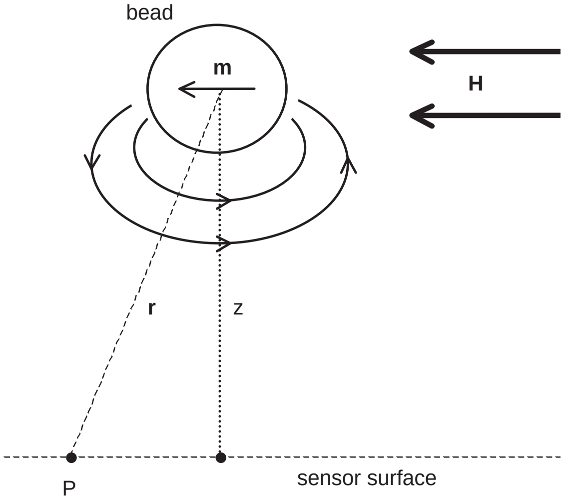

Fig. 3. Magnetic bead with moment, **m**, positioned relative to the sensor surface. The bead is magnetized in the field, **H**, and produces a field in the opposite direction at the sensor.

$$\mathbf{H}_{\text{dip}} = \frac{m}{4\pi r^3}(3\hat{\mathbf{r}}(\hat{\mathbf{m}} \cdot \hat{\mathbf{r}}) - \hat{\mathbf{m}}), \tag{8}$$

where ^ denotes unit vectors, $\mathbf{r} = r\hat{\mathbf{r}}$ is a vector connecting the centre of the bead to a point P on the sensor, $\mathbf{m} = \chi V_{\text{bead}} \mathbf{H}$ is the bead moment and V_{bead} is the bead volume. From this, a crude estimate of the order of magnitude of the dipole field experienced by the sensor is $\sim -\mathbf{H}\chi V_{\text{bead}}(4\pi z^3)^{-1}$, where z is the normal distance between the centre of the bead and the sensor surface. The error made by this assumption becomes smaller when the sensor dimension becomes comparable to or smaller than z. Defining the influenced area, A_{bead}, of the sensor as the cross-section of the bead and averaging the dipole field over the entire sensor surface, one can find that the crude estimate given above should be multiplied by a factor 0.38 to be correct [15]. Thus, defining the fraction of the sensor area influenced by the bead as $f = A_{\text{bead}}/A_{\text{sensor}}$, the total field experienced by the sensor from N independently acting beads is

$$H_y \approx H_{\text{app}} - \frac{0.38 f N H \chi V_{\text{bead}}}{4\pi z^3}, \tag{9}$$

where H_{app} is the applied external field and it is reminded that H is the total magnetic field on a bead in the y-direction. Hence, the presence of the beads reduce the effective sensitivity of the sensor to an external field by a number proportional to the number of beads and the voltage drop over the sensor is estimated to

$$V_y = S_0 H_y I_x \approx V_0 \left(1 - \frac{H}{H_{\text{app}}} \frac{0.38 f N \chi V_{\text{bead}}}{4\pi z^3} \right), \tag{10}$$

where $V_0 = S_0 H_{\text{app}} I_x$.

3. Sensor fabrication and characterization

The PHE sensors are fabricated using conventional clean room fabrication methods. The sensor layer structure of Ta(30 Å)–NiFe(50 Å)–MnIr(200 Å)–NiFe(200 Å)–Ta(30 Å), presented in Fig. 4, is deposited by ion beam deposition on top of a 3″ silicon wafer passivated by Al_2O_3, and a TiWN(150 Å) anti-reflecting layer is sputtered on top. The 50 Å NiFe layer is included to ensure proper growth conditions for the following MnIr layer. For ion beam deposition conditions see Gehanno et al. [13]. Here, MnIr stands for $Mn_{76}Ir_{24}$ and NiFe stands for $Ni_{80}Fe_{20}$. During ion beam deposition a homogeneous magnetic field of 40 Oe is applied in order to form an easy magnetic direction. The sensors are patterned by direct laser writing into photoresist and the excess material is ion-milled away in a physical dry-etch. Current leads and bonding pads of 0.3 μm thick Al are defined in final lithography, physical vapour deposition, and lift-off steps. The whole wafer is then passivated by 0.2 μm sputtered SiO_2, and the contact pads are opened by reactive ion etching. Finally, the wafer is diced and wire bonded to the electrical contacts.

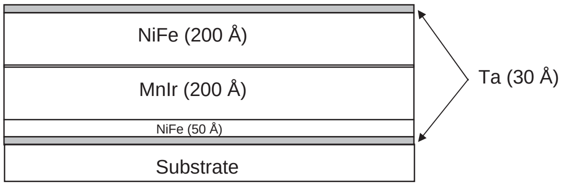

Fig. 4. Sensor material layer structure. The bottom Ta(30 Å) layer is for adhesion and epitaxial growth of NiFe(50 Å), which ensures epitaxial growth of the antiferromagnetic MnIr(200 Å), which pins the sensor layer of NiFe(200 Å), top Ta(30 Å) hinders corrosion.

Fig. 5 shows a micrograph of a sensor. A dotted frame indicates the sensitive area of the sensor, but beads from the vicinity can contribute to the signal with reduced magnitude according to the r^{-3} dependence of the dipole field.

Fig. 6 shows vibrating sample magnetometer data obtained on a continuous film of the stack measured with the applied field along the deposition field. It is seen that the hysteresis loop essentially consists of two hysteretic signals, one accounting for ≈83% of the film moment with $H_E = 41$ Oe and $H_C = 18$ Oe and another accounting for ≈17% of the film moment with $H_E = 274$ Oe and $H_C = 21$ Oe. The two signals are attributed to the 200 and 50 Å NiFe layers, respectively. In addition, there is a small hysteretic

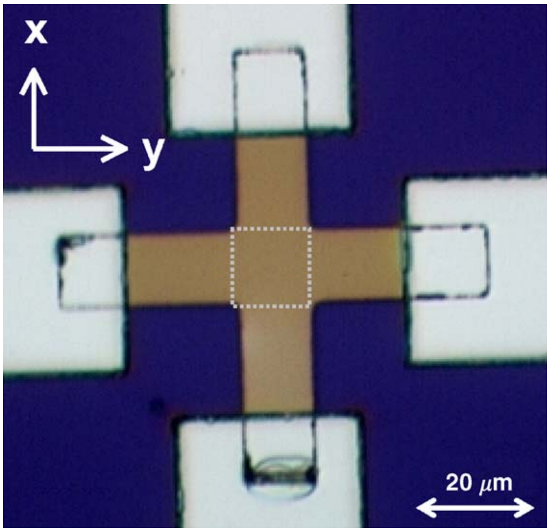

Fig. 5. Top view micrograph of the planar Hall sensor. The cross is made of magnetic layers (see layer structure in Fig. 4), and the central area marked by a dotted frame is the 10 μm × 10 μm sensitive area of the sensor. Current leads are made of 0.3 μm thick Al.

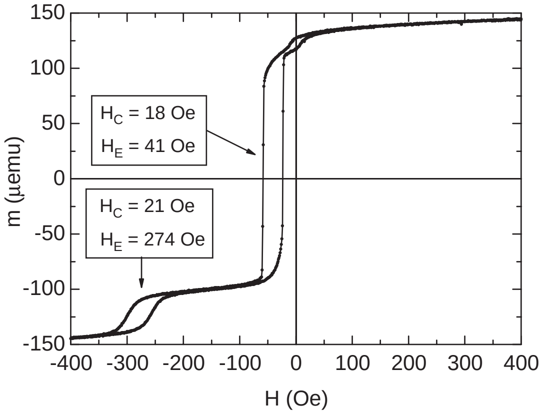

Fig. 6. Vibrating sample magnetometer data on the exchange-biased permalloy film (see Fig. 4 for details on the material structure) measured with the applied field along the easy direction.

impurity near zero field of unknown origin. Note the enhancement of the coercive field with respect to that of unbiased permalloy and that the value of $H_E + H_C$ to enter in Eq. (7) for the 200 Å biased permalloy layer is 59 Oe. This layer is expected to dominate the electrical response of the sensor.

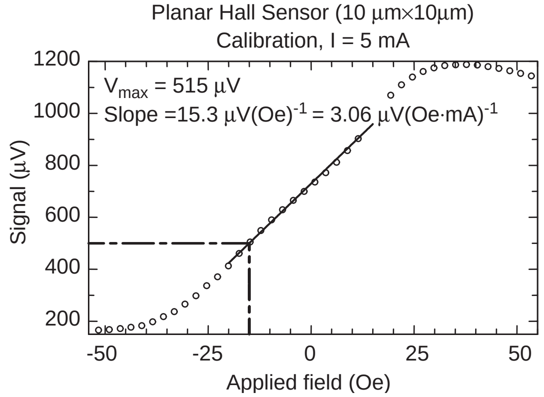

Fig. 7. Calibration curve for the planar Hall effect sensor. $V_{\max}$ is the highest signal minus the offset value at $H = 0\,\mathrm{Oe}$, but the curve is shifted from $H = 0\,\mathrm{Oe}$ due to a remanent magnetization of the coil used to produce the applied field. Hence, $V_{\max}$ is measured as $\frac{1}{2}\times$peak-to-peak signal. The slope of the linear region gives the sensitivity of the sensor as $S = 3.06\,\mu\mathrm{V(Oe\,mA)}^{-1}$ linear to within 2.8%. At $H = -15\,\mathrm{Oe}$, $V_y = 500\,\mu\mathrm{V}$.

Table 1
Experimental and theoretical values for sensor calibration

Property	Experimental	Theoretical
R_{DC}	51.9 Ω	25 Ω
AMR ($\Delta R \cdot R^{-1}$)	1.3%	1.9%
$V_{\max}$ (Eq. (3) for $\varphi = \pi/4$)	515 μV	458 μV
$H(V = V_{\max})$	44 Oe	47 Oe
S_0	$3.06\,\mu\mathrm{V(Oe\,mA)}^{-1}$	$3.86\,\mu\mathrm{V(Oe\,mA)}^{-1}$

The electrical characterization of the PHE sensors was carried out by measuring the DC sensor response using a digital multimeter as function of the magnetic field provided by electromagnetic coils. The sensor voltage measured for fields between ≈ ±50 Oe for a sensing current $I_x = 5\,\mathrm{mA}$ is shown in Fig. 7. It is seen that there is a significant additional voltage offset due to, e.g., imperfections of the lithographic process and a small field offset due to a remanent field of the electromagnet. Though present throughout the measurements, the voltage offset does not influence the sensitivity of the PHE sensor and is hence subtracted from the following results. It is seen that the general trend of the signal is in agreement with that expected from the simple theory (Fig. 2). The low-field part of the curve (between +15 and −20 Oe applied field strength) is linear to within 2.8% with a slope of $S_0 = 3.06\,\mu\mathrm{V(Oe\,mA)}^{-1}$. The slope is reproducible both for the particular sensor and for all sensors on the same wafer. Table 1 summarizes the experimental characteristics of the sensor and the theoretical predictions for comparison. In the theoretical estimates of R_{DC} and the AMR, based on the values for AMR of NiFe and resistivities found in [13], shunting of the current through the other layers is taken into account. For the estimate of $V_{\max}$ and the slope, only the NiFe(200 Å) layer is considered; though the NiFe(50 Å) might affect the signal, its contribution should be much smaller than that from the thick layer.

4. Detection of magnetic beads

In a recent paper [16], we have demonstrated that the present sensors are feasible for the detection of commercial 2 μm Micromer-M and 250 nm Nanomag-D magnetic beads (Micromod, Germany [17]). These experiments were performed by measuring the voltage drop across the sensor while droplets containing magnetic beads were introduced to the sensor and subsequently washed off. A sensing current of 10 mA and an applied external field of −15 Oe were used. From a comparison of a direct counting of beads flowing by the sensor under an optical microscope with the corresponding sensor signals, it was estimated that each 2 μm Micromer-M bead contributed with a signal of ~0.3 μV. The corresponding noise level of the unshielded DC measurements was of the same magnitude.

Here, we present experiments on the detection of 2 μm Micromer-M beads with and without applying an external field from the electromagnetic coils of −15 Oe. The properties of the Micromer-M beads are summarized in Table 2. A bead magnetized by −15 Oe gives rise to a field just below the bead of +1.5 Oe. The contribution to the field outside the sensor from the sensing current can be estimated using Ampère's law to

$$H_{\text{sense}}(z) \approx \frac{I_x}{2w + 2\pi z}, \tag{11}$$

where w is the width of the current line. At $z =$ 1.5 μm, which is a typical value for the first layer of 2 μm beads, this field amounts to ≈0.4 Oe per mA applied sensing current.

Fig. 8 shows an example of a bead detection experiment performed in an applied field of −15 Oe. The current applied to the sensor is $I_x =$ 15 mA giving rise to an estimated field of 6 Oe from the sensing current at the first monolayer of beads. At time $t = 250$ s beads are added and the signal changes as the beads settle on top of the sensor, at time $t = 550$ s the beads are washed off the sensor and the signal returns to its previous value. At times $t = 750$ and 1025 s, respectively, the experiment is repeated yielding the same result though with a little higher saturation signal. An estimate of the sensor coverage assuming that the dipole fields from the beads are independent and that the beads are close packed on the sensor surface yields ≈1.5 monolayers. The electrical noise level of the measurement is ≈250 nV.

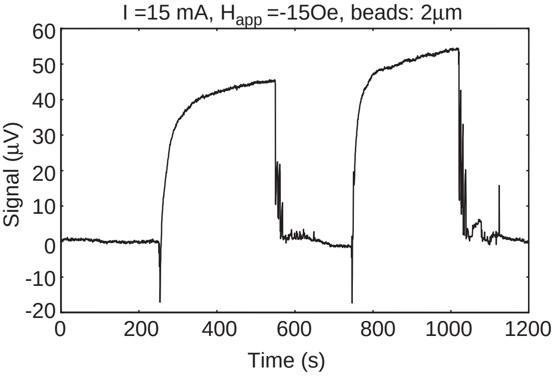

Fig. 8. Bead detection in an applied field, $H_{\text{app}} = -15$ Oe and a sensing current of $I_x = 15$ mA. A voltage offset of 1483 μV is subtracted. At times $t = 250$ and 750 s the beads are added onto the chip, and the signal changes according to Eq. (10) until it reaches a saturation value. At times $t = 550$ and 1025 s the beads are washed off the sensor, and the signal returns to the baseline.

Fig. 9 shows detection measurements of beads without applying a magnetic field. The current through the sensor, $I_x = 10$ mA, corresponds to a field 1.5 μm above the sensor of ≈4 Oe. At time $t = 580$ s a dilute bead solution is added to the chip and at time $t = 660$ s the beads are washed off the sensor. At times $t = 675$ and 795 s groups of beads are observed on top of the sensitive area. The first group constitutes two beads, the other four beads. They are removed by flushing with water at times $t = 700$ and 810 s, respectively. At time $t = 840$ s a concentrated solution of beads is added to the chip and the signal saturates at approximately $V =$ 30 μV, then the beads are removed between $t =$ 920 and 950 s and the signal returns to its baseline. The electrical noise level of the measurement is ≈250 nV.

These measurements show that the magnetic field generated from the sensing current is

Table 2
Physical properties of Micromer-M beads [16]

Micromer-M beads	
Diameter	2 μm
Concentration	>25 mg ml^{-1}
Density (ρ)	1.4 g cm^{-3}
χ (measured at INESC-MN)	0.3 ± 0.1 [SI]

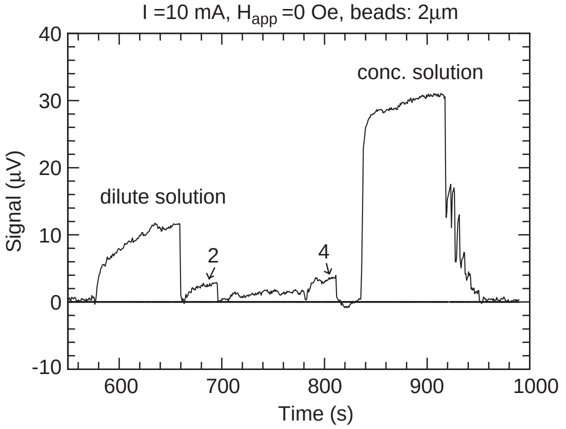

Fig. 9. Bead detection in zero applied field, $H_{\mathrm{app}} = 0\,\mathrm{Oe}$ and a sensing current of $I_x = 10\,\mathrm{mA}$. A voltage offset of $1775\,\mu\mathrm{V}$ is subtracted. The sensor senses a diluted bead solution, then few beads (2 and 4), and a concentrated bead solution with a saturation signal of $V = 30\,\mu\mathrm{V}$.

sufficient to yield a significant response from the beads. Due to the inhomogeneous nature of this field, it will also assist in the collection of beads on top of the sensor. The fact, that the peaks for two and four beads are clearly distinguishable indicates that the sensors are feasible for the detection of a few beads or a single bead even in the absence of an externally applied magnetizing field. It is noted that the noise level of the unshielded DC measurements is expected to be improved significantly by use of lock-in technique. Although the sensor signal of PHE sensors is lower compared to equivalent spin valve and GMR sensors, the $1/f$ dominated low-frequency noise level is even lower due to the higher number of charge carriers such that the signal-to-noise ratio turns out to be a factor of 3–4 higher [15]. Thus, PHE sensors are promising candidates for the detection of single magnetic beads with diameters well below 1 μm.

Similar experiments have been carried out for a number of sensing currents between 5 and 15 mA and an analysis of the sensor response and estimates of the number of beads collected on the sensor using Eq. (10) with the magnetizing field given by Eq. (11) yield roughly a constant coverage of 1.4 monolayers and no clear dependence on the applied sensing current is observed. This is likely due to the rather high initial concentration of beads in the fluid such that the sensor is essentially saturated with beads and that the addition of more beads does not lead to a significant signal increase due to the r^{-3} decay of the dipole field from the beads. Also, it is difficult to exactly repeat experimental conditions (fluid amounts, settle times, number of beads, etc.) from one experiment to the next. Experiments on systems integrated with microfluidic channels with very dilute bead solutions and a constant fluid flow will probably aid in the clarification of the contribution of the sensing current to the capture efficiency and bead signal.

5. Conclusion

The planar Hall effect sensor is demonstrated capable of detecting the presence of 2 μm Micromer-M beads. These beads are used for attaching biomolecules in biological applications such as biosensing, separation and purification protocols. The bead surfaces are covered with streptavidin to enable binding of DNA or proteins. Hence, with a suitable biochemical coating of the sensor surface, the planar Hall effect sensor can detect the presence of DNA or proteins via the presence of the magnetic bead. The sensor is demonstrated sensitive enough to detect very few beads. Due to the simple fabrication scheme, the planar Hall sensor can be easily integrated into lab-on-a-chip systems, and the demonstration of bead detection in the field generated by the sensing current, i.e., without applying external fields, is promising for chip integration.

Due to the cross geometry, the planar Hall effect sensor uses its entire active surface for bead and biomolecule detection, which is not the case for meandering-type GMR or spin valve sensors. In addition, the sensing geometry, compared with the ordinary Hall sensor, utilizes all the magnitude of the magnetic dipole field induced by the bead. Another advantage, not exploited here, is that the theoretical signal-to-noise ratio of planar Hall effect sensors is higher than those of corresponding GMR and spin-valve sensors [15].

Future work includes demonstration of the planar Hall effect sensor as a biosensor, and integration with fluidic biochips. Another prospect is to demonstrate detection of single nanometer-sized beads.

References

[1] D.R. Baselt, G.U. Lee, M. Natesan, et al., Biosensors Bioelectron. 13 (1998) 731.
[2] R.L. Edelstein, C.R. Tamanaha, P.E. Sheehan, et al., Biosensors Bioelectron. 14 (2000) 805.
[3] M.M. Miller, P.E. Sheehan, R.L. Edelstein, et al., J. Magn. Magn. Mater. 225 (2001) 138.
[4] D.L. Graham, H. Ferreira, J. Bernardo, et al., J. Appl. Phys. 91 (2002) 7786.
[5] H.A. Ferreira, D.L. Graham, P.P. Freitas, et al., J. Appl. Phys. 93 (2003) 7281.
[6] D.L. Graham, H.A. Ferreira, P.P. Freitas, et al., Biosensors Bioelectron. 18 (2003) 483.
[7] G. Li, V. Joshi, R.L. White, et al., J. Appl. Phys. 93 (2003) 7557.
[8] P.-A. Besse, G. Boero, M. Demierre, et al., Appl. Phys. Lett. 80 (2002) 4199.
[9] F. Montaigne, A. Schuhl, F.N. Van Dau, et al., Sensors Actuators 81 (2000) 324.
[10] F.N. Van Dau, A. Schuhl, J.R. Childress, et al., Sensors Actuators A 53 (1996) 256.
[11] L. Ejsing, M.F. Hansen, A.K. Menon, Planar Hall effect magnetic sensor for microbead detection, Extended Abstract, Eurosensors 2003, 2003, p. 1095.
[12] R.C. O'Handley, Modern Magnetic Materials, Wiley, New York, 2000.
[13] V. Gehanno, P.P. Freitas, A. Veloso, et al., IEEE Trans. Magn. 35 (1999) 4361.
[14] A. Schuhl, F.N. Van Dau, J.R. Childress, Appl. Phys. Lett. 66 (1995) 2751.
[15] P.P. Freitas, H.A. Ferreira, D.L. Graham, et al., in: M. Johnson (Ed.), Magnetoresistive Biochips, Elsevier, Amsterdam, 2004.
[16] L. Ejsing, M.F. Hansen, A.K. Menon, et al., Appl. Phys. Lett. 84 (2004) 4729.
[17] http://www.micromod.de.

Available online at www.sciencedirect.com

SCIENCE DIRECT

Biosensors and Bioelectronics 21 (2006) 1327–1332

BIOSENSORS & BIOELECTRONICS

www.elsevier.com/locate/bios

Short communication

Immobilisation of DNA to polymerised SU-8 photoresist

Rodolphe Marie[a], Silvan Schmid[b], Alicia Johansson[a], Louise Ejsing[a], Maria Nordström[a], Daniel Häfliger[a], Claus BV Christensen[a], Anja Boisen[a], Martin Dufva[a,*]

[a] *Department of Micro- and Nano-Technology, Technical University of Denmark, Bldg. 345, DK-2800 Lyngby, Denmark*
[b] *Department of Mechanical and Process Engineering, Nanotechnology Group, Swiss Federal Institute of Technology, ETH Zentrum CLA, CH-8092 Zurich, Switzerland*

Received 12 January 2005; received in revised form 10 March 2005; accepted 11 March 2005
Available online 31 March 2005

Abstract

SU-8 is an epoxy-based photosensitive resist, which is currently used for a large variety of MEMS and lab-on-a-chip applications. Here, we demonstrate a one-step process to functionalise SU-8 with DNA probes. The immobilisation procedure relies on direct coupling of DNA to SU-8 and resulted in surfaces with functional capture probe densities of approximately 10 fmol/mm^2 as determined by hybridisation assays with fluorescent labelled target molecules. A comparable density of functional capture probes was measured on commercial aldehyde coated glass. DNA probes did not decrease in hybridisation performance after 10 min incubation in water at 98 °C prior to hybridisation, indicating a covalent bond between DNA and SU-8. Finally, DNA microarrays of high quality were obtained on SU-8 by contact printing of probe solution directly on SU-8 demonstrating a simple method for the implementation of microarrays in microsystems.

Keywords: SU-8; DNA; Immobilisation; Photoresist; Hybridisation; Microstructure; MEMS; Lab-on-a-chip

1. Introduction

A future goal of the lab-on-a-chip is to integrate every step needed for detecting an analyte in the sample. The analysis of a sample is often based on size separations or interaction with a probe molecule either in solution or attached to a solid support. Using high throughput solid phase reactions like microarray, tens of thousands of analytes can be detected in one batch process. An efficient procedure for immobilising DNA or proteins to a solid support is essential for solid phase biochemical reactions. DNA has been successfully attached to glass (Zammatteo et al., 2000), oxidized silicon (Chrisey et al., 1996), silicon wafers (Strother et al., 2000), gold surfaces (Steel et al., 2000) and PMMA (Fixe et al., 2004a, 2004b) which all are relevant surfaces that can be micro-fabricated.

Because of its attractive mechanical properties, the epoxy-based photoresist SU-8 has become widely used for the fabrication of mechanical structures such as probes for scanning probe microscopy (Genolet et al., 1999, 2001). Furthermore, SU-8 can be fabricated into optical waveguides (Lee et al., 2002) and into microfluidic structures (Chuang et al., 2003; Heuschkel et al., 1998, Jackman et al., 2001; Seidemann et al., 2002a, 2002b). Those functionalities can be combined and integrated to build complete biosensors (Calleja et al., 2003; Mogensen et al., 2003). Since SU-8 is an attractive material for MEMS and micro fluidic devices, it is desirable to develop procedures for immobilising DNA directly on its surface. Here we describe a one-step procedure for attaching DNA directly onto cured micropatterned SU-8.

2. Materials and methods

2.1. Processing of photoresist

Commercially available SU-8 5 (glycidyl ether of bisphenol A) (Microresist Technology, Berlin, Germany) and re-

---

[*] Corresponding author. Tel.: +45 45 25 57 00; fax: +45 45 25 77 62.
E-mail address: mdu@mic.dtu.dk (M. Dufva).

0956-5663/$ – see front matter © 2005 Elsevier B.V. All rights reserved.
doi:10.1016/j.bios.2005.03.004

Table 1
Probes and target molecules

Probe name	Sequence	5′-End modification
MT(19)	5′-CCACGCTCATTGACAAGCT-3′	None
WT(19)	5′-CCACGCTCATCGACAAGCT-3′	None
MT(19)-NH2	5′-CCACGCTCATTGACAAGCT-3′	Amine
WT(19)-NH2	5′-CCACGCTCATCGACAAGCT-3′	Amine
WT(60)	5′-AAT TGC GAC AGT TGA AGA TGC TGC CAC GCT CAT CGA CAA GCT TGT CTC TGC GAA GTC ATC-3′	None
WT(60)-NH2	5′-AAT TGC GAC AGT TGA AGA TGC TGC CAC GCT CAT CGA CAA GCT TGT CTC TGC GAA GTC ATC-3′	Amine
W54-Cy3	5′-GAT GAC TTC GCA GAG ACA AGC TTG TCG ATG AGC GTG GCA GCA TCT TCA ACT GTC GCA ATT-3′	Cy3

“WT” refers to wild type probes and “MT” refers to single mismatch mutant probes.

sist thinner (gamma butyrolactone) were mixed in a 2:1 ratio. An SU-8 thickness of 0.8 μm was obtained when spin-coating the resist onto a glass wafer at a spinning speed of 3000 rpm. After spinning, the excess solvent was evaporated in a soft bake for 3 min at 65 °C and 2 min at 95 °C. The SU-8 was exposed to UV-light through a mask for 30 s at 9 mW/cm^2 and baked for 1 h at 90 °C. The wafers were developed 2 min in 1-methoxy-2-propyl acetate (PGMEA) and rinsed in isopropanol. Alternatively, SU-8 2002 (with the solvent cyclopentanone) was used to pattern SU-8 as 20 μm wide lines on glass. An SU-8 thickness of 1.7 μm was obtained by spin-coating the SU-8 2002 at 5000 rpm. The excess solvent was evaporated in a soft bake for 1 min at 60 °C and 1 min at 90 °C. The SU-8 was exposed to UV-light through a mask for 50 s at 8.1 mW/cm^2 and baked for 5 min at 60 °C and 10 min at 90 °C. The wafers were developed 2 min in PGMEA and rinsed in isopropanol. Free hanging SU-8 cantilevers were fabricated as described previously (Calleja et al., 2004).

2.2. Immobilisation of DNA

DNA probes (Table 1) were diluted to 10 μM in 1 M potassium phosphate pH 7.4 (Sigma–Aldrich Co., Steinheim, Germany) and manually spotted at a volume of 0.5 μL per spot on polymerised SU-8 or on aldehyde coated slides (CEL Associates Inc., Pearland, TX, USA). Alternatively the solutions were micro-spotted using a pin arrayer (Qarray, Genetix, New Milton, Hampshire, UK) at 50% humidity. Free hanging SU-8 cantilevers were functionalised by totally immersing the cantilevers in a few microliters of the DNA probe solution. The samples were incubated in a humid atmosphere for 1 h at 37 °C and washed for 10 min in MilliQ water. The arrays and structures were dried in a nitrogen stream.

2.3. Hybridisation

The SU-8 samples (SU-8, structured SU-8 and cantilevers) were hybridised for 1 h at 37 °C with a solution containing 10 nM W54-Cy3 (Table 1), 5 × sodium chloride sodium citrate (SSC) (Promega Corporation, Madison, US) and 0.1% sodium dodecylsulfate (SDS) (Sigma–Aldrich). The SU-8 samples were washed either in low stringent conditions (10 min in 1 × SSC containing 0.1% SDS at room temperature) or at high stringency (10 min in 0.1 × SSC containing 0.5% SDS at 45 °C). The arrays were rinsed in a buffer without SDS and dried with a gentle stream of nitrogen. Aldehyde coated slides were hybridised and washed using the same procedure.

2.4. Fluorescence detection

The arrays were scanned using a CCD scanner (ArrayWorX, Applied Precision, Issaquah, WA, USA). Mean values of the fluorescence density were obtained using the analysis software Data Inspector (Arrayworx). Spot intensity values on microarrays were obtained using the ScanAnalyze software (Eisen and Brown, 1999). The quantification of the density of the hybridisations were obtained by reporting the mean values of fluorescence density on a calibration curve made by spotting a dilution series of Cy3 labelled oligonucleotide (W54-Cy3) on an SU-8 substrate by hand (0.5 μL/spot) or by microarray printing on aldehyde coated slides (1 nL/spot).

3. Results and discussion

3.1. Auto-fluorescence of SU-8

SU-8 was deposited onto glass wafers at different thicknesses and scanned in the Cy3 channel to evaluate the optical properties of SU-8 in a Cy3-based fluorescent assay. An SU-8 layer of 0.8 μm thickness had approximately 20% higher fluorescence signal than the glass wafer alone, while 1.7, 12 and 120 μm thick layers of SU-8 had 50, 400 and 6600% more signal than glass, respectively, indicating that the thinnest SU-8-layer as possible should be used in order to minimise the background signal. This effect was apparent in hybridisation reaction in which the thinnest layer of SU-8 tested (0.8 μm) resulted in the highest signal to noise ratio (data not shown).

3.2. Immobilisation of DNA to SU-8

Investigating SU-8, we suspected the ability of DNA binding by condensation of primary and secondary amine groups with the non-cross linked epoxy rings present on the surface. Determination of optimal binding conditions showed that DNA could efficiently be immobilised using a “wet” incubation in which the DNA was spotted onto SU-8 in 0.5 μL

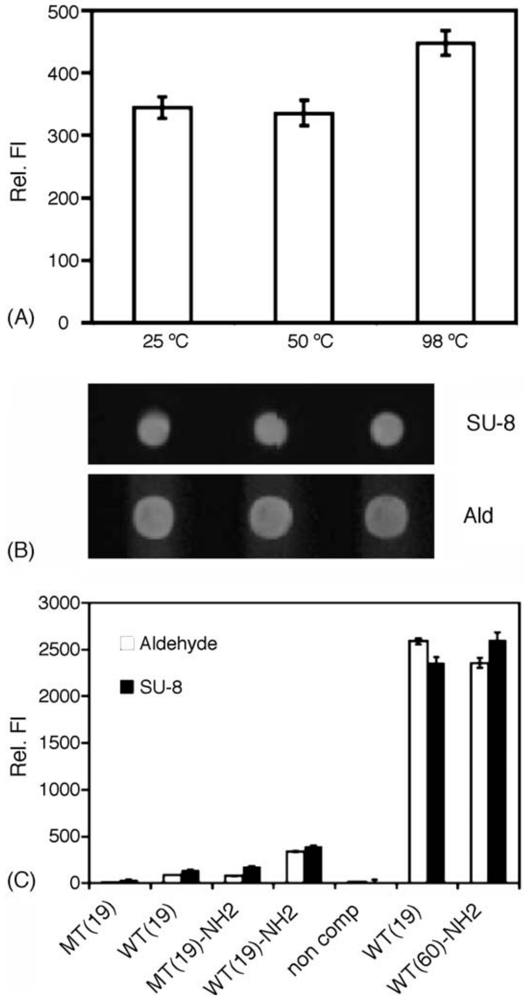

Fig. 1. Immobilisation of DNA to SU-8. (A) Heat stability of aminated 60 bp probe immobilised on SU-8. Three samples were washed at 25, 50 and 98 °C, respectively, before being hybridised to W54-Cy3. Note, the fluorescent signal was collected for 10-fold shorter time in Fig. 1A than in Fig. 1C and Fig. 2 hence, the lower fluorescent signal. (B) Image of spots on SU-8 and aldehyde coated slides after hybridisation reactions. W60-NH_2 probe was printed by contact printing according to material and methods section. (C) The quantified fluorescence hybridisation signal from DNA-capture probes dispensed on SU-8 and aldehyde coated slides using contact printing. "WT" and "MT" refers to wild type and mutant 19′mer probes, respectively.

drops followed by incubation in a humid environment for 1 h at 37 °C. A baking or UV-cross-link procedure did not improve DNA binding to the SU-8 surface (data not shown). To estimate the amount of probes that were available for hybridisation, the SU-8 pieces with immobilised DNA were hybridised with Cy3 labelled complementary target molecules (W54-Cy3, Table 1). The hybridised density was determined to be 6 fmol/mm^2 and no cross-hybridisation was observed to non-related probes (see also results from microarrays printed on SU-8, Fig. 1C). The DNA molecules were likely to be covalently attached to the SU-8 surface since 10 min incubation at 98 °C prior to hybridisation resulted in no loss of functional probes (Fig. 1A).

3.3. *DNA microarrays on SU-8*

Fabrication of DNA microarray on SU-8 was investigated by spotting 60 and 19 bp long probes, with and without amino-modification, onto SU-8 and aldehyde coated slides. The hybridised density of the 60 bp probes immobilised on SU-8 was between 8 and 13 fmol/mm^2 while microarrays on commercial aldehyde coated glass had a hybridised density of 9 fmol/mm^2. These hybridisation densities were comparable with those obtained previously on 2D microarray substrates (Dufva et al., 2004; Fixe et al., 2004a, 2004b). The microarray spots on SU-8 were perfectly circular with a diameter of 100 μm and appeared more homogeneous than the corresponding spots on the aldehyde coated slides, which had diameters of 150 μm (Fig. 1B). The smaller spot size on SU-8 is most likely due to the higher hydrophobicity of SU-8 as compared to aldehyde coated slides. These results demonstrate that high quality microarrays can be fabricated using SU-8 as substrate, which enables easy incorporation of microarrays into microfluidic systems.

3.4. *Specificity of immobilised probes*

The specificity of immobilised probes was investigated by hybridising W54-Cy3 to 19 base pair probes differing in only one base in the middle. After stringency wash, W54-Cy3 target bound three-fold better to the perfect match probes (WT(19)-NH2) than to the mismatch probes (MT(19)-NH2) immobilised on SU-8 while W54-Cy3 bound four-fold better to the perfect match amino-modified probes immobilised on aldehyde slides compared to the corresponding mismatch probe (Fig. 1C). The unmodified probes on both substrates resulted in ratio of four between the signal obtained from the WT probe and the MT probe (Fig. 1C). Thus, also unmodified probes that must be attached to SU-8 through at least one of the bases, can discriminate a mismatch hybridisation. These results corroborate previous findings that short unmodified probes, in this case immobilised to an agarose film by UV cross-linking, could discriminate a mismatch hybridisation (Dufva et al., 2004).

3.5. *Influence of amino modification and nature of the bond*

An amino modification in the terminal of the oligo probe had no influence on the hybridised signal from 60 bp probes immobilised on SU-8 substrates or the aldehyde coated slides (Fig. 1C). By contrast, the amino modified 19 bp probes resulted in a four to five-fold higher signal than the unmodified 19 bp probes (Fig. 1C). This apparently conflicting result might be explained by the facts that the 60 bp probes have more bases that can form bonds with the substrate and thus, have a larger likelihood to be attached through intra-DNA chain bonds than 19 bp probes.

The above results strongly indicate that the DNA is attached to the SU-8 by a covalent bond. However, it is not clear which functional groups are involved in the bond between DNA and SU-8. It is not likely that the DNA is connected to free epoxy groups since pre-treatment of SU-8 with epoxy ring opening agents (ethanolamine, HCl or acetic acid) did not influence probe binding and functionality (data not shown). A chrome etch (Cr etch 1020 (Transene Co Inc.)) did, however, block the SU-8 probe binding as assessed by hybridisation reaction indicating that a specific chemical group in the SU-8 is involved. Although the bond between DNA and SU-8 is not well defined, the bond could withstand boiling temperatures for 10 min, which is important for de-hybridisation reactions to regenerate sensor surfaces. It should be noted that unmodified DNA bound strongly to SU-8 indicating that DNA assays performed in SU-8 structures could suffer as a result of SU-8 sequestering sample DNA. Our results indicate that SU-8 surfaces were pacified by the hybridisation solution which was made of 5 × SSC and 0.1% SDS. We speculate that SDS binds to SU-8 and thereby blocks unspecific binding of target DNA to SU-8.

3.6. Immobilisation of DNA to structured SU-8

It would be desirable to be able to direct the DNA to certain parts of a microfluidic system, for example at sites of

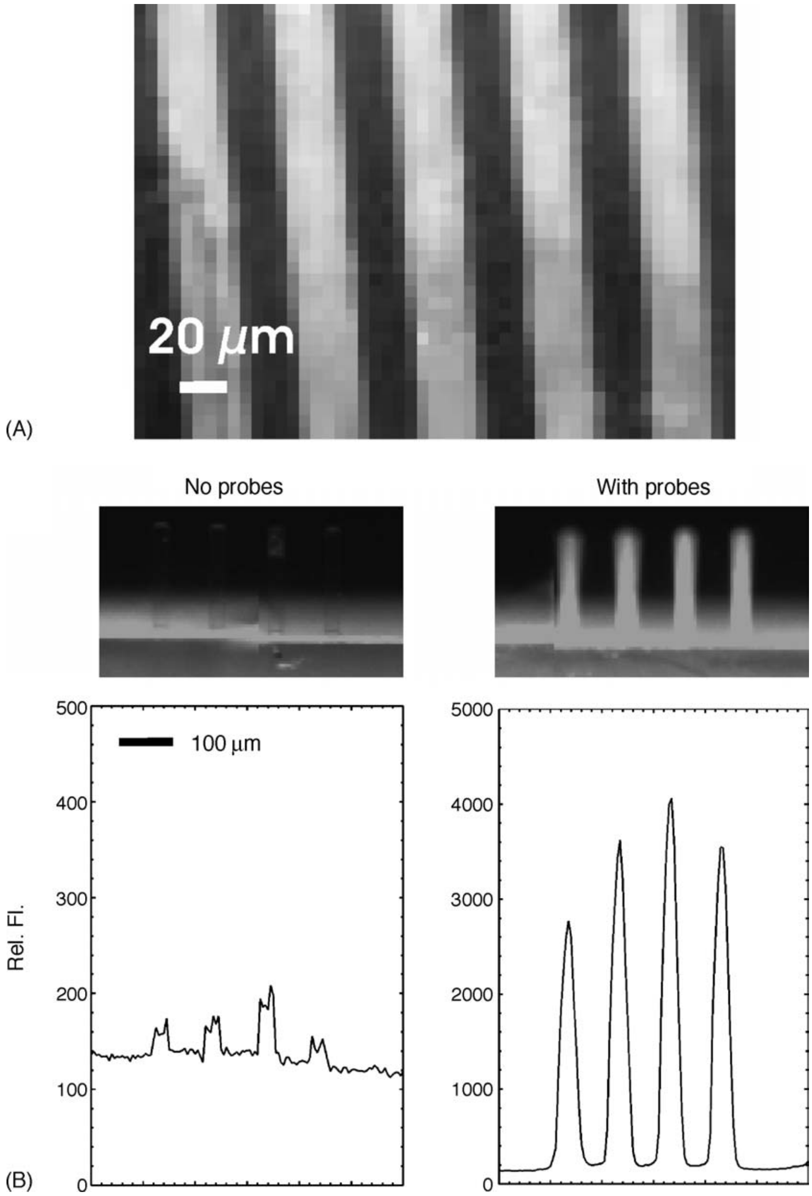

Fig. 2. Immobilisation of DNA to structured SU-8. (A) Fluorescence image showing the 20 μm wide lines of SU-8 (bright) on glass (dark). The image was scanned at the maximum resolution of the scanner (5 μm^2/pixel). (B) Image of hybridisation signals from SU-8 cantilevers that were not exposed to DNA-capture probe solution (upper left panel) and cantilevers exposed to DNA capture probe solution (upper right panel) prior to hybridisation. Lower panel shows quantification of the fluorescent signal on the cantilevers.

detection. To demonstrate the possibility of such localisation, SU-8 was structured as 20 μm wide lines on glass with 20 μm spacing. WT(60)-NH_2 was immobilised on the structured SU-8-sample and hybridised with W54-Cy3. Most of the hybridisation signals were localised on the SU-8 lines (Fig. 2A). The hybridised density on the SU-8 lines was estimated to be 9 fmol/mm^2 indicating good reproducibility of the immobilisation method, especially considering that the SU-8 samples were made of a SU-8 2002 instead of SU-8 5 as in Fig. 1. Since SU-8 5 and SU-8 2002 are based on two different solvents it is likely that it is chemical groups belonging to the SU-8 polymer chain that are involved in binding DNA. There was up to 20-fold difference in signals on the SU-8 lines as compared to the area between the lines. However, there was usually >100-fold difference in functional probes on SU-8 as compared to unmodified glass, indicating the presence of residual SU-8 on the glass after structuring. However, AZ5214E resist (Hoechst, Germany) binds DNA approximately as an unmodified glass wafer (data not shown) suggesting the possibility of fabricating localised SU-8 structures with high selectivity of probe binding using another layer of AZ5214E resist on top of the SU-8.

3.7. Immobilisation of DNA to SU-8 cantilevers

To demonstrate that DNA can be attached to relevant MEMS structures, free hanging cantilevers were functionalised with amine modified DNA probes. The cantilevers (20 μm wide, 200 μm long and 5 μm thick) were functionalized by dipping them in capture probe DNA solution and hybridised with a complementary 60′-mer long target DNA labelled with Cy3′. A reference chip was only exposed to target DNA solution. Hybridisation was only observed on cantilevers exposed to probe solution prior to hybridisation (Fig. 2B) indicating that SU-8 cantilevers can be functionalised with DNA capture probes. It is, however, likely that the cantilevers are functionalised on both sides of the cantilever but this can be avoided by spotting probe solution onto the chip using a dispensing machine. As demonstrated above (Fig. 1) the DNA immobilised by spotting nL droplets onto SU-8 functions equally well in hybridisation reactions as compared to DNA immobilised by wet incubation.

The drawback of SU-8 being auto-fluorescent will not influence sensors based on electrical readouts like free hanging SU-8 cantilevers and magnetoresistive biochips, another example of a biosensor that we currently pursue (Ejsing et al., 2004). SU-8 based devices can be modified by immobilising thiolated DNA on gold coated SU-8 (Calleja et al., in press). This, however, has several drawbacks. A gold layer can for example cause unwanted bimorph effects and short-circuiting of electrical wires. On both sensors types, SU-8 would be used as a combined insulation/immobilisation layer, hereby saving several process steps.

4. Conclusions

SU-8 could be functionalised with DNA capture probes with functional probe densities of 6–13 fmol/mm^2. The immobilised DNA has excellent specificity down to single base pair level indicating that probes immobilised on SU-8 could be used for genotyping. The stable bond between SU-8 and DNA makes regeneration of sensor surfaces possible. The immobilising of DNA directly to SU-8 avoids several process steps otherwise needed to link DNA to glass and simplifies integration of DNA in biosensors like cantilevers and magnetoresistive biochips.

Acknowledgements

We thank Dorthe Thybo Ganzhorn for spending time in the cleanroom fabricating the photoresist substrate. This project was funded by the Danish research council (Grant #2014-00-0003, DABIC and Grant #26-02-0280, Polymeric cantilevers)

References

Calleja, M., Nordström, M., Álvarez, M., Tamayo, J., Lechuga, L., Boisen, A., in press. Highly sensitive polymer-based cantilever-sensors for DNA detection. Ultramicroscopy.

Calleja, M., Rasmussen, P., Johansson, A., Boisen, A., 2003. Polymeric mechanical sensors with integrated readout in a microfluidic system. In: Proceedings of the SPIE—the International Society for Optical Engineering 5116, pp. 314–321.

Calleja, M., Tamayo, J., Johansson, A., Rasmussen, P., Lechuga, L., Boisen, A., 2004. Polymeric cantilever arrays for biosensing applications. Sens. Lett. 1, 20–24.

Chrisey, L.A., Lee, G.U., O'Ferrall, C.E., 1996. Covalent attachment of synthetic DNA to self-assembled monolayer films. Nucleic Acids Res. 24, 3031–3039.

Chuang, Y.-J., Tseng, F.-G., Cheng, J.-H., Lin, W.-K., 2003. A novel fabrication method of embedded micro-channels by using SU-8 thick-film photoresists. Sens. Actuators A: Phys. A 102, 64–69.

Dufva, M., Petronis, S., Bjerremann Jensen, L., Krag, C., Christensen, C., 2004. Characterization of an inexpensive, non-toxic and highly sensitive microarray substrate. Biotechniques 37, 286–296.

Eisen, M.B., Brown, P.O., 1999. DNA arrays for analysis of gene expression. Methods Enzymol. 303, 179–205.

Ejsing, L., Hansen, M., Menon, A., Ferreira, H., Graham, D., Freitas, P., 2004. Planar Hall effect sensor for magnetic micro- and nanobead detection. Appl. Phys. Lett. 84, 4729.

Fixe, F., Dufva, M., Telleman, P., Christensen, C.B., 2004a. Functionalization of poly(methyl methacrylate) (PMMA) as a substrate for DNA microarrays. Nucleic Acids Res. 32, e9.

Fixe, F., Dufva, M., Telleman, P., Christensen, C.B., 2004b. One-step immobilization of aminated and thiolated DNA onto poly(methylmethacrylate) (PMMA) substrates. Lab. Chip. 4, 191–195.

Genolet, G., Brugger, J., Despont, M., Dreschler, U., Vettiger, P., de Rooj, N., Anselmetti, D., 1999. Soft, entirely photoplastic probes for scanning force microscopy. Rev. Sci. Instrum. 70, 2398.

Genolet, G., Despont, M., Vettiger, P., Staufer, U., Noell, W., de Rooj, N., Cueni, T., Bernal, M.-P., Marquis-Weible, F., 2001. Micromachined photoplastic probe for scanning near-field optical microscopy. Rev. Sci. Instrum. 72, 3872.

Heuschkel, M.O., Buisson, B., Renaud, P., 1998. Buried microchannels in photopolymer for delivering of solutions to neurons in a network. Sens. Actuators B: Chem. 48, 356–361.

Jackman, R.J., Floyd, T.M., Ghodssi, R., Schmidt, M.A., Jensen, K.F., 2001. Microfluidic systems with on-line UV detection fabricated in photodefinable epoxy. J. Micromech. Microeng. 11, 263–269.

Lee, G.-B., Lin, C.-H., Chang, G.-L., 2002. Multi-cell-line micro flow cytometers with buried SU-8/SOG optical waveguides. In: Proceedings of the 15th IEEE International Conference on Micro Electro Mechanical Systems. In Technical Digest. MEMS 2002 IEEE International Conference, p. 503.

Mogensen, K.B., El-Ali, J., Wolff, A., Kutter, J.P., 2003. Integration of polymer waveguides for optical detection in microfabricated chemical analysis systems. Appl. Opt. 42, 4072–4079.

Seidemann, V., Butefisch, S., Buttgenbach, S., 2002a. Fabrication and investigation of in-plane compliant SU8 structures for MEMS and their application to micro valves and micro grippers. Sens. Actuators A: Phys. 97–98, 457–461.

Seidemann, V., Rabe, J., Feldmann, M., Buttgenbach, S., 2002b. SU8-micromechanical structures with in situ fabricated movable parts. Microsyst. Technol. 8, 348–350.

Steel, A.B., Levicky, R.L., Herne, T.M., Tarlov, M.J., 2000. Immobilization of nucleic acids at solid surfaces: effect of oligonucleotide length on layer assembly. Biophys J. 79, 975–981.

Strother, T., Hamers, R.J., Smith, L.M., 2000. Covalent attachment of oligodeoxyribonucleotides to amine-modified Si (0 0 1) surfaces. Nucleic Acids Res. 28, 3535–3541.

Zammatteo, N., Jeanmart, L., Hamels, S., Courtois, S., Louette, P., Hevesi, L., Remacle, J., 2000. Comparison between different strategies of covalent attachment of DNA to glass surfaces to build DNA microarrays. Anal. Biochem. 280, 143–150.